

SEARCH FOR CHARGED LEPTON FLAVOUR VIOLATION WITH CMS

Von der Fakultät für Mathematik, Informatik und Naturwissenschaften
der RWTH Aachen University zur Erlangung des akademischen Grades
eines Doktors der Naturwissenschaften genehmigte Dissertation

vorgelegt von

Master of Science RWTH Aachen University

SÖREN ERDWEG

aus Erkelenz

Berichter: Univ.-Prof. Dr. rer. nat. Thomas Hebbeker
Priv. Doz. Dr. rer. nat. Oliver Pooth

Tag der mündlichen Prüfung: 25.04.2018

Diese Dissertation ist auf den Internetseiten der Universitätsbibliothek verfügbar.

SEARCH FOR CHARGED LEPTON FLAVOUR VIOLATION WITH CMS

SÖREN ERDWEG

Winter 2018

ABSTRACT

Events with an electron muon pair and high invariant mass are the ideal place to search for physics beyond the standard model of particle physics. Over a low background of the standard model many models of new physics could be discovered. The final state with one electron and one muon allows for the interpretation in three channels: $e\mu$, $e\tau_\mu$ and $\mu\tau_e$, which are used to search for R-parity violating supersymmetry. Quantum black holes and new Z' bosons were also searched for in the $e\mu$ channel. No sign for new physics was found and the so far most stringent limits for direct searches were put on the parameters of the models.

ZUSAMMENFASSUNG

Ereignisse mit einem Elektron und Muon Paar und hoher invarianter Masse sind der ideale Platz um nach neuer Physik die über das Standard Modell der Teilchenphysik hinausgeht zu suchen. Über einem niedrigen Untergrund vom Standard Modell können viele Theorien von neuer Physik entdeckt werden. Der Endzustand mit einem Elektron und einem Muon erlaubt die Interpretation in drei Kanälen: $e\mu$, $e\tau_\mu$ und $\mu\tau_e$, welche zur Suche nach R-Parität verletzender Supersymmetrie genutzt werden. Nach schwarzen quanten Löchern und neuen Z' Bosonen wurde ebenfalls im $e\mu$ Kanal gesucht. Kein Zeichen von neuer Physik wurde gefunden und die bisher restriktivsten Ausschlussgrenzen für direkte Suchen wurden auf die Parameter der Modelle gesetzt.

CONTENTS

1	INTRODUCTION	1
2	THEORY	5
2.1	Standard Model	5
2.2	Beyond standard model with LFV	8
2.2.1	RPV SUSY	8
2.2.2	QBH	12
2.2.3	Zprime	15
2.2.4	Existing cLFV limits	16
3	EXPERIMENTAL SETUP	19
3.1	LHC	19
3.2	CMS	21
3.2.1	Electron reconstruction	24
3.2.2	Muon reconstruction	26
3.2.3	Missing transverse energy reconstruction	30
4	ANALYSIS	33
4.1	Signal simulation	33
4.2	Object selection	37
4.2.1	Electron	37
4.2.2	Muon	40
4.2.3	Tau	42
4.3	Event pre-selection	44
4.3.1	All channels	44
4.3.2	$e\mu$ channel	47
4.3.3	$e\tau_\mu$ and $\mu\tau_e$ channels	47
4.4	Background description	49
4.4.1	Prompt backgrounds	50
4.4.2	Misidentified or non-prompt backgrounds	51
4.5	Event corrections	54
4.5.1	Global event corrections	55
4.5.2	Electron corrections	57
4.5.3	Muon corrections	57
4.5.4	E_T^{miss}	58
4.6	Kinematic event selection	58
4.6.1	$e\tau_\mu$ channel	58
4.6.2	$\mu\tau_e$ channel	62
4.7	Selection efficiencies	66
4.7.1	$e\mu$ channel	67
4.7.2	$e\tau_\mu$ channel	68
4.7.3	$\mu\tau_e$ channel	70
4.8	Mass resolution	71

4.8.1	$e\mu$ channel	73
4.8.2	$e\tau_\mu$ channel	74
4.8.3	$\mu\tau_e$ channel	76
4.9	Systematic uncertainties	77
4.9.1	Experimental uncertainty sources	77
4.9.2	Theoretical uncertainty sources	83
4.9.3	Effect on the $e\mu$ channel	87
4.9.4	Effect on the $e\tau_\mu$ channel	91
4.9.5	Effect on the $\mu\tau_e$ channel	92
5	RESULTS	97
5.1	Invariant mass distribution	97
5.1.1	$e\mu$ channel	97
5.1.2	$e\tau_\mu$ channel	102
5.1.3	$\mu\tau_e$ channel	108
5.2	Statistical Interpretation	111
5.3	Limits	115
5.3.1	$e\mu$ channel	118
5.3.2	$e\tau_\mu$ channel	129
5.3.3	$\mu\tau_e$ channel	132
5.3.4	Comparison to other direct searches	136
6	SUMMARY & CONCLUSIONS	139
A	SAMPLES	141
A.1	Datasets	141
A.2	Signal simulation	141
A.3	Background simulation	144
B	CONVENTIONS	147
B.1	Definitions in additional distributions	147
B.2	Coordinate system	148
B.3	Conventions	148
B.3.1	Natural units	148
C	SUPPLEMENTARY FIGURES AND TABLES	149
	BIBLIOGRAPHY	165

INTRODUCTION

This thesis presents the latest search for lepton flavour violation at high mass in the context of the CMS experiment at CERN. This search has been performed with the proton–proton collisions recorded during the year 2016 at a centre of mass energy of 13 TeV. This is the highest energy every utilized for such an analysis. The proton–proton collisions are delivered by the LHC accelerator of CERN and are recorded by the CMS detector.

Lepton flavour violation has been well established in the neutrino sector many years ago. Therefore, it seems reasonable to assume that also in the charged lepton sector lepton flavour violation occurs (charged lepton flavour violation = CLFV). In the standard model of particle physics, lepton flavour is conserved, but there is no associated symmetry to support this behaviour. The observation of a lepton flavour violating (LFV) process would be evidence of physics beyond the standard model. Many models of physics beyond the standard model predict new states that do not conserve lepton number and can therefore be discovered in the final states of a proton–proton collisions that violate lepton number. In these final states the expected background from standard model processes, mis-identified as lepton flavour violating, is small. Therefore the observation of an excess of events would be a clear indication for physics beyond the standard model. The three models studied in this thesis are R-parity violating supersymmetry, quantum black holes in models with extra dimensions and new heavy Z' bosons. They cover a large range of potential signal shapes in the invariant mass distribution, from very narrow resonances in the supersymmetry model to a very broad signal by quantum black holes.

The principle combinations for final states with two charged leptons that violate lepton number are $e\mu$, $e\tau$ or $\mu\tau$. As the tau is not a stable particle, it decays before it can be detected directly either into an electron (τ_e), a muon (τ_μ) or a hadronic jet (τ_h). All decays are accompanied by neutrinos. This then results in seven possible final states, that can be studied. Five of them have only leptons in the final state while two have one hadronic jet in the final state. From the five leptonic final states, three have leptons of different flavour in the final state ($e\mu$) with or without neutrinos, the other two have two same flavour leptons including neutrinos. This analysis only studies the three leptonic opposite flavour final states pictured in Fig. 1. The schemata for the other channels are included in the Appendix in Fig. 100.

The analysis, presented in this thesis, was published in a preliminary publication with 2015 data for only the $e\mu$ channel (See Ref. [1]) and was submitted to JHEP for publication in a simplified version of the $e\mu$ channel analysis with 2016 data (See Ref. [2]).

The thesis is structured to follow the flow of the analysis, it starts therefore with an introduction first of the theoretical aspects relevant to the analysis. In this theory introduction the standard model as the basis of our current knowledge and as the model for all background processes is presented, followed by the potential beyond the standard model theories studied in this thesis. The next step in the analysis flow after estab-

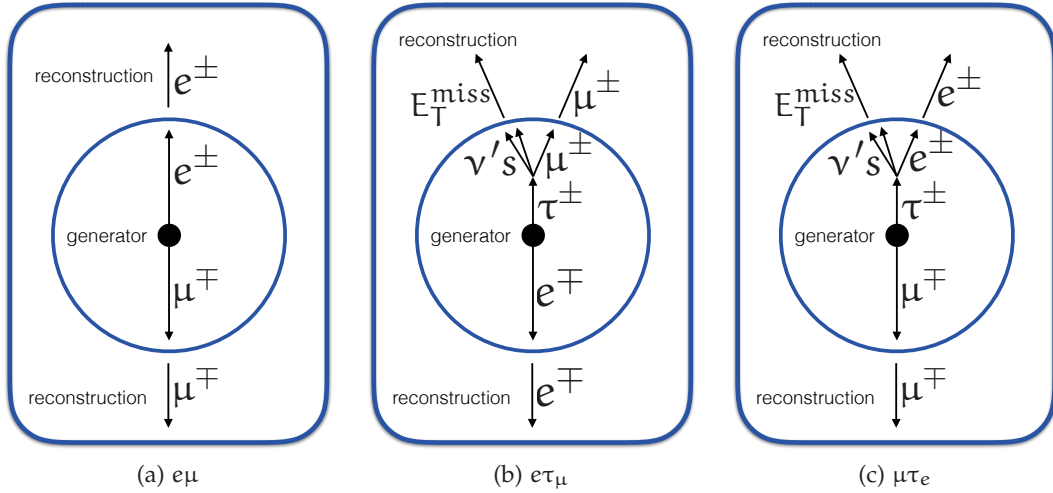


Figure 1: Schematic illustration of the possible channels with two charged leptons that do not conserve lepton number and are studied in this analysis. Shown is the part of the interaction which is not detected, labelled generator, which is the production of $e\mu$, $e\tau$ or $\mu\tau$ and the subsequent decay of the tau if applicable in either electron or muon plus neutrinos. On the outside the signature of the event as seen in the detector is illustrated, labelled reconstruction. The charged leptons are reconstructed as they are, while the neutrinos can be detected only indirectly as missing E_T .

lishing the theoretical models is the experimental setup. In this experimental chapter the LHC accelerator and the CMS detector are introduced, including the techniques used to reconstruct the particles from the proton–proton collisions and making them available for the analysis.

After these more general introductory chapters the detailed steps of the analysis are explained. At first there is the simulation of the studied signal processes, which leads to the pre-selection criteria. These pre-selection criteria derive from the expected signal events and apply to all events in the different studied channels. This leads to the invariant mass reconstruction of the final state objects for the three studied channels. From these selection criteria the background composition can be derived, by looking which standard model process could contribute to the pre-selected events. Afterwards different corrections that need to be applied are introduced, followed by the kinematic selection criteria. These criteria are used to further separate signal from background events. These selection steps are applied to all events and the performance of the analysis can be measured in two quantities, the efficiency of the selection and the invariant mass resolution. These two quantities are shown for all studied channels. The last step of the analysis chain is then to quantify the systematic uncertainties that are relevant for the analysis.

The last part of this thesis are the results. This section starts with the different invariant mass distributions, which are the result of all the selection criteria and corrections. These invariant mass distributions are then the input for the statistical interpretation. This is used to quantify the agreement between background and signal expectation on the one hand and the observed data on the other hand. It is also used to derive limits on the various parameters of the beyond the standard model physics models, which

are compatible with the observed data. These limits are compared to other available analyses to put them in the broader context of searches for lepton flavour violation.

The thesis concludes with a summary of the results. In the appendix some details are given first for the Monte Carlo simulations used throughout the analysis, followed by the used conventions as well as various additional figures, which are referenced to at appropriate locations within the thesis.

This chapter introduces the theoretical background of the analysis from two perspectives. First there is the standard model of particle physics (Sec. 2.1) which is a set of theories which comprehend the best current knowledge of particle physics. The standard model describes the background processes expected in the analysis and should be separated from the new physics models that are studied in this analysis. The basic concepts which are relevant for this analysis are introduced. A comprehensive introduction into the standard model can be found e. g. in Ref. [3] while all the masses and other measurements in this section are from Ref. [4] if not indicated otherwise.

The second part introduces the theories beyond the standard model (Sec. 2.2) which are studied in this analysis. The models are chosen because they predict final states with charged lepton flavour violation and because they are theoretically well motivated. The model choice also tries to cover as many different potential signal shapes as possible, from a narrow resonance over a wide resonance to a very broad signal.

The main focus of this thesis is on the search for new particles predicted by this possible new physics model with charged lepton flavour violation, therefore the focus of this theory chapter is on the phenomenology of the models and not so much on the underlying mathematical details of the theory. Nevertheless an example motivation for the theories beyond the standard model is given, starting from a shortcoming of the standard model. The solution of this shortcoming motivates the formulation of beyond the standard model (BSM) theories, some of them are studied in this analysis.

In the last section of this chapter a short overview is given on already existing constraints on the studied BSM models, either from other collider searches or from low energy experiments which are sensitive to charged lepton flavour violations.

2.1 STANDARD MODEL

The standard model of particle physics is the result of many decades of experimental and theoretical work. It describes all known matter particles and their interactions, including the particles mediating the interaction, in a mathematically consistent way. The only known interaction in nature which is not described by the standard model is gravity, this is one of the shortcomings of the theory. All matter particles of the standard model are summarized in Tab. 1, while the interactions are summarized in Tab. 2 with the mediating particles and also the Higgs boson.

All these particles interact if they are charged in the interaction, e. g. electrically charged particles can interact with photons and therefore take part in the electromagnetic interaction. Colour charged particles interact via the strong interaction mediated by gluons and all particles carrying the weak charge participate in weak interactions. In addition to the particles listed in Tab. 1 an antiparticle exists for each listed particle with the same properties but reversed sign for all charges.

The particle properties together with the dynamics for each kind of charge describe all possible interactions between particles. However, some quantities have been found

Table 1: Matter particles of the standard model, separated in leptons (upper block) and quarks (lower block), sorted by number of particle generation from 1st to 3rd. For each particle its mass is given, or, if the mass is not known, the upper limit on the mass (for neutrinos). Also listed are the charges for each particle of electromagnetism (q_e), colour charge of the strong interaction (q_c) and of the weak interaction (q_w).

Generation	Particle	mass (MeV)	charge (q_e, q_c, q_w)	Particle	mass (MeV)	charge (q_e, q_c, q_w)
1st	e	0.511	(-1, 0, 1)	ν_e	$< 2 \cdot 10^{-6}$	(0, 0, 1)
2nd	μ	105.7	(-1, 0, 1)	ν_μ	< 0.19	(0, 0, 1)
3rd	τ	1777	(-1, 0, 1)	ν_τ	< 18.2	(0, 0, 1)
1st	up u	2.3	(2/3, 1, 1)	down d	4.8	(-1/3, 1, 1)
2nd	charm c	1275	(2/3, 1, 1)	strange s	95	(-1/3, 1, 1)
3rd	top t	173200	(2/3, 1, 1)	bottom b	4180	(-1/3, 1, 1)

Table 2: Bosons of the standard model sorted by their corresponding interaction. The Higgs boson gives the weak interaction bosons their masses and is therefore not associated with an explicit interaction. In addition the masses of the bosons and their charges are listed.

Interaction	Particle	mass (GeV)	charge (q_e, q_c, q_w)
Electromagnetic	γ	0	(0, 0, 0)
Weak	W^\pm, Z^0	80.4, 91.2	($\pm 1/0, 0, 1$)
Strong	g	0	(0, 1, 0)
	H	125.7	(0, 0, 1)

to be conserved in the standard model and further constrain the possible interactions, e. g. the conservation of charge in all interactions or the conservation of number of leptons. There are also individual lepton numbers, which is a quantity assigned to each generation of leptons, so the electron and electron neutrino have both an electron lepton number of +1, all other particles have zero. The corresponding antiparticles have the same numbers with reversed sign (e. g. the positron -1). The conservation of these individual lepton numbers is purely motivated by observations and is not based on a fundamental theory. The violation of this conservation was already observed in the neutrino sector, where e. g. the process $\nu_e \rightarrow \nu_\mu$ was observed [4]. In the charged lepton sector the conservation of individual lepton numbers holds up to all tests up to now, so an observation of such a process would be a clear sign for new physics which is studied in this thesis [5].

Combining these particles, interactions and constraints leads to the processes of the standard model that can be observed and can contribute to the background expectation in a search for new physics. One example of such a standard model process is the pair

production of top quarks which decay into two b quarks, two neutrinos, an electron, and a muon. This process can be seen in the Feynman diagram in Fig. 2.

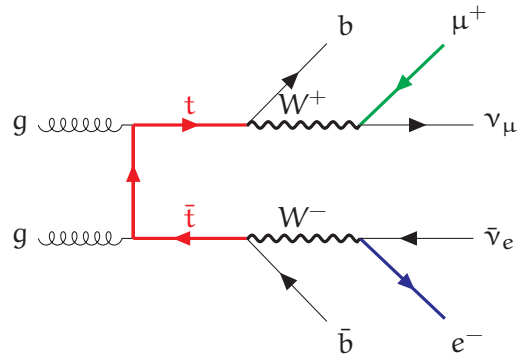


Figure 2: One possible Feynman diagram for the top quark pair production via gluon-gluon fusion and the subsequent decay into the $e\mu + x$ final state. The final state also contains two neutrinos and two b quarks.

The probability for a process to occur can be calculated from these Feynman diagrams. It depends on the masses and momenta of the particles and each vertex contributes with the corresponding coupling constant which is proportional to the charge of the interaction. Therefore, diagrams with more vertices which result in the same process need to be considered, but their contribution to the probability and consequently to the rate gets lower with the number of vertices if the coupling constant is smaller than 1. This is the case for all standard model interactions. All these interactions can contribute to the background of this analysis if they contain an electron and muon in the final state. Therefore they need to be modeled with high precision.

The Higgs particle plays a special role in the standard model as it doesn't belong to the matter nor the mediating particles. The unified electro-weak interaction is separated into the observed electromagnetic and weak interactions by the spontaneous symmetry breaking. The Higgs is essential for this process to work. It also gives the W and Z bosons its masses and ensures that the photon is massless.

The masses of particles depend on their interaction with the Higgs boson and can therefore be described by Feynman diagrams. These Feynman diagrams for the Higgs boson mass can also be affected by higher order corrections due to the contribution of diagrams with more vertices of closed loops. This effect can be illustrated by the following equation Eq. 1.

$$\text{---} \text{---} \text{---} \text{---} \text{---} \text{---} = \text{---} \times \text{---} \text{---} + \text{---} \text{---} \text{---} \text{---} \text{---} \text{---} + \dots \left(\text{---} \text{---} \text{---} \text{---} \text{---} \text{---} \right) \tag{1}$$

This Feynman diagrams shows that the observed mass (left side of the equation) can be calculated from the bare mass (first term) and higher order corrections (other terms). The effect of these higher order corrections depends on the momenta of the particles in the loop, which can be as big as the highest energy scale Λ in the theory. As the standard model does not include gravity, it is natural to assume that this high scale

Λ is when gravity plays an important role in particle interactions and the standard model is no longer valid. This is the so called Planck scale M_P of about 10^{18} GeV. This would result in huge corrections to the bare mass. This big correction can in principle be canceled by the free parameter of the bare Higgs mass, but this mass then would have to be precisely tuned to the corrections to the mass to cancel to the observed mass of 125.7 GeV. This would require a fine tuning to 1 in 10^{14} which seems highly unlikely. This so called fine tuning or hierarchy problem, because of the huge hierarchy between the strength of gravity and of the other interactions, is one of the big open questions of the standard model [6]. For the matter particles, W/Z bosons or the other matter particle these higher order corrections to the mass are in principle also possible but can be cancelled by symmetries in the theory which do not allow big corrections. The Higgs boson does not have such a protection mechanism.

This hierarchy problem can be solved by theories beyond the standard model which are studied in this analysis and are shortly introduced in the following.

2.2 BEYOND STANDARD MODEL WITH LFV

In this section the three theories beyond the standard model studied in this thesis are shortly introduced. The first two models are designed to solve some problems of the standard model, especially the hierarchy problem.

There are two possibilities to solve the problem, either by introducing additional particles which cancel the huge mass corrections exactly or by lowering the upper scale relevant for the corrections. For the first approach to work there has to be a symmetry between the standard model particles and the new particles. This is illustrated in Eq. 1 as the additional corrections in the brackets. This symmetry can be supersymmetry (SUSY), which is the first model that is studied. As the most general approach to SUSY does not produce lepton flavour violation a variant is studied in this analysis, the R-parity violating (RPV) SUSY (Sec. 2.2.1).

The second possibility is to change the energy scale of gravity, assuming this is the high scale Λ in the theory, so that the corrections to the bare mass are small by design. This can be seen in Eq. 1, if Λ is small, the corrections are also small. This can be achieved by introducing new spatial dimensions to the three dimensions of the standard model. If gravity is the only force which could penetrate these extra dimensions, the strength would be greatly reduced and the corresponding energy scale lowered. Extra dimensions would also lead to new phenomena, like quantum black holes (QBHs) which would decay into a lepton flavour violating final state (Sec. 2.2.2).

The basic idea of the third model is motivated by many extensions of the standard model, therefore a benchmark model for high mass particles is chosen. The decay of the particle does not conserve lepton flavour. This is not motivated directly by solving problems of the standard model or explaining new observations, but to cover the phenomenology of many models. It is a carbon copy of the Z boson, called Z' , with a higher mass and the decay into an electron and muon (Sec. 2.2.3).

2.2.1 RPV SUSY

Supersymmetry is regarded as one of the most promising theories of physics beyond the standard model due to its potential to solve not only the hierarchy problem, but

also some other open questions about the standard model like the unification of gauge couplings or providing a dark matter candidate. The following introduction in SUSY and RPV is based on Refs. [6, 7].

Supersymmetry is a symmetry in particle spins, it assigns each half integer spin particle (like the matter particles in the standard model) an integer spin partner particle and vice versa every integer spin particle (like the force mediating particles in the standard model) a half integer spin partner particle. Through these so called super partners a symmetry in spins is created, and as loops of particles with different spin carry a different sign, the additional loops for the Higgs mass correction by supersymmetric particles exactly cancel the standard model corrections and solve therefore the hierarchy problem [6].

The most generic formulation of supersymmetry introduces interactions which violate lepton number, but also baryon number, similar as lepton number but for quarks. The violation of baryon number is tightly constrained by experimental observation (See Ref. [8]). In many models of supersymmetry these interactions are forbidden by an additional \mathbb{Z}_2 symmetry, called R-parity.

In this model the conservation of R-parity is not assumed. The R-parity violating (RPV) terms of the superpotential lead to the three possible couplings indicated in Fig. 3. For details, see Ref. [7].

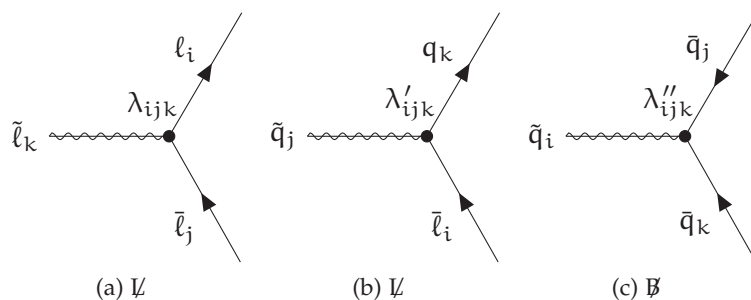


Figure 3: Basic couplings allowed in the RPV SUSY model. They either violate lepton number \mathbb{L} ((a) and (b)) or baryon number \mathbb{B} . ((c)). The supersymmetric partner particles $\tilde{\ell}$ or \tilde{q} (indicated by wavy lines) couple to either standard model leptons ℓ or quarks q . The three possible couplings are λ , λ' or λ'' . The generation is given for each particle and coupling by the indices $i, j, k \in \{1, 2, 3\}$ [7].

The couplings λ and λ' lead to lepton number (L) violating interactions, whereas baryon number (B) violation is introduced by the couplings λ'' . All the couplings exist for the different generations of leptons and quarks and might differ from each other. They are therefore labelled with the generation indices $i, j, k \in \{1, 2, 3\}$ (e. g. λ_{123}). There are some relations between different couplings due to the global requirements of the theory to be valid for a wide energy range, these are $\lambda_{ijk} = -\lambda_{jik}$ and $\lambda''_{ijk} = -\lambda''_{ikj}$. Due to the large number of additional interactions and parameters in RPV SUSY, it is customary to adopt the dominant coupling scheme, i. e. assuming the couplings relevant for the analysis at hand are finite and all other couplings equal zero.

In order to account for the tight constraints that the measured lower limit on the proton lifetime puts on baryon number violating processes [8], at least one of the sets of couplings leading to lepton or baryon number violation must be extremely small. The smallness of the couplings is guaranteed by a discrete symmetry, like R-parity

in many SUSY models. Other discrete symmetries are well motivated and have been studied in the literature [9, 10]. For this study, the baryon triality symmetry (B_3) that cancels the baryon number violating terms with couplings λ'' is considered [10].

The relevant aspects of RPV SUSY in the production of a resonance decaying into a lepton flavour violating lepton pair at hadron colliders are given in the following list. A minimum of three SUSY parameters has to be chosen for this simplified RPV signal model used in this analysis:

1. The single production of supersymmetric partner particles (called sparticles) is allowed. In particular, sparticles can be produced resonantly. The tau sneutrino $\tilde{\nu}_\tau$ is chosen as the resonantly produced slepton. It is a viable lightest supersymmetric particle (LSP) candidate and is assumed to be the LSP for the simplified signal model [11]. In this case, only decays into standard model particles are allowed. The corresponding parameter is the tau sneutrino mass $m_{\tilde{\nu}_\tau}$.
2. The coupling λ'_{311} leads to the production of the tau sneutrino (supersymmetric partner to the neutrino) in $d\bar{d}$ annihilation. The $\tilde{\nu}_\tau$ production cross section for a given value of λ'_{3ii} at a proton-proton collider is largest for the coupling to the first generation because of the parton densities in the proton. According to the possible couplings in Fig. 3, the slepton couples to the down-type quark/anti-quark pairs only.
3. The couplings λ_{1i2} or λ_{2i1} lead to a lepton number violating decay of a sneutrino into an electron/muon pair. Both couplings are considered in the analysis and assumed to be of the same value $\lambda_{132} = \lambda_{231}$ ¹. The decay into an electron/tau pair is possible via the coupling λ_{1i3} , while the decay into a muon/tau pair happens via the λ_{2i3} coupling. For the decays containing a tau only one coupling is contributing in each channel as the couplings λ_{3i1} and λ_{3i1} are not allowed by the symmetry of the model.

In this simplified model, the tau sneutrino can decay either into the final state under study, a lepton flavour violating lepton pair, via the coupling λ_{132} (λ_{133} or λ_{233}) or into a $d\bar{d}$ pair via the coupling λ'_{311} . This process studied in this analysis is illustrated in the Feynman diagram in Fig. 4. In the narrow width approximation² and leading order, the dependence of the partonic cross section of the process shown in Fig. 4 on λ_{132} and λ'_{311} is given by the formula:

$$\sigma \cdot \text{BR}(\tilde{\nu}_\tau \rightarrow e\mu) \sim (\lambda'_{311})^2 \frac{\Gamma_{\tilde{\nu}_\tau}^{e\mu}}{\Gamma_{\tilde{\nu}_\tau}^{\text{tot}}} \sim \frac{(\lambda'_{311})^2 \left((\lambda_{132})^2 + (\lambda_{231})^2 \right)}{3 (\lambda'_{311})^2 + \left((\lambda_{132})^2 + (\lambda_{231})^2 \right)}. \quad (2)$$

The equation holds also for the $e\tau$ and $\mu\tau$ final state, just with $(\lambda_{133})^2$ or $(\lambda_{233})^2$ instead of $\left((\lambda_{132})^2 + (\lambda_{231})^2 \right)$. It is later used to derive limits on the two individual couplings contributing to the signal.

¹ Throughout the text only λ_{132} is mentioned for simplicity, it is always assumed that both couplings are non zero and $\lambda_{132} = \lambda_{231}$. In formulas all relevant couplings are mentioned explicitly.

² Narrow width approximation means here that the natural width of the $\tilde{\nu}_\tau$ is negligible to the detector resolution and can be approximated with zero.

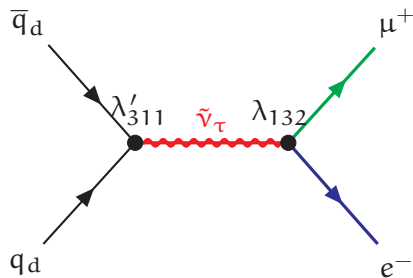


Figure 4: Resonant production of a $\tilde{\nu}_\tau$ in $d\bar{d}$ annihilation and subsequent decay into a $e\mu$ pair with the production and decay couplings λ'_{311} and λ_{132} . A similar diagram also contributes to the $e\mu$ final state with the decay coupling λ_{231} . The process for the $e\tau$ or $\mu\tau$ final states are identical, just with different final state leptons and the decay couplings λ_{133} and λ_{233} respectively. All four Feynman diagrams are shown in Fig. 101 in the appendix.

If the production coupling is much larger than the decay coupling (e. g. for the decay into an electron and muon: $\lambda'_{311} \gg \lambda_{132} = \lambda_{231}$) the dependence on λ'_{311} vanishes. With increased λ'_{311} the production cross section increases, but also the branching ratio for the decay into the $d\bar{d}$ (dijet) final state. In the inverted case, when the decay coupling is much larger than the production coupling (e. g. for the decay into an electron and muon: $\lambda'_{311} \ll \lambda_{132} = \lambda_{231}$), the branching fraction into the desired final state (e. g. electron and muon) is close to 100 % and the sensitivity of the search depends on the production cross section and λ'_{311} .

The total width of the tau sneutrino $\Gamma_{\tilde{\nu}_\tau}$ is given for individual mass points in Tab. 3. It can be approximated at leading order in the narrow width approximation by

$$\frac{\Gamma_{\tilde{\nu}_\tau}}{m_{\tilde{\nu}_\tau}} \approx 0.02 \cdot \left(3(\lambda'_{311})^2 + 2(\lambda_{132})^2 \right). \quad (3)$$

Table 3: Width of the $\tilde{\nu}_\tau$ in the RPV signal model evaluated at LO with CALCHEP generator [12].

$\lambda_{132} = \lambda_{231}$	λ'_{311}	$m_{\tilde{\nu}_\tau}$ (GeV)	$\Gamma_{\tilde{\nu}_\tau}$ (GeV)
0.01	0.01	1000	0.01
0.05	0.05	500	0.12
0.05	0.05	1000	0.25
0.05	0.05	2000	0.50
0.1	0.1	1000	0.99
0.1	0.2	1000	2.79
0.2	0.1	1000	2.19
0.2	0.2	1000	3.98

At the coupling parameter range with sneutrino masses at the TeV scale that is still allowed by other direct searches, the relation $\frac{\Gamma_{\tilde{\nu}_\tau}}{m_{\tilde{\nu}_\tau}} \ll \frac{\sigma(m_{e\mu})}{m_{e\mu}}$ for the narrow width

approximation applies, therefore in the analysis the width of the signal itself can be ignored and the signal is dominated by the detector resolution.

Next-to-leading order (NLO) Feynman diagrams can also significantly contribute to the rate of events via an enhancement of the cross section [13]. The studied higher order processes include corrections to the leading order process of standard model processes, like gluon loops, but also corrections due to supersymmetric particles in loops. All these corrections are summarized in a k-factor, which is a mass dependent factor which scales the leading order cross section to the next-to-leading order one.

Figure 5 shows a comparison of RPV signal cross section in 8 TeV and 13 TeV. The different values of the NLO k-factor are also shown for 8 TeV and 13 TeV as dashed lines.

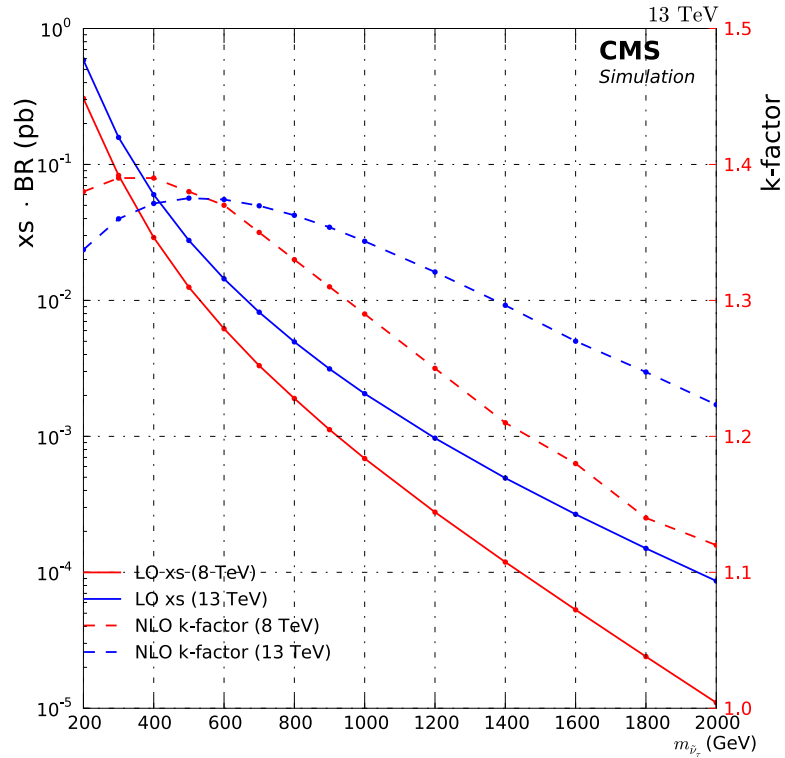


Figure 5: Comparison of the RPV signal cross section for center of mass energies of 8 TeV and 13 TeV, shown in solid lines corresponding to the y-axis on the left side. The different values of the NLO k-factor are also shown for 8 TeV and 13 TeV as dashed lines corresponding to the y-axis on the right side.

2.2.2 QBH

The idea of extra dimensions on top of the usual four of space and time came up in the beginning of the 20th century as a possibility to unite the forces of gravity and electromagnetism. As gravity is described in the general theory of relativity as a property of space itself, it is obvious that it should influence all spatial dimensions and propagate into the so called bulk of the extra dimensions. This would then lead to an reduction of the of the fundamental energy scale Λ for gravity from the Planck scale

M_p . There are two different models for extra dimensions which are studied in this thesis, both can lead to quantum black holes in particle collisions.

RS The first studied model is the Randall-Sundrum (RS) or warped extra dimensions model [14] with one extra dimension. In this model the extra dimension is warped and orbifolded with the radius R . This results in a circle with identified upper and lower halves and two three dimensional spaces at the two fix points, one being the normal three dimensional space. The Planck scale would then be lowered via the radius of the extra dimension

$$M_p^2 \cdot \frac{c}{2(1 - e^{-c\pi R})} = \Lambda^3$$

ADD The second model is the ADD or large extra dimension model, named after Arkani-Hamed, Dimopoulos and Dvali with more than one extra dimension [15]. In this model the potential extra dimensions are finite in contrast to the infinite spatial three dimensions of the standard model. If the size of this extra dimension is then small enough, it explains why it is not yet observed. Therefore, one extra dimension is excluded in this model as it would yield a huge extra dimension, two extra dimensions are disfavoured by astrophysical observations [16], but three or more extra dimensions are in agreement with current observations [17]. The lowering of the Planck scale would then be propotional to the volume of the extra dimensions

$$\frac{M_p^2}{V_n} = \Lambda^{2+n}$$

These models allow for the production of microscopic black holes in high energy particle collisions. These black holes are different to their astrophysical counterparts in the fact that their masses are expected to be close to the Planck scale which is in the TeV region for these models. Semi-classical black holes are thermal objects, their decays are expected to be well described by Hawking radiation and they are expected to have masses of 5 to 20 times the Planck scale [18]. With masses expected to be above at least 5 TeV for a 1 TeV Planck scale it is unlikely that semi-classical thermal black holes will be observed at the LHC within proton-proton collision at a centre of mass energy of 13 TeV, which is even further reduced by the fact that not the protons collide but the partons inside the proton.

It is the idea of the model to extrapolate the semi-classical black hole close to the Planck scale in the regime where quantum gravity dominates. These so called quantum black holes (QBH) are expected to have a mass close to the Planck scale of a few TeV and that they decay into final states with just very few high energy particles. They are expected to conserve colour and electromagentic charge, but not global charges, like lepton flavour. QBHs can therefore decay to many different final states. Studied in this analysis is the annihilation of two quarks, forming a QBH and the subsequent decay $QBH \rightarrow e\mu$. This process is illustrated in the Feynman diagram in Fig. 6.

The cross section is then extrapolated from the semi classical black hole into the quantum regime as the underlying theory of quantum gravity is not yet known. In this

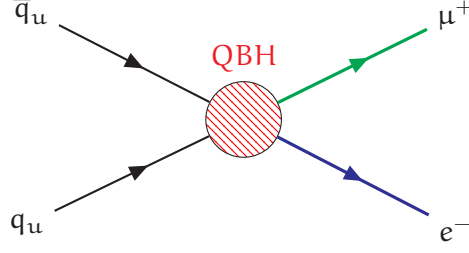


Figure 6: Feynman diagram of the studied QBH process. Quarks and anti-quark annihilate to form a QBH, which then decays into an electron and muon. All quarks flavours in the initial state are possible and u is selected here just as an example.

non-thermal black hole model, masses are quantised in terms of the Planck scale, the cross section is then given by the sum over the individual ones

$$\sigma_{\text{tot}}^{\text{pp}}(s, n, \Lambda) = \sum_i \sigma_{\text{QBH}}^{\text{pp}}(s, m_{\text{QBH}}^i, n, \Lambda) \quad (4)$$

where m_{QBH} is the mass of the black hole, \sqrt{s} is the centre of mass energy, n is the number of extra dimensions and Λ is the reduced Planck mass. One can therefore describe QBHs as heavy particle states with a very short life time ($\Gamma(\text{QBH} \rightarrow 2 \text{ particles}) \sim \frac{1}{64\pi^2} m_{\text{QBH}}$ using dimensional analysis). Each individual production cross section has the following form

$$\begin{aligned} \sigma_{\text{QBH}}^{\text{pp}}(s, m_{\text{QBH}}, n, \Lambda) = \pi r_s^2(m_{\text{QBH}}, n, \Lambda) \int_0^1 2zdz \int_{\frac{(m_{\text{QBH}})^2}{y(z)^2 s}}^1 du \int_u^1 \frac{dv}{v} \\ \times F(n) \sum_{i,j} f_i(v, Q) f_j(u/v, Q) \end{aligned} \quad (5)$$

with the Schwarzschild radius r_s , which is

$$r_s(M_{\text{QBH}}, n, M_{\text{D}}) = k(n) \Lambda^{-1} [m_{\text{QBH}}/\Lambda]^{1/(1+n)} \quad (6)$$

where $z \equiv b/b_{\text{max}}$ is the rescaled impact parameter, $F(n)$ and $y(z)$ describe the effects of inelasticity numerically fitted by Yoshino and Nambu [19, 20]. The labels i, j run over the different particle species, f_i, f_j are the parton distribution functions evaluated at the scale of momentum transfer Q , u and v are the momentum fractions of the incoming particles and $x_{\text{min}} = m_{\text{th}}/\Lambda$ is the ratio of the threshold of the black hole production m_{th} over the reduced Planck mass. The n -dimensional Schwarzschild radius is given in Eq. 6 with

$$k(n) = \left[2^n \sqrt{\pi}^{n-3} \frac{\Gamma((3+n)/2)}{2+n} \right]^{1/(1+n)}. \quad (7)$$

Another approach to get insight in the phenomenology is to estimate the cross section by the classical geometric cross section, as defined by the hoop conjecture for the

creation of a black holes [21]. Also taking into account the production threshold, the cross section would be proportional

$$\sigma \propto \pi r_s^2 \Theta(\sqrt{s} - \Lambda) \quad (8)$$

where Θ is a threshold function [22].

The consequence of Θ in Equation 8 is that the mass distribution of these QBHs can be described as a step function, the amplitude being non-zero from the nominal mass of the black hole, m_{th} (which is the threshold mass for QBH production), and remaining constant at higher mass values. However the effect of PDFs distorts this shape, causing the rising edge of the step function to be less sharp and rather than a plateau following the maximum, there is a monotonically decreasing tail. The shape of different QBHs is shown in Fig. 7 for three different threshold masses and $n = 1, \dots, 6$ extra dimensions. To compare the shape all signals are normalized to unity. For low masses there is a slight difference as a function of n , higher number of extra dimensions yield a steeper signal, for higher masses the effect is no longer present.

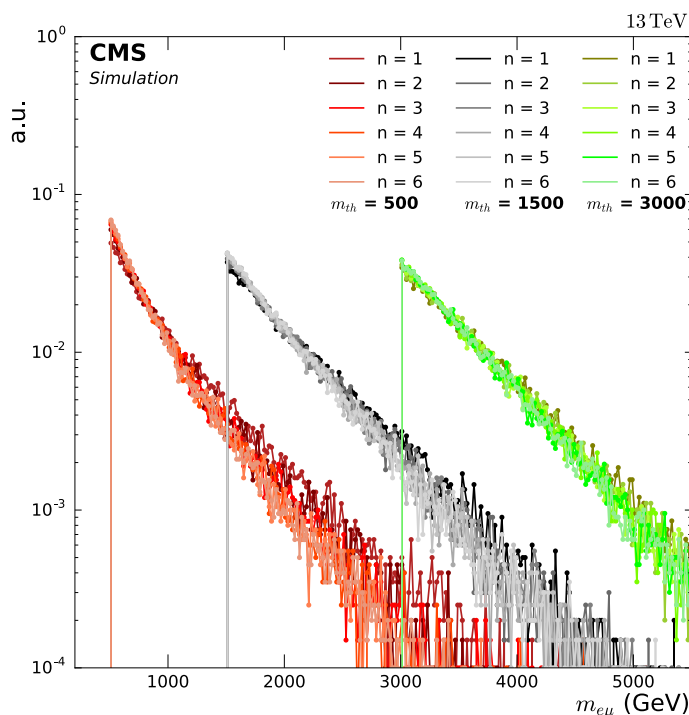
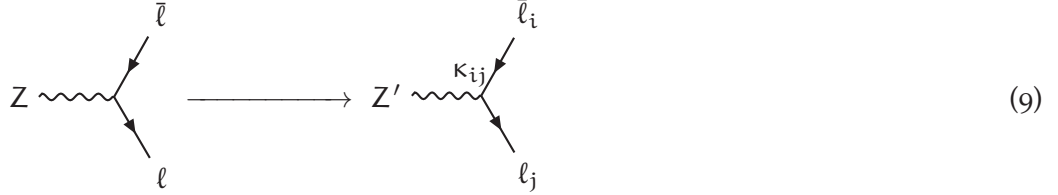


Figure 7: Simulated distributions of different QBHs as a function of the $e\mu$ mass normalized to unity. The varied parameters are the threshold mass and the number of extra dimensions ($n = 1$ corresponds to the RS model, while all other values correspond to the ADD model). The effect of n is only present for low threshold masses, for higher n it vanishes.

2.2.3 Z_{prime}

Many different models predict the existence of new interaction bosons, especially partners to the Z boson, called Z' [23]. To study as many of these models as possible without the dependence on the different specific models, a benchmark model is chosen to

cover them. The choice is the sequential standard model (SSM), which is designed to cover the phenomenology of many models [24]. It works by introducing a new heavy Z' boson as a carbon copy of the standard model Z boson. All properties of the Z boson are kept, the mass is changed to a higher value and the coupling is modified by a factor κ_{ij} :



$$(9)$$

The only difference to the standard model coupling is the constant κ_{ij} . As for the RPV SUSY model a single dominant coupling assumption is imposed, i.e. $\kappa_{12} = 1$, all other $\kappa_{ij} = 0$. In other words, only the LFV decay $Z' \rightarrow e\mu$ is considered. The resulting process which is studied in this analysis is illustrated in the Feynman diagram in Fig. 8.

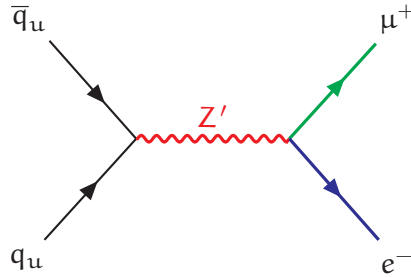


Figure 8: A Feynman diagram of the studied Z' process, first quarks annihilate into a Z' and the subsequent decay into an electron and muon. All quarks flavours in the initial state are possible and u is selected here just as an example.

The branching ratio is chosen to be $\text{BR}(Z' \rightarrow e\mu) = 10\%$ to be comparable to the branching ratio of the standard model Z boson to decay into charged leptons. The branching ratio is also assumed to be constant over the whole mass range from 500 GeV up to 5 TeV. The resulting relative width is about 3% and fairly constant over the whole mass range. The absolute and relative width of the Z' as a function of the mass are shown in Fig. 9.

2.2.4 Existing cLFV limits

In the last section of this theory overview the existing constraints on the studied models from various sources are shortly summarized. These sources include experiments at low energy where the new models could be seen as small corrections and results from previous direct searches like this thesis for this new models at either lower energy or with less amount of data. Not all constraints are completely comparable as some studies include additional assumptions or some analysis are not sensitive to all phenomena.

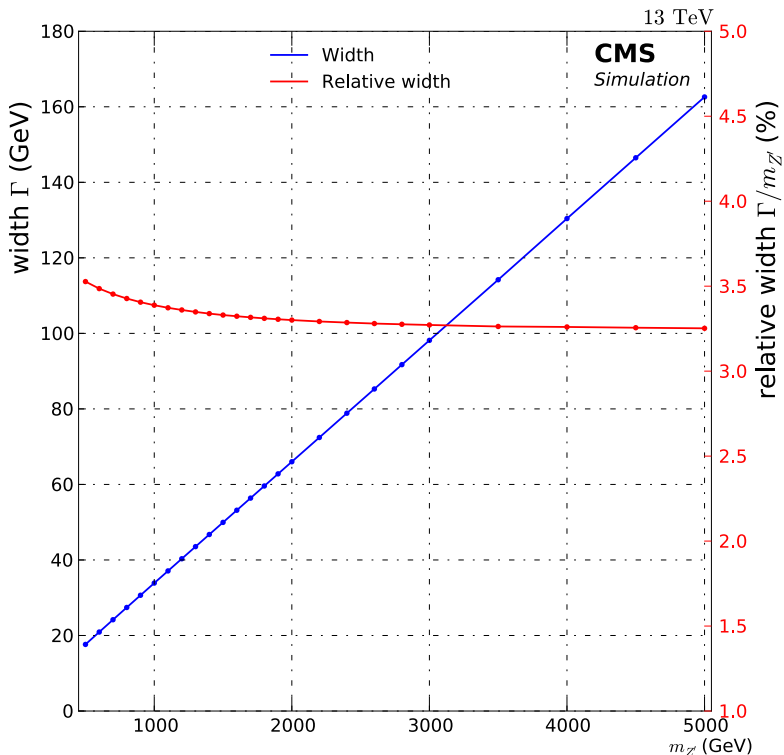


Figure 9: Width of the Z' as function of the Z' mass. Shown is the absolute width in blue (left y-axis) and the relative width in % in red (right y-axis).

RPV SUSY Indirect constraints on the studied RPV SUSY model can be derived from low energy muon to electron conversion experiments. There the process $\mu N \rightarrow eN$ is studied, where the corresponding Feynman diagram is illustrated in Fig. 10.

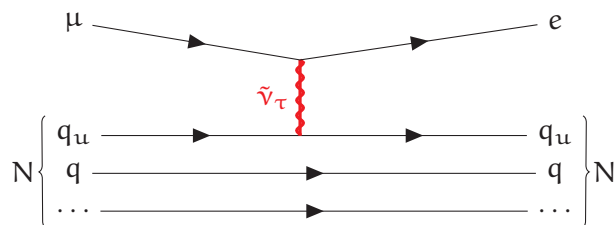


Figure 10: The Feynman diagram for the muon to electron conversion in the vicinity of a nucleus N which can be mediated by a $\tilde{\nu}_\tau$ and can therefore be used to put constraints on the RPV SUSY model.

The measured upper limit of this process can be translated in a limit on the product of the two couplings of $|\lambda'_{311} \cdot \lambda_{312}| < 4.1 \cdot 10^{-9}$ [5, 25]. Some assumption limits the applicability of the constraints, first only the product of both couplings can be probed on the other hand the mass of the $\tilde{\nu}_\tau$ has to be assumed, which is 100 GeV in this interpretation. Direct searches for the resonant production of $\tilde{\nu}_\tau$ at colliders have been performed for quite some time first at the Tevatron by the CDF [26] and Do [27] collaborations. Later, at the LHC this analysis was performed on all data taking eras, first at 7 TeV [28], then 8 TeV [29, 30] and finally at 13 TeV [1, 31]. The most stringent limits are

from the 2015 data taking period at 13 TeV and yield a limit on $m_{\tilde{\nu}_\tau}$ of about 1.0 TeV for couplings of 0.01 and 2.7 TeV for couplings of 0.1.

QBH For a significant contribution of QBHs to low energy observations an infinite number of QBH states is necessary [32, 33]. If that is not the case, decays like $K_L \rightarrow e\mu$ would proceed with no significant contribution from QBHs and hence offer no indirect constraints on QBH production. There have also been direct searches of QBHs in various decay channels. The decay into two quarks was studied by CMS [34], yielding lower bounds on the threshold mass for QBH production of 5.3 TeV (7.8 TeV) for $n = 1$ ($n = 6$). ATLAS performed a similar search, resulting in a lower limit of 8.9 TeV for $n = 6$ [35]. Other final states like lepton plus jets were also studied by the ATLAS collaboration in the past but yielding weaker limits [36, 37]. A search for QBHs decaying to $e\mu$ final state was performed previously by CMS [1] and ATLAS [31] with 13 TeV data from 2015. The resulting limit on the threshold mass range from 2.5 TeV to 4.6 TeV for $n = 1$ and $n = 6$ by ATLAS, while CMS yields 2.5 TeV and 4.5 TeV respectively.

Z' Muon to electron conversion experiments could also be sensitive to lepton flavour violating Z' , by just replacing the $\tilde{\nu}_\tau$ in the Feynman diagram in Fig. 10 with a Z' . Following the calculation of Ref. [38] results in a lower limit on $m_{Z'}$ of about 266 TeV. In this calculation many assumptions are made on the size of the coupling constant or on the nuclear modification factors relevant for the muon to electron conversion studies, therefore a direct comparison is not easy. A directly applicable limit on the studied process $q_u \bar{q}_u \rightarrow Z' \rightarrow e\mu$ comes from direct searches for this model at the LHC by the ATLAS collaboration in the data set from 2015 at 13 TeV, which yields a lower mass limit of 3.0 TeV [31].

EXPERIMENTAL SETUP

In this chapter the experimental setup for this analysis is summarized. The first part gives a short introduction in the LHC accelerator (section 3.1), its performance and important parameters which are relevant for the analysis of the collisions provided by it. In the second part the CMS detector and its infrastructure (section 3.2) used to record the produced collisions is introduced. The focus there lies on the particles used later in the analysis and how they are reconstructed from the different detector components.

3.1 LHC

The Large Hadron Collider (LHC) is the particle accelerator with the highest beam energy in the world and is located at the European centre for nuclear research (CERN) near Geneva, Switzerland. Detailed information on the accelerator can be found in Ref. [39].

The LHC is embedded in CERN's accelerator complex of various linear and circular accelerators which are summarized in Fig. 11.

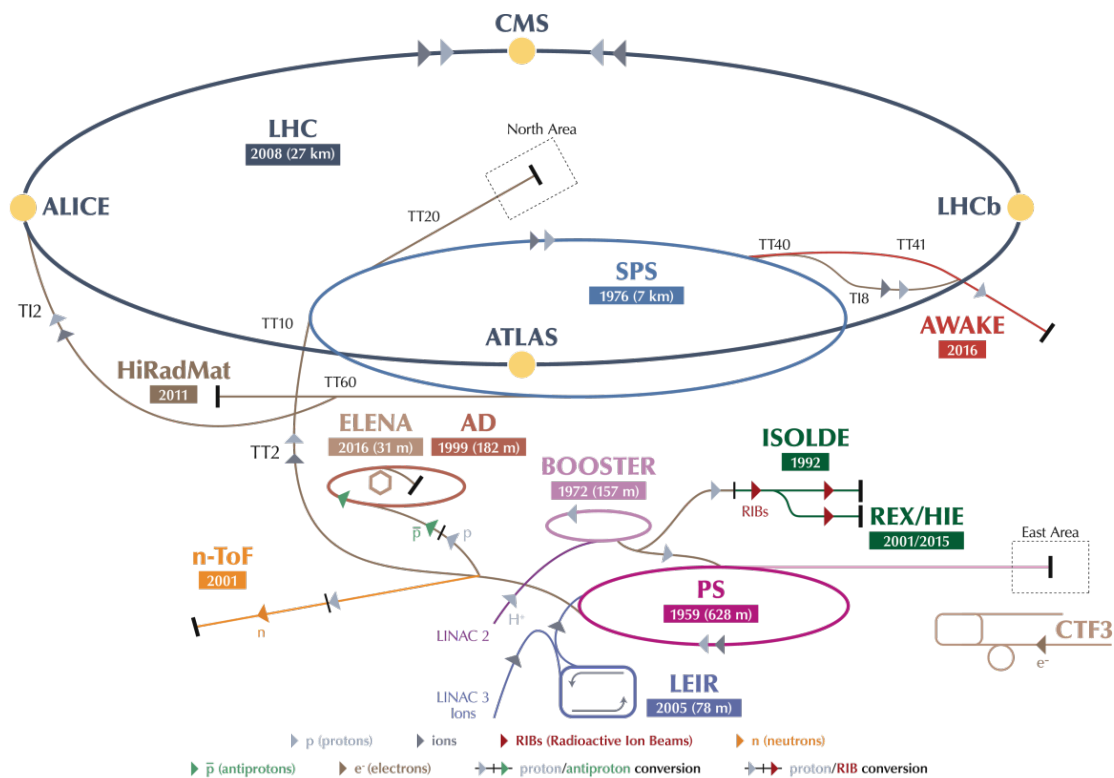


Figure 11: CERN accelerator complex: shown are the different accelerators at CERN, their year of construction and for ring accelerators their circumference (modified from [40]).

The relevant chain for this analysis of high energy proton-proton collisions is starting with the proton source at the linear accelerator (LINAC 2). In this source protons are

produced by ionizing hydrogen and accelerating them in a high-voltage field. They are then grouped in so called bunches by radio frequency fields before entering the first accelerator LINAC 2 which as all following accelerating steps use an alternating high voltage for acceleration. After LINAC 2 the proton bunches are accelerated step by step in three ring accelerators (BOOSTER, PS and SPS). They are then injected into the LHC at an energy of 450 GeV in both directions, are accelerated to their final energy of 6.5 TeV and are brought into collision in the four interaction regions. All these different steps are shown in Fig. 11 including the other possible beam lines and experiments performed at CERN which are not relevant for this analysis.

There are quite a few parameters describing the performance of the accelerator like emittance, bunches in the machine or time spent in stable beam. All these parameters were pushed as far as possible in 2016 and resulted in the most important performance number for the analysis of the collision data, the luminosity. The evolution of the peak instantaneous luminosity is shown in Fig. 12

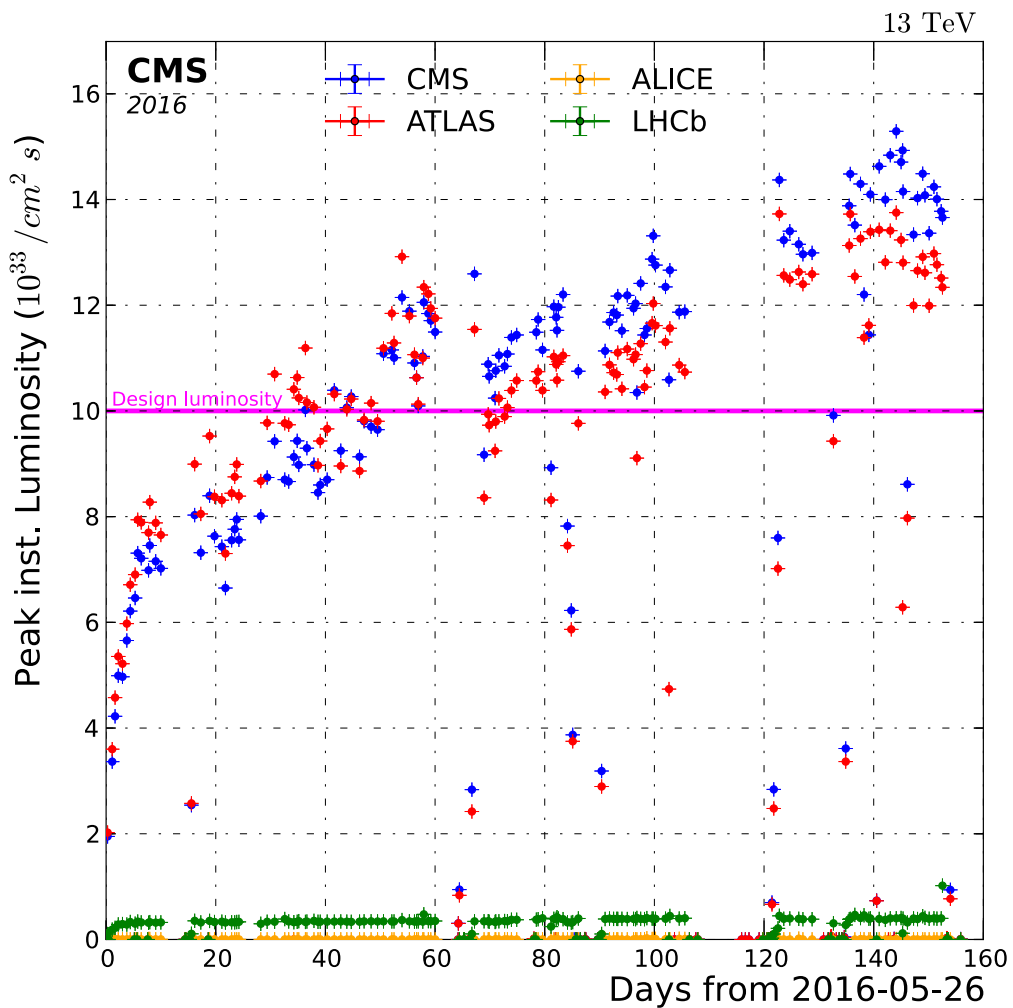


Figure 12: Evolution of the peak instantaneous luminosity through the year 2016 starting from the first day with beam, the 26th May for the four different experiments. As a comparison the luminosity for which LHC was designed in the beginning is also shown as a pink line (Data from [41]).

The instantaneous luminosity gives the collision rate while the integrated luminosity gives the total number of collisions. Integrating the values from Fig. 12 over time for 2016, therefore results in the integrated luminosity of 35.6 fb^{-1} which is the amount of data used for this analysis.

3.2 CMS

The Compact Muon Solenoid (CMS) is one of the two general purpose detectors at the LHC, designed to detect a wide variety of physics processes. An overview picture of CMS is shown in Fig. 13 which gives an impression of the scale of the detector and the various sub-detector parts (for the definition of the coordinate system see Sec. B.2).

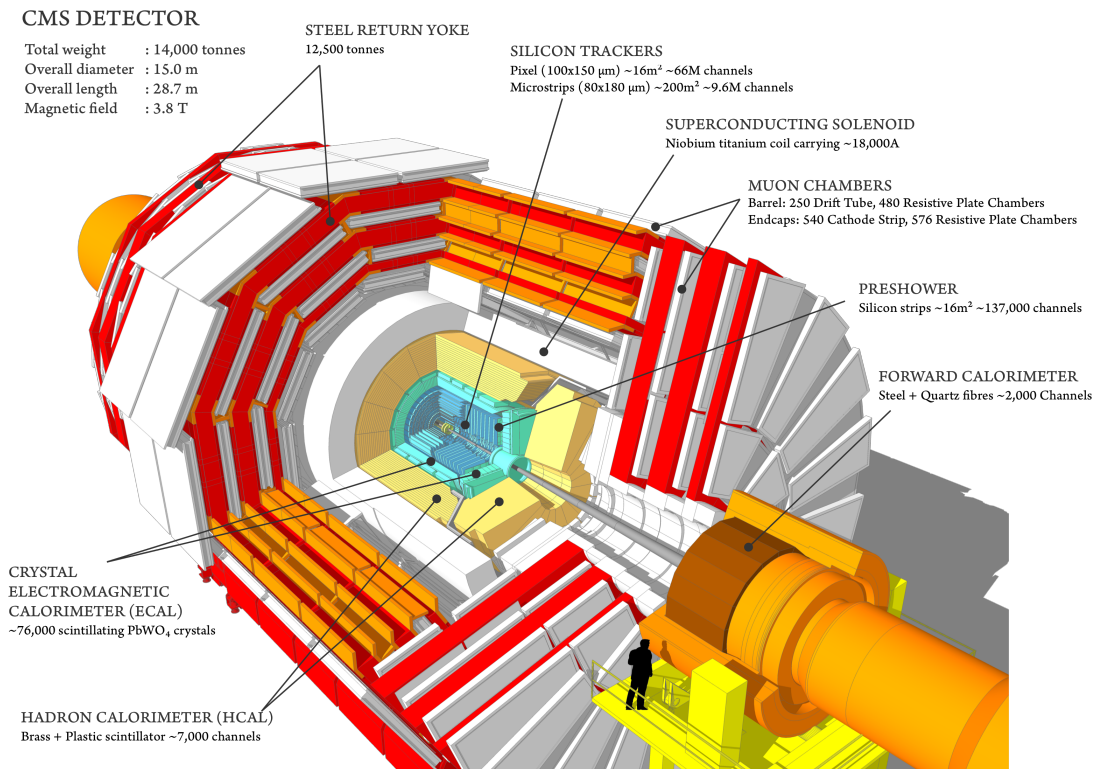


Figure 13: Overview picture of the CMS detector. The two proton beams enter from the bottom right and top left. The collisions, then occur right in the middle of the detector. The different sub-detectors of CMS are then layered around this interaction point and are labelled in the figure with some key numbers for each part [42].

CMS is designed to have a large geometric coverage of the interaction region and is divided into a barrel region and two end-caps¹. This shape is given by the big solenoid magnet which gives CMS its name. The magnet is a superconducting solenoid which produces a homogenous magnetic field parallel to the beam direction at a field strength of 3.8 T inside the solenoid. The different detector components are then arranged inside the solenoid and the steel return yoke of the magnet. A detailed cross section of the top

¹ There are also some special detectors to cover the region close to the beampipe and far away from the collision point, e.g. CTPPS, which do not follow this geometry.

right quadrant of CMS along the beam pipe is shown in Fig. 14 with all the different sub-detectors labelled and also different η ranges.

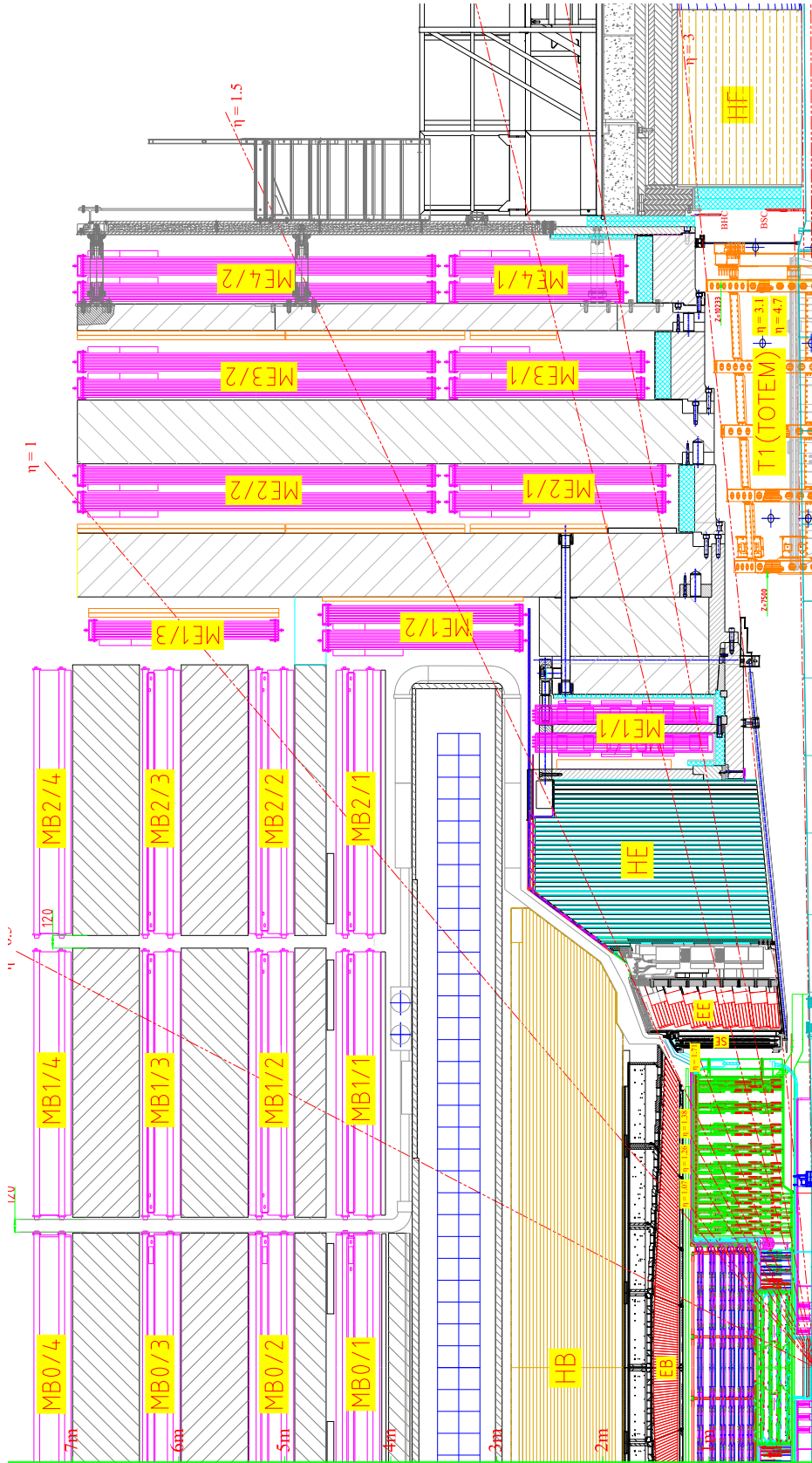


Figure 14: Longitudinal cross section view of the top right quadrant of CMS.

Starting from the innermost layer around the interaction region the different sub-detector components are first the silicon tracker which is split into pixel (inside) and strip (outside) parts. This is followed by the electromagnetic calorimeter (ECAL) and the hadronic calorimeter (HCAL). After that the solenoid and the iron layers of the return yoke follow. Between these iron layers the muon system is embedded.

The focus of the following sections is on the physics objects relevant for this analysis instead of the details of the different sub-detectors. It is explained how they interact with the detector leading to an observation in different detector parts and are then reconstructed from these observations. How different particles leave different signatures in the detector is illustrated in Fig. 15. The objects relevant for this analysis are the electrons (Sec. 3.2.1), the muons (Sec. 3.2.2) and missing transverse energy (E_T^{miss} , Sec. 3.2.3) which accounts for all undetected particles.

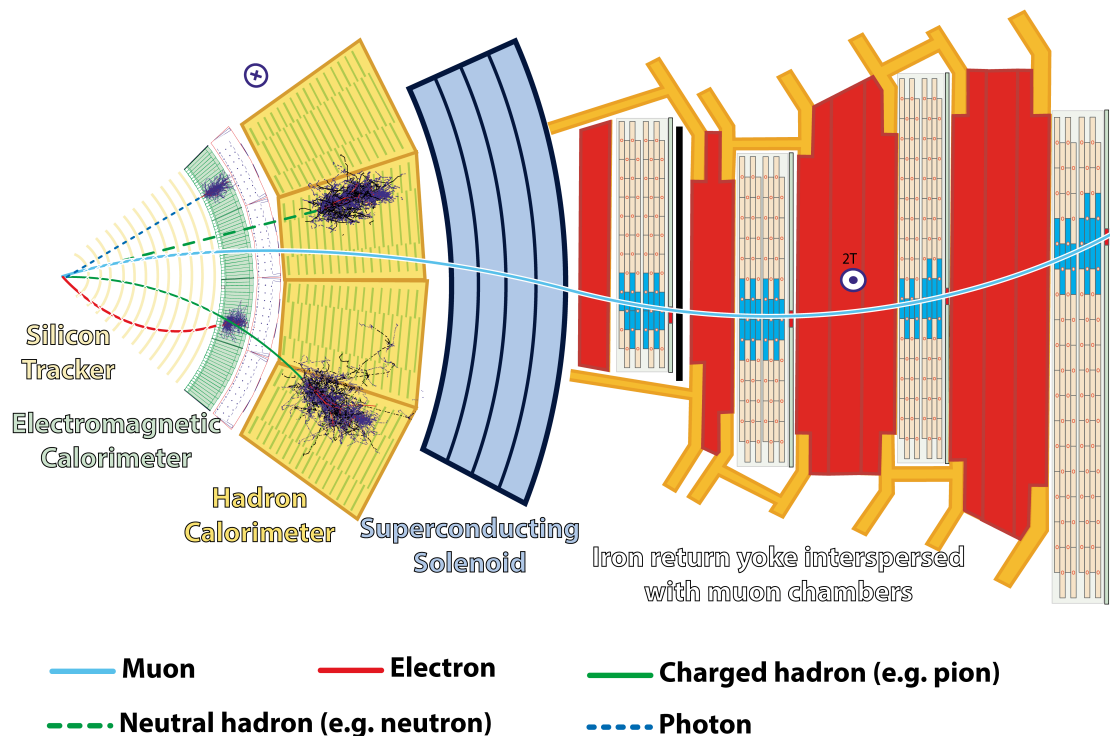


Figure 15: Transversal slice of the CMS detector. Shown are the different detectable particles and the signature they leave in the different sub-detector parts [43].

The major challenge at the LHC is, that collisions happen every 25 ns (a rate of 40 MHz). At this rate it is impossible to read out the whole detector and reconstruct every event. Also not every event is interesting for later analysis, therefore a filtering of the events by the Trigger happens to only select interesting events for processing. This trigger decision has to be fast, between two collisions, and therefore uses only partial information from the muon system and the calorimeters in the first step. The trigger is separated into two levels, the Level 1 (L1) trigger and the high-level-trigger (HLT), both are briefly explained in the following [44].

L1 The L1 trigger is implemented in hardware and analyses the hits from the muon system or calorimeters. In each subsystem a local reconstruction determines from which bunch crossing an event originates and reconstructs a track segment or

calorimeter cluster. The global trigger, then combines this information from the subsystems to calculate L1 candidates. Depending on the trigger selection criteria, like their p_T or isolation, it is decided if an event passes the trigger or not. If yes the detector is read-out and the event is passed to the HLT.

HLT The HLT is implemented as software and runs on the online event filter parallel computer farm. The HLT event reconstruction is quite similar to the later applied reconstruction, but optimized foremost for speed by e.g. reducing the number of iterations while the offline reconstruction is optimized for performance. Due to this approach no dedicated HLT reconstruction is needed as the offline reconstruction, explained in the following is sufficient. If the event passes at least one possible trigger the event is recorded for later analysis.

DATA ACQUISITION AND COMPUTING In the L1 trigger stage, the event rate is reduced to ~ 100 kHz from the collision rate of 40 MHz which is then sent to the High Level Trigger (HLT) computing farm. Therefore the detector data has to be transferred to this computer farm by the data acquisition (DAQ) system for the HLT processing (~ 100 GByte/s). If the HLT decision is positive, the event is recorded for the actual analysis at the CERN computing centre (at a rate of ~ 1 kHz). All the necessary data transfer, communication and synchronization between the different systems is provided by the DAQ system.

The full reconstruction of the whole event and all following steps are done by the Worldwide LHC computing Grid (WLCG) [45]. This grid-based network of computing centres all over the world, provides the computing power to reconstruct recorded events and for the simulation of Monte Carlo events. It also provides the storage capacity for data and Monte Carlo events to be accessible from all over the world.

3.2.1 *Electron reconstruction*

The interactions of electrons with the detector are illustrated in Fig. 15, they interact with the detector material by ionization and Bremsstrahlung. The ionization is used in the silicon tracker to reconstruct the electron trajectory, therefore the two parts of the silicon tracker are shortly introduced in the following.

The whole tracker is based on silicon detector technology which is fast, measures precisely hits from charged particles and works in this area in spite of the high radiation level. It is divided in a barrel and two end-caps and covers a pseudorapidity range of $|\eta| < 2.5$ and extends from a radial distance of 4.4 cm from the interaction point to 1.1 m.

PIXEL DETECTOR The pixel detector is the inner most sub-detector, and is used to get a first measurement as close as possible to the interaction point, which is important for the reconstruction of possible secondary vertices or to match tracks to a specific vertex. In order to avoid two particles hitting the same detector element at a high particle flux (1 MHz/mm^2 for the first pixel layer at design luminosity), it has to have a high granularity. This granularity is achieved by using pixel detectors which are quite small with a size of $100 \times 150 \mu\text{m}^2$. The pixel detector consists out of 3 barrel layers and two end-cap disks on both sides.

STRIP DETECTOR The silicon strip detector covers the radial range from 20 cm to 116 cm and each element can reconstruct a hit in two dimensions (η or ϕ and the position r of the strip sensor). At these distances the occupancy is small enough to get a precise measurement with a strip detector. By combining two modules which are tilted against each other they can also reconstruct hits in three dimensions. The whole strip detector consists of 10 barrel layers and 12 end-cap disks.

The Bremsstrahlung is used in the ECAL to detect the electron energy by stopping it. In the ECAL the process of Bremsstrahlung and pair production by the produced photon results in an electromagnetic shower, which deposits the complete energy of the electron in the ECAL. Therefore the ECAL is also introduced here.

ECAL The electromagnetic calorimeter (ECAL) is made of lead tungstate PbWO_4 crystals which are absorber and detection material for electromagnetic showers. The energy of the primary particle is measured via the scintillation light of the shower particles which is detected by Avalanche photodiodes (APDs) in the barrel and by vacuum phototriodes (VPTs) in the end-caps. The thickness of the calorimeter corresponds to about 26 radiation lengths X_0 , to fully contain the electromagnetic shower.

As two energy loss processes and two sub-detectors are relevant for the reconstruction of electrons, it is also split into two parts. The reconstruction of the energy in the calorimeter (called clustering) and the reconstruction of the trajectory in the tracker (called tracking). These two parts are briefly explained, afterwards the information is combined to form the final electron.

CLUSTERING Relativistic electrons tend to radiate a big fraction of their energy (on average from 33 % for $\eta \approx 0$ up to 86 % for $|\eta| \approx 1.4$ [46]) as Bremsstrahlung photons. As the electron trajectory bends in the magnetic field these photons are spread along ϕ in the detector. This fraction has to be included in the energy reconstruction for an accurate measurement. For this a seed crystal is selected as the one with the highest energy, then crystals in both ϕ directions are added if they contain energy deposits. They are then combined to a supercluster with the direction as the energy weighted direction of all contributing crystals.

TRACKING As the electron loses a large fraction of its energy while traversing the tracker it changes direction which cannot be covered by the normal tracking algorithms used e. g. for muons. A dedicated tracking procedure is therefore used. The tracks are either seeded by the superclusters in the ECAL extrapolated to the tracker or track segments which match to superclusters. The first track is built similar to e. g. muons (see Sec. 3.2.2) by a combinatorial Kalman filter, but with looser criteria for matching hits to the track to account for the potential energy loss. These hits are then used to perform a Gaussian sum filter fit to get the final electron trajectory. In this approach the energy loss of the electron is modelled by a sum of Gaussians in each detector layer (For a detailed description see Ref. [47]).

Both these information are then combined to form a reconstructed electron by combining the seeding supercluster with the one from it reconstructed trajectory. Some

quality criteria on the matching of both reconstructions are later applied in dedicated identification criteria for electrons (see Sec. 4.2.1).

Most relevant for this analysis are high-energy electrons produced from heavy states. As high energy electrons have very little track bending the energy is mainly determined in the ECAL, therefore the supercluster energy resolution is the important figure of merit. As the relative energy resolution is constant for most of the energy range it is shown as a function of $|\eta|$ in Fig. 16. A resolution of just a few percent is achieved.

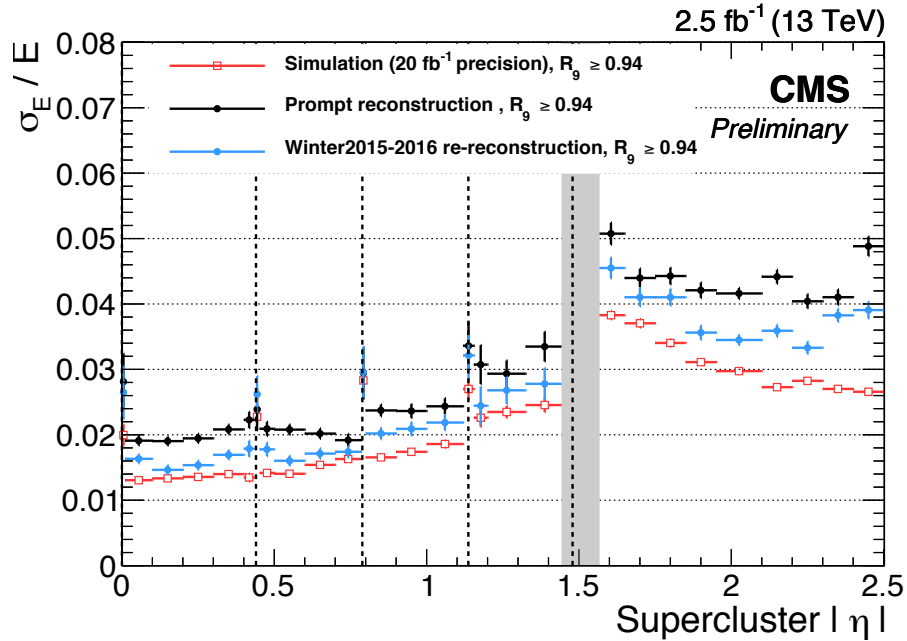


Figure 16: The relative energy resolution for electrons with little bremsstrahlung ($R_9 \geq 0.94$) is shown as a function of the supercluster $|\eta|$. The resolution was extracted from $Z \rightarrow ee$ events by a Gaussian convoluted with a Breit-Wigner function for the Z boson's natural width. The resolution is shown in the prompt reconstruction of 2015 data (black markers), for the re-reconstruction after optimized calibrations (blue markers) and for the expected performance after 20 fb^{-1} as used in the simulation (red markers) [48].

3.2.2 Muon reconstruction

The muon interacts with the detector mostly by ionization, which is illustrated in Fig. 15. Due to its high critical energy it is a minimal ionizing particle over a huge energy range² which leaves a trace in the tracker similar to electrons (See Sec. 3.2.1). The tracking system was already introduced in the electron section. But the muon is the only detectable standard model particle that penetrates the whole detector and can therefore also be measured in the muon chambers which are placed in between the different iron layers of the magnet return yoke. As it is the only particle which can reach these stations the identification is quite easy, but as the total energy cannot be

² For muon momenta of $\mathcal{O}(0.1 \text{ GeV}) - \mathcal{O}(100 \text{ GeV})$.

measured in a calorimeter the only measurement is the momentum due to the track bending in the magnetic field.

The muon system is a combination of three types of gaseous detectors to reconstruct muons. The general layout of the CMS muon system with its three sub-components, Drift Tubes (DTs) used in the barrel, Cathode Strip Chambers (CSCs) for the end-caps and Resistive Plate Chambers (RPCs) in addition, both in the barrel and the end-caps can be seen in Fig. 14.

The hits or measurements in individual detector channels come either from the silicon tracker (See Sec. 3.2.1) or from the different muon sub-systems which are shortly introduced here.

DRIFT TUBES Drift Tubes (DTs) are detectors which are installed in the barrel region where the particle flux is low and a large area has to be covered.

The volume is filled with an Ar – CO₂ gas mixture, where passing muons produce electrons and ions which are separated in the electric field and collected at the central wire giving a signal.

These drift cells are combined to a drift tube chamber. Each muon has to cross up to four muon DT chambers before leaving the detector, producing up to 12 hits per station.

CATHODE STRIP CHAMBERS The Cathode Strip Chambers (CSCs) are multi-wire proportional chambers and are used as tracking detectors in the end-caps.

A muon crosses the gas volume and produces electrons and ions. The electrons are detected by the wires. The avalanche of electrons induces a charge in the cathode strips which can also be detected. By combining the two pieces of information, a two dimensional ($\phi - \eta$) hit can be reconstructed.

Muons in the end-cap region have to cross 4 (or 3, depending on η) CSCs before they leave the detector.

RESISTIVE PLATE CHAMBERS Resistive Plate Chambers (RPCs) are used in the barrel and the end-caps. The RPC modules are made of two gaps, operated in avalanche mode and common read-out strips in the middle. In the RPC, crossing muons produce electrons and ions. The electrons and ions drift in the electric field between the two resistive plates (bakelite) and induce a charge in the readout strip.

The track reconstruction algorithm reconstructs a trajectory from the different hits in the detector and is basically the same on trigger level and in the final event reconstruction. The different available reconstructions are different not because they treat the reconstructed hits differently, but which hits are considered for a specific reconstruction differ [49, 50].

The algorithm works iteratively, starting with the best quality hits, reconstructs the track and removes hits associated with the track and starting all over again. For reconstructed tracks, a χ^2 can be calculated as a measure for the fit quality. All track parameters have uncertainties, which are propagated to the physical parameters of the particle, like the momentum or charge. The resulting uncertainties are stored for every track. One can summarize the algorithm in four steps:

1. Seeding: Find a track seed to start the reconstruction. There are two possible seeds for the reconstruction, a hit-pair or hit-triplet in the tracker compatible with the beam spot or a track segment with initial momentum and direction in the DTs or CSCs.
2. Trajectory building: Starting from the track seed, the trajectory is build by locating compatible hits on the next detection layer. The track finding and fitting is done with a combinatorial Kalman filter [51]. The Kalman filter starts with track parameters $\tilde{\mathbf{p}}_i$ and its covariance matrix $C(\tilde{\mathbf{p}}_i)$ and propagates them to the next detector layer. For this propagation, the magnetic field \vec{B} and the effects of the detector material have to be taken into account. On this next detector layer, the trajectory state is updated with the information of a compatible hit and the propagation is continued.
3. Trajectory cleaning: Removing hits to solve ambiguities which are produced by the trajectory building for tracks which share hits.
4. Trajectory smoothing: Taking the information from the full covariance matrix for the final track fit into account a backward fitting is done when the information for all hits are available at the end of the trajectory cleaning.

3.2.2.1 High momentum muon reconstruction

At high muon p_T ($p_T > \mathcal{O}(100\text{ GeV})$) the minimum ionizing particle assumption is no longer valid as radiative losses contribute significantly to the muon energy loss. Therefore, in this energy regime refits are used to have a good muon measurement despite these radiative losses. As high- p_T muons are an important part of this analysis all these different track reconstructions are shortly introduced here.

There are first the default reconstruction algorithms for global and tracker-muons [49] which do not focus on the high- p_T regime, which nevertheless can also be used if there is no radiative loss. On the other hand, there are special refits to take into account the effects which occur at high momenta, TPFMS, DYT and Picky [52]. To take advantage of all algorithms, the TuneP algorithm is used in this analysis, which tries to select the best algorithm for each event individually.

TRACKER MUON For the tracker muon, the track is reconstructed in the tracker and matched to compatible segments in the muon system. The final muon track fit is done with information only from the tracker.

GLOBAL MUON For this algorithm, all hits from the tracker and from the muon system are taken into account for the final track fit.

TPFMS MUON To combine the information from the muon system with the tracker, but avoiding the problems of muons traversing the iron yoke and producing radiative losses, the tracker-plus-first-muon-station (TPFMS) algorithm takes the hits from the tracker and only the first valid hit in the muon system for the final track fit into account [53].

DYT The dynamic truncation (DYT) algorithm, tries to handle muons which lose a large fraction of their energy and therefore change direction. This is done by starting from a tracker muon and propagate the track via the Kalman filter to the next layer. If there is a large incompatibility between the found hit and the extrapolated track the Kalman filter is stopped and this layer and all following ones are no longer taken into account. Otherwise the procedure is repeated from the compatible layer to the next one.

PICKY MUON Another approach is to only take muon stations with no shower due to radiative losses, or to use hits, which are compatible with the muon track. In order to detect if a shower occurred in a muon station, the occupancy of the muon station is used. For these stations the χ^2/NDF of each hit with the muon track is calculated. If it is below the threshold (10 for DT, 150 for CSC and 1 RPC), the hit is taken into account for the track fit [54].

TUNEP MUON The TuneP is designed to extract the best muon candidate from the different reconstruction methods. For this Tracker, Global, TPFMS, DYT and Picky muons are considered. The algorithm is summarized in the following step by step list [55]:

1. Check if at least one muon with $\frac{\Delta p_T}{p_T} < 0.25$ exists, if not raise the threshold by 0.15 and check again. The Δp_T is the uncertainty on p_T , resulting from the uncertainty on the track parameters in the track fit. The procedure is repeated until at least one muon is found the fulfils that requirement, all other muons are marked as invalid.
2. Start by choosing the Picky muon as default.
3. Compare the Picky muon with the DYT muon, chose the one with the lower p_T uncertainty.
4. Check if the selected muon is valid³. If not, choose Tracker muon.
5. If not the tracker muon is chosen, check if the probability

$$P(\text{Picky}) - P(\text{Tracker}) > 17$$

where P is defined as the negative logarithm of the probability to get the same or smaller χ^2 for the track fit:

$$P(\chi^2, \text{NDF}) = -\log \left(\frac{\int_0^{\chi^2} t^{\frac{\text{NDF}}{2}-1} e^{-\frac{t}{2}} dt}{\Gamma(\frac{1}{2}\text{NDF}) \cdot 2^{\frac{\text{NDF}}{2}}} \right) \quad (10)$$

6. Check if Tracker muon is valid³. If not, choose TPFMS muon.
7. Check if TPFMS muon is valid³. If not, choose Global muon.
8. Compare the chosen muon to TPFMS and if

$$P(\text{chosen}) - P(\text{TPFMS}) > 40$$

choose TPFMS.

³ In this context, valid means that the reconstructed track exists and the reconstruction did not fail.

9. If tracker p_T or chosen $p_T < 200$ GeV, choose the Tracker muon.

As a comparison the resolutions are shown in Fig. 17 for all the different reconstruction methods as determined from cosmic muons. Especially for high p_T the resolution of TuneP muons is significantly better compared to the other reconstruction algorithms.

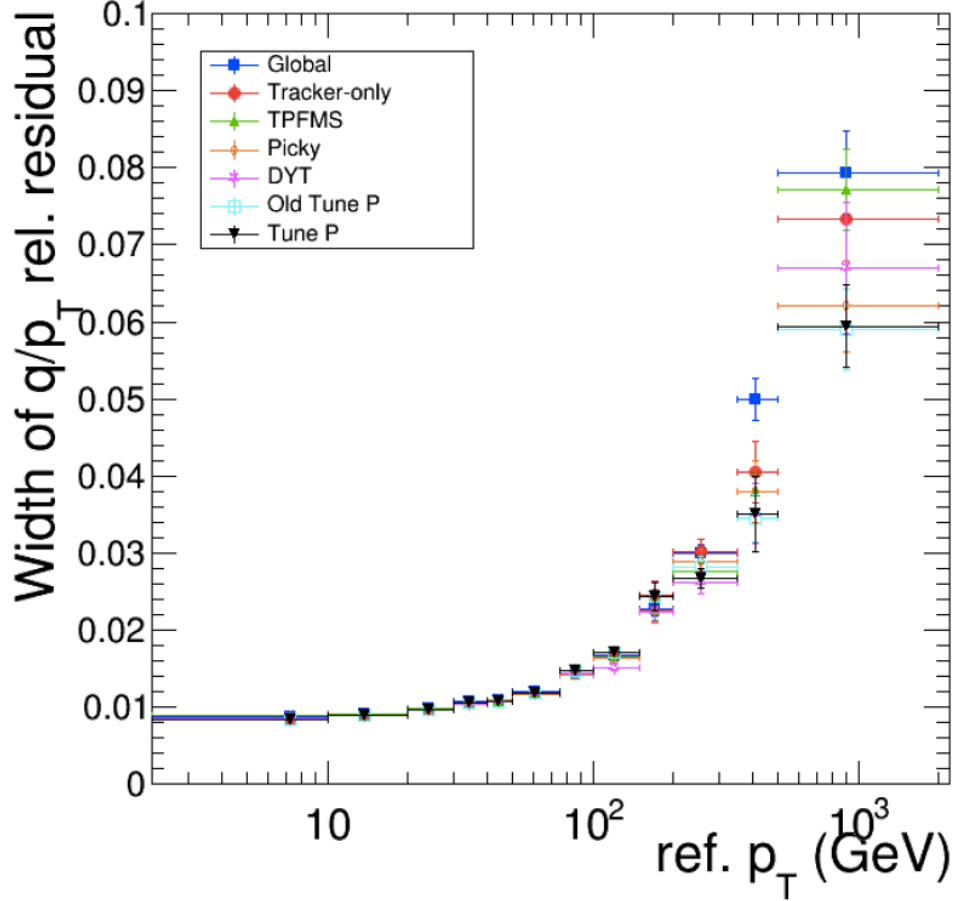


Figure 17: Inverse transverse momentum core resolution for different muon reconstruction versions mentioned in the text (old TuneP is TuneP without DYT as it was used before 2016) as measured in cosmic data from 2015. Cosmic muons give two independent measurements of the muon in the top half and the bottom half of the detector and therefore allows to probe the muon momentum resolution. The core width of the $(q/p_T - q/p_{T,ref})/q/p_{T,ref}$ distribution is shown here as a measure for the $1/p_T$ resolution as a function of p_T [56].

3.2.3 Missing transverse energy reconstruction

The missing transverse energy (E_T^{miss}) is the measurable representation of all unmeasured particles like neutrinos in the plane transverse to the beam direction. It is reconstructed as the negative sum of the momenta of all particle flow objects in the event [57]. These are electrons or photons, muons and jets. Electron or photon as well as muon reconstruction are as described in the previous sections. Jets are reconstructed from clusters of energy deposits and tracks in a given direction. Hadronic particles that are the constituents of jets have a long interaction length and are not stopped in

the ECAL. Therefore the hadronic calorimeter is also an important part in the E_T^{miss} reconstruction as the total energy of hadronic particles can be measured there.

HCAL The hadronic calorimeter (HCAL) consists of the barrel and endcap parts, and two parts cover the high η region (Hadron Forward, HF). The HCAL is a sampling calorimeter with brass absorber plates and scintillator plates as detection element. The scintillation light is detected with hybrid photodiodes (HPDs). The thickness of the calorimeter is about $6\lambda_1$ radiation lengths at $\eta = 0$ and increases with η .

The particle-flow (PF) algorithm reconstructs and categorizes all stable particles in an event (electrons, muons, photons, charged hadrons and neutral hadrons) by combining information from all CMS sub-detectors. The information from the sub-detectors are processed in the form of particle tracks and calorimeter clusters. These basic building blocks are then used by the particle flow algorithm to reconstruct the stable particles (details in Ref. [58]).

The PF E_T^{miss} is calculated from all particle flow objects as

$$\vec{E}_T^{\text{miss}} = - \sum_i \vec{p}_T^i$$

and is then used in the analyses.

The resolution that can be achieved is about 10% for an energy scale of 200 GeV for boson recoil events. This performance depends greatly on the event content and is for this analysis completely dominated by both, the electron and muon momentum resolutions mentioned in the previous sections.

This chapter presents all the different steps of the analysis, which try to separate the signal from the background processes. This results in the final distribution used for the statistical interpretation in Chapter. 5. This walk through the analysis starts with the simulation of the different signal models (Sec. 4.1), followed by the object selection criteria for the particles or objects in the different final states (Sec. 4.2). The general pre-selection of the channels is explained next (Sec. 4.3) which directly leads to the background description needed (Sec. 4.4). Corrections that need to be applied to correct for known mis-modelling effects complete the first steps of the analysis (Sec. 4.5). For the two tau channels a kinematic selection is applied afterwards (Sec. 4.6). The performance of the analysis steps can be summarized in the efficiencies and mass resolutions of the analysis which are presented in Sec. 4.7 and Sec. 4.8. In principle also the ratio of signal to background events, the so called purity, is an important figure of merit for any analysis. But the background expectation from the standard model is very small in the studied energy regime. The analysis is therefore performed with a small to zero background expectation, with the consequence that the signal efficiency is the quantity that dictates the analysis sensitivity and not the ratio of signal to background events as the purity is close to unity anyways. The last part in this chapter then explains the different sources of systematic uncertainties and how they are handled in the analysis (Sec. 4.9).

4.1 SIGNAL SIMULATION

The signal simulation is the first step of the analysis, to know what to look for. There are three steps in the simulation of any process, either signal or background [59]. All these steps are based on the Monte Carlo techniques used to evaluate probability distributions and are therefore called Monte Carlo simulation.

1. The first step is the simulation of the hard interaction, which is the part of the interaction shown in a Feynman diagram like Fig. 4 for the signal or Fig. 2 for a background process. The events are simulated by dicing all the input parameters like the momenta or identity of incoming particles according to the corresponding probability distributions like parton density functions (PDF) for the incoming particles. Then the production and decay of elementary particles are calculated following the probability for the different steps in the Feynman diagram. All these steps have to happen according to the physics model of the process (e. g. RPV or the standard model). The result of this simulation step is a list of elementary particles with their identity, momentum and direction of flight. Also the cross section or the rate of the simulated process can be calculated in this way as a way of evaluating the Feynman diagrams with this simulation approach. The inputs for this simulation step are the Feynman diagrams of the process, the PDFs for the incoming particles and the physics model (e. g. the stan-

standard model). The available simulation programs, called generators, differ in the possible processes and their precision.

2. The second step in the event simulation is the part of the event which cannot exactly be described by Feynman diagrams, or are too computing intensive to be calculated in that way. The first part of this step is the additional radiation of particles. High energy particles can radiate other particles, especially photons and gluons, which influence the kinematics of the particles in the event and also the particles in the final state. This radiation is called parton shower. The radiation can either happen by the incoming particles (initial state radiation = ISR) or by the final state particles (final state radiation = FSR). This additional radiation is simulated in a phenomenological model that is tuned to observations on actual collision events. The second part is the possible decay or hadronisation of particles. Unstable particles can decay before they are detected while quarks and gluons hadronise before they can be observed. Hadronisation means that due to the underlying theory of quantum chromo dynamics (QCD) quarks and gluons can not be free particles, but will produce additional quarks and gluons to form colour neutral particles, called hadrons. The process of hadronisation describes the evolution from quarks and gluons to jets of hadrons and is also described by phenomenological models tuned to observed collision events. The last part is the underlying event, which consists of the remnants of the protons after the collision and potential additional proton-proton collisions that happens at the same time as the interesting one. These parts have also to be simulated to get an accurate simulation of the event content later observed in measured data. The underlying event is also simulated by simple phenomenological models that have proven to describe the data in actual collisions. The output of this second step is then an even longer list of particles, their identities and their momenta and direction. This list now contains everything in the event that could reach the sensitive parts of the detector.
3. The last step is to simulate the behaviour of the particles in the detector and their interactions with it [60]. Therefore the detector and all its sub-components are simulated in a geometric model in the software GEANT4 [61–63]. The propagation of the particles through the detector is simulated under the consideration of their interactions with the detector material and influences like the magnetic field in the detector. To make sure that all these processes are simulated correctly, they were tuned at test beams for a wide variety of particles and energies [60]. The simulated detection of the signal, the readout of the detector and the influence of the detector electronics on the simulated signal as well as the trigger decision are also part of the simulation. The result of this last simulation step is an output similar to actual collision data.

The first two steps are done by dedicated generators and can be different for different processes. The generator can be the same for the two steps, but in some cases, special generators are used for the first step, while more general purpose generators are used in the second step. The third step is done centrally for all physics processes and is therefore identical to all samples. After these three dedicated simulation steps, the same event processing chain as for data events is applied (e.g. the reconstruction of hits in the detector as described in Sec. 3.2).

The technical details on the different signal samples used in the analysis are summarized in the appendix in Tab. 12, while an overview on the different parameters and generators used for the simulation of the three studied signal models is given in the following paragraphs.

RPV SUSY The RPV signal events have been generated with CalcHEP [12] for the first step of the event generation. PYTHIA 8 is used for the hadronisation and parton showering step of the simulation [64, 65]. The model has been implemented based on an RPV SUSY model publicly available on HEPMDB [66]. The parton level events have been passed to the detector simulation, using the standard conditions for Monte Carlo simulations for the 2016 period.

A wide variety of parameters were simulated. The complete list of all parameter points, their values, leading order (LO) cross sections and next-to-leading order (NLO) k-factors are documented in Tab. 13 in the appendix. In the narrow width approximation ($\Gamma_{\tilde{\nu}_\tau} \ll m_{\tilde{\nu}_\tau}$), Eq. 2 can be used to scale the cross section to the wanted coupling values. The parameters of the simulated samples are chosen such as to cover a wide range of masses with a small step size in order to justify a parameterized fit of the signal efficiency. Samples with different coupling parameter values have been produced to show that the benchmark coupling value of 0.01 does not impact the signal's acceptance times efficiency. The scaling k-factor from the LO cross section to the NLO QCD is determined by the code used in [13] as a function of the parameters λ'_{311} and $m_{\tilde{\nu}_\tau}$. A comparison of the results from the CalcHEP generator with an implementation in the HERWIG [67] generator was done in the context of the 2012 analysis [68], resulting in good agreement. Therefore only the CalcHEP version is used in this analysis.

QBH The QBH signal events were generated with the QBH event generator [69]. PYTHIA 8 is used for parton showering and hadronisation. The different parameter points which have been produced are summarized in Tab. 14 in the appendix, including the parameters threshold mass, number of extra dimensions and cross section. The same configuration for the detector simulation as above were used.

As seen in Fig. 7 the shape of the signal is nearly independent of the number of extra dimensions, therefore $n = 1$ is mainly used throughout the analysis. To cross check this assumption signal points are also simulated for $n = 4, 5, 6$. To validate the results from the QBH generator, a comparison with the implementation of the CalcHEP model (contains only the quark-quark initial state) is performed. The shape comparison for different parameter values is shown in Fig. 102 in the appendix and show perfect agreement over the whole range of parameters and masses. In addition, the product of cross section and branching ratio of the two generators have been compared. This is shown as a function of the threshold mass in Fig. 18. Different number of extra dimensions and different production channels for the QBH generator are tested. The possible initial states quark-quark or gluon-gluon plus quark-quark are probed. The gluon-gluon initial state contributes mainly at low threshold masses. To use the conservative signal estimation for the analysis only the quark-quark initial state produced by the QBH generator is considered throughout the analysis. This also allows to compare the results to the CalcHEP generator as it also only considers the quark-quark initial state.

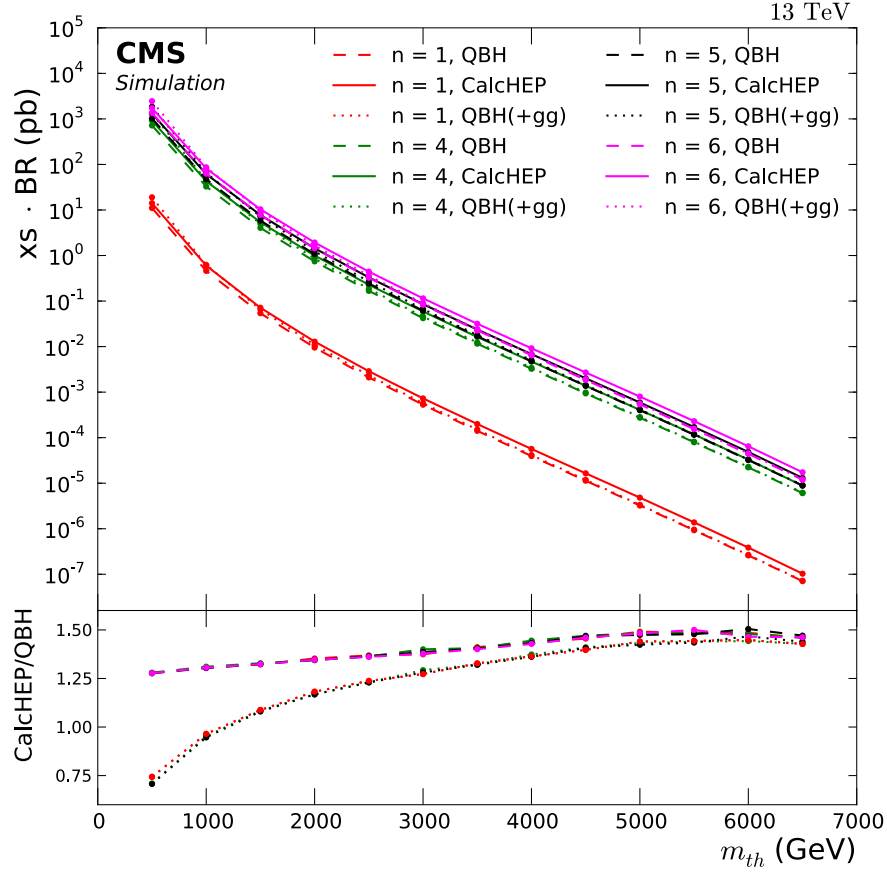


Figure 18: Comparison of the cross section calculated by different Monte Carlo generators as a function of the threshold mass. The other varied parameter is the number of extra dimensions, which ranges from $n = 1$ (red) over $n = 4$ (green) and $n = 5$ (black) to $n = 6$ (pink). The cross section is calculated either by `CALCHEP` (solid lines), by the `QBH` generator (dashed lines) and by the `QBH` generator also including gluon initial states (dotted lines). Also shown is the ratio of the cross section from `CALCHEP` to the cross section from `QBH`. For the comparison including only quark initial states `CALCHEP` yields a factor 1.25 – 1.5 higher cross section, while the gluon initial states contribute only for low threshold masses.

Z' The sequential standard model Z' signal points have been generated with `PYTHIA 8` used for the first two steps in the event simulation while the detector simulation is done similar to all other generated processes. A table giving the produced signal points with the Z' mass $m_{Z'}$ and the LO cross sections can be found in Tab. 15 in the appendix.

As this signal is a benchmark to be able to compare to another analyses, the most important aspect is not to have the best motivated physics process but to have the exact same configuration used by the other experiments. This is guaranteed by comparing the relevant parts of the `PYTHIA` simulation with `ATLAS` and making sure, they are identical.

4.2 OBJECT SELECTION

In this section the different requirements are introduced that a particle has to fulfill to enter the analysis. This is split into two steps, first the reconstruction, which was already introduced in Sec. 3.2 and second the particle identification or ID which is introduced in the following sub-sections for electrons (Sec. 4.2.1), muons (Sec. 4.2.2) and taus (Sec. 4.2.3).

4.2.1 Electron

The electron selection used in the analysis is applied on top of the electron reconstruction as explained in Sec. 3.2.1. As all studied signal models predict high energy electrons the selection is optimized for this energy regime. This set of selection criteria is called HEEP for ‘High Energy Electrons and Photons’ and is centrally maintained and optimized by the EGamma group of CMS [70]. The different requirements to the electrons are listed in Tab. 4 and are shortly explained afterwards. The last part of this section shows the efficiencies of the electron reconstruction and identification as these are important figures of merit for the analysis.

Table 4: HEEP (v7.0) ID requirements for high energy electrons [71]. The different quantities are introduced in the text. The requirements are split into four categories (blocks in the table), first the electron acceptance, second to make sure there is a good reconstruction, third that the electron is isolated and fourth, that it comes from the primary vertex.

Variable	Barrel	Endcap
Acceptance (1):		
E_T	$> 35 \text{ GeV}$	$> 35 \text{ GeV}$
η range	$ \eta_{SC} < 1.4442$	$1.566 < \eta_{SC} < 2.5$
Good reconstruction (2):		
isEcalDriven	$= 1$	$= 1$
$ \Delta\eta_{in}^{seed} $	< 0.004	< 0.006
$ \Delta\phi_{in} $	< 0.06	< 0.06
H/E	$< 1/E + 0.05$	$< 5/E + 0.05$
full $5 \times 5 \sigma_{i\eta i\eta}$	-	< 0.03
full $5 \times 5 E^{2 \times 5} / E^{5 \times 5}$	> 0.94 OR $E^{1 \times 5} / E^{5 \times 5} > 0.83$	-
Inner Layer Lost Hits	≤ 1	≤ 1
Isolation (3):		
EM	$< 2 + 0.03 \cdot E_T / \text{GeV} + 0.28 \cdot \rho$	$< 2.5 + 0.28 \cdot \rho$ for $E_T < 50 \text{ GeV}$ else
+ Had Depth 1 isolation		$< 2.5 + 0.03 \cdot (E_T / \text{GeV} - 50) + 0.28 \cdot \rho$
Track Isolation	< 5	< 5
Impact parameter (4):		
$ d_{xy} $	< 0.02	< 0.05

The first set of requirements on the electron ensures a good reconstruction of the event. First, there are the acceptance criteria on E_T and η (labelled (1) in the table). To match the geometric acceptance of the ECAL, the η value of the electron supercluster η_{SC} is used in the selection. This is followed by the requirements for a good reconstruction (labelled (2) in the table). The electron reconstruction has to be seeded by the ECAL and the track reconstruction has to match the super cluster in $\Delta\eta$ and $\Delta\phi$. The energy deposit should be mainly in the ECAL (E) and not in the HCAL (H). This requirement is ensured by setting a energy dependent threshold on the ratio of energy in the ECAL and in the HCAL. Two different requirements on the shower shape in the calorimeter barrel or endcap are imposed to veto particles being misidentified as electrons, e. g. hadrons or hadronic jets. The energy deposits from electrons are more collimated along η than hadronic, this difference is used for the separation. The shower shape difference along ϕ can not be used in the selection as the energy deposits of electrons are also spread in ϕ due to Bremsstrahlung. In the endcap the variable $\sigma_{i\eta i\eta}$ should be smaller than 0.03. The variable $\sigma_{i\eta i\eta}$ is an energy-weighted spread of the 25 crystal positions η_i as defined:

$$\sigma_{i\eta i\eta}^2 = \frac{\sum_i^{5 \times 5} w_i (\eta_i - \langle \eta \rangle_{5 \times 5})^2}{\sum_i^{5 \times 5} w_i}$$

with the weights w_i , which logarithmically depend on the energy in the crystal i . For high values of $\sigma_{i\eta i\eta}$ the energy deposited in the ECAL is widely spread and corresponds to a hadronic jet while small values correspond to an electron. In the barrel the energy ratio in crystal strips along ϕ , with different widths in η , has to be above a threshold ($E^{1 \times 5}$: Energy in a 1×5 strip of crystals in the $\eta - \phi$ plane). If the energy in the narrow strip (1×5 or 2×5) is higher than in the wider one (5×5) and therefore the ratio of energies is large, it is most likely from an electron and not a hadronic jet. The last requirement is that at most one hit of the inner track should be lost in the track fit to keep a high quality of the track fit, meaning, that all but at most one hit should be included in the track reconstruction. The next set of requirements (labelled (3) in the table) is that the electron should be isolated from other particles in the event as this is expected from all studied BSM models. This is ensured by two requirements first on the isolation in the calorimeter and second on the isolation of the track. The isolation in the calorimeter (EM + Had Depth 1 isolation) is defined as the energy deposited in the ECAL + HCAL in a cone around the electron with a size of $R = 0.3$. The energy of the electron is removed via subtraction of the energy in a tighter cone around the electron. To not take the energy deposit from pileup interactions into account, the average energy density from pileup ρ is also subtracted from the isolation cone. If the energy in the isolation cone is smaller than 3% of the electron E_T , the electron is isolated. The tracker isolation is defined similarly as the scalar sum of p_T for all additional tracks around the electron within a cone with a size of $R = 0.3$. This momentum sum should be smaller than 5 GeV for the electron to be isolated. The final requirement (labelled (4) in the table) is that the particle should be close to the primary vertex in the $x - y$ plane to reject pileup events.

These selection criterias are optimized for high E_T electrons and focuses therefore on the information from the ECAL as the track reconstruction is influenced by Bremsstrahlung at high energies.

4.2.1.1 Electron reconstruction and identification efficiency

The next step in the analysis is to measure the efficiencies of the applied requirements, so first the electron reconstruction and second the electron identification. The reconstruction efficiency is defined as a function of E_T in Eq. 11.

$$\epsilon_{\text{RECO}}(E_T) = \frac{N(\text{Reconstructed } \ell)(E_T)}{N(\text{generated } \ell)(E_T)} \quad (11)$$

The reconstructed ℓ (electron) has to match a generator level ℓ (electron) within $\Delta R < 0.5$. The identification (steps (1)-(4) in Tab. 4) efficiency is defined similarly also as a function of E_T in Eq. 12.

$$\epsilon_{\text{ID}}(E_T) = \frac{N(\text{Reconstructed } \ell + \text{ID} + \text{ISOLATION})(E_T)}{N(\text{Reconstructed } \ell)(E_T)} \quad (12)$$

The reconstructed ℓ has also to match a generator level ℓ within $\Delta R < 0.5$. As can be seen from the efficiency definitions, combined they describe the complete electron efficiency. This definition can only be used on simulated events due to the matching to the generator level information, therefore differences to efficiencies in observed data have also to be taken into account as efficiency corrections (See Sec. 4.5). The electron reconstruction and identification efficiencies are shown in Fig. 19 as a function of generated electron E_T .

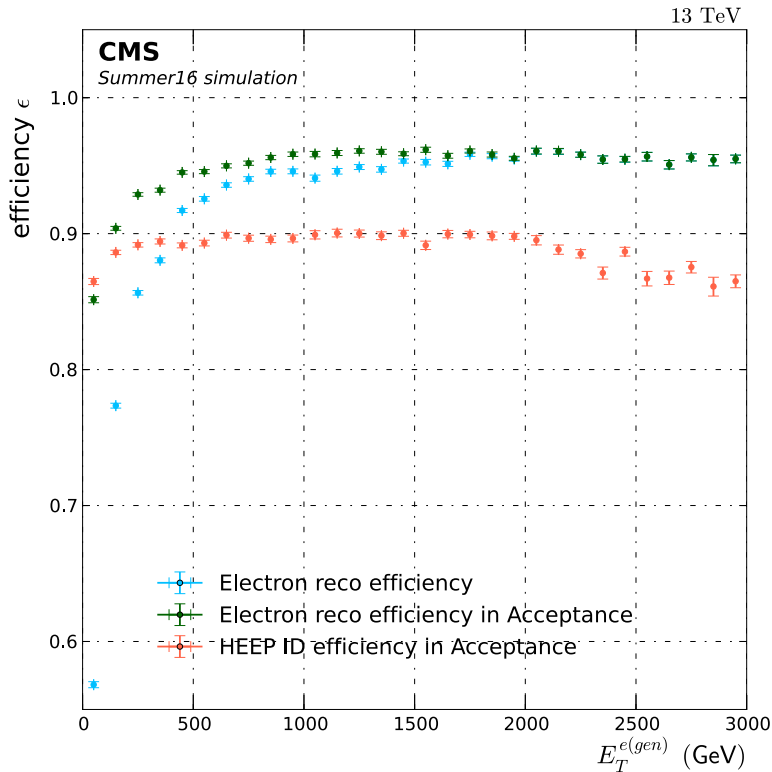


Figure 19: Reconstruction and ID efficiency as a function of generated electron E_T for simulated RPV signal events. The used definitions are given in Eq. 11 and Eq. 12 respectively. The reconstruction efficiency is shown first for all electrons and for electrons in the geometric η acceptance (labeled (1) in Tab. 4). The efficiency rises with E_T until it reaches the efficiency plateau. The identification efficiency includes the steps (2)-(4) in Tab. 4.

These efficiencies were obtained from RPV signal simulation, but as the individual particles in the events are quite similar for all signal models they also hold for the other models. The rise of the efficiency with E_T until the efficiency plateau is reached can be seen. The reconstruction reaches an efficiency of $\sim 95\%$ in the plateau, while the identification goes up to $\sim 90\%$. These efficiencies stay fairly constant up to very high electron E_T . At very high energies additional effects can contribute to losses of efficiency, like saturation of ECAL crystals.

4.2.2 Muon

For the selection of muon candidates dedicated high- p_T muon identification requirements are applied, they are maintained by the Muon group of CMS [72]. As for the electrons they are applied on top of the muon reconstruction introduced in Sec. 3.2.2. The complete list of requirements for the muon selection is given below [73] which is split into three categories, first the acceptance requirements, second the identification criteria to ensure a good reconstruction and finally the isolation requirement.

1. Muon acceptance requirements

- The muon should have $p_T > 53$ GeV.
- The pseudorapidity of the muon should be $|\eta| < 2.4$.

2. Muon identification requirements

- The muon is required to be reconstructed in the muon system and tracker.
- At least one muon-chamber hit should be included in the global-muon track fit. This is done to suppress hadronic punch-through¹ and muons from decays in flight.
- Muon segments should be present in at least two muon stations. This requirement is made in order to suppress punch-through and accidental track-to-segment matches. Also, it makes the selection consistent with the logic of the muon trigger, which requires segments in at least two muon stations to obtain a meaningful estimate of the muon p_T .
- The relative p_T error from the uncertainty of muon best track is less than 30%.
- The tracker track of the muon candidate should have a transverse impact parameter $d_{xy} < 2$ mm with respect to the primary vertex. This requirement suppresses cosmic muons and further suppresses muons from decays in flight.
- The longitudinal distance of the tracker track with respect to the primary vertex has to be $d_z < 5$ mm. This is a loose cut to further suppress cosmic muons, muons from decays in flight and tracks from pile-up vertices.
- The number of pixel hits has to be > 0 , to further suppress muons from decays in flight.

¹ Hadrons, which have enough energy that they punch through the calorimeters and solenoid and leave a signal in the muon system.

- The number of silicon-strip tracker layers with hits should be more than 5, to guarantee a good p_T measurement and also to suppress muons from decays in flight.

3. Muon isolation requirements

- The muon should be isolated in the tracker. The transverse momentum of the measured tracks in a cone of $\Delta R < 0.3$ around the muon direction is summed up and divided by the muon p_T for this relative track based isolation. The value of the relative isolation is required to be less than 0.1.

These selection requirements result in a clean selection of high- p_T muons that are used throughout the analysis.

4.2.2.1 Muon reconstruction and identification efficiency

The efficiencies for muon reconstruction and identification are defined exactly as for electrons in Eq. 11 and Eq. 12. The resulting muon reconstruction and identification efficiencies are shown in Fig. 20 as a function of generated muon p_T .

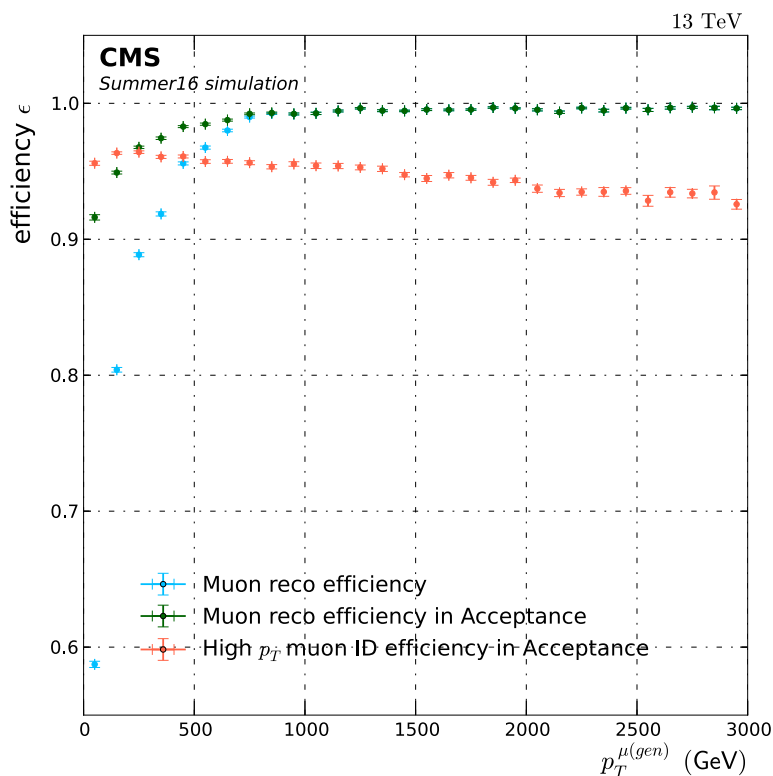


Figure 20: Reconstruction and ID efficiency as a function of the generated muon p_T for simulated RPV signal events. The used definitions are given in Eq. 11 and Eq. 12 respectively. The reconstruction efficiency is shown first for all muons and for muons in the geometric η acceptance (as defined in the muon acceptance requirements). The efficiency rises with E_T until it reaches the efficiency plateau. The ID efficiency includes the identification and isolation criteria.

These efficiencies were obtained from RPV signal simulation, but as the individual particles in the events are quite similar for all signal models they also hold for the

other models. The rise of the efficiency with p_T can be seen until the efficiency plateau is reached. The reconstruction reaches an efficiency of $\sim 99\%$ in the plateau ², while the identification goes up to $\sim 95\%$. The identification efficiency has a slight decreasing trend with p_T due to the increased probability of the muon to radiate photons at higher p_T .

4.2.3 *Tau*

The tau lepton will decay inside the detector, due to the short mean life time of $\tau = 290 \cdot 10^{-15}$ s [4]. This results in a mean flight path of $\gamma\tau = \gamma \cdot 87.11 \mu\text{m}$ [4]. To reach the inner most detector layer at $r = 4.4$ cm the tau has to have 890 GeV of momentum for a γ value corresponding to a mean flight distance that is large enough. The tau therefore decays mostly inside the beam pipe and only the decay products can be detected. If there is only one tau in the event and no other source for E_T^{miss} other than the neutrinos of the tau decay, the decay kinematics can be used to reconstruct the tau. For this analysis this is either an electron or a muon plus the two neutrinos. These conditions can only be fulfilled if lepton flavour is violated, otherwise taus can only be produced in pairs or in association with a tau neutrino. How this kinematic reconstruction approach works is illustrated in Fig. 21.

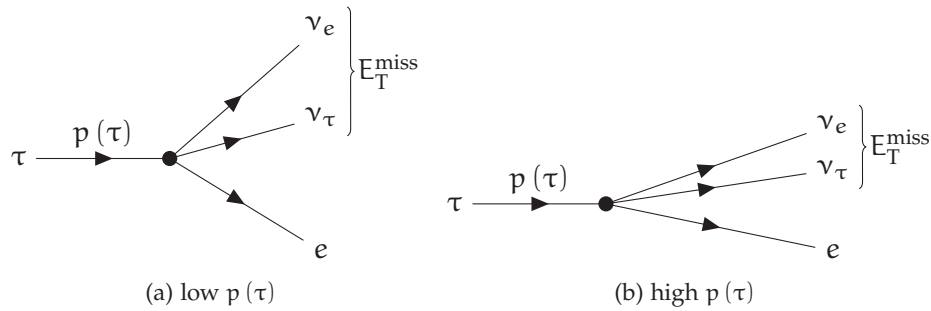


Figure 21: Schematic illustration of the decay of the tau lepton into an electron and two neutrinos for two scenarios. On the left (a) the case for a low tau momentum $p(\tau)$ is shown while the high momentum case is shown on the right (b). In the high momentum case the decay products are all close together and also close to the original tau trajectory, therefore a reconstruction of the tau is possible for high tau momenta if no other neutrino or other undetected particle is in the event. The idea works exactly the same for muons, just replacing the electron with a muon and the ν_e with a ν_μ .

For this reconstruction to work the following requirements need to be fulfilled:

- The tau has to have high momentum. This is fulfilled for the signal as due to the high mass of the $\tilde{\nu}_\tau$ the tau from the decay will get high p_T .
- If the tau has high p_T , the decay products of the tau will be highly boosted.
- Due to the high boost of the decay products, they are collinear in the detector. This can be seen in Fig. 21, that for high p_T the decay products are close together.
- Due to this collinearity, the η values for the visible decay products and the neutrinos are nearly identical.

² A study how the efficiency can reach values up to 99%, which is higher than expected for the acceptance of muons which are uniformly distributed in $\cos\theta$, is given in Fig. 103 of the appendix.

- Therefore the measurement of E_T^{miss} combined with the η measurement of the visible decay products can be used as a good approximation for the neutrino momentum.

This approach allows to use E_T^{miss} and the visible decay product direction to estimate the combined neutrino momentum and to reconstruct the complete collinear reconstructed tau. This gives a good measurement of the tau from the hard interaction. The p_T resolution for taus in this reconstruction approach is shown in Fig. 22 for different RPV signal points. The p_T resolution is defined as

$$\frac{p_T - p_T^{\text{gen}}}{p_T^{\text{gen}}}$$

and should be centred at zero for a good reconstruction.

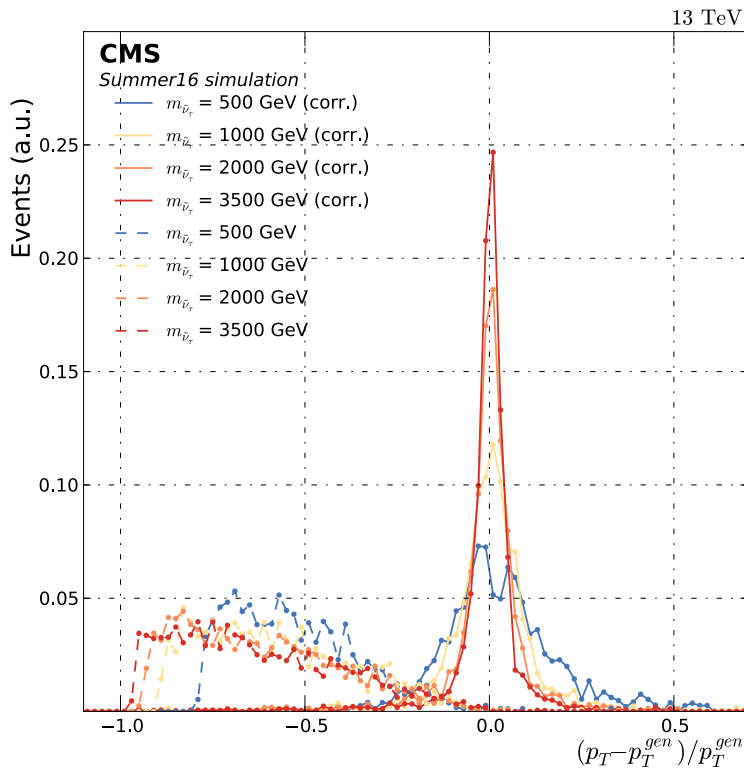


Figure 22: Transverse tau momentum resolution for different RPV signal masses. The results for the decay of $\tau \rightarrow \mu\nu\nu$ are shown, similar results could be obtained for the τ_e case. Shown are the resolution for the visible decay products (dashed lines) and the resolution for the collinear reconstructed tau (solid lines). It is clearly visible that the collinear reconstructed tau gives a clear peak at zero, while the visible decay products are shifted to lower values with no clear peak. It can also be seen that for higher masses and therefore higher tau p_T the mass resolution gets better as the peak gets sharper. This is mainly driven by the higher tau momentum for which the assumptions of the collinear reconstruction are better fulfilled.

The resulting p_T resolution is centred at zero. Not taken the E_T^{miss} into account leads to a reconstructed p_T that is shifted to lower values compared to the true tau p_T and no clear peak structure is visible. Taking E_T^{miss} into account gives a sharp peak at zero, meaning a good reconstruction of the tau p_T . The tau p_T is only smeared out by the p_T

resolution of the visible particles used in the collinear reconstruction. The reconstruction gets also better for higher p_T values or masses as the assumption of collinearity is fulfilled better. This reconstruction makes it therefore possible to do a resonance search in the $e\tau_\mu$ and $\mu\tau_e$ final states. The efficiencies of reconstruction and identification are exactly the same as for the pure electron or muon reconstruction (Sec. 4.2.1 and Sec. 4.2.2) as they are the particles that are measured.

4.3 EVENT PRE-SELECTION

The basic pre-selection of events is presented in this section. The objects that should be in the event and some global features are required. The first step is the trigger requirement. As all three studied final states contain an electron and a muon, the trigger selection is the same for all. Also an additional requirement is imposed on electrons to suppress the mis-reconstruction of electrons from muon showers. These requirements are summarized in the first sub-section (Sec. 4.3.1), while the channel specific requirements are summarized in Sec. 4.3.2 for the $e\mu$ channel and in Sec. 4.3.3 for the τ channels.

4.3.1 All channels

All studied final states in this analysis contain at least one high momentum muon and at least one high energy electron. These two particles can therefore also be used to trigger the events, as high energy leptons can be triggered with a very high efficiency. To get the highest possible efficiency a combination of three triggers is used, where as long as one fires, the event is selected. These High-Level Trigger (HLT) paths are two different single muon triggers and one single photon trigger.

The two single muon triggers have the lowest p_T threshold of single triggers and do not include any isolation requirements. They are sensitive up to $|\eta| < 2.4$ and have a lower p_T threshold of 50 GeV. The two single muon triggers differ in the last step of muon reconstruction in the trigger. The HLT_MU50 uses as a last step a global muon reconstruction in the tracker and muon system, while the HLT_TkMU50 uses only the tracker, it is therefore called muon track trigger. This approach can compensate some inefficiencies in the muon system due to e. g. showering muons.

The single photon trigger selects electron candidates based on the energy deposits in the electromagnetic and hadronic calorimeters. The track of the electron is not used in the trigger as it would be the case if a single electron trigger were used. At high energies the photon trigger has a higher efficiency as there are no track reconstruction inefficiencies due to e. g. bremsstrahlung. The single photon trigger has also no requirements on the isolation of the electron, has a transverse energy threshold of 175 GeV and is sensitive up to $|\eta| < 2.5$.

The trigger efficiencies are defined with respect to well reconstructed particles that fulfil the identification criteria introduced in Sec. 4.2.1 and Sec. 4.2.2 in the following way for the muon trigger:

$$\epsilon_{\text{Muon-Trigger}} = \frac{N(\text{Muon ID} + \text{Trigger})(p_T, \eta, \phi)}{N(\text{Muon ID})(p_T, \eta, \phi)} \quad (13)$$

and for the electron trigger as

$$\epsilon_{\text{Ele-Trigger}} = \frac{N(\text{HEEP ID} + \text{Trigger})(p_T, \eta, \phi)}{N(\text{HEEP ID})(p_T, \eta, \phi)}. \quad (14)$$

The efficiencies of the trigger are shown as a function of η and ϕ in Fig. 104 as determined with simulated RPV signal points. There both muon triggers are combined with a logical 'or'. All observable effects are due to the geometry of the detector e. g. the shape of the ECAL or the muon chambers. The combined trigger efficiency of all three triggers is shown in Fig. 23 as a function of muon p_T and electron E_T .

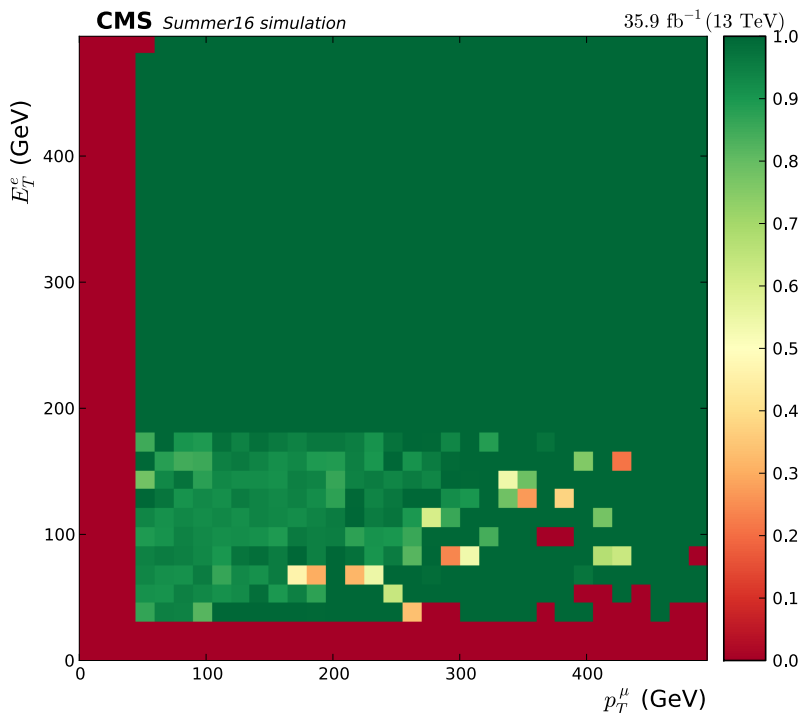


Figure 23: Combined trigger efficiency of all three triggers used in the analysis. The efficiency is shown as a function of muon p_T and electron E_T and determined on RPV signal simulations. The electron trigger threshold is 175 GeV and is fully efficient for higher energies. In the region below the threshold only the two single muon triggers are used which have a very high efficiency at the low p_T range and are nearly fully efficient for high p_T .

This efficiency is determined by RPV signal simulation. Differences between the actual trigger in the data and the simulated one have to be considered. The corresponding efficiency corrections are described in Sec. 4.5. Another cross check of the trigger performance is the fraction of events that are triggered by a specific one. This fraction can be determined for events only triggered by a single muon trigger, events triggered by only the single photon trigger and events triggered by both possibilities. These fractions as a function of invariant electron-muon mass are shown for all simulated background processes and recorded data in the $e\mu$ channel in Fig. 24.

Within the uncertainties the fractions in simulation and data are comparable. For low masses the events are mostly triggered by the single muon triggers due to their lower threshold. For higher energies the fraction of events triggered by both trigger is dominant.

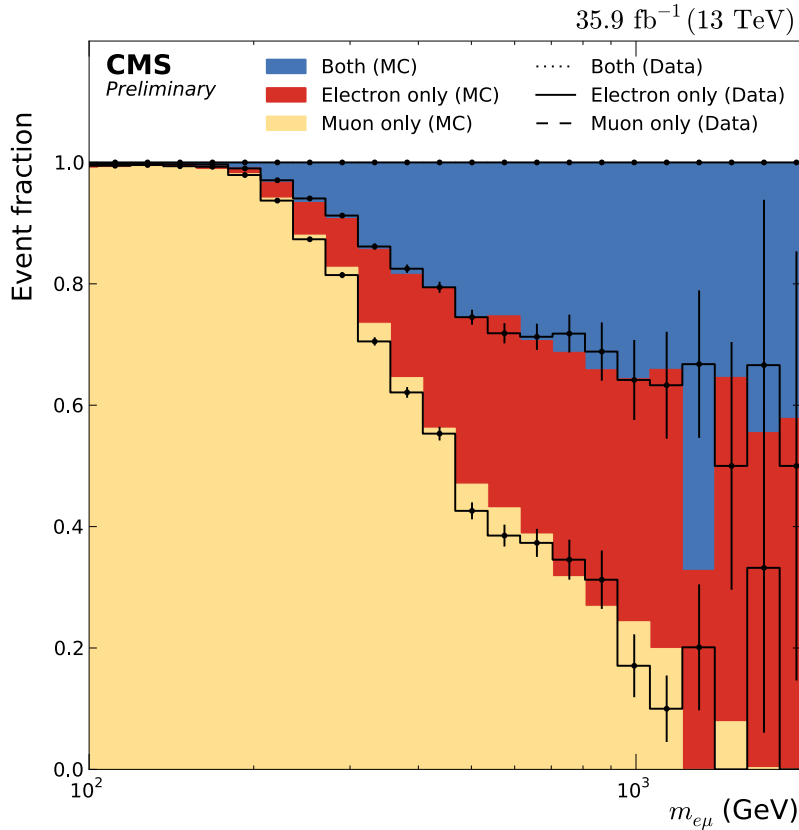


Figure 24: Fraction of events triggered by different trigger combinations as a function of invariant $e\mu$ mass. First the fraction of events triggered only by the single muon trigger is shown (yellow / dashed line). Also shown are the fraction of events triggered only by the single photon trigger (red / solid line) and the fraction of events triggered by both triggers (blue / dotted line). The fractions are determined for the complete background simulation and the observed data in the $e\mu$ channel. Within the uncertainties the values of data and simulation agree with each other.

Due to the trigger selection the analysis is based on the so called SingleMuon and SinglePhoton datasets. To improve the availability of data, the recorded events are split into data-streams according to the triggers that fired in the event. The SingleMuon stream, for example, contains all events that have fired one single muon trigger. Duplicate events between the two used datastreams SinglePhoton and SingleMuon are removed to avoid double counting. A detailed list of the used datasets is given in Tab. 11 in the appendix. The recorded data is then cleaned to only contain events which were recorded during times where the whole detector was working perfectly. The integrated luminosity of the data sample used in this analysis is 35.9 fb^{-1} .

The other requirement for all events is to suppress Bremsstrahlung by muons. High energy muons can produce Bremsstrahlung which results in a supercluster in the ECAL in the direction of the inner track of the muon. Therefore the muon can lead to fake electron candidates. To suppress these candidates an electron veto is applied to electrons if there is a global muon with p_T greater than 15 GeV within $\Delta R < 0.1$ of the electron direction.

The other event requirements are slightly different for the $e\mu$ channel and the two channels containing decaying taus, and are therefore summarized in the following sections.

4.3.2 $e\mu$ channel

In the $e\mu$ channel, all events are required to contain at least one good electron as defined in Sec. 4.2.1 and one good muon as defined in Sec. 4.2.2. Requirements on other particles in the event are not imposed e.g. no veto on other particles. This is to be as independent from any assumptions on the signal as possible. The leptons in the $e\mu$ pair are not required to carry opposite electric charge. This is to not be affected by lepton charge misidentification. In 8 TeV, the electron charge misidentification probability was 0.02% in ECAL barrel and 0.2% in ECAL endcaps for $Z \rightarrow ee$ decays [46]. The muon charge misidentification rate is less than $< 3 \times 10^{-4}$ up to a p_T of 300 GeV and $< 2 \times 10^{-3}$ above a p_T of 300 GeV as measured with cosmics [74].

If there is more than one possible combination of an $e\mu$ pair in the event, the pair with the highest invariant mass $m_{e\mu}$ is chosen³. Therefore, additional electrons or muons are allowed in the event, but only the two selected leptons are used in the further analysis.

To enhance the sensitivity of the analysis, the events are split according to the η of the electron and muon in four categories. The two dimensional distribution of η_e versus η_μ is shown in Fig. 25 for the complete background simulation. Also shown are the four categories, which are defined as:

- BB (barrel-barrel): Both electron and muon are in the barrel: $|\eta_e| < 1.4442$ and $|\eta_\mu| < 1.2$.
- BE (barrel-endcap): The electron is in the barrel, while the muon is in the endcap: $|\eta_e| < 1.4442$ and $|\eta_\mu| \geq 1.2$.
- EB (endcap-barrel): The electron is in the endcap and the muon in the barrel: $|\eta_e| > 1.566$ and $|\eta_\mu| < 1.2$.
- EE (endcap-endcap): Both electron and muon are in the endcaps: $|\eta_e| > 1.566$ and $|\eta_\mu| \geq 1.2$.

The main gain of this approach is that the different detector regions result in different resolutions. Splitting them instead of looking at the events inclusively allows to gain sensitivity in the high resolution regions.

4.3.3 $e\tau_\mu$ and $\mu\tau_e$ channels

The final states of the $e\tau_\mu$ and $\mu\tau_e$ channels contain a high E_T electron and a high p_T muon in the final state. Therefore the same basic selection of trigger and showering muon veto as for the $e\mu$ channel are applied in both channels. The particle selection is the same as for the $e\mu$ channel, so requiring a well reconstructed electron (Sec. 4.2.1) and a well reconstructed muon (Sec. 4.2.1). No constraints on potential other particles

³ Less than one percent of the selected events contain two or more $e\mu$ pairs.

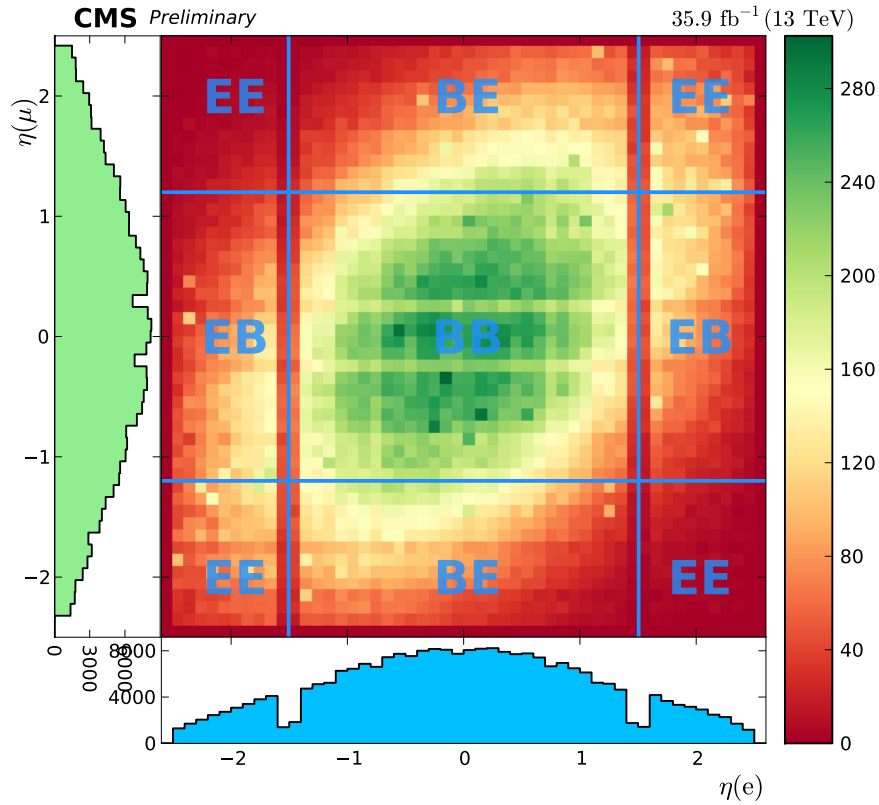


Figure 25: Distribution of η_e versus η_μ for all simulated events in the $e\mu$ channel. Shown also are the projections along the two axes. Also shown are the boundaries of the four event categories and the corresponding labels. The features in the distributions are given by the geometry of the detector, especially the gaps between the muon chambers and the transition of the ECAL barrel to the endcap can be seen. The general oval shape of the distribution is the consequence of the different background processes of light, but boosted particles that decay into an electron and muon. Therefore, they tend to go in the same region in the detector. This results in an enhancement of events along the diagonal line ($\eta(\mu) = \eta(e)$) while the off-diagonal is depleted.

in the event are imposed. In this channel a tau that decays leptonically is required and will be reconstructed as described in Sec. 4.2.3, therefore the event should contain at least 50 GeV of E_T^{miss} .

E_T^{miss} can be influenced by many detector effects, like mis-reconstructed particles or inefficient detector parts. To account for these known features all events are filtered to veto events with such problems. All events have to pass the following list of E_T^{miss} -filters [75] at the analysis level. These filters are especially important for data events as inefficient detector parts are present in the actual detector and not the simulated one. To keep the selection symmetric between data and simulation and not introduce a bias the filters are also applied to all simulated events.

- HCAL noise filter: This filter tries to detect instrumental noise in the HCAL or the HCAL read-out, which can be a source of E_T^{miss} . This is done by looking at the timing, pulse shape, hit multiplicity and other variables [76].
- HCAL isolated noise filter: The same approach as for the HCAL noise filter, but specially tuned for isolated noise.

- Beam halo filter: Interaction of the proton bunches with the LHC or the rest gas in the beam pipe can produce particles with very high η . These so called beam halo particles can travel nearly parallel to the beam and can be a source for E_T^{miss} . By using the timing information from the CSC and calorimeters the events can be vetoed [77].
- Good vertex filter: The selected event should contain at least one good vertex, so one vertex with at least three degrees of freedom in the reconstruction (reconstructed from at least three tracks). The position of the reconstructed vertex should be $|d_z| < 30 \text{ cm}$ and $|d_{xy}| < 3 \text{ cm}$. This filter suppresses events which didn't originate in a proton-proton collision in the interaction region.
- Endcap bad supercrystal filter: Two ECAL endcap supercrystals give anomalously high energies, resulting in very high E_T^{miss} , contributions from these crystals are therefore filtered [78].
- ECAL trigger primitive filter: Some crystals in the ECAL are masked in the reconstruction because they are either not operational or have a high level of noise. If a physical particle hits these crystals, their energy is underestimated, resulting in high E_T^{miss} , therefore such an event is filtered [79].
- Bad particle flow muon filter: Events where the muon is badly mis-reconstructed with high p_T values, but good enough to be declared a particle flow muon will result in high E_T^{miss} . These events are filtered by requiring compatibility between the muon segments and the reconstructed track or some upper value on the uncertainty of the reconstruction [80].
- Bad charged hadron filter: Muons where the quality of the reconstruction is even lower than in the bad particle flow muon filter can be included in the E_T^{miss} calculation as charged hadron candidates. The filtering of these events is similar to the bad particle flow muon filter [80].

All selected events contain after the selection either an electron and a τ_μ candidate reconstructed from a muon and E_T^{miss} , or a muon and a τ_e candidate, reconstructed from an electron and E_T^{miss} . If there is more than one possible combination the pair with the highest invariant mass is selected for the analysis.

4.4 BACKGROUND DESCRIPTION

With the pre-selection of events defined the contributing background processes can be derived. All standard model processes that contain an electron and a muon in the final state or could be identified as an electron and a muon could contribute. Therefore the background processes can be categorized into two categories, either the two leptons can be produced promptly in the hard interaction, the other possibility is that the leptons are produced in the decay of other particles or other particles are misidentified as electrons or muons. The contributions to these two categories are summarized in the following sub-sections.

4.4.1 Prompt backgrounds

Processes which produce a prompt pair of electron and muon are described by simulation, the different processes are summarized in the following, sorted in decreasing yield of events to the background expectation. A detailed list of all simulated processes is given in Tab. 16 in the appendix.

- $t\bar{t}$: The pair production of top quarks can produce an electron and a muon in the decay. The top quarks each decay into a bottom quark and a W boson. The charged leptons result from the subsequent decay of the W . The dominant process is illustrated in the Feynman diagram in Fig. 2. The top quark is the heaviest particle in the standard model (See Tab. 1), the decay products are therefore highly boosted, resulting in electrons and muons at high energies. All events also contain additional jets and neutrinos resulting in E_T^{miss} . The process has a very high cross section as the production couplings are of the strong interaction. Due to the high cross section and the similar signature to the signal it is the dominant background process throughout the analysis in all channels.
- WW : The pair production of W bosons can produce an electron and a muon similar to the two W bosons in the pair production of top quarks. In addition the event contains E_T^{miss} due to the neutrinos in the final state. The cross section of this process is slightly lower than for the leading top pair contribution due to the production of W bosons via the weak interaction. At high masses the contribution of this process gets equally important as the top pair production.
- WZ : The production of a W boson and a Z boson is very similar to the pair production of W bosons. Due to the Z boson the process can contribute via the decay $Z \rightarrow \tau_e \tau_\mu$. The cross section for this process is lower than for W pair production, which is even further reduced by the branching ratio of the tau decays. This results in only a small contribution to the final background event yield.
- ZZ : The cross section for the production of two Z bosons is even lower than for WZ , and the final state can contain up to four leptons. The contribution of this process is therefore quite small.
- Single top: The production of an individual top quark and the subsequent decay can happen in combination with a W boson (tW channel) and therefore contains two W 's in the final state like the W pair production, resulting in an electron, a muon and E_T^{miss} . Other possible single top channels (s - or t -channel) have a higher cross section (t channel) but do not produce the exact final state of this analysis. For these channels to contribute they have to be misidentified in the analysis, therefore their contribution is small.
- DY : The resonant production of a Z boson or a γ , called Drell–Yan (DY) process, will contribute to the background expectation if the Z boson or γ decays into two leptons. If the leptons are two taus, they could further decay into an electron and a muon plus neutrinos, resulting in E_T^{miss} . The invariant mass of the decay products will be small, therefore the contribution of this process is mostly at low masses. This low mass region is important to compare the observed data

to the background expectations, therefore a good description of this background process is vital.

The simulation of all the background processes is done similar to the signal simulation described in Sec. 4.1. The processes are all simulated with the POWHEG [81–83] generator, PYTHIA 8 is used for the showering and hadronisation. Only the process $DY \rightarrow \tau\tau$ is simulated with MADGRAPH5_AMC@NLO [84] for both simulation steps. The detector simulation used is the default one used for all simulated events in 2016.

As this analysis is a search for new high mass phenomena, the background description at high mass is crucial. The two leading backgrounds $t\bar{t}$ and WW produce a falling invariant mass spectrum. The generators simulate events according to their probability to be present in data, therefore high mass events are rarely produced. This effect results in poor simulation statistic at high mass. To overcome this problem dedicated high mass events were produced in so called extension samples. For these events, the simulation is the same as for normal events, but only events in a given mass range are kept. Measuring the fraction of these events allows to scale the events according to the actual rate which is expected of them. To save computing resources, this filtering was done before the hadronisation and detector simulation, so that only selected events go through the whole simulation chain. Nevertheless about 20 000 000 000 generated events are necessary to get sufficient statistic for $t\bar{t}$ events with $m_{e\mu} > 1800$ GeV. The effect of these extension samples can be seen in Fig. 26, the event statistics in the high mass region is dramatically increased compared to the mass inclusive or bulk simulation.

4.4.2 Misidentified or non-prompt backgrounds

The other source of background events is due to particles which are misidentified as an electron or muon. The probability of particles to be misidentified as muons is very low, therefore this possibility is not considered. The electron can be misidentified from two sources, either photons or hadronic jets. For these events to be considered in the analysis, the events have to also contain a muon. These criteria result in the sources of background due to misidentified electrons:

- $W\gamma$: The production of a W boson in association with a high energy γ photon can be a source for high mass $e\mu$ events, if the W decays into a muon and a neutrino. The γ can be misidentified as an electron. These events are simulated with the MADGRAPH5_AMC@NLO generator.
- W +Jets: This process is similar to $W\gamma$, but an additional high energy hadronic jet due to a quark or gluon radiation instead of a photon. As the accurate simulation of jets misidentified as electrons is very difficult, therefore this background contribution is derived directly from the data as explained in this section.
- QCD: The last possibility for misidentified background processes is due to multi-jet events, which are produced by strong interaction processes. Therefore, they are called QCD processes. In hadronic jets particles can decay into muons, producing the muon for the selection. Many of these muons are vetoed by the isolation selection criteria, therefore the rate of these events is small. The electron is misidentified from another hadronic jet. The contribution from these events

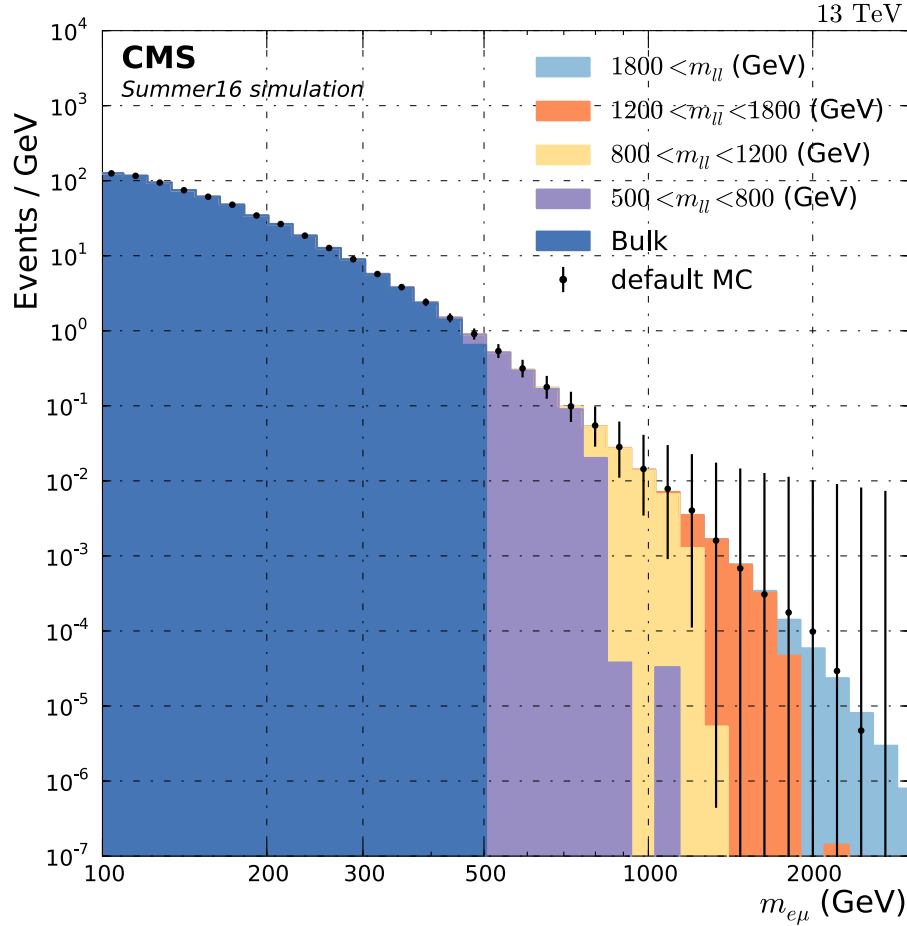


Figure 26: Generator level invariant $e\mu$ mass distribution of $t\bar{t}$ events. The filled histograms are the different extension samples binned in dilepton mass and matched to the bulk sample which is produced mass inclusive. In black the mass inclusive sample is shown as a comparison. The statistics of the bulk sample reaches until about $m_{e\mu} \sim 1000$ GeV, as illustrated by the statistical uncertainty bars. The statistics of the extension samples reaches up to a few TeV instead.

is also derived directly from the data, as the simulation is difficult. How this contribution is derived from the data is explained in the following.

The two background processes due to hadronic jets misidentified as electrons are directly derived from the data. This is done for both processes together via the so called fake rate method. The event selection except the electron part is identical, for the electron a loose selection is applied and the full HEEP selection is vetoed. This loose selection is given by the following selection criteria:

- The shower shape variable $\sigma_{i\eta i\eta}$ should be smaller than 0.013 in the barrel and smaller than 0.034 in the end caps.
- The ratio of energy in the HCAL and ECAL H/E has to be smaller than 0.15 in the barrel and smaller than 0.10 in the end caps.
- Only one hit can be missed in the inner track reconstruction.

- The transverse impact parameter $|d_{xy}|$ has to be smaller than 0.02 in the barrel and smaller than 0.05 in the end caps.
- In addition, selected electrons should be matched to the first step of one of two HLT trigger paths. This so called seeding leg could be either of the HLT_DOUBLEELE33_CALOIdL_GSFTrkIdVL trigger or of HLT_DOUBLEELE33_CALOIdL_MW.

This loose event selection contains still a significant contribution from prompt background events. These contributions are subtracted via simulated events that pass the loose selection. The fake rate is the ratio of events passing the HEEP selection to events passing the HEEP selection. It is measured by the $Z' \rightarrow ee$ analysis in events triggered only by a photon trigger [85]. The parameterisation of the fake rate is given in Tab. 5.

Table 5: Functional form of the measured fake rate F_R for HEEP as a function of electron E_T (from ref. [85]).

Region	E_T range (GeV)	Functional form
barrel	$35 \leq E_T < 131$	$0.11 - 0.0025 \times \frac{E_T}{\text{GeV}} + 2.3 \cdot 10^{-5} \times \left(\frac{E_T}{\text{GeV}}\right)^2 - 7.2 \cdot 10^{-8} \times \left(\frac{E_T}{\text{GeV}}\right)^3$
	$131 \leq E_T < 356$	$0.014 - 0.00010 \times \frac{E_T}{\text{GeV}} + 3.6 \cdot 10^{-7} \times \left(\frac{E_T}{\text{GeV}}\right)^2 - 4.3 \cdot 10^{-10} \times \left(\frac{E_T}{\text{GeV}}\right)^3$
	$E_T \geq 356$	$0.0028 + 2.4 \cdot 10^{-6} \times \frac{E_T}{\text{GeV}}$
endcap	$35 \leq E_T < 122$	$0.12 - 0.0013 \times \frac{E_T}{\text{GeV}} + 4.7 \cdot 10^{-6} \times \left(\frac{E_T}{\text{GeV}}\right)^2$
$ \eta < 2.0$	$122 \leq E_T < 226$	$0.035 - 4.8 \cdot 10^{-5} \times \frac{E_T}{\text{GeV}}$
	$E_T \geq 226$	$0.026 - 9.1 \cdot 10^{-6} \times \frac{E_T}{\text{GeV}}$
endcap	$35 \leq E_T < 113$	$0.081 - 0.00034 \times \frac{E_T}{\text{GeV}}$
$ \eta > 2.0$	$E_T \geq 113$	0.042

The events that pass the loose electron selection, after the subtraction of the contribution of prompt backgrounds, are weighted by the factor:

$$\frac{F_R}{1 - F_R}$$

with the fake rate F_R . This then gives the contribution from hadronic jets misidentified as electrons.

To validate the result of this background expectation derived from the data, it is compared to an independent method to determine this background. The method is called same sign method, which also derives the background contribution of hadronic jets, misidentified as electrons, directly from the data. In the same sign method, it is exploited that the probability of assigning a positive or a negative charge to the misidentified jets is equal. Therefore, opposite and same-sign electron and muon pairs are a similar description for misidentified jets first in the total number as well as the distribution shape for many variables. On the other hand, all other standard model processes have an opposite sign electron and muon pair and do not contribute to

the same sign control region. The contributions of prompt background processes are subtracted from the data in the same sign region using simulation. Figure 27 shows a comparison between the jet background, estimated from the data in the same sign region and estimated by applying the fake rate method. They agree within the 50% uncertainty assigned to the fake rate estimation, and especially at high mass where this background component becomes relevant both methods agrees within the statistical uncertainties. The fake rate method has also the advantage that the reach in mass is bigger than in the same sign method.

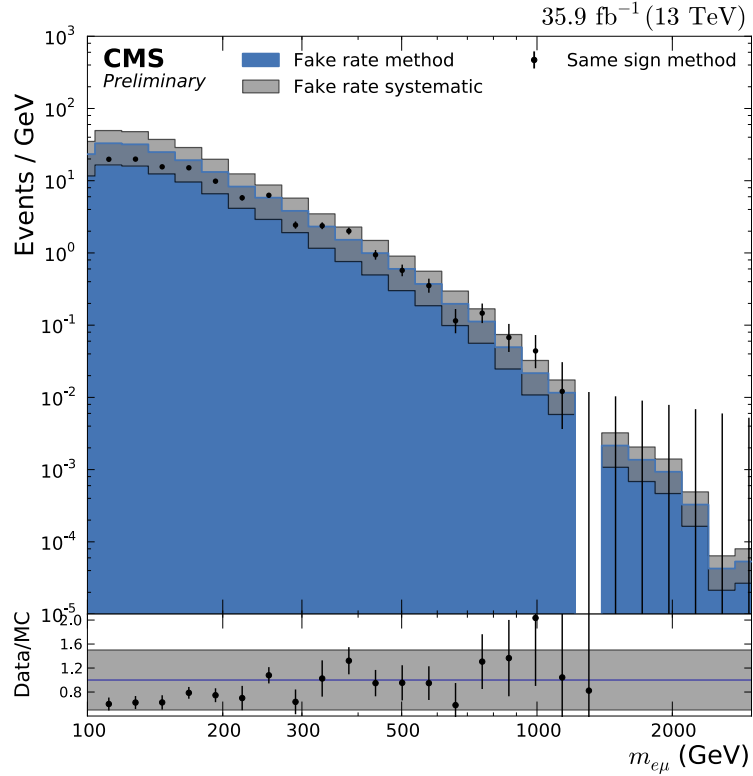


Figure 27: Validation of the background processes derived from data. Black points show the $e\mu$ invariant mass distribution derived via the same sign method. The filled histogram shows the misidentified background derived with the fake rate method which is used in the analysis. Both methods agree within the assigned uncertainty of 50% on this background estimate. At high masses the methods even agree within the statistical uncertainties, while the fake rate method has a bigger reach in mass.

4.5 EVENT CORRECTIONS

In this section corrections for the known mis-modellings of simulated events are presented. No simulation is perfect and some effects were not known at the time that the simulation was produced. To account for these effects and reproduce the observed data, correction factors are applied. Global event corrections are applied as well as corrections for the reconstructed objects, all are introduced in the following.

4.5.1 Global event corrections

Additional interactions in the same event, called pile-up, are simulated. The configuration for this simulation is created before the data taking starts to directly compare simulation with observed data, but the configuration does not exactly match the conditions in data. To account for the actual conditions, the difference has to be corrected for an accurate description of collision data. The number of all interactions per time N depends on two parameters

$$N = \sigma_{\text{mb}} \cdot \mathcal{L}_{\text{int}}$$

with the instantaneous luminosity \mathcal{L}_{int} as measured during data taking and the minimum bias cross section σ_{mb} . This number of interactions can then be modelled with a Poisson distribution, with the mean number of interactions as determined above. Integrating this distribution over the whole data taking period gives the distribution of the number of interactions observed in the data. The ratio of this distribution to the simulated one gives then the correction factor for the simulation as a function of the number of interactions. The two parameters for this correction are the instantaneous luminosity measured during the data taking and the minimum bias cross section, so the cross section for any interaction to happen. This cross section is assumed to be 69.2 mb for this reweighting [86]. The value is chosen to give a good agreement between observed data and simulation. The effect of this reweighting procedure can be seen in Fig. 28, which shows the number of reconstructed vertices in the observed data and simulation, first before the reweighting and then after the correction factors are applied. The agreement between observation and simulation clearly improves.

Some differences which remain even after the reweighting are due to the different vertex reconstruction efficiencies in the observed data and simulation and other effects that are not covered by the reweighting procedure, like out-of-time pileup. That are interactions which occur at a different collision, before or after the recorded event, but due to the finite flight time of the particles and latencies in the detector electronics, they can also contribute to the recorded event. To take all these differences into account in the analysis a systematic uncertainty is assigned to this reweighting method. As there is only one free input parameter to the reweighting method, the minimum bias cross section, this value has to be varied to estimate an uncertainty. This is a quantitative approach to estimate a systematic uncertainty without treating all the different problems with this method individually. Therefore the uncertainty is estimated by shifting the minimum bias cross section up and down by $\pm 5\%$. The resulting uncertainty of this approach is also shown in Fig. 28-right as a grey band around the background expectation. Within these uncertainties the observed data agree with the expectation from simulation.

The other global event content which is simulated is the trigger decision, which could differ between the observed data and the simulation. The trigger efficiency is not exactly equal in data and simulation, therefore the differences have to be corrected. The single photon trigger has an efficiency of 100% as can be seen in Fig. 23, therefore no corrections are necessary as no source for a potential inefficiency is present. This was checked in simulated events, where all events containing an electron with at least $E_T = 175 \text{ GeV}$ fire the trigger. In real data this was cross checked by looking at events triggered by the muon trigger and checking how many electrons fire the single photon trigger. Also in the data all electrons which could fire the trigger do so, resulting in

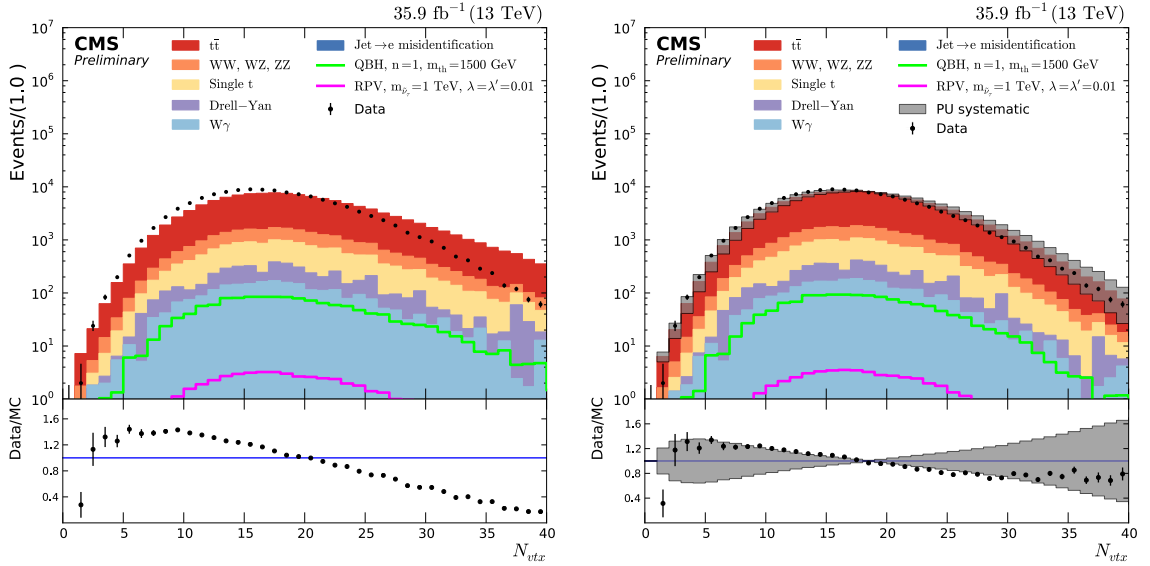


Figure 28: Number of reconstructed vertices before (left) and after (right) pile-up reweighting. The filled histograms show the contribution of the different background processes, while the black markers represent the observed data. All events have passed the event selection as described in Sec. 4.3.2. To compare the simulation with the observed data the ratio of the number of events is also shown for both distributions. After the reweighting the systematic uncertainty due to the $\pm 5\%$ shift of the minimum bias cross section is shown as a grey shaded band. The agreement after the reweighting is greatly improved and covered by the systematic uncertainty of the method.

an efficiency of 100%. The two single muon triggers have efficiencies slightly lower, therefore the difference of the efficiency in the simulation have to be corrected to match the efficiencies measured in data. For this correction the efficiency has to be determined from the data and simulation in a similar way. This is done centrally by the muon group in CMS [72]. This is done by the Tag and Probe method, where the Z boson resonance is used to produce two muons. Two muons are selected if they give a combined invariant mass compatible with the Z mass, the first muon is the Tag, which should fulfil strict selection criteria. This selection assures that a second muon should be present, this Probe muon can be used to test different steps of the reconstruction, identification or triggering. The ratio of muons fulfilling the tested criteria to all muons gives the efficiency independently of generator information. The ratio of the results in simulated events and observed data events is used as a scale factor to correct the simulation. The scale factors are determined as a function of p_T and $|\eta|$ and are plotted in Fig. 105 and listed with the corresponding uncertainties in Tab. 17 in the appendix [87]. This scale factor is only applied if the event is triggered only by the muon trigger and the photon trigger did not fire. The correction is close to unity, in the range of a few percent, for most of the p_T and $|\eta|$ range. The systematic uncertainties of this reweighting are introduced in Sec. 4.9.1.

4.5.2 Electron corrections

The electron reconstruction and identification can be split in two parts, which can differ between the simulation and the data. These two are:

- Electron reconstruction
- Electron identification (HEEP)

Both are covered by scale factors to account for differences between the data and simulation. Both scale factors are determined similar to the muon trigger scale factor, by the Tag and Probe method, but from $Z \rightarrow ee$ decays. The resulting scale factors can be seen in Fig. 105 in the appendix [88]. The scale factor is independent of E_T and close to unity over most of the η range. The scale factors of the HEEP electron identification criteria have also been measured by the Tag and Probe method [89] and are listed in Tab. 6. The systematic uncertainties assigned to these scale factors are introduced in Sec. 4.9.1.

Table 6: Electron identification scale factors and the associated uncertainties from the Tag and Probe method.

Region	Scale factor	Tot. Uncert.
Barrel	0.971	± 0.006
Endcap	0.983	± 0.007

4.5.3 Muon corrections

The muon selection is split into three different parts where differences between the simulation and data have to be corrected. The three parts are:

- Muon reconstruction
- Muon identification
- Muon isolation

All three scale factors are determined with the Tag and Probe method. The muon reconstruction efficiency is independent of p_T and determined as a function of η_μ . It is shown in Fig. 105 in the appendix and very close to unity [90]. The scale factors of the high- p_T muon identification are determined as a function of p_T and $|\eta|$ and are shown in Fig. 105 and listed in Tab. 18 in the appendix. They are a few percent below unity [91]. The scale factors for the muon isolation are also determined as a function of p_T and $|\eta|$ [91]. They are very close to unity and are shown in Fig. 105 and listed in Tab. 19 in the appendix. The systematic uncertainties are introduced in Sec. 4.9.1 for these scale factors.

4.5.4 E_T^{miss}

The E_T^{miss} in an event has to be corrected for mis-measurements of jet energies, the jet energy scale. This is done by Eq. 15

$$E_T^{\text{miss}}(\text{corr}) = E_T^{\text{miss}}(\text{raw}) - \sum_{p_T^{\text{L123}} > 10 \text{ GeV}} (p_T^{\text{L123}} - p_T) \quad (15)$$

by taking the difference between the raw jet p_T and the corrected jet p_T^{L123} for each jet above 10 GeV. Three levels of jet energy correction are included in p_T^{L123} , first the subtraction of pileup, electronic noise and the effects due to thresholds in the electronic. Second the relative difference of the energy response as a function of η is corrected to get a flat response. The third correction is to get an energy response of unity.

In our selected events, the E_T^{miss} measurement should be dominated by the high energy electron and muon in the event, therefore the effect of the jet energy scale corrections is very small.

4.6 KINEMATIC EVENT SELECTION

After the pre-selection of events, the determination of the contributing background processes and the application of corrections for the known mis-modelling effects, the final selection can be applied. The minimum event content is fixed by the pre-selection, so the relations of the objects in the final state can be used to enhance the signal to background ratio. For the $e - \mu$ channel no further selection is applied as this channel is independent of other objects in the final state. Therefore, it is possible to be very model independent by not applying further selection criteria. For the tau channels ($e\tau_\mu$ and $\mu\tau_e$) the selection is not independent of other objects in the final state of the event, as everything contributes to E_T^{miss} . Therefore the same model independence as in the $e - \mu$ channel is impossible. To enhance the signal to background ratio, further selection criteria are applied in the $e\tau_\mu$ and $\mu\tau_e$ channels. These selection criteria are introduced in the following sub-sections. The motivation for these selection criteria is to ensure a good reconstruction of the $e\tau$ or $\mu\tau$ resonance. Therefore the criteria are motivated by the fulfilment of the steps of the collinear tau reconstruction introduced in Sec. 4.2.3. The assumptions in the tau reconstruction should be fulfilled for signal events, but not for background processes. This allows for a reduction of background events without losing much signal efficiency. Later with the statistical interpretation, it becomes clear that most of the analysis is performed with little to zero background expectation, therefore the pure signal efficiency is the measure for the analysis sensitivity and not the signal to background ratio. This results in the main criteria to choose a selection value, the signal efficiency should be as high as possible and ideally $> 99\%$.

4.6.1 $e\tau_\mu$ channel

In this channel four additional kinematic selections are applied. They are derived directly from the kinematics of the $\tilde{\nu}_\tau$ decay into the tau and an electron as well as the kinematics of the subsequent decay of the tau into a muon and E_T^{miss} . These four selection criteria are motivated in the following paragraphs and are also illustrated with

$N - 1$ distributions for each selection. For a $N - 1$ distribution all events are shown which pass all selections (N) except the probed one (-1). The variable on which the selection is applied is plotted in this $N - 1$ distribution, therefore only the effect of this selection can be seen. The effect of all these four selection criteria on the integrated number of events is shown at the end of this section in the cut-flow distribution in Fig. 33.

SELECTION ON $\Delta\phi(e, \mu)$ The electron and tau in this channel should be back-to-back for a high mass $\tilde{\nu}_\tau$. Therefore also the electron and muon should be back-to-back. This assumption does not hold for the background processes. This can be seen in Fig. 29, the $N - 1$ distribution of the angular difference in the transverse plane of the electron and muon $\Delta\phi(e, \mu)$.

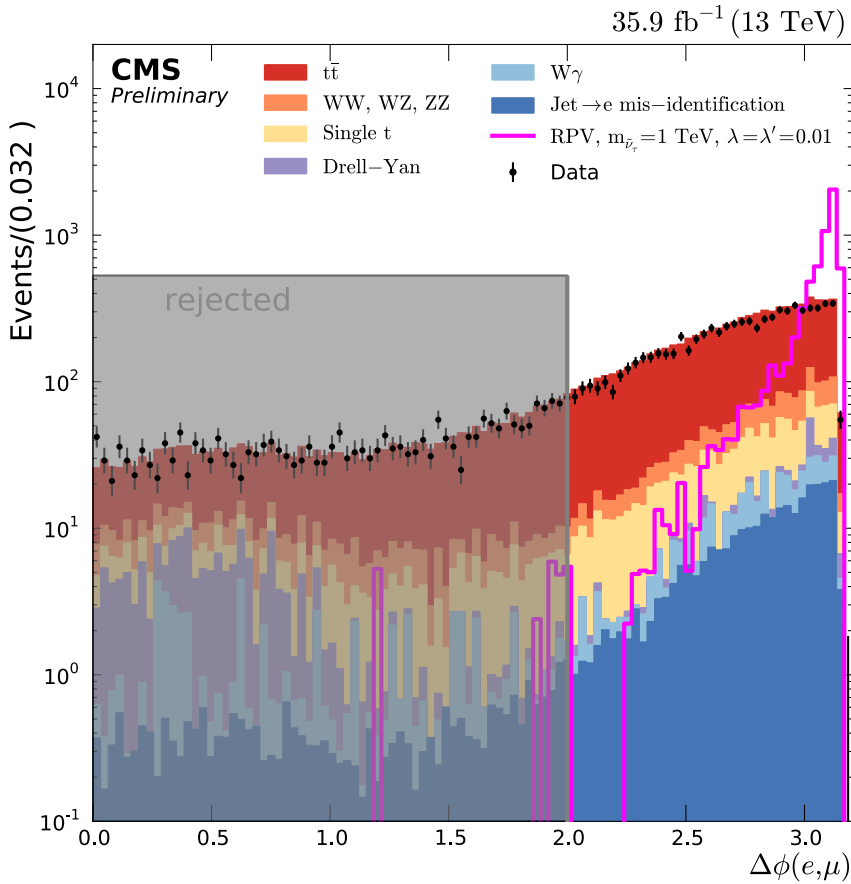


Figure 29: $N - 1$ distribution of $\Delta\phi(e, \mu)$ for the different background processes, the observed data and an example RPV signal point. The chosen selection criterium of this variable is > 2.0 , as indicated by the gray box in the figure.

To keep a very high signal selection efficiency a selection criteria of $\Delta\phi(e, \mu) > 2.0$ is chosen, which does not affect the example RPV signal shown in Fig. 29.

SELECTION ON $\Delta\phi(\mu, E_T^{\text{MISS}})$ In the decay of the boosted tau into a muon and E_T^{MISS} , they should be both very close together. As E_T^{MISS} can only be measured in the transverse plane, the angular difference of muon and E_T^{MISS} $\Delta\phi(\mu, E_T^{\text{MISS}})$ should be

small. This assumption does not have to be true for the background processes. The $N - 1$ distribution of $\Delta\phi(\mu, E_T^{\text{miss}})$ can be seen in Fig. 30.

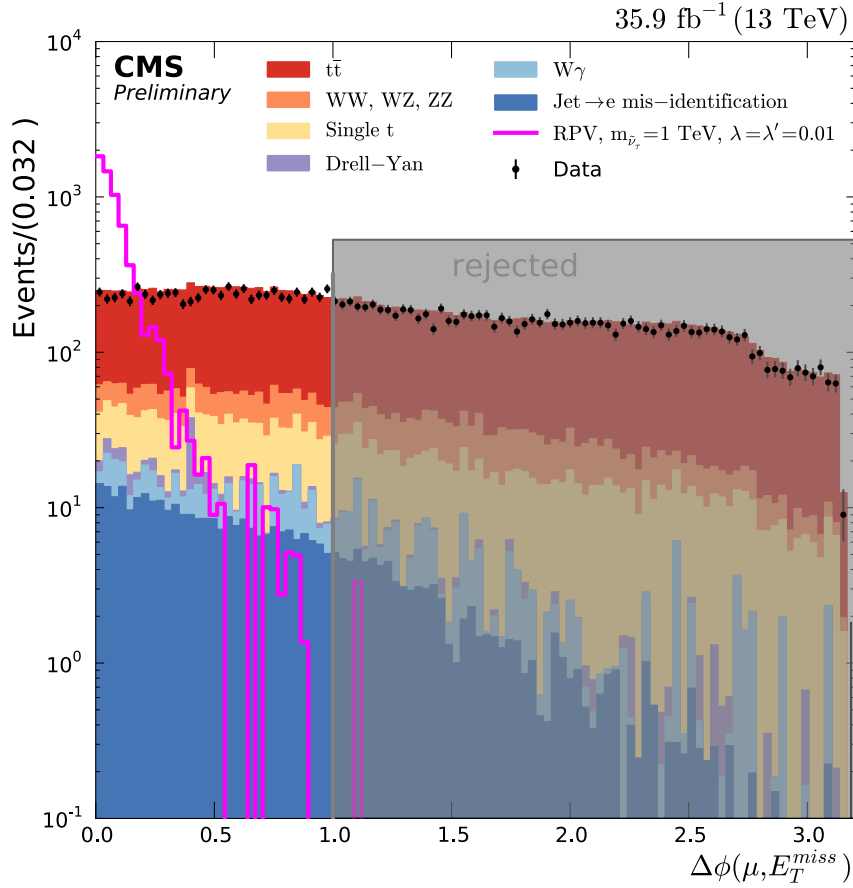


Figure 30: $N - 1$ distribution of $\Delta\phi(\mu, E_T^{\text{miss}})$ for the different background processes, the observed data and an example RPV signal point. The chosen selection criterium on this variable is < 1.0 , as indicated by the gray box in the figure.

The example RPV signal point is concentrated at low values of $\Delta\phi(\mu, E_T^{\text{miss}})$, while the different background processes have a broader distribution. To keep a very high signal efficiency a selection criteria of $\Delta\phi(\mu, E_T^{\text{miss}}) < 1.0$ is chosen.

SELECTION ON p_T^e/p_T^μ After the geometric selection on the relative flight directions towards each other, also the energy ratios have potential for selecting the signal. In the decay of the $\tilde{\nu}_\tau$, the electron and tau should be p_T balanced. The muon comes then from the decay of the tau, therefore the muon p_T should be smaller than the one of the electron. This relation does not have to hold for the background processes. This can be seen in the $N - 1$ distribution of the ratio p_T^e/p_T^μ , which is shown in Fig. 31.

The muon p_T should be smaller than the electron E_T , therefore the selection requirement is $p_T^e/p_T^\mu > 1.0$.

SELECTION ON p_T^μ/p_T^τ The electron and tau should be p_T balanced, therefore the ratio p_T^e/p_T^τ should be close to unity. For the various background processes this is not true. The $N - 1$ distribution of p_T^e/p_T^τ is given in Fig. 32, showing a clear peak at one for the example RPV signal, while the background distribution peaks at lower values.

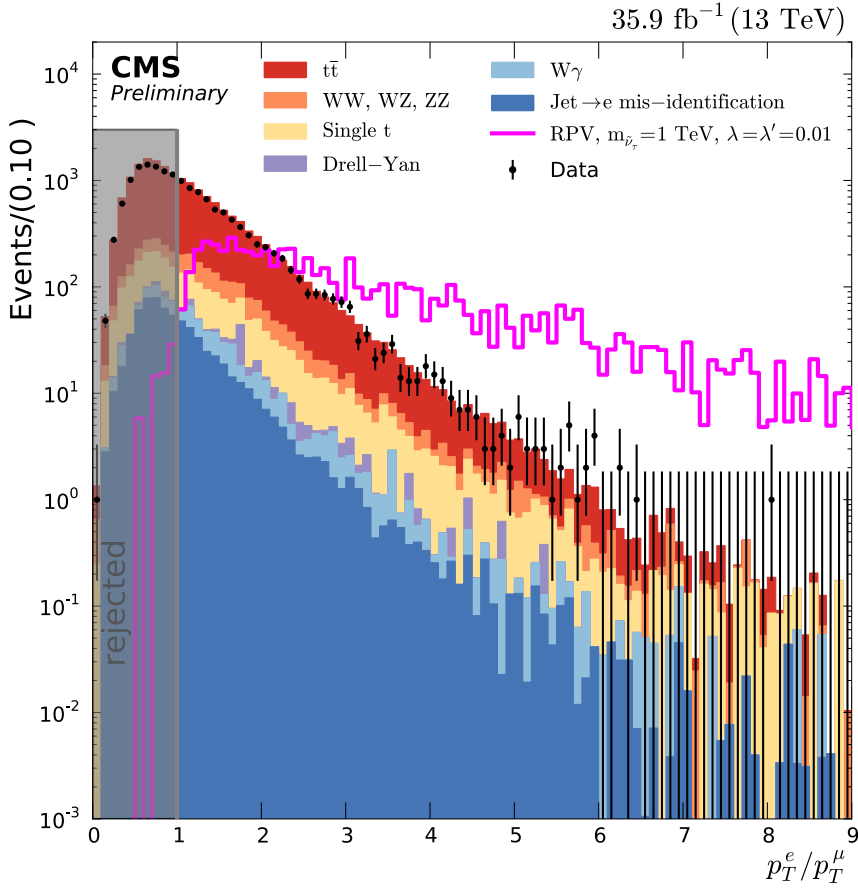


Figure 31: $N - 1$ distribution of p_T^e/p_T^μ for the different background processes, the observed data and an example RPV signal point. The chosen selection criterium on this variable is > 1.0 , as indicated by the gray box in the figure.

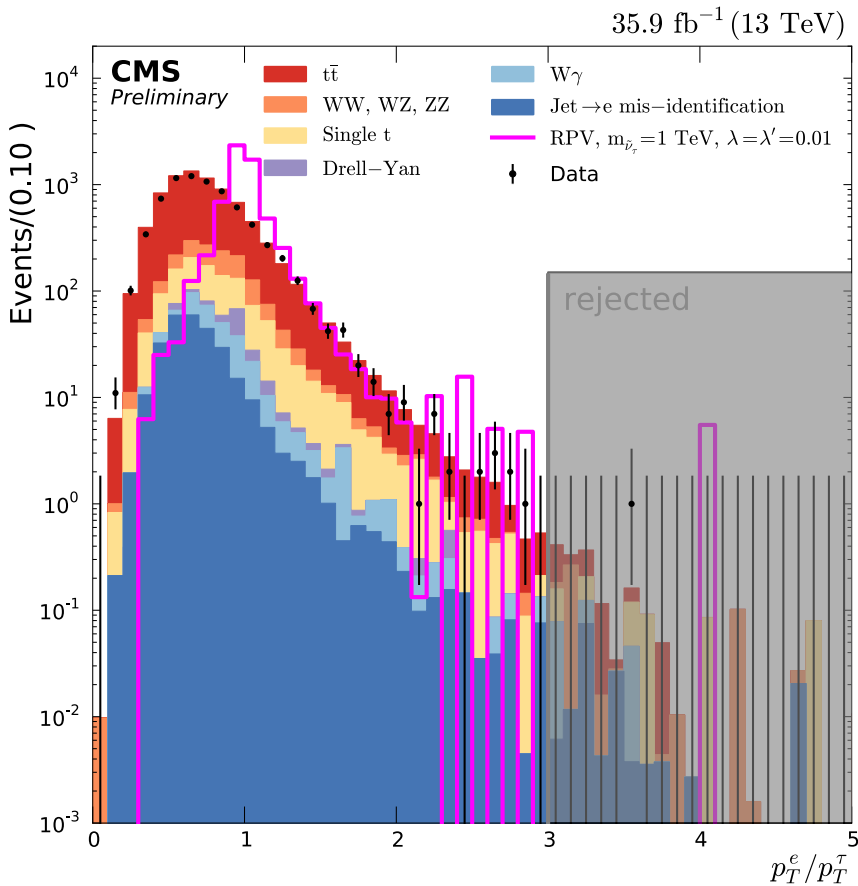


Figure 32: $N-1$ distribution of p_T^μ/p_T^τ for the different background processes, the observed data and an example RPV signal point. The chosen selection criterium on this variable is < 3.0 as indicated by the gray box in the figure.

To keep a very high signal efficiency a selection criterium of $p_T^e/p_T^\tau < 3.0$ is applied.

The overall performance of the four selection criteria on the integrated number of events is illustrated in the cut-flow in Fig. 33 as well as in Tab. 20 in the appendix. It shows the integrated number of events after the pre-selection and after every selection criteria. The different effect on the signal and background expectation can be seen. The number of signal events keeps quite constant as 98 % of events is kept, while the background expectation is reduced by an order of magnitude.

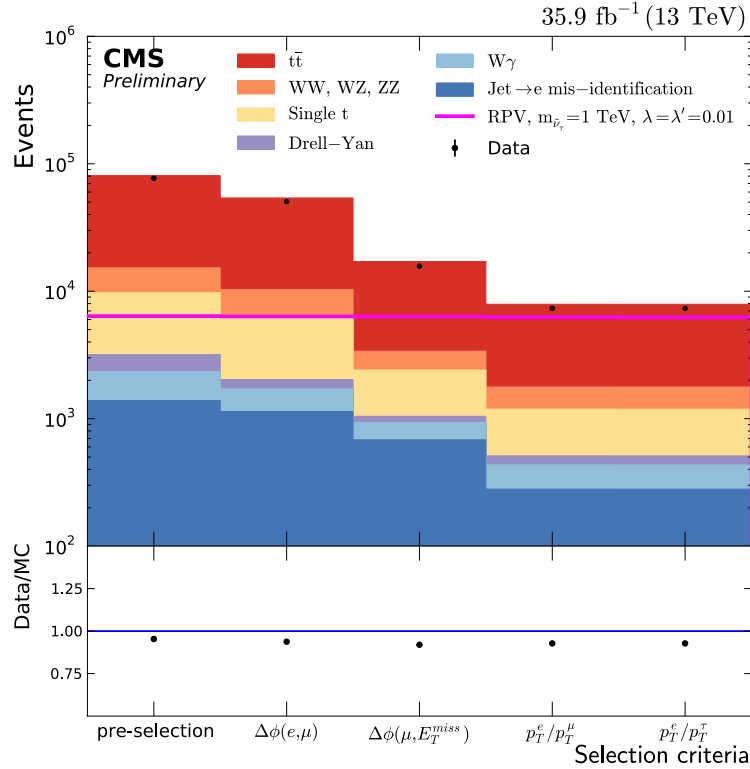


Figure 33: Cut-flow of events in the $e\tau\mu$ channel. Shown are the impact of all four applied kinematic selection criteria on the different background processes, on an example RPV signal and on data. A detailed table of all the different components in the figure is given in Tab. 20 in the appendix. The total background expectation is reduced to about 10 % of the events at pre-selection level, while 98 % of the signal events is kept.

4.6.2 $\mu\tau_e$ channel

The kinematics of the $\tilde{\nu}_\tau$ decay into a muon and a tau and the subsequent decay of the tau into an electron and E_T^{miss} are the same as in the $e\tau\mu$ channel, just exchanging electron and muon with each other. Therefore the selection criteria are also quite similar, nevertheless they are shortly introduced in the following paragraphs including the corresponding $N - 1$ distributions. The summarizing cut-flow for the four selection criteria is shown in Fig. 38.

SELECTION ON $\Delta\phi(\mu, e)$ In the decay of the high mass $\tilde{\nu}_\tau$ the muon and tau in the decay are back-to-back. The tau is highly boosted, therefore the electron from the tau decay is also back-to-back with the muon. This is not fulfilled for the

background processes as the final state object's origin from a different decay chain. This can be seen in the $N - 1$ distribution of the angular difference of the flight directions of muon and electron in the transverse plane $\Delta\phi(\mu, e)$. The distribution is shown in Fig. 34, and shows a clear trend of the example RPV signal towards high values, while the background processes have a wider distribution.

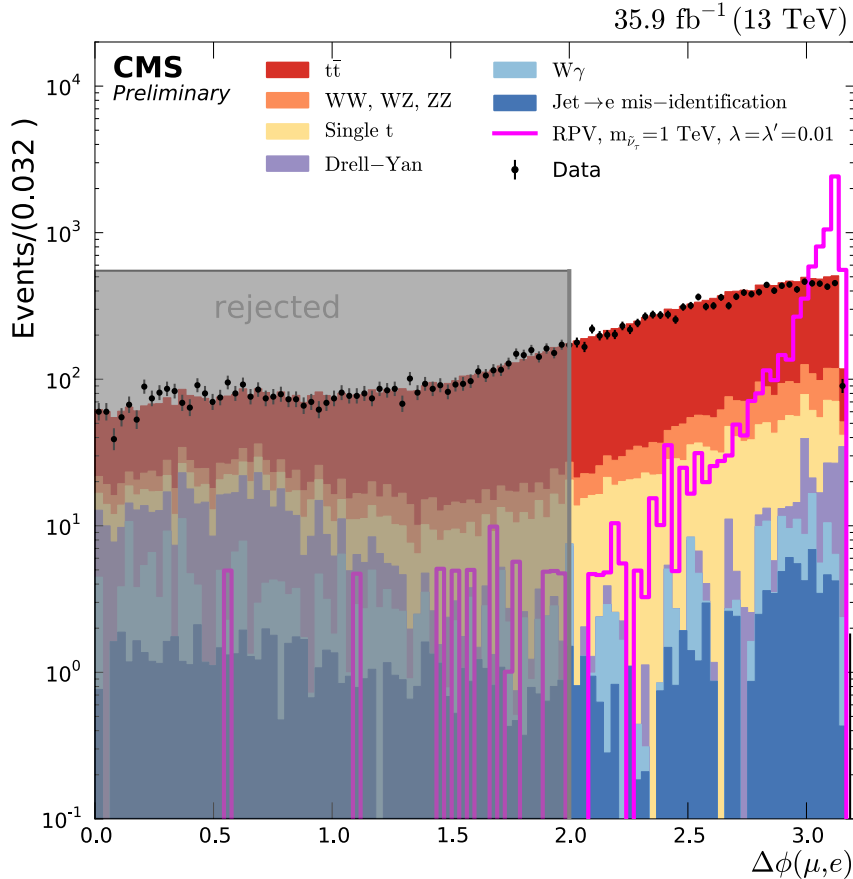


Figure 34: $N - 1$ distribution of $\Delta\phi(\mu, e)$ for the different background processes, the observed data and an example RPV signal point. The chosen selection criterium on this variable is > 2.0 as indicated by the gray box in the figure.

To keep the signal efficiency as high as possible a selection criteria of $\Delta\phi(\mu, e) > 2.0$ is chosen.

SELECTION ON $\Delta\phi(e, E_T^{\text{MISS}})$ The two objects from the highly boosted tau decay, the electron and E_T^{MISS} should be close together. E_T^{MISS} can only be measured in the transverse plane, therefore the angular difference of the flight directions of the electron and E_T^{MISS} in the transverse plane can be used to separate the signal from background processes. The $N - 1$ distribution of $\Delta\phi(e, E_T^{\text{MISS}})$ is shown in Fig. 35. The signal has a clear peak for values close to zero, while the different background processes produce a wide distribution.

A selection criteria of $\Delta\phi(e, E_T^{\text{MISS}}) < 1.0$ is chosen to keep a very high signal efficiency.

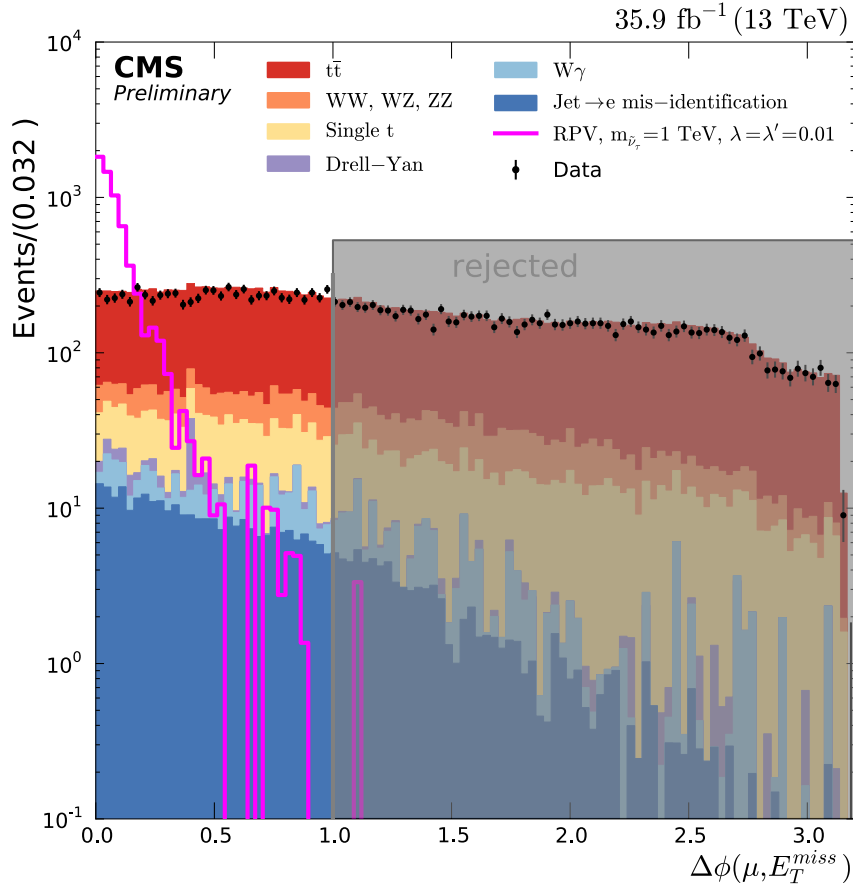


Figure 35: $N - 1$ distribution of $\Delta\phi(e, E_T^{\text{miss}})$ for the different background processes, the observed data and an example RPV signal point. The chosen selection criterium on this variable is < 1.0 as indicated by the gray box in the figure.

SELECTION ON p_T^μ/p_T^e After the selection on the directions of the final state objects, the next step is to use the ratios of momenta for the selection. The muon and tau should be p_T balanced from the decay of the $\tilde{\nu}_\tau$. As the electron comes from the tau decay, it's momentum should be smaller than the one of the muon. The ratio p_T^μ/p_T^e is then a good measure for this behaviour, which should be bigger than one. The $N - 1$ distribution of p_T^μ/p_T^e is shown in Fig. 36.

The signal distribution has the majority of events for values larger than one, while the background processes peak at lower values. Therefore the chosen selection criteria is $p_T^\mu/p_T^e > 1.0$, which also keeps a high signal efficiency.

SELECTION ON p_T^e/p_T^τ The muon and tau are p_T balanced in this channel, therefore the ratio p_T^e/p_T^τ should be close to one for the signal. This relation is not fulfilled for the different background processes. The $N - 1$ distribution of the ratio p_T^e/p_T^τ is shown in Fig. 37. The distribution of the example RPV signal point shows the clear peak at one, while the background processes give a broader distribution. To keep a high signal efficiency a selection criteria of $p_T^e/p_T^\tau < 3.0$ is chosen.

The overall performance of the four selection criteria on the integrated number of events is illustrated in the cut-flow in Fig. 38 as well as Tab. 21 in the appendix. It shows the integrated number of events after the pre-selection and after every selection criteria. The different effect on the signal and background expectation can be seen.

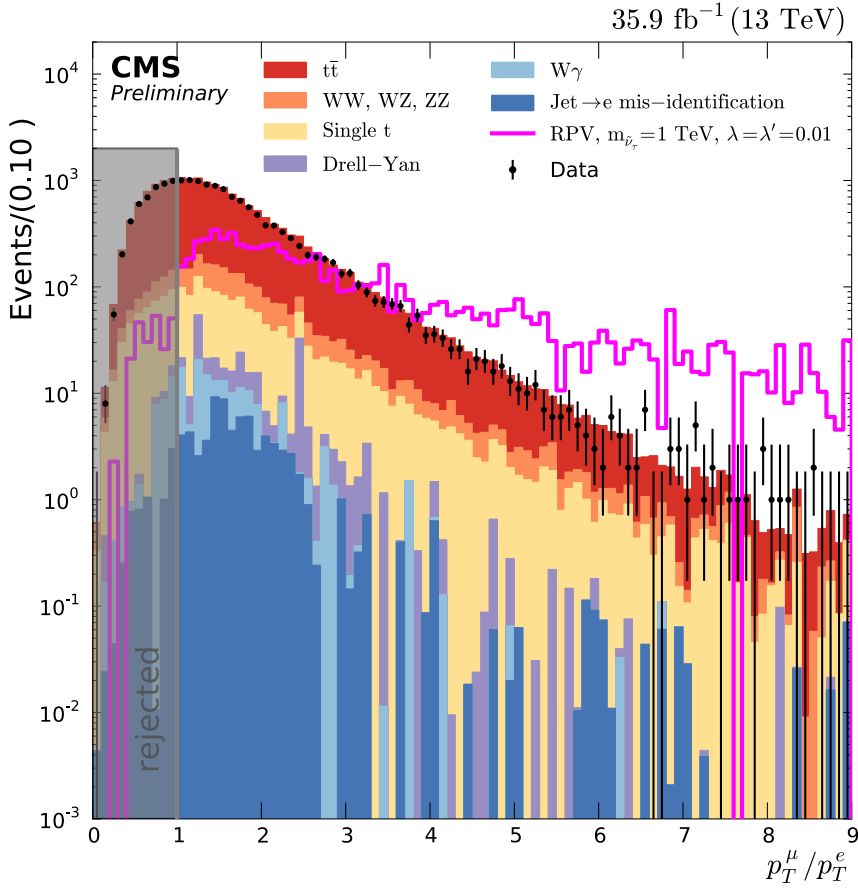


Figure 36: $N - 1$ distribution of p_T^μ/p_T^e for the different background processes, the observed data and an example RPV signal point. The chosen selection criterium on this variable is > 1.0 as indicated by the gray box in the figure.

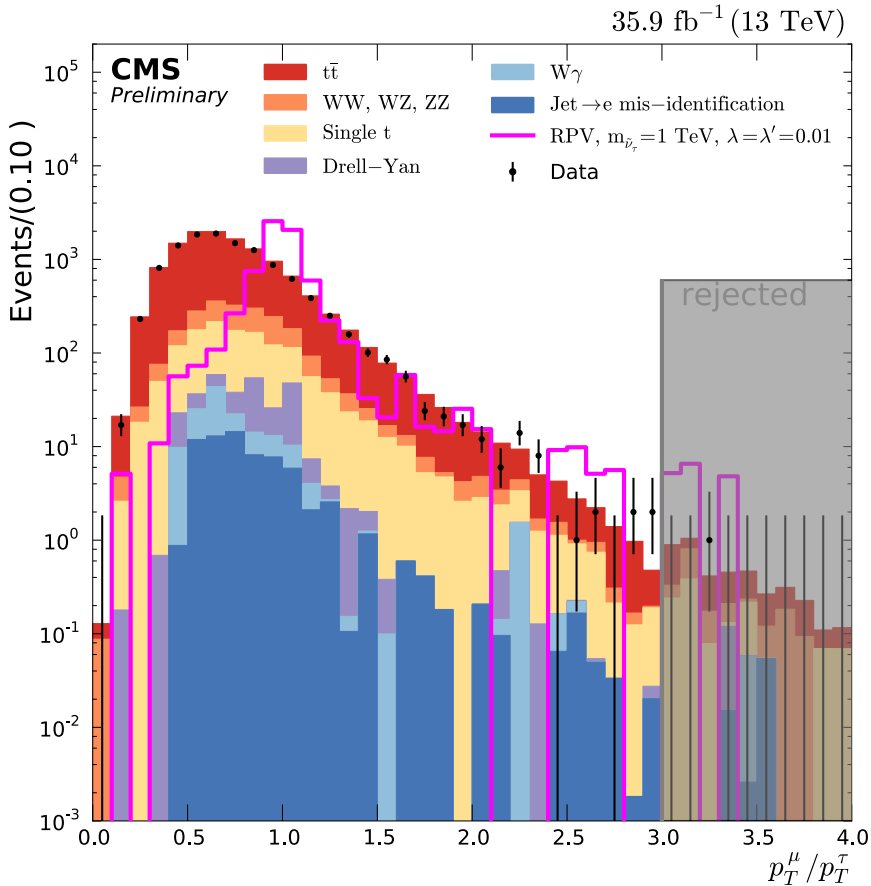


Figure 37: $N - 1$ distribution of p_T^e/p_T^τ for the different background processes, the observed data and an example RPV signal point. The chosen upper cut value on this variable is 3.0 as indicated by the gray box in the figure.

The number of signal events keeps quite constant as only about 2% of events is lost by the selection criteria, while the background is reduced by an order of magnitude.

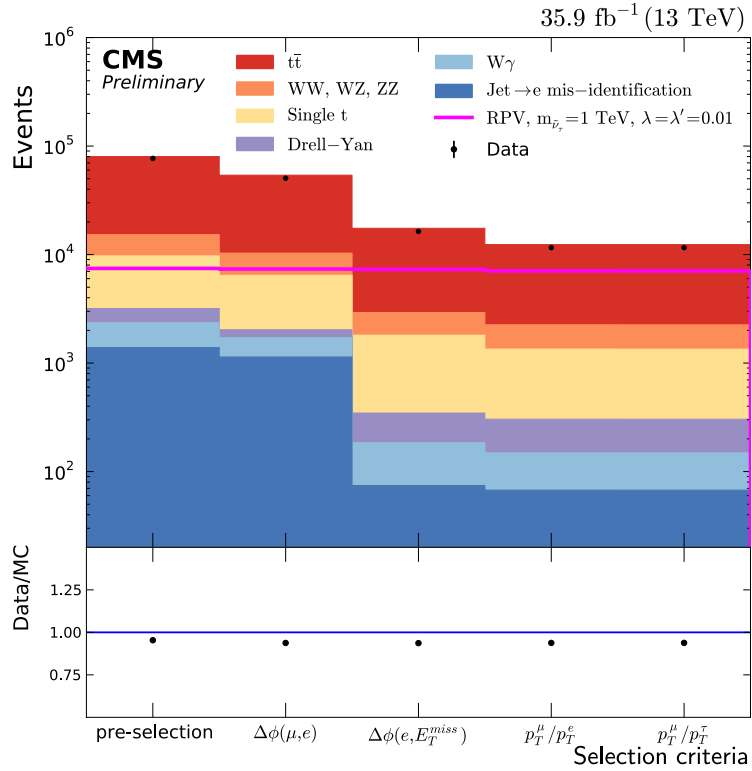


Figure 38: Cut-flow of events in the $\mu\tau_e$ channel. Shown are the impact of all four applied kinematic selection criteria on the different background processes, on an example RPV signal and on data. A detailed table with all the relevant numbers of events is given in Tab. 21 in the appendix. The total background expectation is reduced by an order of magnitude while only about 2% of the signal events are lost.

4.7 SELECTION EFFICIENCIES

All the mentioned selection criteria result in the events in the final invariant mass distributions. The performance of these selection criteria is measured in the selection efficiency, the efficiency to pass all the selection criteria. The selection efficiency is split into three arbitrary sub-efficiencies which highlights different aspects of the analysis.

$$\epsilon = \epsilon_{\text{Acceptance}} \times \epsilon_{\text{Trigger}} \times \epsilon_{\text{Selection}}$$

and determined as function of invariant mass. The first step is to pass the generator level acceptance, the second step is to pass the trigger selection and the last step is the final object reconstruction and selection, consisting out of object identification and kinematic selection. All the efficiencies are determined from RPV signal simulation if not otherwise stated, and are introduced for the different channels in the following sections.

4.7.1 $e\mu$ channel

In the $e - \mu$ channel the event selection consists only of the selection of reconstructed objects, resulting in a very high signal efficiency. The generator level acceptance differs between the studied BSM models, therefore the efficiencies are determined for each model individually.

The efficiency of the RPV model is shown in Fig. 39 for all events combined. For the RPV model, above the turn-on region, i. e. beyond 1000 GeV, the efficiency of selecting $e\mu$ events is constant. In this region the efficiency of finding and reconstructing an $e\mu$ event within the detector acceptance (as defined in (1) in Secs. 4.2.1 and 4.2.2) is above 70%. For the signal modelling in the statistical interpretation at arbitrary signal masses, the efficiency distribution is parameterized. A good parameterization function was found in the context of this thesis and is defined in Eq. 16.

$$f_{\text{eff}} = A + \frac{B}{\left(\frac{m_{e\mu,\text{gen}}}{\text{GeV}}\right)^C + D} + E \cdot \frac{m_{e\mu,\text{gen}}}{\text{GeV}} \quad (16)$$

where $m_{e\mu,\text{gen}}$ is the generator level invariant mass of the $e\mu$ pair. The values of the coefficients A, B, C and D are given in the efficiency distribution shown in Fig. 39.

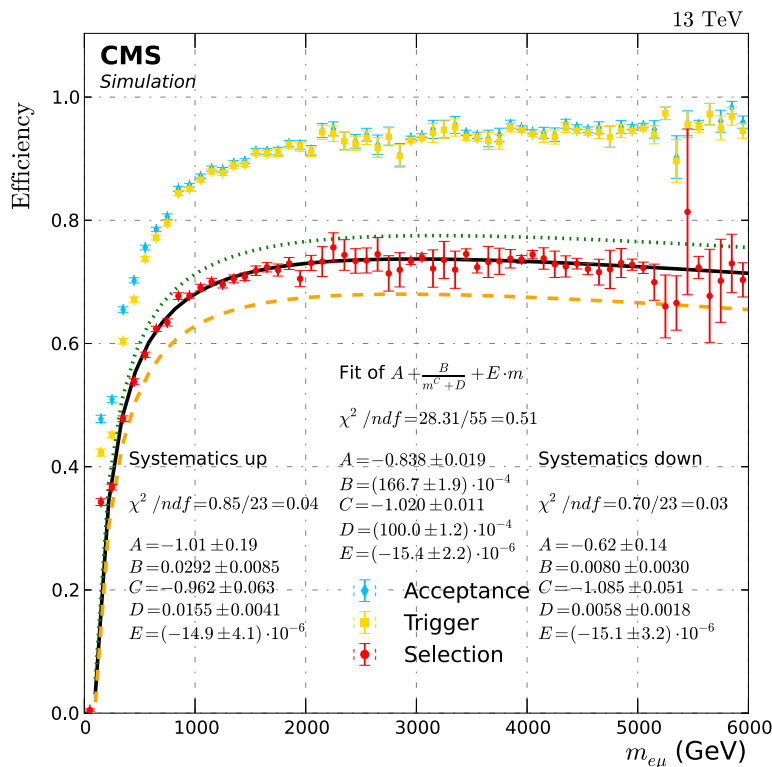


Figure 39: The efficiency of the RPV signal model for all events [a] after the acceptance requirements (light blue points), [b] after acceptance and trigger requirements (dark green points) and [c] after the full selection including acceptance and trigger criteria (red points). In each case, the reconstruction efficiency is also included. This final acceptance times efficiency is then parameterized for the statistical interpretation shown by the black line. The systematic uncertainties are derived by propagating the effect of the systematic uncertainties described in Sec. 4.9 towards the efficiency and are shown via the parameterization of both variations, the upward shift in green and the downward shift in orange.

For the QBH and Z' models a parameterization is not necessary, as no statistical interpretation of arbitrary signal masses is done. The main difference to the RPV model is the difference in generator level acceptance due to a different kinematics in the decay. The acceptance times efficiency for both models is shown in Fig. 40. The final selection efficiency in the plateau is about 70 % for both models.

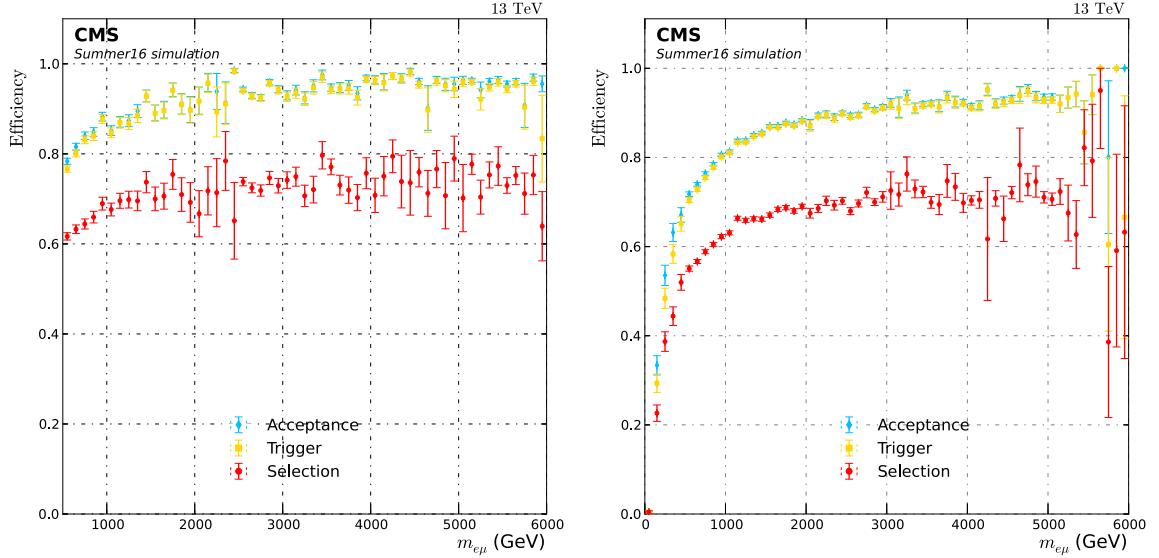


Figure 40: The efficiency of the QBH model (left) and Z' model (right) [a] after the acceptance requirements (light blue points), [b] after acceptance and trigger requirements (dark green points) and [c] after the full selection including acceptance and trigger criteria (red points). In each case, the reconstruction efficiency is also included.

As described in Sec. 4.3.2 to enhance the sensitivity of the analysis, it is split into four categories, defined by the η of the electron and muon. For the statistical interpretation the signal efficiency is therefore also needed to be split into the four categories. The RPV signal efficiency in the four different categories is given in Fig. 41 including the parameterization. The parameterization function used in the different categories is the same as defined in Eq. 16 except in the endcap-endcap category. In this category it is modified by an additional Gaussian to model the shape of the efficiency better. The parameterizations and the corresponding parameters are shown in Fig. 41.

4.7.2 $e\tau_\mu$ channel

In the $e\tau_\mu$ channel the full acceptance times efficiency was determined with the RPV signal simulation. The procedure is similar to the $e\mu$ channel (Sec. 4.7.1), it is split into four sub-efficiencies:

$$\epsilon = \epsilon_{\text{Acceptance}} \times \epsilon_{\text{Trigger}} \times \epsilon_{\text{Pre-selection}} \times \epsilon_{\text{Full selection}}$$

where the first two are identical to the $e\mu$ channel and the last one is split into the pre-selection and full selection efficiency. The full selection efficiency is then parametrized by the same function defined in Eq. 16. The resulting acceptance times efficiency is shown in Fig. 42.

The main difference to the $e\mu$ channel is the additional decay of the tau into a muon and neutrinos. Due to this decay the branching ratio for the decay $\tau \rightarrow \mu\nu\nu$ of 17.4 %

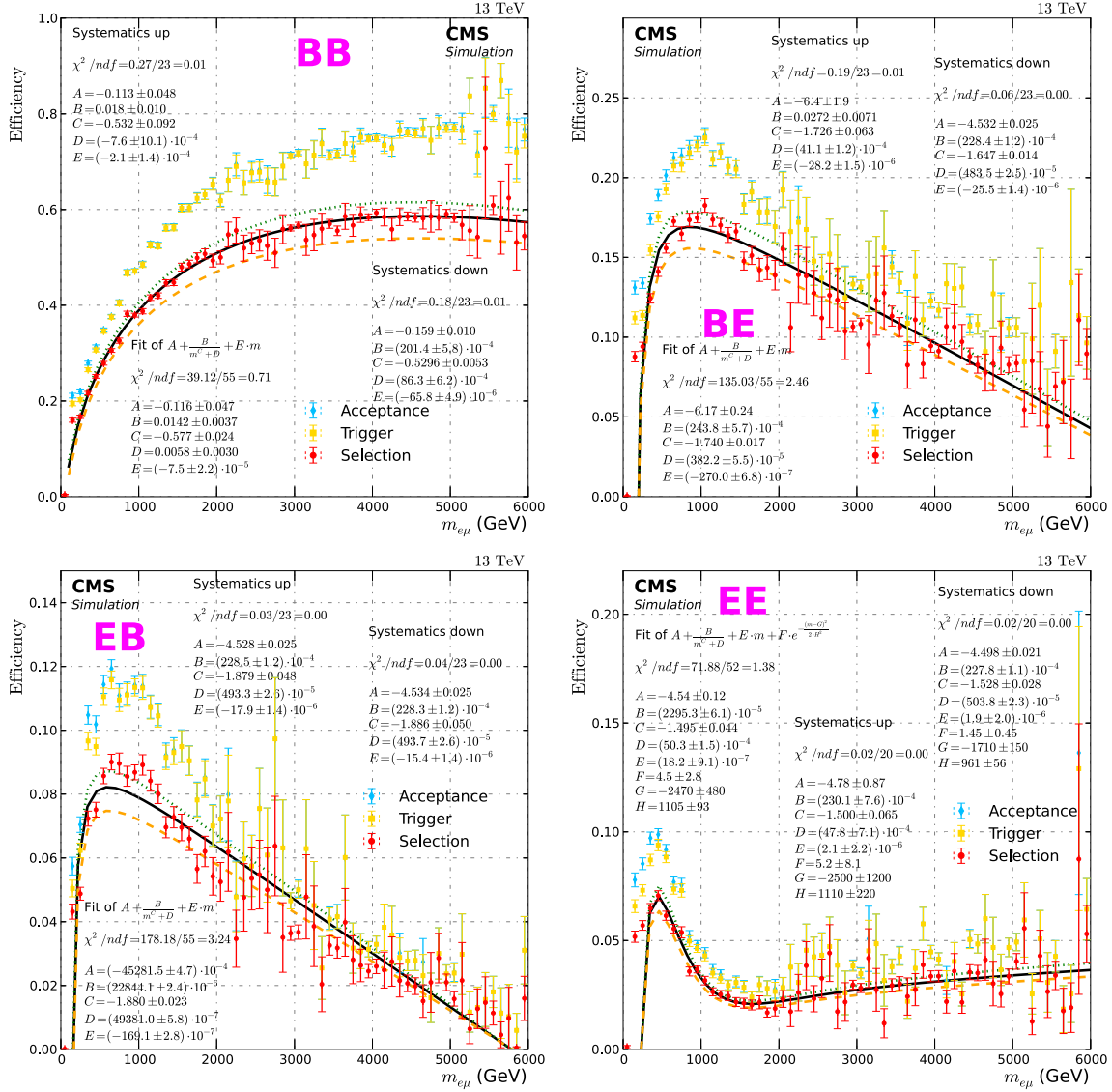


Figure 41: The efficiency of the RPV signal in the different event categories [a] after the acceptance requirements (light blue points), [b] after acceptance and trigger requirements (dark green points) and [c] after the full selection including acceptance and trigger criteria (red points). The systematic uncertainties are derived by propagating the effect of the systematic uncertainties described in Sec. 4.9 towards the efficiency.

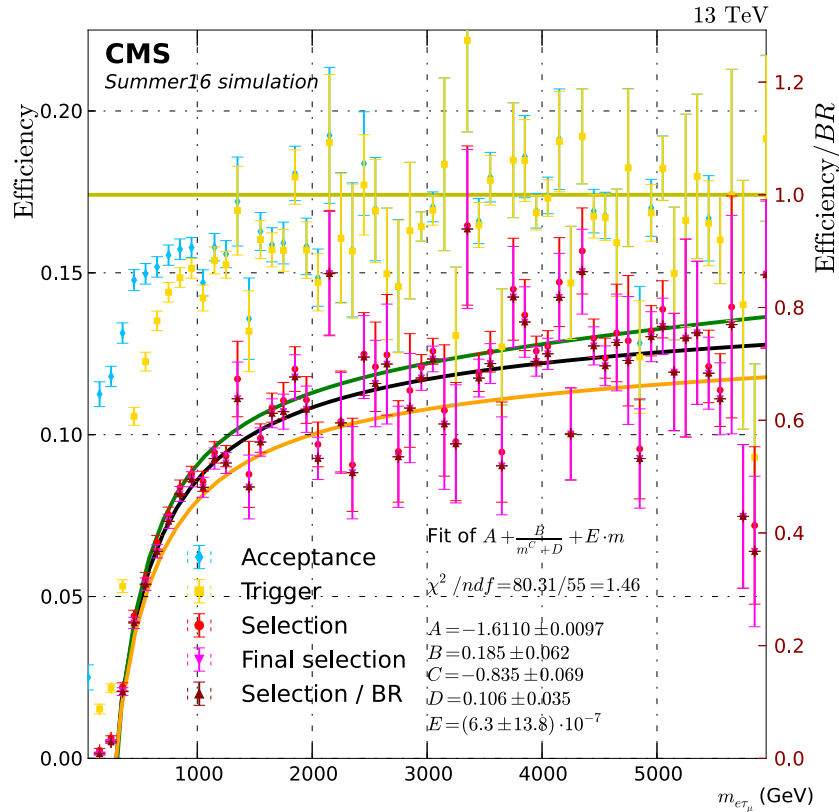


Figure 42: The efficiency of the RPV signal in the $e\tau_\mu$ channel for all events [a] after the acceptance requirements (light blue points), [b] after acceptance and trigger requirements (dark green points), [c] after the pre-selection including acceptance and trigger criteria (red points) and [d] after the final selection (magenta points). This final acceptance times efficiency is then parametrized for the statistical interpretation by the black line. The systematic uncertainties are derived by propagating the effect of the systematic uncertainties described in Sec. 4.9 towards the efficiency. These systematically shifted upper and lower efficiencies are shown in the figure via the parameterization of both variations, upward shift in green and downward shift in orange. To also take the branching ratio of the tau decay into account, the right y-axis of the figure is scaled to the efficiency per BR.

is included in the generator level acceptance. The full acceptance times efficiency can never exceed this branching ratio. To compare it to the performance of the $e\mu$ channel in Fig. 42 also the acceptance per branching ratio is shown on the right y-axis. The acceptance times efficiency per branching ratio reaches 70% in the plateau similar to the $e\mu$ channel, while the pure acceptance times efficiency, which determines the sensitivity of the analysis reaches up to 12%.

4.7.3 $\mu\tau_e$ channel

The $\mu\tau_e$ channel is handled identically to the $e\tau_\mu$ channel, the efficiency is also split into four sub-efficiencies and determined with the RPV signal simulation. The full acceptance times efficiency is parameterized by the same function, defined in Eq. 16. The resulting acceptance times efficiency is shown in Fig. 43.

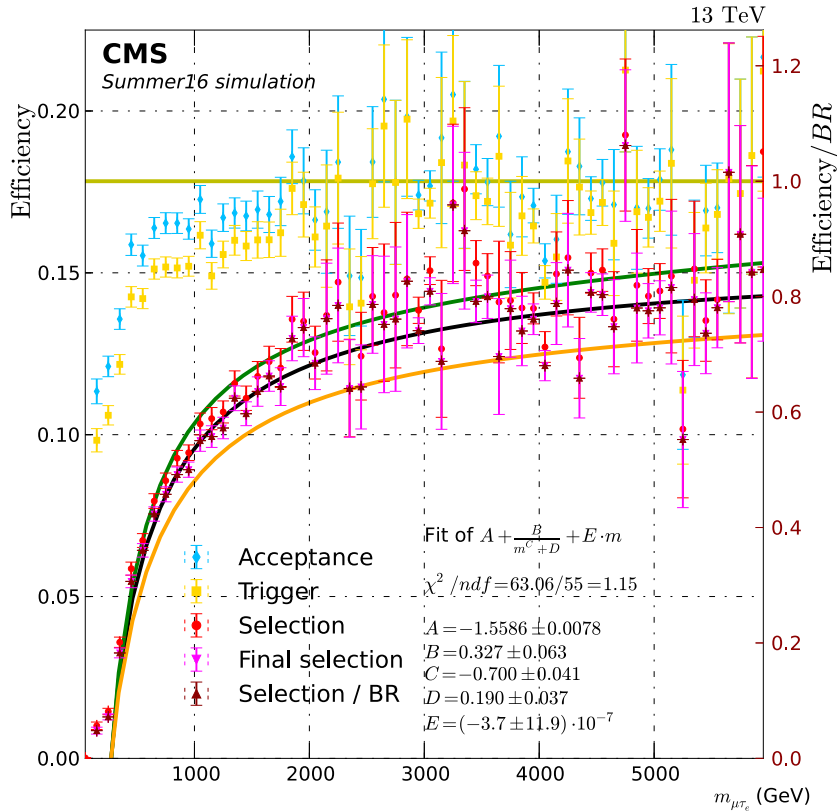


Figure 43: The efficiency of the RPV signal in the $\mu\tau_e$ channel for all events [a] after the acceptance requirements (light blue points), [b] after acceptance and trigger requirements (dark green points), [c] after the pre-selection including acceptance and trigger criteria (red points) and [d] after the final selection (magenta points). This final acceptance times efficiency is then parametrized for the statistical interpretation by the black line. The systematic uncertainties are derived by propagating the effect of the systematic uncertainties described in Sec. 4.9 towards the efficiency. These systematically shifted upper and lower efficiencies are shown in the figure via the parameterization of both variations, upward shift in the green and downward shift in orange. To also take the branching ratio of the tau decay into account, the right y-axis of the figure is scaled to the efficiency per BR.

As in the $e\tau_\mu$ channel also the branching ratio of the tau decay $\tau \rightarrow e\nu\nu$ of 17.8% has to be considered. The acceptance times efficiency per branching ratio reaches 75% in the plateau similar to the $e\mu$ channel, while the pure acceptance times efficiency, which determines the sensitivity of the analysis reaches up to 14%.

4.8 MASS RESOLUTION

The other performance quantity relevant for the analysis is the invariant mass resolution. This mass resolution is mainly driven by the particle momentum resolutions introduced in Sec. 3.2. For the narrow resonance signal of the RPV SUSY model it drives the shape of the signal, as the shape on generator level is just a very sharp peak that is then washed out by the mass resolution. For the other signal models, QBH and Z' it is less important as the signal shape is more dominated by the generator

level shape. The mass resolution is determined in all three channels equal with the RPV signal simulation. The general approach is introduced in the following, while the individual results are given in the later sub-sections.

The relative per-event mass resolution is defined as $(m_{e\mu, reco} - m_{e\mu, gen}) / m_{e\mu, gen}$ and is evaluated for each event passing the event selection. The resulting distribution is parametrized with a Crystal Ball function [92], which is defined as follows:

$$f(x; \alpha, n, \bar{x}, \sigma) = N \cdot \begin{cases} \exp\left(-\frac{(x-\bar{x})^2}{2\sigma^2}\right), & \text{for } \frac{x-\bar{x}}{\sigma} > -\alpha \\ A \cdot \left(B - \frac{x-\bar{x}}{\sigma}\right)^{-n}, & \text{for } \frac{x-\bar{x}}{\sigma} \leq -\alpha \end{cases}$$

with the definitions:

$$\begin{aligned} A &= \left(\frac{n}{|\alpha|}\right)^n \cdot \exp\left(-\frac{|\alpha|^2}{2}\right) \\ B &= \frac{n}{|\alpha|} - |\alpha| \\ N &= \frac{1}{\sigma(C+D)} \\ C &= \frac{n}{|\alpha|} \cdot \frac{1}{n-1} \cdot \exp\left(-\frac{|\alpha|^2}{2}\right) \\ D &= \sqrt{\frac{\pi}{2}} \left(1 + \operatorname{erf}\left(\frac{|\alpha|}{\sqrt{2}}\right)\right) \end{aligned}$$

The Crystal Ball function is chosen in this analysis, as it describes the Gaussian core of the distribution, and due to its exponential tail also describes the tail of the distribution from energy loss.

Two such example Crystal Ball parameterizations for RPV signal mass points of 700 GeV and 1800 GeV are shown in Fig. 44 with the corresponding residual and pull distributions (the definitions of these additional distributions are given in Sec. B.1 in the appendix).

The sigma of the Crystal Ball is chosen as a measure of the mass resolution. The sigma of the mass resolution is then determined as a function of the invariant $e\mu$ mass, which gives the mass resolution as a function of the mass. The resulting distribution is parametrized for a description of the mass resolution at arbitrary masses by the following function:

$$f_{res} = A + B \cdot \frac{m_{e\mu, gen}}{\text{GeV}} + C \cdot \left(\frac{m_{e\mu, gen}}{\text{GeV}}\right)^2 + D \cdot \left(\frac{m_{e\mu, gen}}{\text{GeV}}\right)^3 \quad (17)$$

where $m_{e\mu, gen}$ is the generator level invariant mass of the $e\mu$ pair. This function is later used to model the Gaussian shape of the signal distribution in the statistical interpretation of arbitrary signal masses.

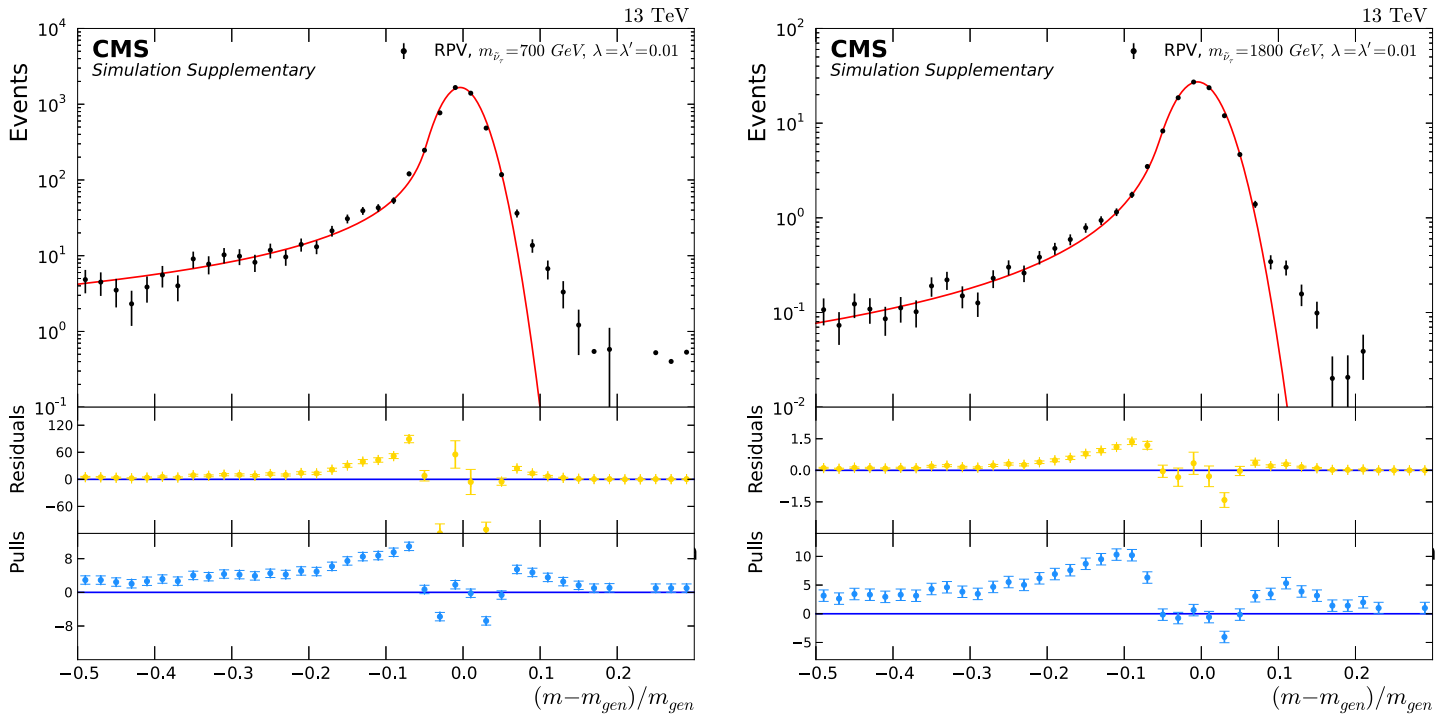


Figure 44: Crystal Ball parameterization of the invariant mass resolution for the simulated RPV signal mass point of 700 GeV (left) and 1800 GeV (right) in the upper distribution. The corresponding residual (centre) and pull (lower) distributions are also shown to see how well the description of the function is, the definitions of these additional distributions are given in Sec. B.1 in the appendix.

4.8.1 $e\mu$ channel

In the $e\mu$ channel the invariant mass resolution is dominated by the momentum resolution of the muon. At high momentum the resolution worsens as seen in Fig. 17 which directly results in a worsening of the mass resolution with higher masses and therefore higher momentum. The resulting invariant mass resolution as a function of the mass for all RPV signal mass points in the $e\mu$ channel is shown in Fig. 45. The values of the coefficients A, B, C and D are given in Fig. 45. Also shown is the effect of the systematic uncertainties (introduced in Sec. 4.9) on the mass resolution. This effect is calculated by propagating all systematic uncertainties on the invariant mass resolution. This procedure can not account for a potential improvement of the mass resolution as it only allows for a worsening of the invariant mass resolution in the simulation. To also account for these potential improvements and chose the most conservative value, the total uncertainty on the mass resolution is as a last step symmetrized around the nominal invariant mass resolution. In the statistical interpretation (from Sec. 5.2 onwards), it becomes clear, that only the worsening of the resolution is relevant for the results of the analysis.

In the $e\mu$ channel the events are then split into categories of η , resulting in four event categories. For all four categories the invariant mass resolution was determined and parametrized. The individual mass resolutions for the different event categories are shown in Fig. 46.

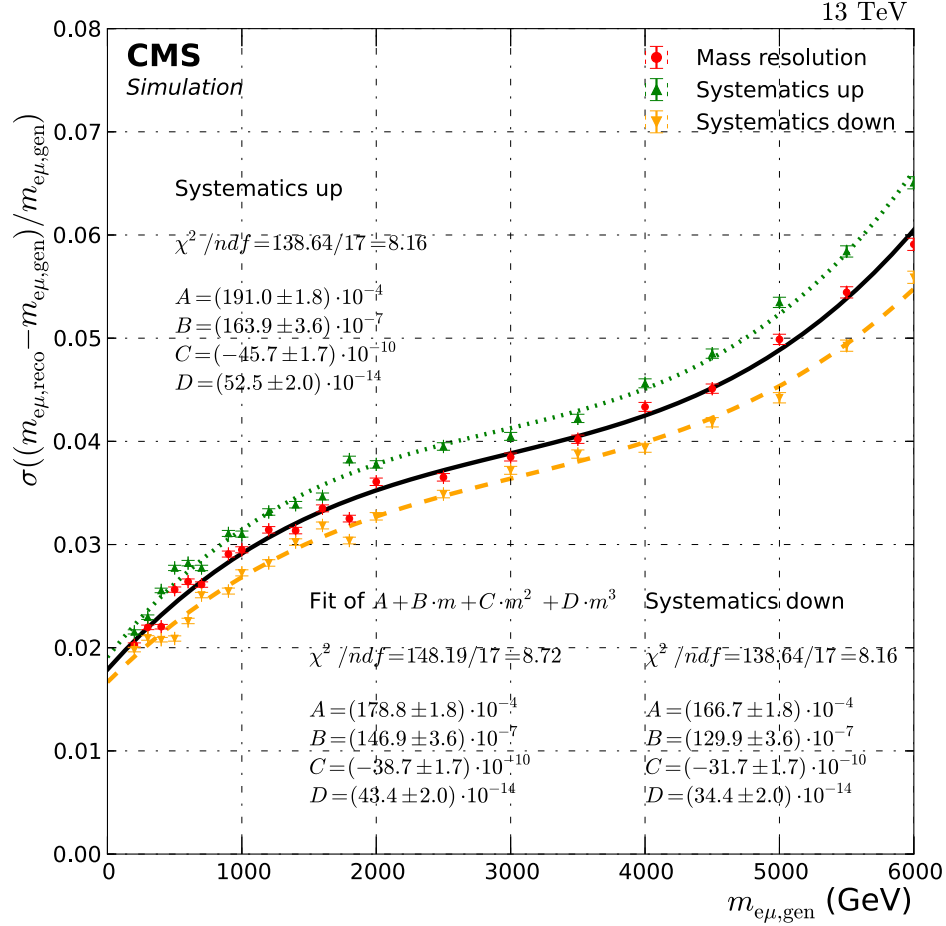


Figure 45: Relative invariant mass resolution for all events of $e\mu$ pairs obtained from RPV signal simulation. The systematic uncertainties are derived by propagating the effect of the systematic uncertainties described in Sec. 4.9 towards the mass resolution and symmetrizing the result. The parameterizations of the nominal mass resolution as well as of the systematic shifts are shown.

4.8.2 $e\tau_\mu$ channel

In the $e\tau_\mu$ channel the invariant mass resolution is influenced by different effects. At low masses the assumptions used in the reconstruction of the collinear tau are no longer valid, therefore the mass resolution deteriorates. At higher masses the momentum resolution of the muon is the dominant factor. As the muon comes from the decay of the tau, the momentum of the muon is lower compared to the electron. This leads to a good mass resolution at high mass, as the momentum range of the muon with a good resolution is relevant for the mass. The approach to determine the mass resolution is similar to the $e\mu$ channel, just the parameterization of the mass resolution as a function of the invariant mass is done by a different function, due to the different effects that influence the resolution. The used function is:

$$f_{\text{res}} = A / \left(\frac{m_{\mu\tau, \text{gen}}}{\text{GeV}} \right) + B + C \cdot \frac{m_{\mu\tau, \text{gen}}}{\text{GeV}} \quad (18)$$

where $m_{\mu\tau, \text{gen}}$ is the generator level invariant mass of the $e\tau$ pair. The resulting invariant mass resolution as well as the parameterization of it are shown in Fig. 47.

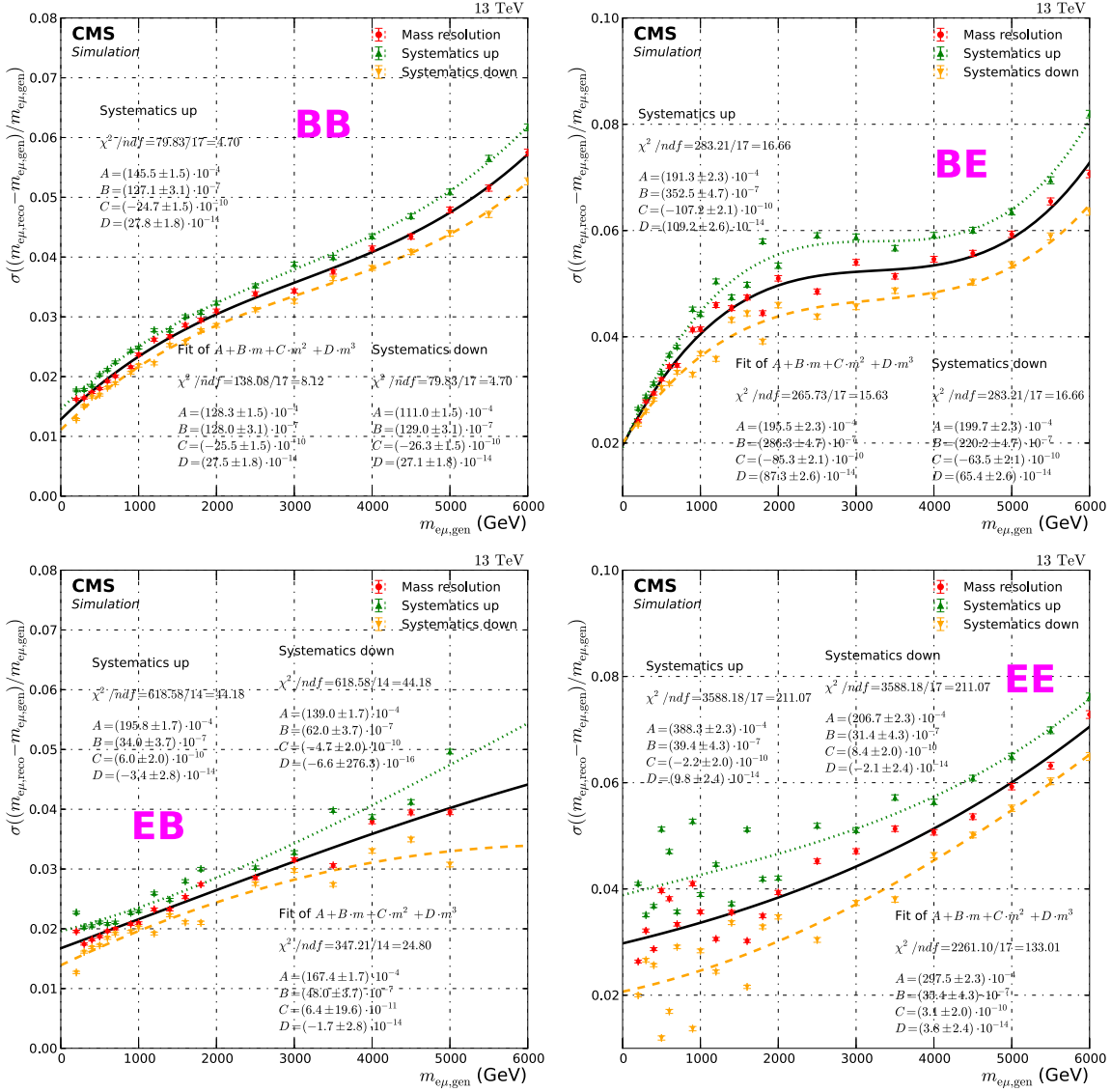


Figure 46: Relative invariant mass resolution for the different categories of $e\mu$ pairs obtained from RPV signal simulation. The systematic uncertainties are derived by propagating the effect of the systematic uncertainties described in Sec. 4.9 towards the mass resolution and symmetrizing the result. The parameterizations of the nominal mass resolution as well as of the systematic shifts are also shown.

The effect of the systematic uncertainties shown in Fig. 47 is bigger than in the $e\mu$ channel, shown in Fig. 45. This is the result of more sources of systematic uncertainty that contribute due to the $E_{\text{T}}^{\text{miss}}$ in the final state. Also the impact of other uncertainties is bigger as it contributes twice, first on the object itself (e.g. the electron energy scale uncertainty) and second it influences $E_{\text{T}}^{\text{miss}}$ and therefore the invariant mass resolution. At very low masses the symmetrization of the uncertainties leads to the artefact, that a mass resolution very close to zero is expected. At this very low mass no statistical interpretation is performed, therefore this artefact has no further impact on the result.

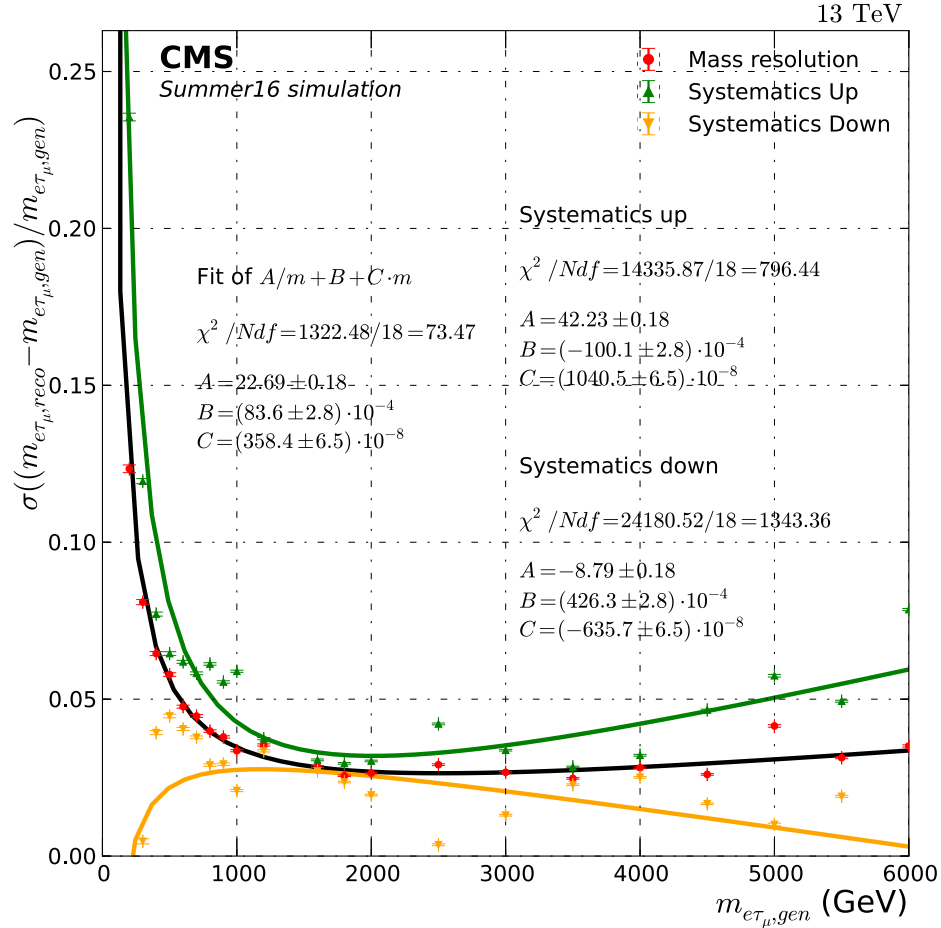


Figure 47: Relative invariant mass resolution for all events of $e\tau_\mu$ pairs obtained from RPV signal simulation. The systematic uncertainties are derived by propagating the effect of the systematic uncertainties described in Sec. 4.9 towards the mass resolution. The parameterizations of the nominal mass resolution as well as of the systematic shifts are shown.

4.8.3 $\mu\tau_e$ channel

The $\mu\tau_e$ channel is very similar to the $e\tau_\mu$ channel, at low masses the mass resolution deteriorates as the collinear tau reconstruction no longer works. At high masses the mass resolution is dominated by the muon momentum resolution and in the $\mu\tau_e$ channel, the muon is the final state particle with the higher momentum, resulting in a worse mass resolution than in the $e\tau_\mu$ channel. The parameterization is the same as for the $e\tau_\mu$ channel, by the function defined in Eq. 18. The resulting invariant mass resolution as a function of mass and the parameterization are shown in Fig. 48.

The systematic uncertainties show a very similar behaviour than in the $e\tau_\mu$ channel, shown in Fig. 47. At high mass a bigger uncertainty, than in the $e\tau_\mu$ channel is observed due to additional uncertainties and a bigger influence of uncertainties via E_T^{miss} . At very low mass the symmetrization results in the artefact of a very low mass resolution in the downward shift of the systematic uncertainties. This region is not included in the statistical interpretation and has therefore no influence on the result.

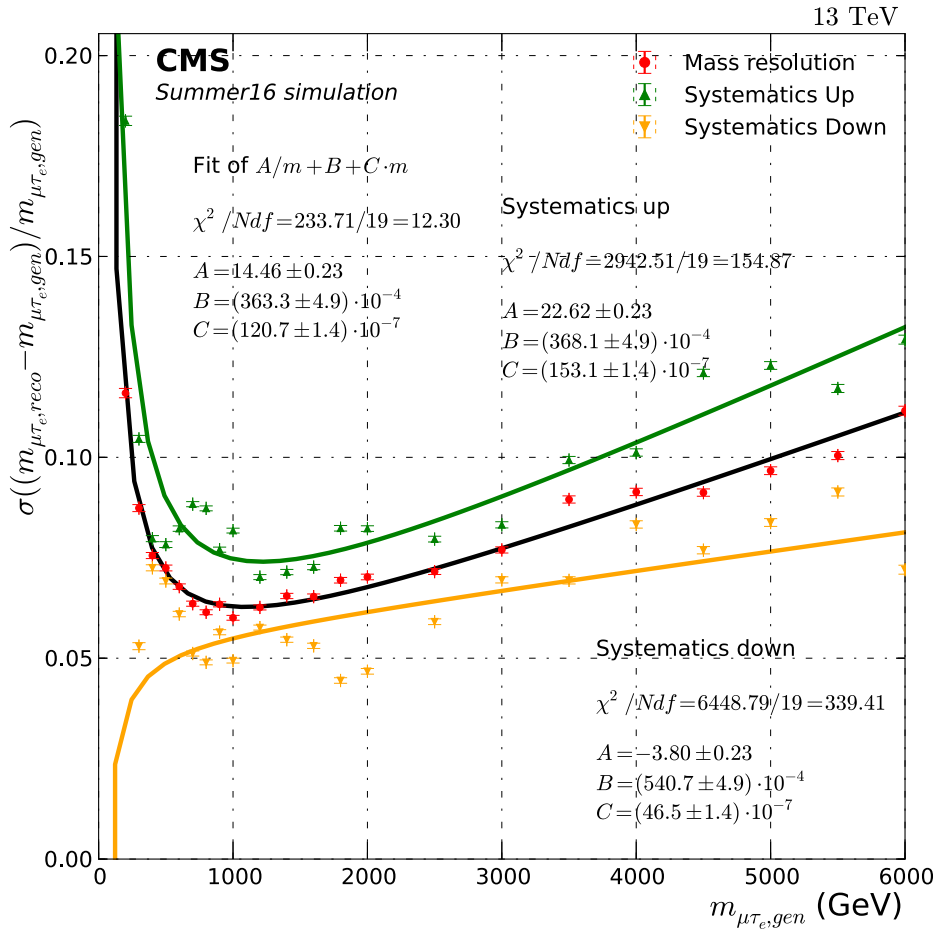


Figure 48: Relative invariant mass resolution for all events of $\mu\tau_e$ pairs obtained from RPV signal simulation. The systematic uncertainties are derived by propagating the effect of the systematic uncertainties described in Sec. 4.9 towards the mass resolution. The parameterizations of the nominal mass resolution are shown, the systematic shifts are also shown.

4.9 SYSTEMATIC UNCERTAINTIES

In this last section of the analysis chapter the different sources of systematic uncertainties are introduced. It will be explained how these uncertainties are treated in the analysis. The considered systematic uncertainties are split into two categories, first systematic uncertainties from experimental sources (Sec. 4.9.1) and second from different theoretical uncertainties (Sec. 4.9.2). Afterwards the application of the different systematic uncertainties in the different channels and the impact on the background and signal expectations are introduced.

4.9.1 Experimental uncertainty sources

The different sources of experimental systematic uncertainties that are considered in the analysis are introduced in the following paragraphs. Also introduced are the treatments of these different systematic uncertainty sources.

MUON p_T SCALE The absolute muon transverse momentum scale could be affected e. g. by the alignment between the tracker and muon system. This could lead to a potential bias on the momentum scale. A distortion of the momentum scale could lead to a wrongly reconstructed transverse muon momentum and consequently to a wrong invariant mass. To consider this effect in the analysis the scale bias and its uncertainty has to be measured. This measurement is performed by the generalized endpoint method by comparing data to simulation [93]. The q/p_T distribution is compared between data and simulation for different simulated biases (two example distributions are shown in Fig. 106 in the appendix). The value which minimizes the difference is used as the measure for the scale bias. This measurement is done as a function of η and ϕ for muons with $p_T > 200$ GeV in the barrel and $p_T > 100$ GeV in the endcaps. The scale bias was found to be independent of the muon p_T range. The resulting scale bias and the corresponding uncertainty are shown in Fig. 49 for the latest values determined with the data from 2016 [94].

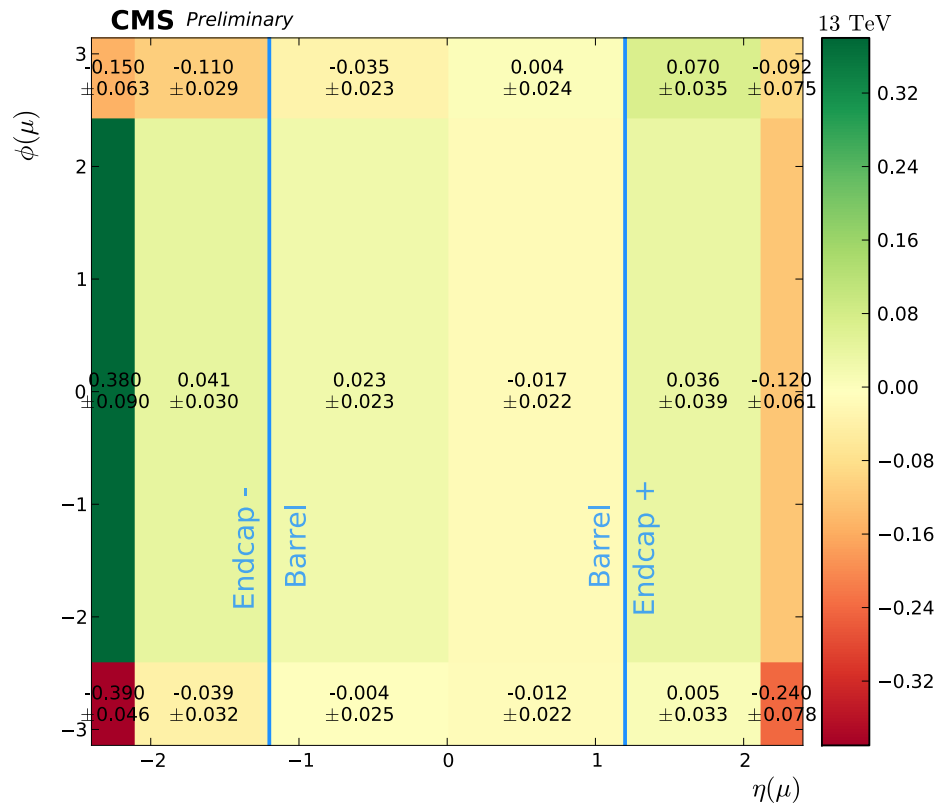


Figure 49: Muon p_T scale bias per TeV as a function of the muon η and ϕ , determined for muons with $p_T > 200$ GeV ($p_T > 100$ GeV) in the barrel (endcaps). This scale bias applied to simulated events reproduces the $1/p_T$ distribution in data. Also shown in the figure are the limits of the barrel and endcap regions via the blue lines.

In the barrel region, the scale bias is consistent with zero, while significant values are present in the endcaps. The uncertainty on this scale bias is used to determine the systematic uncertainty in the whole $\eta\phi$ plane due to a possible scale shift. For all events the muon momentum is shifted up and down by this uncertainty per muon momentum in TeV resulting in shifted final distributions. The difference of these shifted

distributions to the unshifted one is the uncertainty used in the analysis due to a potential scale bias.

MUON p_T RESOLUTION Another source of a systematic uncertainty in the muon reconstruction is the p_T resolution. The p_T resolution was measured in cosmic data as shown in Fig. 17. A similar measurement in simulated events shows that both numbers agree within the uncertainties. However, these uncertainties can lead to a wrong determination of the momentum resolution and therefore a shift of the mass resolution. The uncertainty of this measurement was conservatively estimated to be 10% in the barrel and 20% in the endcaps [94]. To account for this uncertainty in the analysis, the muon p_T resolution has to be changed by this amount and compared to the unshifted events. For this the muon p_T of each event is randomly smeared to worsen the p_T resolution by 10% or 20% respectively. The width of the Gaussian used for the smearing depends on the product of the p_T resolution and the uncertainty on it. A p_T resolution of 10% is assumed for the whole parameter space of muons. This results in an additional p_T smearing of 1% in the barrel and 2% in the endcaps, that will cover these uncertainties. The assumption of a p_T resolution of 10% is very conservative when compared to the measurement shown in Fig. 17. This smeared muon p_T is then propagated to the final distribution or mass resolution and the difference to the unshifted one is taken as the measure for this systematic uncertainty.

MUON SCALE FACTORS As described in Sec. 4.5.3 for different steps of the muon reconstruction and identification, correction factors are used to account for different efficiencies in the observed data and in the simulation. These correction factors have uncertainties which result in a systematic uncertainty due to these muon scale factors. Two sources of uncertainties are taken into account for each applied scale factor. The first part is the statistical uncertainty of the scale factors, which is taken into account as a systematic uncertainty on the scale factor itself. The second part is the uncertainty of the Tag and Probe method used to determine the scale factors. The trigger scale factors are varied by $\pm 0.5\%$ to estimate the systematic uncertainty due to the method. The scale factors used for muon reconstruction, muon identification and muon isolation are varied by $\pm 1\%$ to estimate the systematic uncertainty [95]. Both sources of uncertainty are added in quadrature, all events are scaled by the scale factors varied up and down. The difference on the reweighted distributions to the nominal one is taken as a measure for the uncertainty of the muon scale factors.

ELECTRON E_T SCALE The absolute electron E_T scale can also be a source of a systematic uncertainty, similar to the muon p_T scale. The E_T scale uncertainty is derived from $Z \rightarrow ee$ events, where one electron is used to tag the event while the other one is studied. For high energy electrons the E_T measurement is dominated by the ECAL, therefore only the measurement in the ECAL is considered. The difference of the simulated to the observed mean of the invariant mass distribution is used to determine the difference of the E_T scale for a wide range of energies [46]. The agreement between observation and simulation is better than 2%, therefore a systematic uncertainty of 2% is assigned to the electron E_T scale. In each event the electron E_T is shifted up and down by the uncertainty, the difference of the resulting shifted distributions to the unshifted one is used as the measure for the uncertainty due to the electron E_T scale.

ELECTRON SCALE FACTORS Similar to muons also for electrons scale factors (See Sec. 4.5.2) are applied to correct for the different efficiencies in the observed data and in the simulation. Two scale factors are applied, for the electron reconstruction and the electron identification. The statistical uncertainty of the electron reconstruction scale factor is used as the uncertainty on the corresponding scale factor. For the identification scale factor the corresponding uncertainties are listed in Tab. 6. To also account for uncertainties on this factor which could arise at different energy ranges, an additional uncertainty for the barrel region of 1% for electron energies below 90 GeV is used. This additional uncertainty increases linearly from 1 – 3% for electron energies of 90 GeV – 1 TeV and stays constant at 3% for higher energies than 1 TeV. For the end-caps 1% below energies of 90 GeV is used, which increases linearly from 1 – 4% for the energies of 90 GeV – 300 GeV and a constant value of 4% is used for higher energies. All events are scaled by the scale factors varied up and down. The differences of the reweighted distributions to the nominal one are taken as a measure for the uncertainty of the electron scale factors.

MONTE CARLO SAMPLE SIZE The statistical uncertainty of the simulation due to the limited size of the Monte Carlo samples is another source of a systematic uncertainty. It differs from all the other systematic uncertainties as it is not a global uncertainty. All other sources of uncertainty are applicable to the whole distribution at once, meaning that all bins are fully correlated. For the limited Monte Carlo samples size all bins are independent as the basic uncertainty is of statistical nature. Therefore an uncertainty is introduced for each bin in the final distribution, following the method described in Ref. [96]. The algorithm to assign the uncertainty in one bin is summarized in the following. This procedure is repeated for each bin in the final distribution, resulting in $\mathcal{O}(100)$ additional uncertainties. The uncertainty calculation depends on two quantities for each process in each bin, first the event yield for a process in this bin.

$$n_i = w \frac{\mathcal{L} \cdot \sigma}{N_i} N_i = C \cdot N_i \quad (19)$$

This event yield depends on the number of simulated events N_i , the cross section of the process σ , the integrated luminosity of the data \mathcal{L} and scale factors w to account for differences between simulation and data. All these factors can be summarized in a constant C . Seconds there is the statistical uncertainty on the event yield.

$$e_i = C \cdot \sigma(N_i) = C \cdot \sqrt{N_i} \quad (20)$$

This depends on the statistical uncertainty of the number of generated events $\sigma(N_i)$ which is the square root of the number of generated events, as the number of events is described by a Poisson distribution. Starting with these numbers the following procedure is repeated for each bin to assign an uncertainty.

1. Sum the yields n_i and statistical uncertainties e_i of each background process i in the bin.

$$n_{\text{tot}} = \sum_{i \in \text{bkg}} n_i$$

$$e_{\text{tot}} = \sqrt{\sum_{i \in \text{bkg}} e_i^2}$$

2. If $e_{\text{tot}} = 0$, the bin is skipped and no uncertainties are created.
3. The effective number of unweighted events is defined as $n_{\text{tot}}^{\text{eff}} = n_{\text{tot}}^2/e_{\text{tot}}^2$, rounded to the nearest integer. From Eqn. 19 and 20 follows for one process

$$n_i^{\text{eff}} = \frac{n_i^2}{e_i^2} = \frac{C^2 \cdot N_i^2}{C^2 \cdot N_i} = N_i$$

this motivates to use $n_{\text{tot}}^{\text{eff}}$ as a measure for the total number of unweighted events.

4. If $n_{\text{tot}}^{\text{eff}} \leq 10$: separate uncertainties will be created for each background process. Processes that do not contribute ($n_i = 0$) are skipped. If the number of effective events for a given process is lower than 10 a Poisson constrained uncertainty will be created, otherwise a Gaussian constrained uncertainty is used (see next item in the list).
5. If $n_{\text{tot}}^{\text{eff}} > 10$: A single Gaussian constrained Barlow-Beeston-lite [97] uncertainty is created for the total uncertainty in the bin. This is done to reduce the number of individual systematic uncertainties as much as possible, without losing the details of the uncertainty where necessary.
6. In both cases the uncertainty is modelled by the scaling parameter χ . For a Gaussian-constrained uncertainty the yield scales as $n_{\text{tot}} + \chi \cdot e_{\text{tot}}$, where χ is distributed following a Gaussian with mean zero and width one. For the Poisson-constrained uncertainty the scaling parameter χ is used as a yield multiplier with nominal value one: $n_{\text{tot}} \cdot \chi$. This scaling parameter is then varied in the statistical interpretation for each bin individually to model the systematic uncertainty due to limited Monte Carlo sample size.

LUMINOSITY The value of the integrated luminosity is used to scale the number of simulated events to the amount expected with this luminosity (see e. g. Eq. 19), therefore the uncertainty on the measured luminosity value directly leads to an uncertainty on the background and signal predictions. The uncertainty on the integrated luminosity is 2.5% [98]. The uncertainty on the normalization of the simulation is therefore also 2.5% due to the systematic uncertainty of the luminosity.

$W\gamma$ BACKGROUND The $W\gamma$ background process is simulated in leading order with Madgraph. It simulates the process of a photon being mis-identified as an electron. This is only based on the simulation, which is only available in leading order, therefore a high systematic uncertainty of 50% is assigned. This uncertainty is used to scale the $W\gamma$ up and down, the difference of these shifted distributions to the unscaled version is used as the measure for the systematic uncertainty on the $W\gamma$ background.

PILE-UP REWEIGHTING UNCERTAINTY As mentioned in Sec. 4.5.1 the number of simulated pileup interactions has to be reweighted to reproduce the measurement in the data. This reweighting method results in a systematic uncertainty [99]. The uncertainty is estimated by varying the minimum bias cross section by $\pm 5\%$ and weight the simulated events with the shifted values. The effect of this uncertainty can be seen in Fig. 28-right as a grey band around the background expectation.

DATA-DRIVEN BACKGROUND For the background expectation of events containing hadronic jets mis-identified as electrons derived from data, a similar approach to the $W\gamma$ background is used to assign the systematic uncertainty. Also for this mis-identification process a systematic uncertainty of 50% is assigned. This also covers the difference in the comparison with the same-sign method, shown in Fig. 27.

E_T^{MISS} In the E_T^{miss} measurement itself, there is no uncertainty, but the uncertainties on the detected objects all influence E_T^{miss} and therefore have to be propagated to E_T^{miss} . For the electron and muon uncertainties this is done, e. g. when the electron E_T scale is shifted to estimate the uncertainty, this shift is also propagated to E_T^{miss} . But also other objects in the events which are not considered in the analysis could have an influence on E_T^{miss} , these uncertainties also have to be considered. These are:

- Jet energy resolution: It is observed, that the jet energy resolution in data is worse than in the simulation. To correct for this difference an additional energy smearing is used in the simulation. This method leads to an uncertainty due to the jet energy resolution. The method works for events where the reconstructed jet can be matched to a generator level particle⁴, by scaling the jet p_T with the factor

$$c = 1 + (s - 1) \frac{p_T - p_T^{\text{gen}}}{p_T}$$

For jets where this matching is impossible, the factor is defined as

$$c = 1 + \mathcal{N}(0, \sigma_{\text{gen}}) \sqrt{\max(s^2 - 1, 0)}$$

with a Gaussian distribution \mathcal{N} with a mean of zero and a sigma of the generator jet p_T resolution. The data to simulation factor s has uncertainties [100]; varying it within the uncertainties results in different jet energies and consequently in different E_T^{miss} values. These differences are used as the measure due the uncertainty of the jet energy resolution.

- Jet energy scale: The energy scale is measured to tune the simulation to reproduce the behaviour of the data. The uncertainty of this measurement leads to an uncertainty on the jet energy scale and consequently to an uncertainty on E_T^{miss} . The jet energy scale is measured in events where a jet recoils against a photon or a Z boson. The photons or Z bosons momentum can be measured very precisely via its decay into two electrons or two muons. As the boson should be balanced against the recoil jet, the jet momentum is the same as the bosons momentum with reversed sign. The uncertainties of this measurement come from background events in the Z or γ selection, initial and final state radiation, the simulation of pileup or the extrapolation to higher energies. Combining these uncertainties leads to a total uncertainty on the jet energy scale of < 5% for jets with $p_T > 20$ GeV. The uncertainties are propagated to E_T^{miss} and the up and down shifted E_T^{miss} values are used in the analysis to determine the final invariant mass distribution. These shifted distributions are used as a measure of the uncertainty due to the jet energy scale.

⁴ Matching criterion: $\Delta R < R_{\text{jet}}/2$ with the jet size R_{jet} and $|p_T - p_T^{\text{gen}}| < 3\sigma_{\text{gen}}p_T$ with the generator jet p_T resolution σ_{gen} .

- Unclustered energy: The last part contributing to E_T^{miss} is the unclustered energy, energy in the calorimeters which is not clustered in jets. For the uncertainty on the unclustered energy all contributing particle flow candidate objects (charged hadrons, neutral hadrons, photons and particles in the HF detector) are varied within their energy uncertainty [101]. The resulting shift of E_T^{miss} is used to quantify the uncertainty due to the unclustered energy.

4.9.2 Theoretical uncertainty sources

The uncertainties due to the underlying theory are summarized in this section. The theoretical models which are the basis for the simulation have different sources of uncertainty that are propagated to the finally selected events to account for these uncertainty sources. The different uncertainties and how they are treated in the analysis are introduced in the following.

CROSS SECTION UNCERTAINTY The total cross section of a physical process is used to scale the simulated events of this process to the expected yield. The uncertainty on the cross section directly transfers into an uncertainty on the background yield. The cross section uncertainty is estimated by varying the parameters which are the input for the cross section calculation like e. g. the hadronisation scale. For the different processes the following uncertainties are assigned, derived directly from the uncertainty of the cross section calculation.

- $t\bar{t}$: The cross section uncertainty of 5 % is assigned according to Ref. [102]. Here the combination of three uncertainty sources is used. First, there is the uncertainty due to variation of hadronization and factorization energy scales. Second, there is the uncertainty due the variation of the PDF sets and the variation of the strong coupling constant α_S . The third uncertainty source is the uncertainty on the top quark mass.
- WW : The cross section uncertainty of 3 % is assigned according to Ref. [103]. The uncertainty is estimated from the variation of the energy scale.
- Single top : The assigned cross section uncertainty is 5 %, following Ref. [104]. The combination of four uncertainty sources is used. The first three are similar to the $t\bar{t}$ cross section uncertainties, so scale variation, α_S variation and the uncertainty of the top quark mass. In addition the uncertainty on the beam energy is considered as the fourth uncertainty source.
- Drell Yan : A 2 % uncertainty is assigned according to Ref. [105], which is based on the variation of the energy scale and the uncertainties due to the PDF sets and the variation of α_S .
- WZ and ZZ : Following Ref. [105] a cross section uncertainty of 4 % is assigned to both processes. The uncertainty is based on the variation of the energy scale and the uncertainties due to the PDF sets and the variation of α_S .

PARTON DENSITY FUNCTIONS The PDFs dictate the initial conditions for the particle collisions, therefore the uncertainties on these leads to uncertainties in the

background and signal prediction from simulation. These uncertainties in the simulation can effect the normalization of processes as well as the shape of the invariant mass spectra. The uncertainties are given by the data used to determine the PDFs, the extrapolation into an unmeasured energy regime and the uncertainty in the parameterization. How the uncertainties are handled follows the recommendations by the PDF4LHC group [106]. The PDF set NNPDF 3.0 [107] is used for this method, which is a Monte Carlo PDF set. For this $N_{\text{rep}} = 100$ pseudo-data replicas are produced, from the input data, randomized within the uncertainties. The nominal PDF set is then the mean of the 100 replicas. Also produced are up and down variations of α_S for the mean PDF set (down variation: $\alpha_S(m_Z^2) = 0.1165$, up variation: $\alpha_S(m_Z^2) = 0.1195$ and mean value $\alpha_S(m_Z^2) = 0.118$). The following procedure is used to evaluate the uncertainties on the background simulation. Each event is reweighted to different PDF sets with the ratio of the new PDF set to the one used in the production of the simulation. For the new and original event weight the each of the two initial protons is represented by a one PDF probability factor, resulting in four total factors, two for the original PDF set f_{prod} used in the simulation and two for the new PDF set f_{NNPDF} used for the reweighting. For each quark the two PDF probabilities depend on the same three parameters: the momentum fraction of the quarks $x_{1,2}$, the quarks flavours i, j and the collision energy scale Q . Combining the four factors results in the total event weight w :

$$w = \frac{f_{\text{NNPDF}}(x_1, i, Q) \cdot f_{\text{NNPDF}}(x_2, j, Q)}{f_{\text{prod}}(x_1, i, Q) \cdot f_{\text{prod}}(x_2, j, Q)} \quad (21)$$

The analysis is then repeated with each reweighted set of events, resulting in 100 new final distributions. The standard deviation of the different resulting distributions is calculated for each bin and is taken as the measure for the pdf uncertainty from the bin content of the replica x_k and the nominal bin content x_0 .

$$\sigma_{\text{PDF}} = \left(\frac{1}{N_{\text{rep}} - 1} \sum_{k=1}^{N_{\text{rep}}} (x_k - x_0)^2 \right)^{\frac{1}{2}} \quad (22)$$

In addition the mean of the up and down α_S deviation is added in quadrature to take the α_S uncertainty into account

$$\sigma(x) = \sqrt{\sigma_{\text{PDF}}^2(x) + \left(\frac{\sigma_{\alpha_S}^{\text{Up}}(x) + \sigma_{\alpha_S}^{\text{Down}}(x)}{2} \right)^2} \quad (23)$$

The resulting uncertainty for the background expectation as a function of the invariant $e\mu$ mass is shown in Fig. 50 for the $e\mu$ channel as an example.

For the signal expectation the uncertainty is determined slightly differently. Only the effect on the acceptance is taken into account by dividing the reweighted distributions by the reweighting mean. The effect on the signal expectations is shown in Fig. 51 for the three studied signal models in the $e\mu$ channel. The different kinematics of the three signal models result in quite different invariant mass distributions which result in different uncertainties as a function of the parameter of interest, shown in Fig. 51. For the RPV model $m_{\tilde{\nu}_\tau}$ is very similar to $m_{e\mu}$, therefore the uncertainty is high in the low mass region, where the PDFs at small x are relevant, which have big uncertainties. The

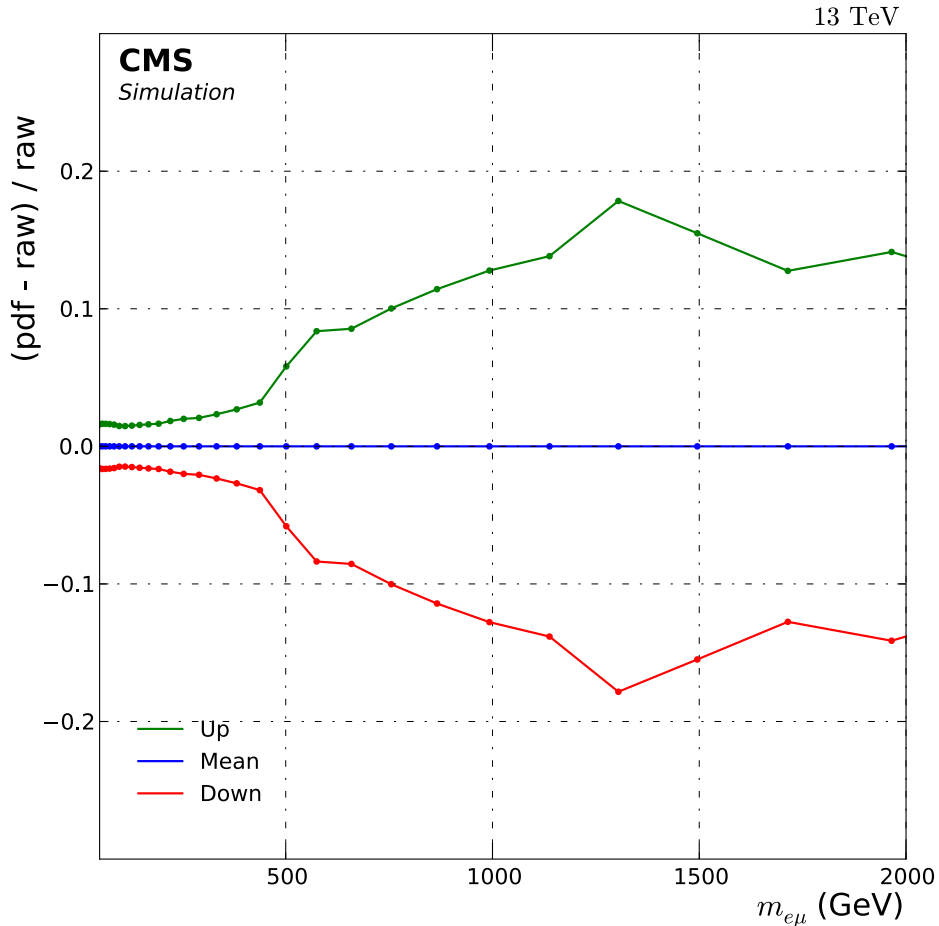


Figure 50: Relative uncertainty on the event yield due to PDF uncertainties for the background expectation as a function of the invariant mass $m_{e\mu}$. Shown is the relative difference between the reweighted sample (called 'pdf') and the unweighted sample from the generator (called 'raw'). Three different reweighted distributions are shown, the mean value and the up and down variations.

QBH model has a tail towards high $e\mu$ masses for all m_{t_h} values, resulting in smaller uncertainties. The Z' model is similar to the RPV model for low Z' masses, at high masses the off-shell production at low invariant mass becomes significant, resulting in larger uncertainties.

WW SHAPE UNCERTAINTY For the WW background expectation also the uncertainty on the differential cross section is considered, as it results in an uncertainty on the $m_{e\mu}$ distribution shape of this process. This uncertainty is important as the WW process is especially at high invariant masses a non negligible background process. The uncertainty on this background shape is estimated from missing differential higher order corrections, which are not considered in the simulation of this process. The uncertainty is derived by the differential NLO electroweak corrections to the LO cross section as calculated in Ref. [108]. They are calculated as a function of the in-

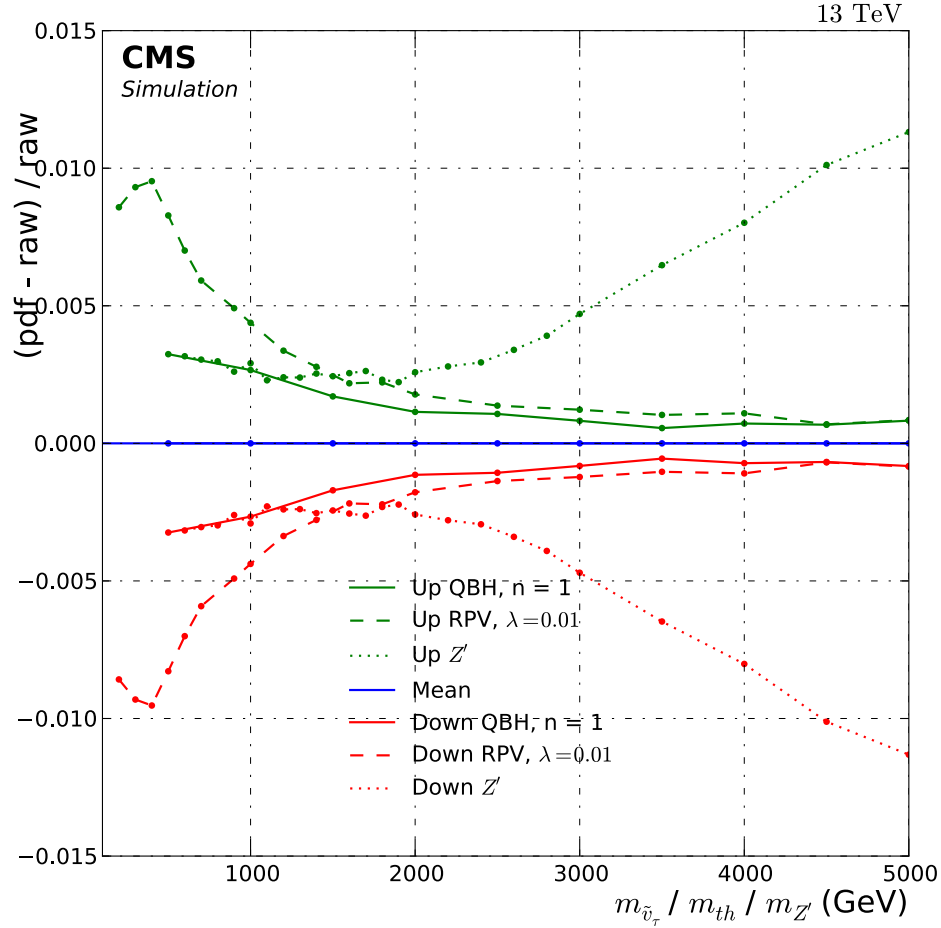


Figure 51: Relative uncertainty on the event yield due to PDF uncertainties for the three signal models studied in the $e\mu$ channel as a function of the signal parameter. For the RPV model this is the generated $\tilde{\nu}_\tau$ mass, for the QBH model the threshold mass m_{th} and for the Z' model the mass of the Z' boson. Shown is the relative difference between the reweighted sample (called 'pdf') and the unweighted sample from the generator (called 'raw'). Three different reweighted distributions are shown, the mean value and the up and down variations for each model.

variant $e\mu$ mass. To apply them in the analysis in the form of $1 \pm \Delta$, the correction is parametrized by a second order polynomial with the form:

$$\Delta = 1 - \left(0.993 - 2.001 \cdot 10^{-4} \times \frac{m_{e\mu}}{\text{GeV}} + 2.838 \cdot 10^{-8} \times \left(\frac{m_{e\mu}}{\text{GeV}} \right)^2 \right)$$

This is used as a symmetric uncertainty and also covers possible contributions from $\gamma\gamma$ induced processes which are not included in this WW simulation.

TOP SHAPE UNCERTAINTY Uncertainties associated with the modelling of the shape of the $e\mu$ invariant mass distribution are taken into account for the leading $t\bar{t}$ background and this leads to an uncertainty in the total background yield. This is the most dominant systematic uncertainty for the background and is estimated from the differential distribution of resummed cross-sections at NLO+NNLL for $m_{t\bar{t}}$ as

presented in Ref. [109] and the variation of the QCD scale in the simulation. The two sources of shape uncertainty are shortly explained below:

- In Figure 5 (upper panel) of Ref. [109], the authors give the relative cross section difference with respect to the MCFM NLO calculation. They split the full difference in two parts, which were combined for this analysis by adding them together. From this the following event weights (up,down) were obtained for the NLO POWHEG simulation as a function of $m_{t\bar{t}}$:

$$\text{weight} = \begin{cases} 1 \pm \left(0.05 \cdot \frac{m_{t\bar{t}} - 2m_t}{0.5 \text{ TeV} - 2m_t} \right) & 2m_t < m_{t\bar{t}} < 0.5 \text{ TeV} \\ 1 \pm \left(0.05 + 0.25 \cdot \frac{m_{t\bar{t}} - 0.5 \text{ TeV}}{1.0 \text{ TeV} - 0.5 \text{ TeV}} \right) & 0.5 \text{ TeV} < m_{t\bar{t}} < 1 \text{ TeV} \\ 1 \pm \left(0.3 + 0.3 \cdot \frac{m_{t\bar{t}} - 1.0 \text{ TeV}}{1 \text{ TeV}} \right) & 1 \text{ TeV} < m_{t\bar{t}} < 3 \text{ TeV} \end{cases}$$

The simulated events were reweighted according to their $m_{t\bar{t}}$ value with these weights to obtain the up and down shifted $m_{e\mu}$ distribution which are then used to get the $m_{e\mu}$ -dependent uncertainty estimate.

- The QCD scales (factorization/renormalization scale) were varied at the matrix-element level in the simulation. Both scales were modified by a factor of two for the up variation and by a factor 0.5 for the down variation. The maximum deviation from the nominal value is taken as the uncertainty for the QCD scale.

For the combined uncertainty on the $t\bar{t}$ background expectation the envelope of the two uncertainty sources is taken as both sources are not independent of each other. The contribution of both sources can be seen in Fig. 52 as the relative difference of the event yield to the nominal invariant mass distribution. At low masses up to $m_{e\mu} \sim 350$ GeV the uncertainty is given by the variation of the QCD scales, at higher masses the missing higher order corrections drive the uncertainty. The uncertainty due the QCD scale variation is calculated only for the bulk $t\bar{t}$ sample and not for the high mass extensions. This can be seen in Fig. 52, as the uncertainty drops to zero for masses above 500 GeV. For masses above 350 GeV the missing higher corrections are the dominant uncertainty therefore the not calculated QCD scale uncertainty is not a problem as the envelope of both uncertainty sources is used.

4.9.3 Effect on the $e\mu$ channel

The last step of the systematic uncertainty studies is to have a look at the effect of the systematic uncertainties on the results. This is done in this section for the $e\mu$ channel. The first step is to look at the effect of the systematic uncertainties on the background expectation, then the effect on the different signal models is shown.

BACKGROUND For the background expectation the effects of the different systematic uncertainties on the event yield are studied. Therefore the uncertainties are propagated to the final invariant mass distribution, the difference to the nominal distribution is used as the measure for the systematic uncertainty on the event yield. The effect of the experimental systematic uncertainties is shown in Fig. 53-left. The dominant uncertainty from low masses up to ~ 1.2 TeV is the uncertainty on the muon scale

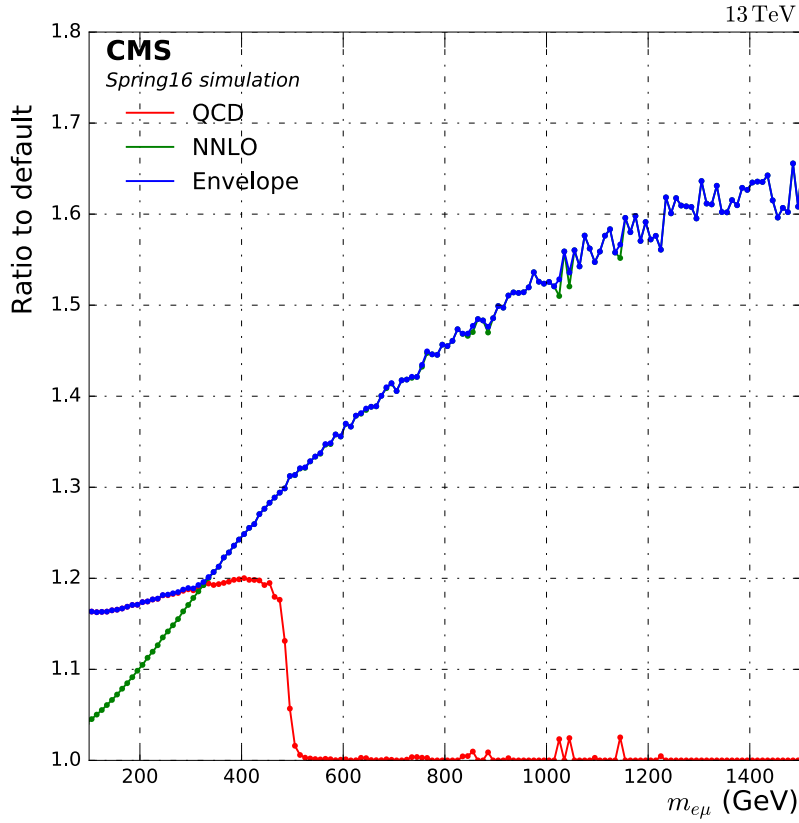


Figure 52: Relative uncertainty on the event yield of the $t\bar{t}$ background as a function of $m_{e\mu}$. Both considered sources of uncertainty are shown and in addition the envelope which is used in the analysis. The drop of the QCD scale variation uncertainty at $m_{e\mu} \sim 500$ GeV is due to the high mass $t\bar{t}$ tail samples, that do not contain the corresponding uncertainty information. As we take the envelope of both uncertainties and in this region the higher order uncertainties are clearly dominant this is no problem for the analysis.

factor, while at higher masses the statistical uncertainty due to the limited number of simulated events becomes dominant. All other uncertainties are less relevant, especially at low masses. In Fig. 53-right the effect of the theoretical uncertainties on the expected background yield is shown. This uncertainty is dominated over the full mass range by the $t\bar{t}$ shape uncertainties, at higher masses the PDF uncertainty gets more relevant. The comparison of all uncertainty sources is shown in Fig. 54, where it gets clear, that the theoretical uncertainties are dominant over the whole mass range.

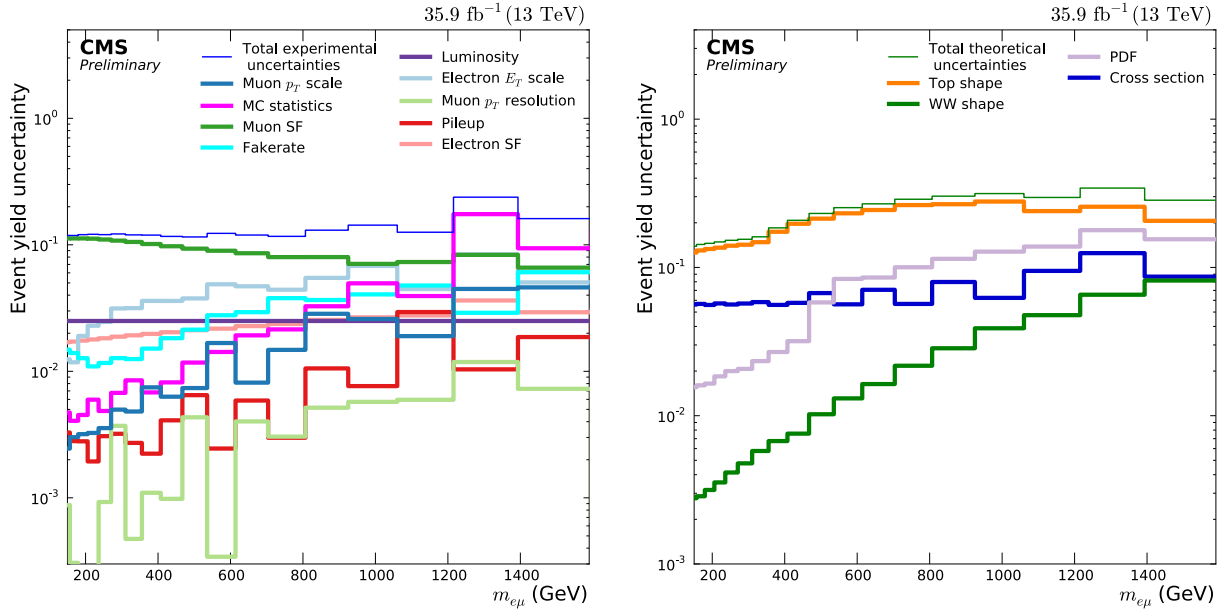


Figure 53: Relative effect on the background event yield of the different sources of systematic uncertainty. The left figure shows the effect of the experimental sources of uncertainty, while the right figure shows the different theoretical sources of uncertainty.

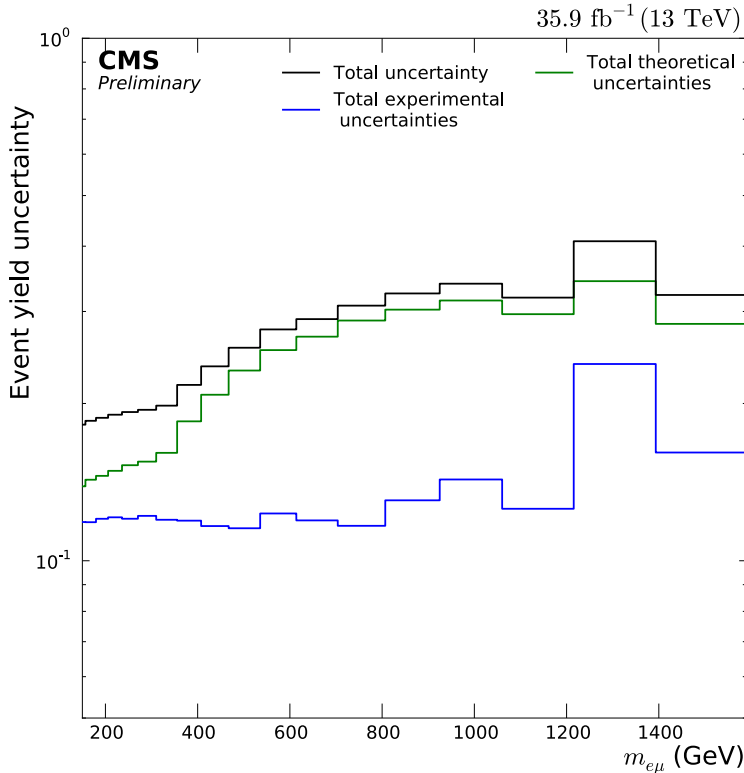


Figure 54: Relative effect on the background event yield of the theoretical and experimental sources of systematic uncertainty and the quadratic sum of both. Over the whole mass range the theoretical uncertainties dominate the total uncertainty.

RPV SUSY MODEL For the RPV SUSY model the effect of the systematic uncertainties is measured in their effect on the shape of the invariant mass distribution and the normalization. The shape in the invariant mass distribution is characterized by the width of the resonant signal shape as defined in Sec. 4.8, where the effect of the

systematic uncertainties on the width is shown already in Fig. 39. How the different sources of uncertainty contribute to the shown uncertainty band is given in Fig. 55. The uncertainty on the signal width is dominated for the whole probed mass range by the muon p_T shape. The effect on the normalization is characterized by the acceptance times efficiency in Sec. 4.7.1, where the effect of the systematic uncertainties is shown in Fig. 39. The contributions to these uncertainties by the different sources of systematic uncertainties are shown in Fig. 56. The uncertainty is dominated by the muon scale factors uncertainty, especially in the downwards uncertainty. For the upwards uncertainty the muon and electron scale factor uncertainties are comparable.

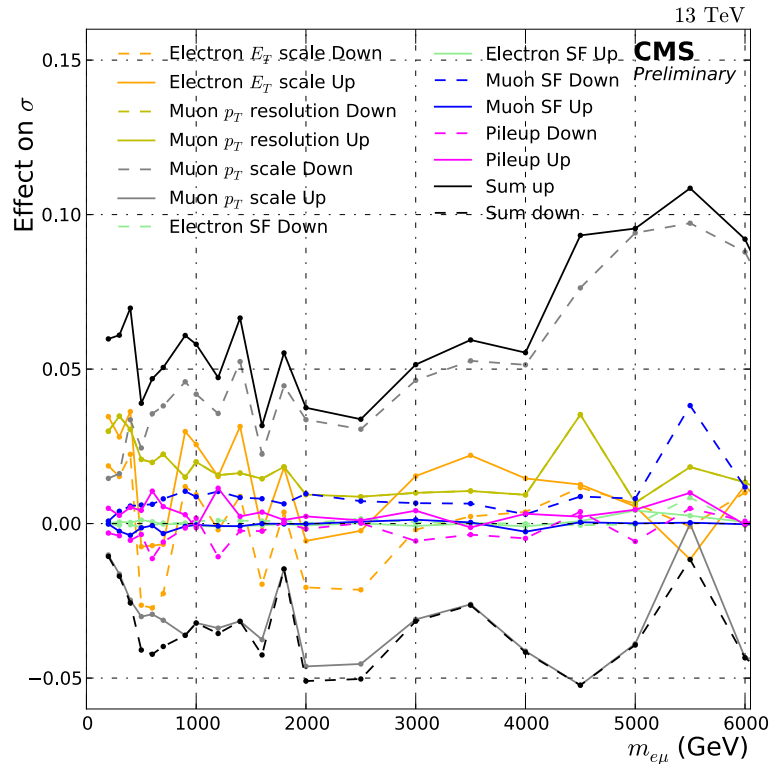


Figure 55: Effect of the systematic uncertainties on the RPV SUSY signal as a function of $\tilde{\nu}_\tau$ mass. It shows the relative effect on the invariant mass resolution and therefore the signal width, which is dominated by the muon p_T scale uncertainty.

The analysis in the $e\mu$ channel the analysis is split into different η categories, therefore the systematic uncertainties also have to be determined in the different η windows. The total effect of the uncertainties is shown in Fig. 46 and Fig. 41 for the mass resolution and acceptance times efficiency, respectively. How the different sources of systematic uncertainties contribute to these results is shown in Fig. 108 and Fig. 107 in the appendix.

QBH AND Z' SIGNAL For the QBH and Z' model the systematic uncertainties are all considered, but the effect is not quantifiable by some simple numbers. The effect on the normalization is similar to the effect on the background, shown in Fig. 53-left. The effect on the shape for the Z' model is similar to the RPV model, shown in Fig. 55, while for the QBH signal shape the effect is more complex, due to the different shape. Therefore there is no way to quantify the effect of the systematic uncertainty in one

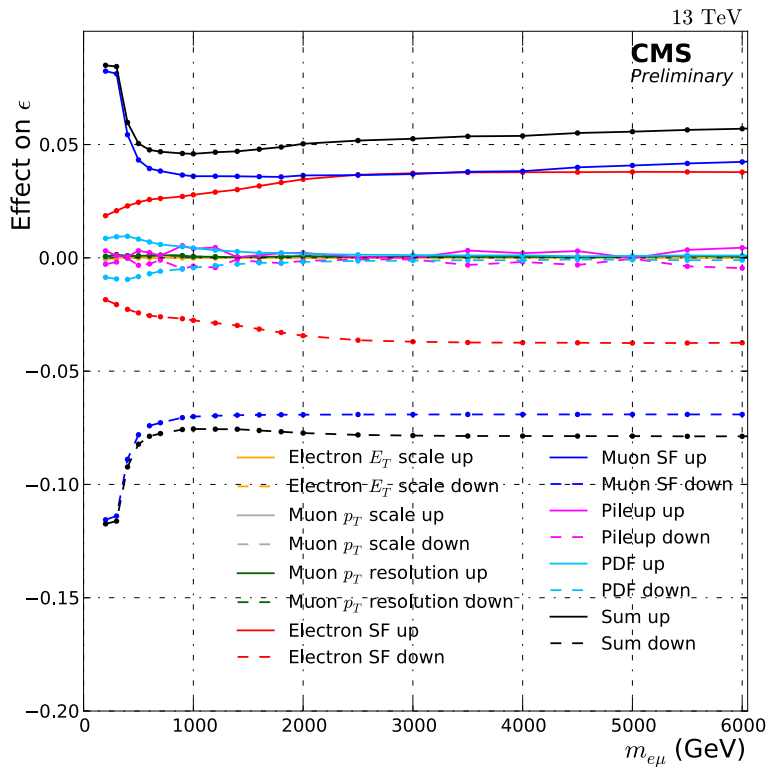


Figure 56: Effect of the systematic uncertainties on the RPV SUSY signal as a function of $\tilde{\nu}_\tau$ mass. It shows the relative effect on the product of acceptance and efficiency, which is dominated by the muon scale factor uncertainty.

number as for the resonances, but the uncertainties are all considered for the QBH model. All the systematic uncertainties are propagated to the statistical interpretation via shifted invariant mass distributions for the correct interpretation.

4.9.4 Effect on the $e\tau_\mu$ channel

The systematic uncertainties in the $e\tau_\mu$ channel are very similar to the $e\mu$ channel. The additional uncertainties in this channel are due to the E_T^{miss} in the final state. The effect on the background event yield and the signal expectation are shown in the following.

BACKGROUND The effect on the background event yield due to the systematic uncertainties is shown in Fig. 57, the uncertainties which are similar to the $e\mu$ channel are not shown individually. The dominant uncertainties are the same as in the $e\mu$ channel, and the additional uncertainties due to E_T^{miss} contribute very little to the total systematic uncertainty. Towards very low masses the uncertainties increase, which is a result of the event selection, which reduces the number of selected MC events at low masses and therefore increases the statistical uncertainties.

RPV SUSY MODEL The effect of the systematic uncertainties on the RPV signal expectation is measured similar to the $e\mu$ channel as the effect on the mass resolution or signal shape and on the acceptance times efficiency or signal normalization. The final effect on these two quantities is already shown in Fig. 47 for the signal width

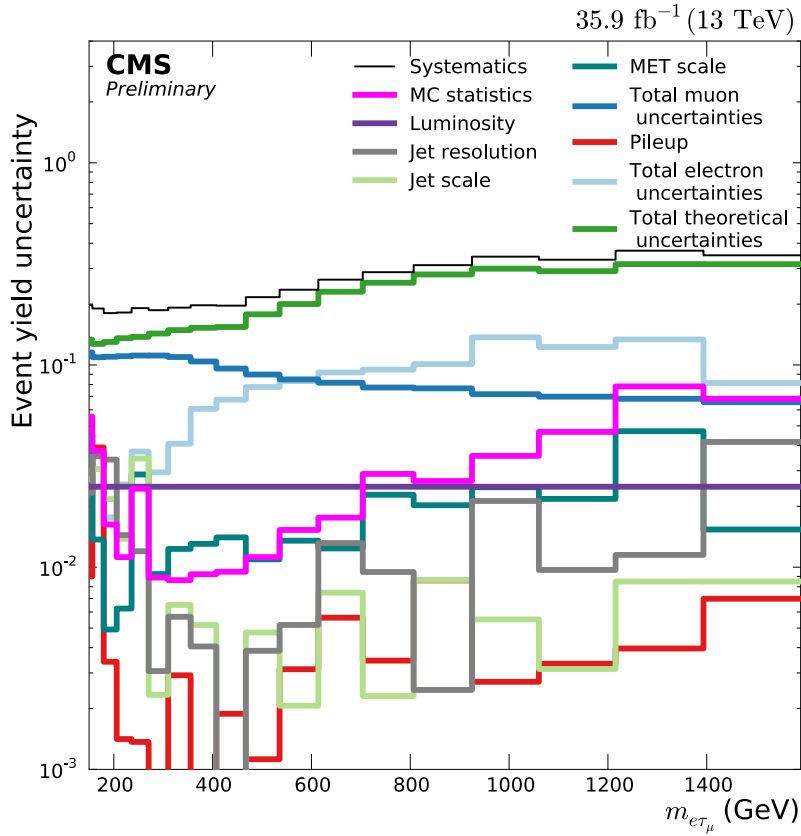


Figure 57: Relative effect on the background event yield of the different sources of systematic uncertainty. The uncertainties which are also present in the $e\mu$ channel, shown in Fig. 53, are summarized for the theoretical uncertainties and the uncertainties from the electron and muon each. The additional uncertainties due to E_T^{miss} (Jet scale, Jet resolution and MET scale) contribute only very little to the total uncertainty. The dominant uncertainty is as in the $e\mu$ channel the theoretical uncertainty.

and in Fig. 42 for the acceptance times efficiency. How the different sources of systematic uncertainty contribute to these final uncertainties is shown in Fig. 58 for the signal width and in Fig. 59 for the normalization. For the acceptance the dominating uncertainties are the same as in the $e\mu$ channel, the muon scale factor for the downwards uncertainty, while the electron and muon scale factor uncertainties are of similar size in the upwards uncertainty. For the signal width the muon p_T scale uncertainty is still an important uncertainty, while the additional MET scale and Jet energy scale uncertainties also contribute significantly.

4.9.5 Effect on the $\mu\tau_e$ channel

The systematic uncertainties in the $\mu\tau_e$ channel are comparable to the $e\tau_\mu$ channel. The main difference between these two channels is the different momentum ratios.

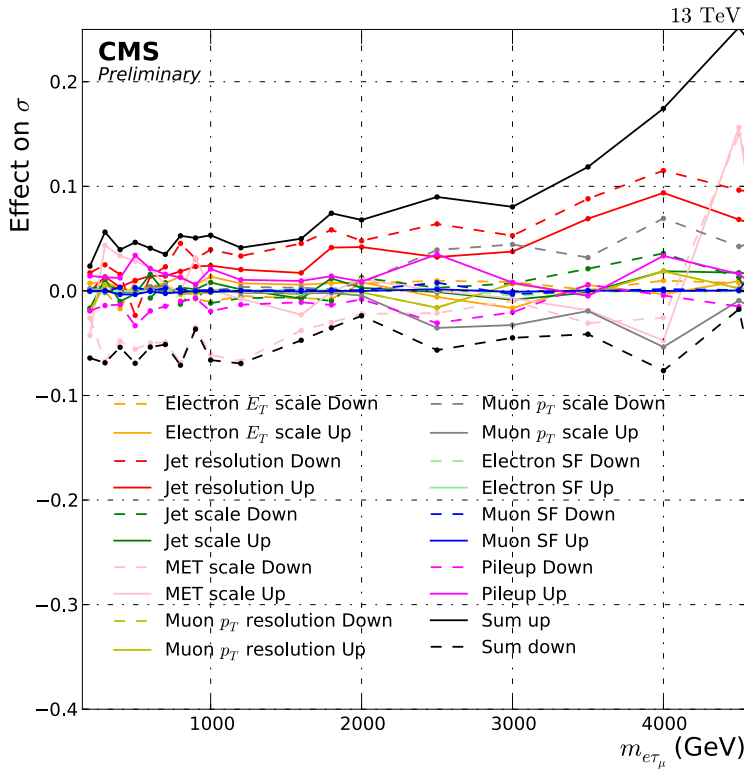


Figure 58: Effect of the systematic uncertainties on the RPV SUSY signal as a function of $\tilde{\nu}_\tau$ mass. It shows the relative effect on the invariant mass resolution and therefore the signal width, which is dominated by the muon p_T scale uncertainty as well as the MET and Jet energy scale uncertainties.

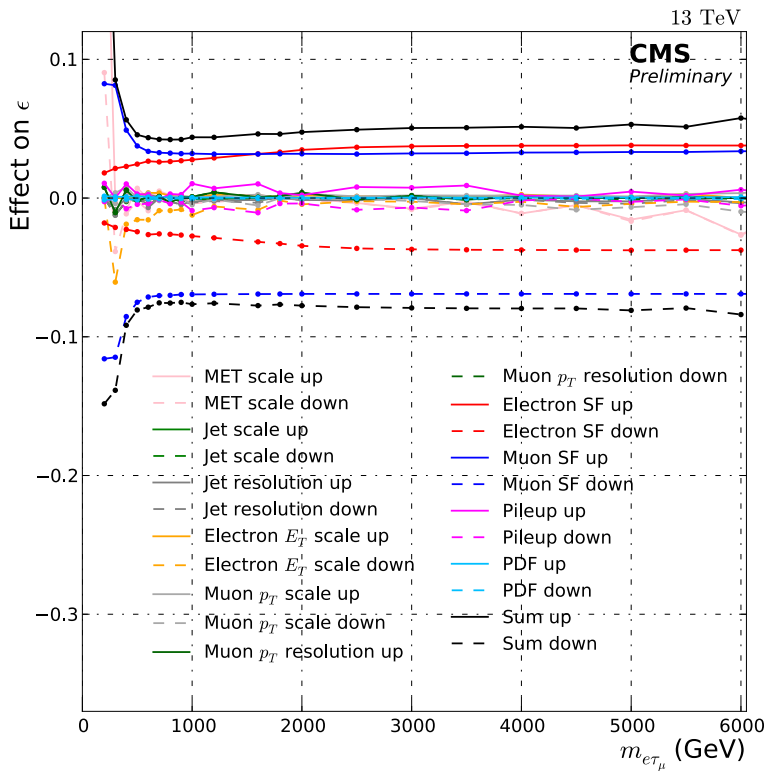


Figure 59: Effect of the systematic uncertainties on the RPV SUSY signal as a function of $\tilde{\nu}_\tau$ mass. It shows the relative effect on the acceptance times efficiency, which is dominated by the muon scale factor uncertainty.

In the $\mu\tau_e$ channel, the muon has a higher momentum, then the electron for a given mass, which is reversed in the $e\tau_\mu$ channel. The results are slightly different between the two channels as the contributing p_T value is different for a given invariant mass. The effect of the systematic uncertainties on the background expectation and on the RPV signal model is shown in the following.

BACKGROUND The effect on the background event yield due to the systematic uncertainties is shown in Fig. 60, the uncertainties which are similar to the $e\mu$ channel are not shown individually. The dominant uncertainties are the same as in the $e\mu$ channel, and the additional uncertainties due to E_T^{miss} contribute very little to the total systematic uncertainty. The electron uncertainties are smaller as in the $e\tau_\mu$ channel because the electron p_T is smaller than in the $e\tau_\mu$ channel.

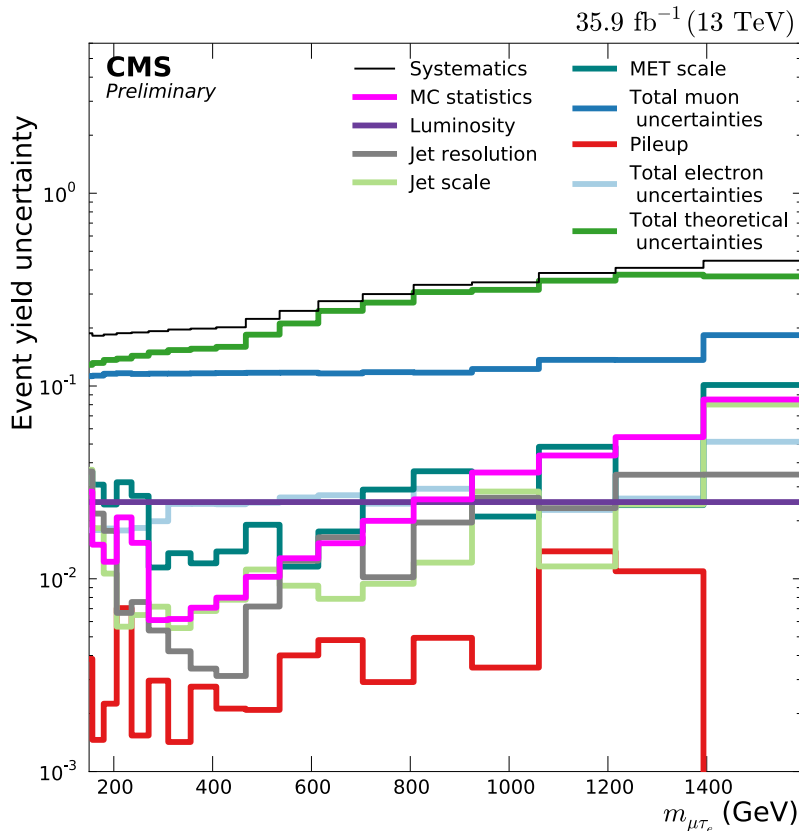


Figure 60: Relative effect on the background event yield of the different sources of systematic uncertainty. The uncertainties which are also present in the $e\mu$ channel, shown in Fig. 53, are summarized for the theoretical uncertainties and the uncertainties from the electron and muon each. The additional uncertainties due to E_T^{miss} (Jet scale, Jet resolution and MET scale) contribute only very little to the total uncertainty. The dominant uncertainty is as in the $e\mu$ channel the theoretical uncertainty.

RPV SUSY MODEL The effect of the systematic uncertainties on the RPV signal expectation is measured similar to the $e\mu$ channel as the effect on the mass resolution or signal shape and on the acceptance times efficiency or signal normalization. The final effect on these two quantities is already shown in Fig. 48 for the signal width and in Fig. 43 for the acceptance times efficiency. How the different sources of sys-

tematic uncertainty contribute to these final uncertainties is shown in Fig. 61 for the signal width and in Fig. 62 for the normalization. For the acceptance the dominating uncertainties are the same as in the $e\mu$ channel. The uncertainty due to the muon scale factor dominates the upwards as well as the downwards total uncertainty. The electron uncertainties are smaller due to the smaller electron p_T values. For the signal width the muon p_T scale uncertainty is still an important uncertainty, while the additional MET scale and Jet energy scale uncertainties also contribute significantly.

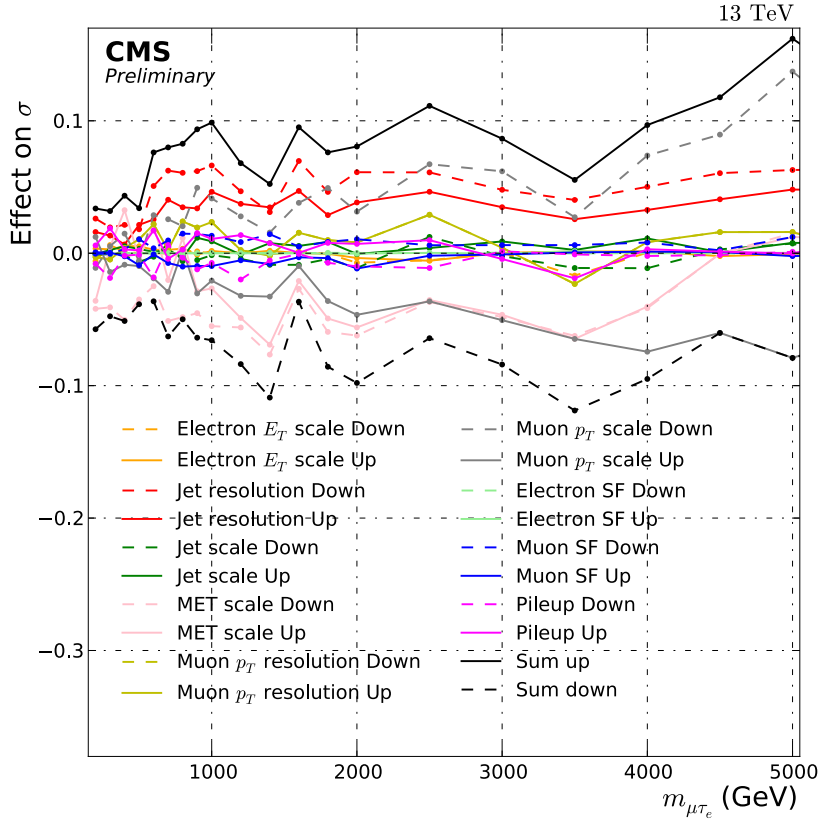


Figure 61: Effect of the systematic uncertainties on the RPV SUSY signal as a function of \tilde{v}_τ mass. It shows the relative effect on the invariant mass resolution and therefore the signal width, which is dominated by the muon p_T scale uncertainty as well as the MET and Jet energy scale uncertainties.

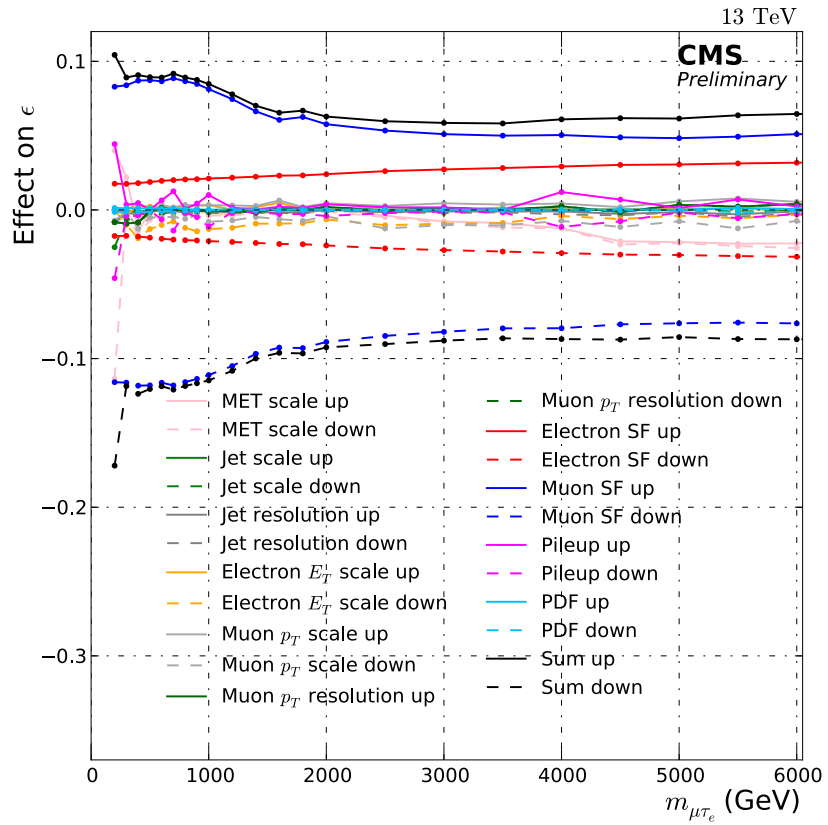


Figure 62: Effect of the systematic uncertainties on the RPV SUSY signal as a function of $\tilde{\nu}_\tau$ mass. It shows the relative effect on the acceptance times efficiency, which is dominated by the muon scale factor uncertainty.

RESULTS

This chapter presents the results of the analysis. The previous chapters summarized how events are reconstructed and how they are selected for the analysis. The background and signal expectation as well as necessary corrections to the simulation were applied. Combining all these steps with the estimate of the systematic uncertainty results in the final invariant mass distributions of the analysis. A potential signal is expected to be clearly visible above the steadily falling background in this distribution, either as a peak for the RPV and Z' model or as an edge for the QBH model. Therefore the invariant mass distribution is chosen as the final discriminating distribution to decide if a signal is observed. In this chapter first the invariant mass distributions of the studied channels are presented (Sec. 5.1), followed by the statistical interpretation methods used to decide if there is a signal or not in the observed data (Sec. 5.2). The results of this statistical interpretation are presented at the end of this chapter (Sec. 5.3) and compared to other existing analyses.

5.1 INVARIANT MASS DISTRIBUTION

The invariant mass distribution is the input for the final step of the analysis, the statistical interpretation, and therefore one of the most important results of the analysis. It compares the background expectation and its systematic uncertainties with the observed data. Including also the signal simulation allows to see if the data describe the background only hypotheses or the background plus signal one. The bin widths for each distribution are chosen according to the mass resolution, determined in Sec. 4.8, so the bin width increases as a function of the invariant mass as the resolution gets worse. To compare the simulation to the observed data the ratio of the number of events is calculated for each bin and plotted in addition to the invariant mass distribution. The distributions for the $e\mu$, $e\tau_\mu$ and $\mu\tau_e$ channels are presented in the next sections.

5.1.1 $e\mu$ channel

For the $e\mu$ channel the event selection is described in Sec. 4.3.2, all events that pass these selection criteria and are corrected following Sec. 4.5 end up in the final invariant mass distribution. The invariant mass distribution with a coarse binning is shown in Fig. 63, it allows to compare the background expectation to the observed data on a general level, while for the statistical interpretation a finer mass binning, according to the mass resolution is optimal and possible due to a very good background description.

The invariant mass distribution with this final binning according to the mass resolution for all selected events is shown in Fig. 64. To compare the background expectation to the observed data more easily the ratio of the number of events in data and simulation is used. However, there is a caveat to this comparison as these are not the final numbers used in the statistical interpretation. For this comparison next to the default,

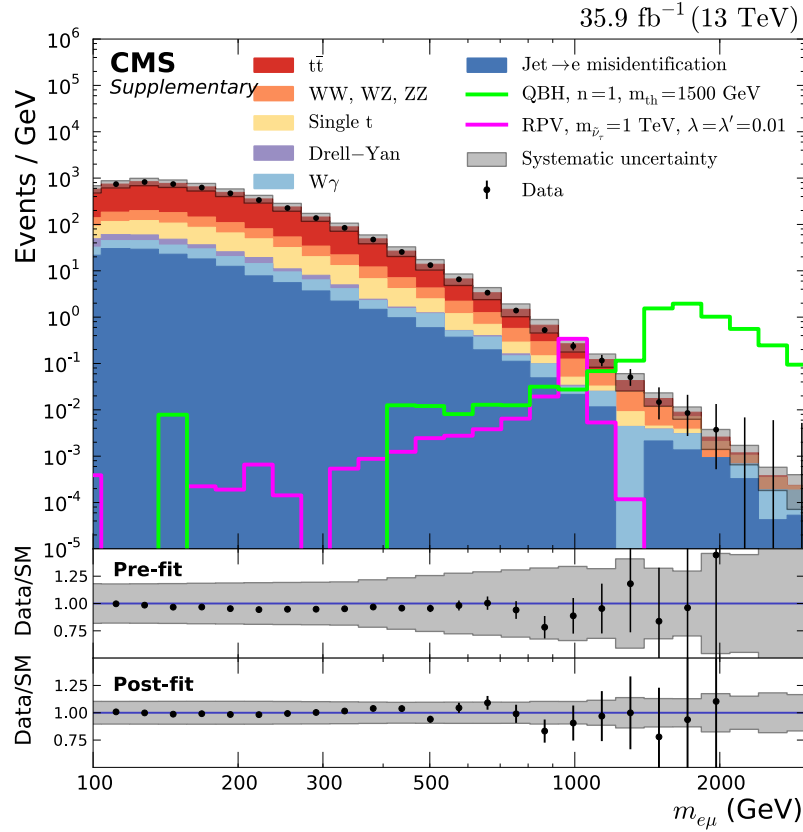


Figure 63: Distribution of invariant mass of the $e\mu$ pair. The difference between this distribution and the final mass distribution is the coarser binning, which is more suitable for presentation purposes as an overall disagreement between the simulation and the observed data would be clearly visible. Shown are the different background processes as coloured histograms, the observed data as black points, two example signals as coloured lines and the total systematic uncertainty as a grey band around the background expectation. For a comparison of background expectation and data the ratio of the number of events is displayed at the bottom. The ratio is calculated once from the shown pre-fit distribution and once from the post-fit one, which is the input to the statistical interpretation.

so called pre-fit ratio, a post-fit ratio is calculated for each bin. This post-fit ratio is a close estimate of the input to the statistical interpretation.

To get a handle on the agreement between the observed data and the background expectation with its systematic uncertainties as it used in the statistical interpretation a multidimensional maximum likelihood fit is performed. This post-fit is used to constrain the background normalization, as well as the systematic uncertainties. The systematic uncertainties on the background expectation cannot be varied at will in the maximum likelihood fit, they have to be compatible with the observed data. Therefore, in the fit to the observed data, the width and mean of each systematic uncertainty can be constraint. The resulting background expectation and uncertainties are then used to calculate the post-fit ratio shown in Fig. 63 and Fig. 64. The effect of this post-fit distribution can be seen in Fig. 65. For this background only fit the signal strength is fixed to zero, a signal plus background fit, where the signal strength is left floating, is also performed. The default used in the different figures is the background only fit as

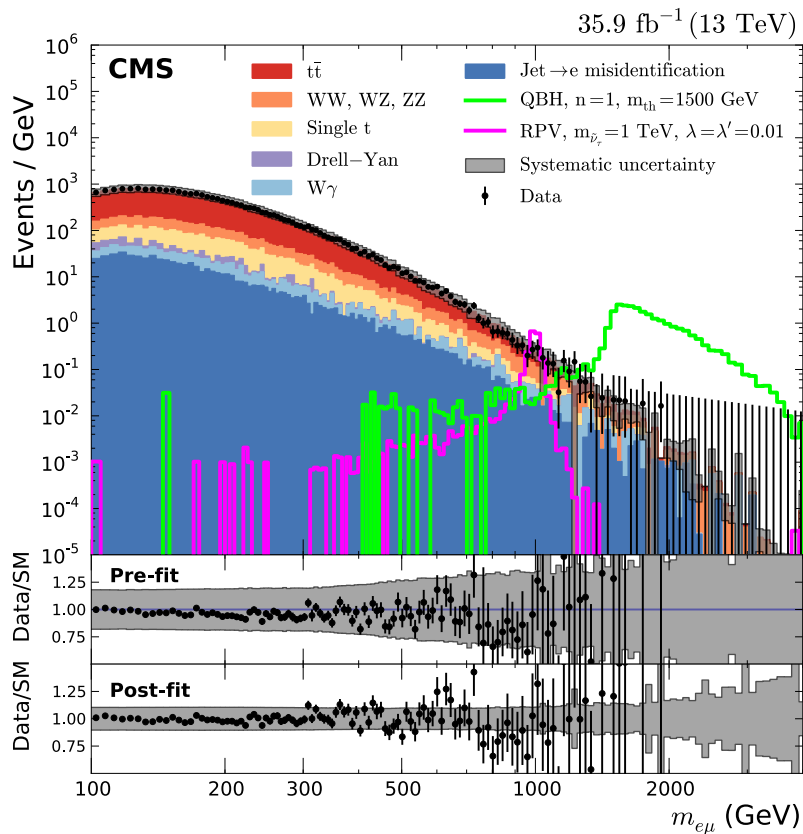


Figure 64: Invariant mass distribution of all selected $e\mu$ pairs in the analysis. The binning is chosen according to the invariant mass resolution determined in Sec. 4.8. The ratio of the number of data and the number of background events is calculated from the shown pre-fit distribution and the post-fit one, which is the input to the statistical interpretation.

it not depends on a specific choice of signal parameters. The systematic uncertainties are reduced by a factor of four and the data to Monte Carlo ratio gets closer to unity. This big reduction of the total systematic uncertainties indicates, that the systematic uncertainties overestimate the uncertainty of the background simulation and smaller uncertainties are better compatible with the observed data. Overall the observed data agrees quite closely with the background expectation and its post-fit uncertainties.

How the different systematic uncertainties are constrained is illustrated in Fig. 66. The size of the uncertainty is shown relative to the pre-fit one for two approaches. The first is the fit of the background only hypothesis, which is used in all other figures. Secondly the background plus signal hypothesis is fitted, which results in different post-fit uncertainties. Overall, they are reduced in the post-fit and even more in the background only fitting. The total systematic uncertainty is given by the quadratic sum of all systematic uncertainties. The quadratic sum of the reduced post-fit systematic uncertainties result in the total post-fit systematic uncertainty.

To compare the background expectation with the observed data also at high mass, where the data is dominated by statistical fluctuations due to the small number of events, a cumulative mass distribution is used. In this distribution for each bin the number of events above this bin is integrated. The cumulative mass distribution for all

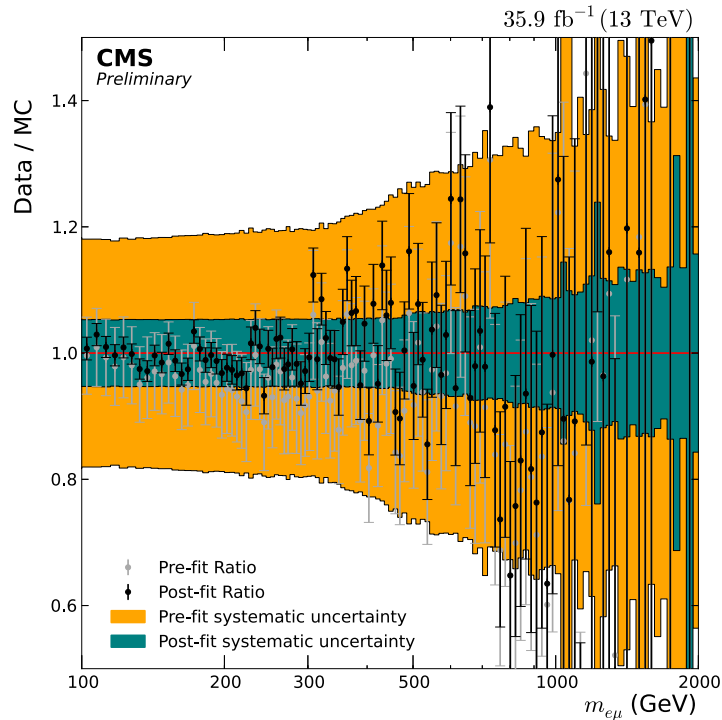


Figure 65: Comparison of the pre-fit and post-fit ratios of the invariant mass distribution shown in Fig. 64. The pre-fit ratio in grey with the corresponding systematic uncertainty in orange, as well as the post-fit ratio in black with its systematic uncertainty in green. The systematic uncertainties are reduced by a factor four in the post-fit, while the ratio gets closer to unity.

selected events of the $e\mu$ channel is shown in Fig. 68 and at high invariant masses, it shows a good agreement between the background expectation and the observed data.

Another way of comparing the background expectation to the observed data is given in Tab. 7, by comparing the number of events with each other in four bins of invariant masses. Within these pre-fit uncertainties the observed data agree with the background expectation.

Table 7: Number of expected and observed events for different bins of invariant mass. Also the statistical and systematic uncertainties on the number of background events are given.

Mass range (GeV)	Observed events	Expected events \pm (stat.) \pm (sys.)
$m_{e\mu} < 500$	124756	$128100 \pm 200 \pm 18100$
$500 < m_{e\mu} < 1000$	1411	$1510 \pm 10 \pm 400$
$1000 < m_{e\mu} < 1500$	39	$39.9 \pm 2.2 \pm 12.6$
$1500 < m_{e\mu}$	4	$4.7 \pm 0.42 \pm 1.01$

The observed event with the highest invariant mass in 2016 is shown in Fig. 67, it has an invariant mass of $1895 \pm 63 \text{ GeV}^1$. The event displays of the three next to highest mass events are shown in the appendix in Fig. 110.

¹ The uncertainty of the invariant mass measurement is derived from the uncertainty on the electron energy and muon p_T measurement.

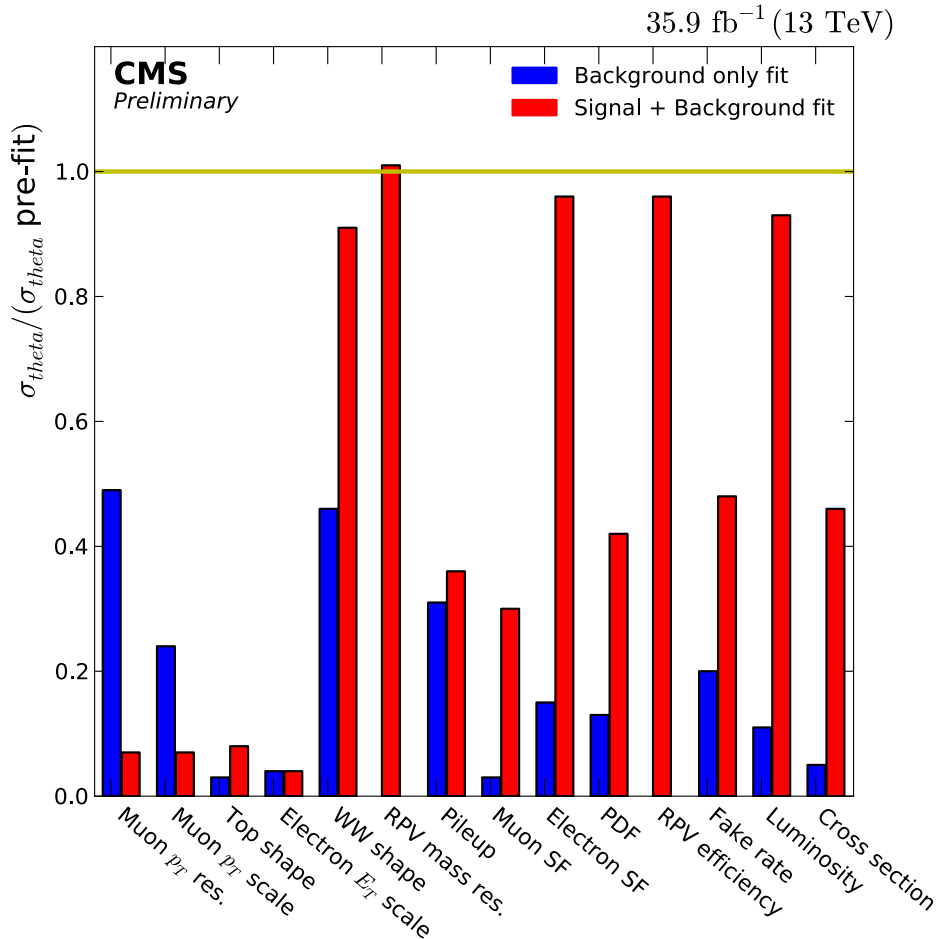


Figure 66: Size of the systematic uncertainties in the post-fit σ_θ , relative to the pre-fit ones (σ_θ pre-fit). Shown is the fit of the background only fit in blue, as well as the background plus signal fit (RPV $m_{\tilde{\nu}_\tau} = 1$ TeV, $\lambda_{132} = \lambda_{231} = \lambda'_{311} = 0.01$) in red. In the post-fit the uncertainties are reduced, even more pronounced in the background only fit. The names of the systematic uncertainties correspond to the labels in Sec. 4.9, where the different sources of uncertainty are introduced. For the uncertainties that are only applied on the signal expectation only the background+signal fit result is shown, as it is not constraint in the background only fit.

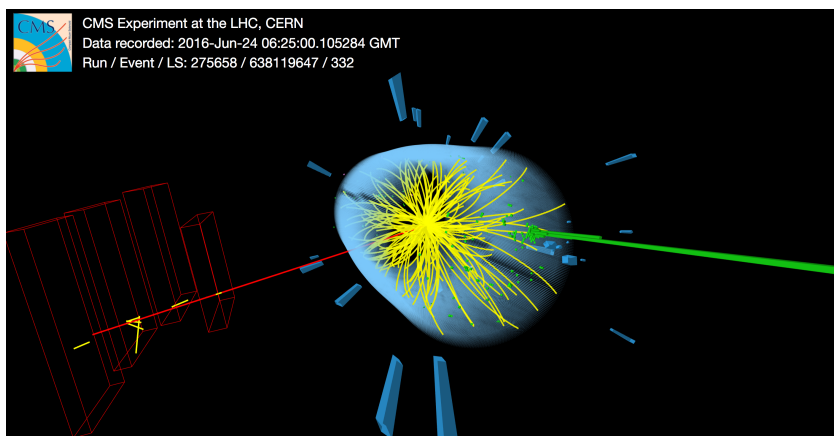


Figure 67: Event visualization of the event with the highest invariant mass in the $e\mu$ channel, that was recorded in 2016. Clearly visible is the muon in red, with the corresponding hits in the muon chambers, as well as the energy deposit in the ECAL in green from the electron. The $e\mu$ pair has an invariant mass of 1895 ± 63 GeV.

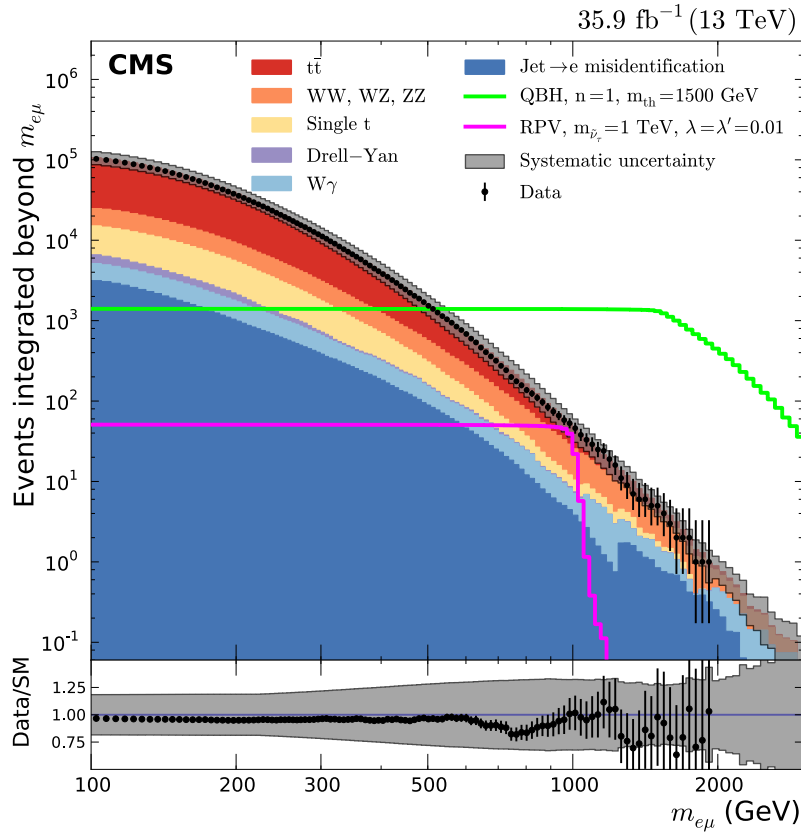


Figure 68: Cumulative invariant mass distribution of all selected $e\mu$ pairs. For each bin the number of events above this bin is integrated. The ratio shows clearly that there is an agreement between data and background expectation at high invariant masses, which is not so clearly visible in the non-cumulative mass distribution in Fig. 64.

The $e\mu$ channel is split into four η categories to enhance the sensitivity (see Sec. 4.3.2). The corresponding invariant mass distributions for each category are shown in Figs. 69, 70, 71 and 72. The corresponding comparisons between the pre-fit and post-fit distributions for all four categories are shown in the appendix in Fig. 109.

The agreement between the background expectation and the observed data is very similar in all four event categories. The data agrees with the background within the systematic uncertainties in all categories over the whole mass range. The four distributions are then used as the input for the statistical interpretation as the final step of the analysis.

5.1.2 $e\tau_\mu$ channel

For the $e\tau_\mu$ channel the event pre-selection is described in Sec. 4.3.3, all events that pass these selection criteria and are corrected following Sec. 4.5 end up in the final invariant mass distribution if they pass the kinematic selection criteria of Sec. 4.6. The invariant mass distribution of these selected events is shown in Fig. 73. To compare the background expectation with the observed data the event yield ratio is also shown in the figure for the pre-fit and post-fit distributions.

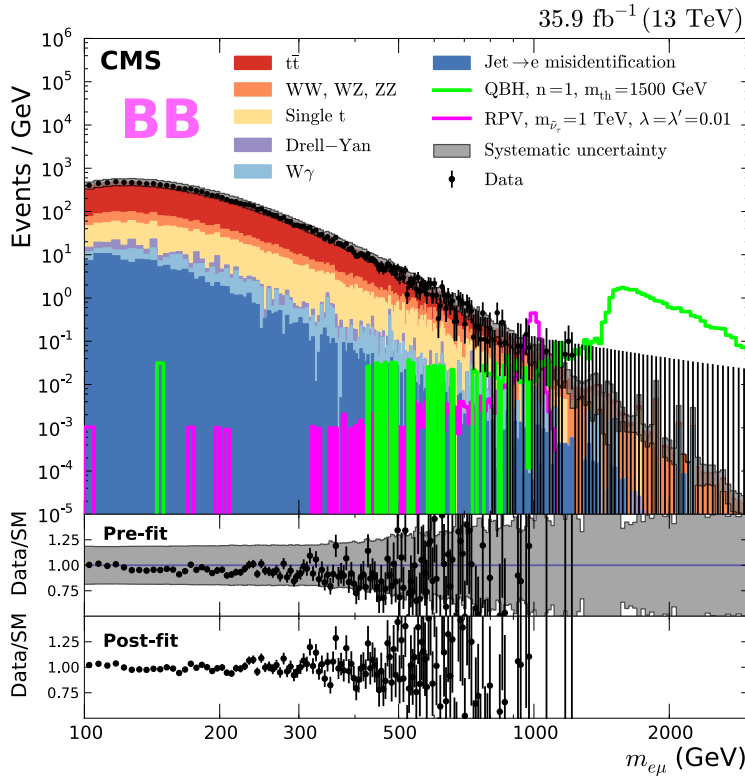


Figure 69: Invariant mass distribution of all selected $e\mu$ pairs in the analysis with both the electron and muon in the barrel. The binning is chosen according to the invariant mass resolution determined in Sec. 4.8. The ratio of the number of data to the number of background events is calculated from the shown pre-fit distributions and the post-fit one, which is the input to the statistical interpretation.

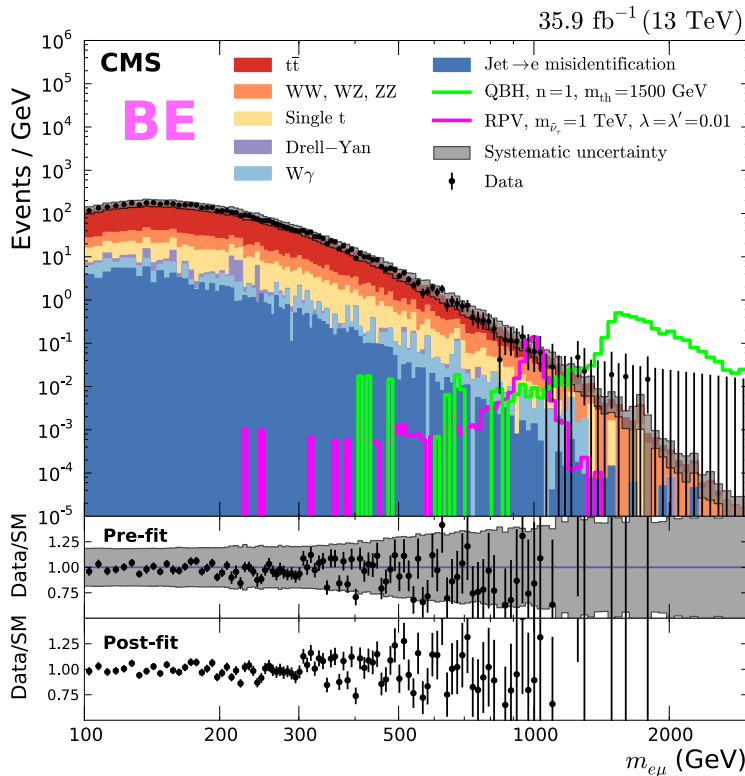


Figure 70: Invariant mass distribution of all selected $e\mu$ pairs in the analysis with the electron in the barrel and the muon in the endcap. The binning is chosen according to the invariant mass resolution determined in Sec. 4.8. The ratio of the number of data to the number of background events is calculated from the shown pre-fit distributions and the post-fit one, which is the input to the statistical interpretation.

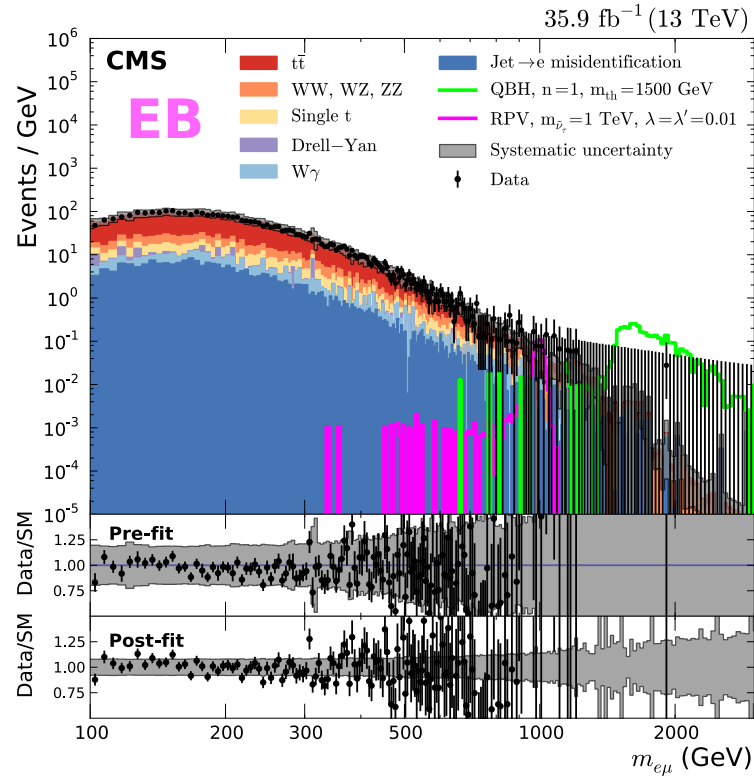


Figure 71: Invariant mass distribution of all selected $e\mu$ pairs in the analysis with the muon in the endcap and the muon in the barrel. The binning is chosen according to the invariant mass resolution determined in Sec. 4.8. The ratio of the number of data to the number of background events is calculated from the shown pre-fit distributions and the post-fit one, which is the input to the statistical interpretation.

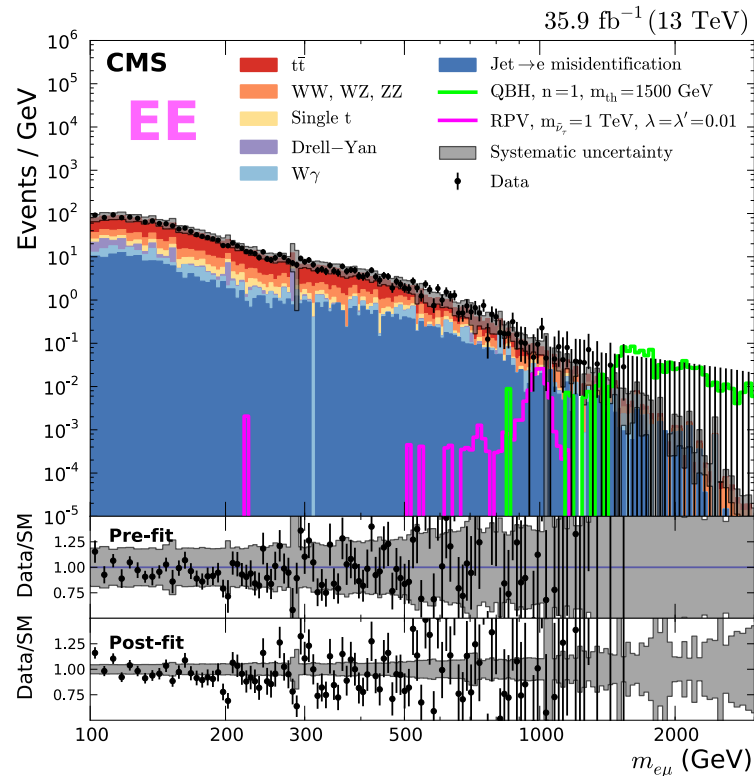


Figure 72: Invariant mass distribution of all selected $e\mu$ pairs in the analysis with both the electron and muon in the endcaps. The binning is chosen according to the invariant mass resolution determined in Sec. 4.8. The ratio of the number of data to the number of background events is calculated from the shown pre-fit distributions and the post-fit one, which is the input to the statistical interpretation.

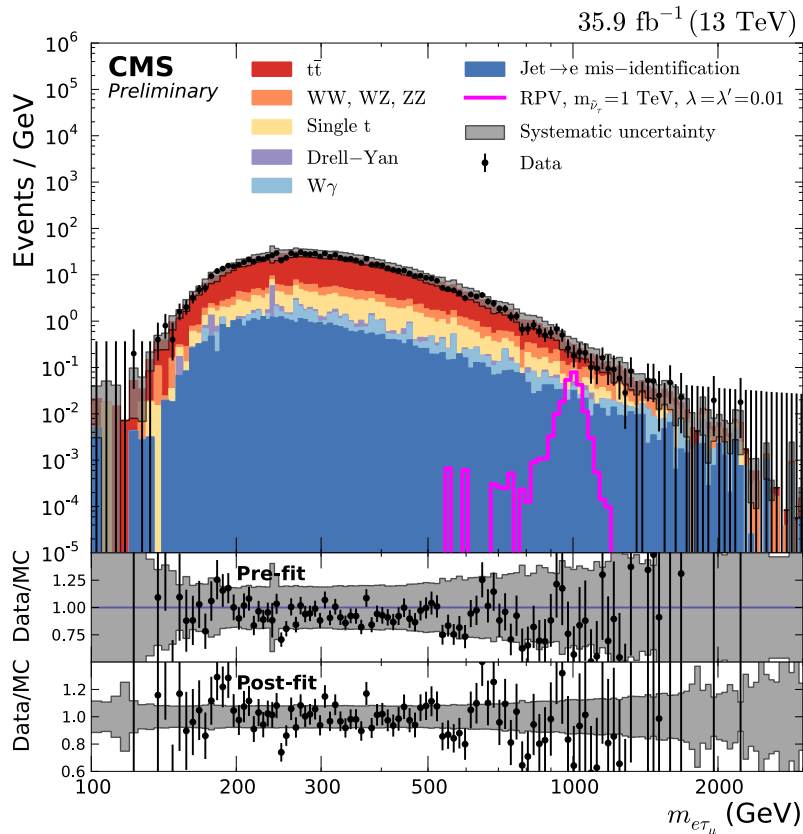


Figure 73: Invariant mass distribution of all selected $e\tau_\mu$ pairs in the analysis. The binning is chosen according to the invariant mass resolution determined in Sec. 4.8. The ratio of the number of data to the number of background events is calculated from the shown pre-fit distribution and the post-fit one, which is the input to the statistical interpretation.

A comparison of the pre-fit and post-fit distributions with its corresponding systematic uncertainty bands is shown in Fig. 74. The total systematic uncertainty is reduced by about a factor of four, while the data to Monte Carlo ratio gets closer to unity.

How this reduction of the systematic uncertainties is driven by the different sources of systematic uncertainties is illustrated in Fig. 75. The size of the uncertainty is shown relative to the pre-fit one for the background only fit as well as for the background plus signal fit. Overall, all uncertainties are reduced in the post-fit. The uncertainties which are not reduced are negligible, therefore the increase of these uncertainties is irrelevant for the overall reduction.

To compare the background expectation with the observed data in a quantitative way, Tab. 8 gives a comparison of event numbers. The number of observed events and the number of expected background events with its corresponding statistical and systematic uncertainties are given in four bins of invariant mass.

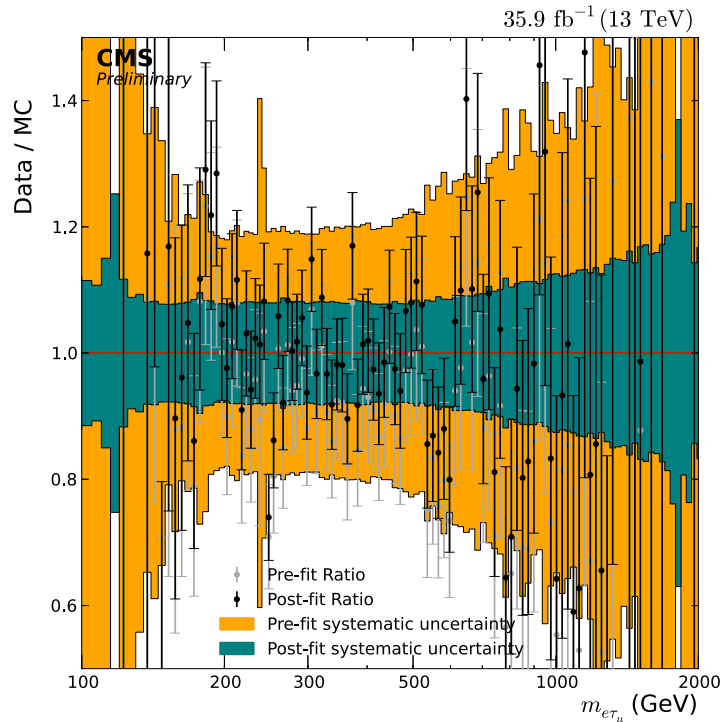


Figure 74: Comparison of the pre-fit and post-fit ratios of the invariant mass distribution shown in Fig. 73. The pre-fit ratio in grey with the corresponding systematic uncertainty in orange, as well as the post-fit ratio in black with its systematic uncertainty in green. The systematic uncertainties are reduced by a factor of four in the post-fit, while the ratio gets closer to unity.

The cumulative mass distribution, shown in Fig. 76, shows the comparison of background expectation to observed data integrated above the mass threshold for each bin. This allows for a better comparison of data and background expectation at high masses, where small event numbers result in big statistical fluctuations, leading to a difficult comparison in the differential distribution (Fig. 73).

Table 8: Number of expected and observed events for different bins of invariant mass. Also the statistical and systematic uncertainties on the number of background events are given.

Mass range (GeV)	Observed events	Expected events \pm (stat.) \pm (sys.)
$m_{e\tau} < 500$	6188	$6620 \pm 30 \pm 1240$
$500 < m_{e\tau} < 1000$	1092	$1210 \pm 10 \pm 31$
$1000 < m_{e\tau} < 1500$	43	$58.4 \pm 1.9 \pm 19.5$
$1500 < m_{e\tau}$	6	$9.3 \pm 0.68 \pm 3.00$

The highest observed mass event in the 2016 data taking is shown in Fig. 77. It has an invariant mass of $2206 \pm 18 \text{ GeV}^2$, calculated as described in Sec. 4.2.3.

² The uncertainty of the invariant mass measurement is derived from the uncertainty on the electron energy and muon p_T measurement.

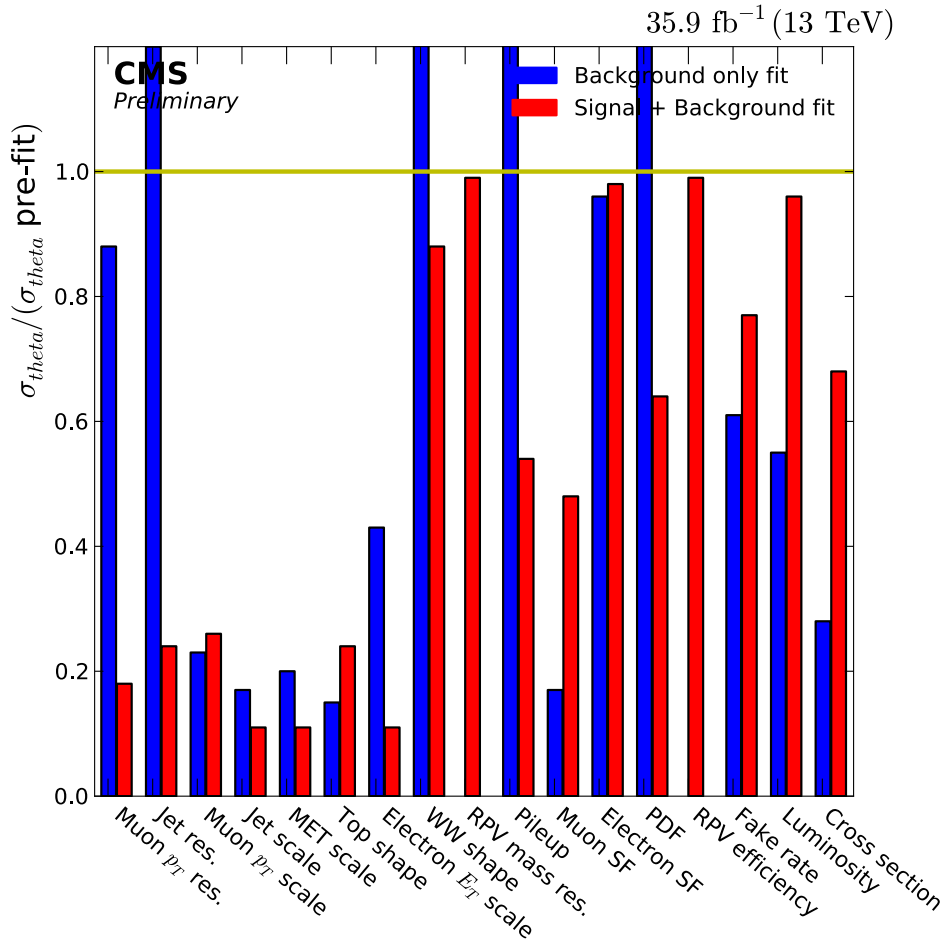


Figure 75: Size of the systematic uncertainties in the post-fit σ_θ , relative to the pre-fit ones (σ_θ pre-fit). Shown is the fit of the background only fit in blue, as well as the background plus signal fit (RPV $m_{\tilde{\nu}_\tau} = 1$ TeV, $\lambda_{331} = \lambda'_{311} = 0.01$) in red. In the post-fit most uncertainties are reduced, even more pronounced in the background only fit. For the uncertainties that are only applied on the signal expectation only the background+signal fit result is shown, as it is not constraint in the background only fit.

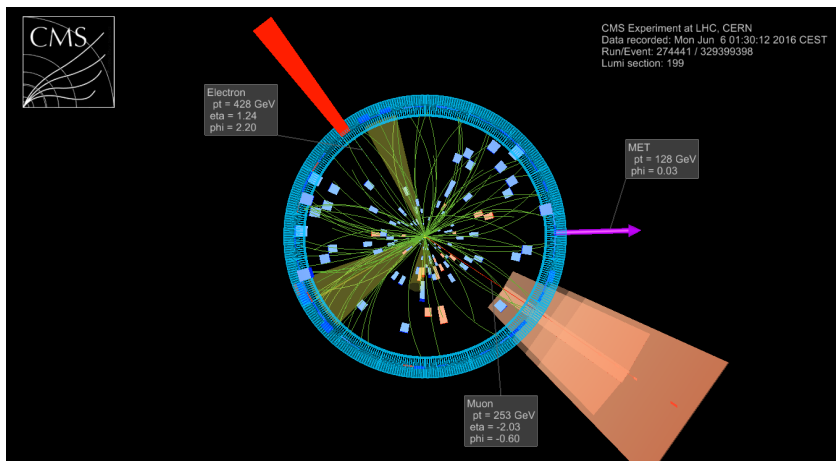


Figure 77: Event visualization of the event with the highest invariant mass of 2206 ± 18 GeV in the $e\tau_\mu$ channel, that was recorded in 2016. Visible is the muon in red, with the corresponding hits in the muon chambers in orange, as well as the energy deposit in the ECAL in red from the electron. The E_T^{miss} is illustrated by the pink arrow.

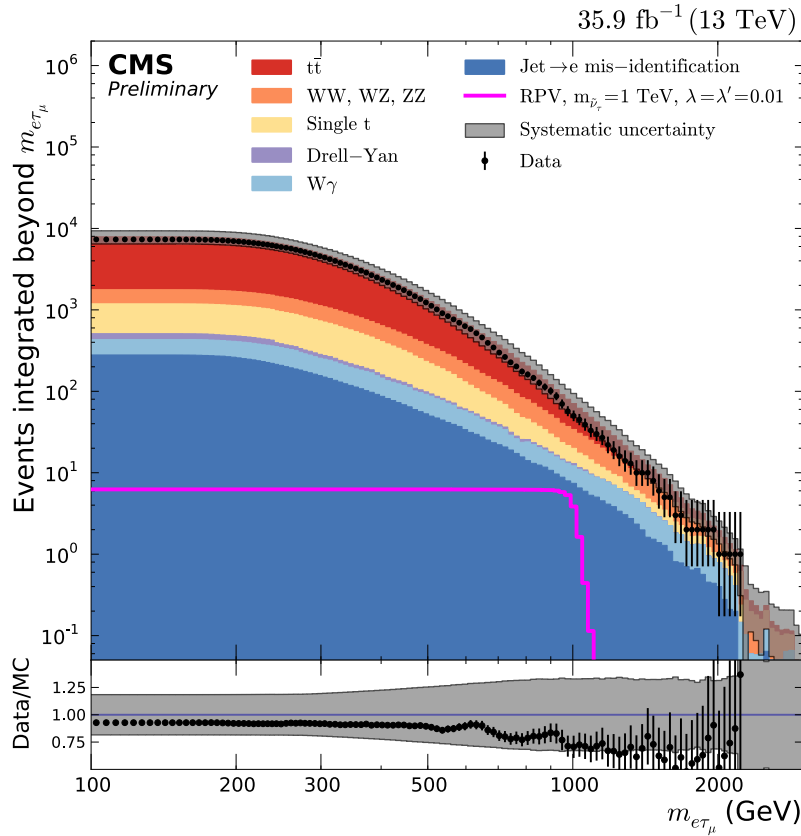


Figure 76: Cumulative invariant mass distribution of all selected $e\tau_\mu$ pairs. For each bin the number of events above this bin is integrated. The ratio shows clearly that there is an agreement between data and background expectation in the shape of the distribution, but the normalization is off. This can also be seen in Fig. 73, as well as that the normalization agreement improves significantly in the post-fit.

All these different distributions lead to the conclusion that the background expectation describes the observed data well in shape within the systematic uncertainties over the whole mass range. The differential invariant mass distribution is then the input for the final step of the analysis, the statistical interpretation.

5.1.3 $\mu\tau_e$ channel

Also in the $\mu\tau_e$ channel all events have to pass the pre-selection introduced in Sec. 4.3.3. The selected events are then corrected for the various known effects that differ between data and simulation (Sec. 4.5), and if they pass the kinematic selection defined in Sec. 4.6 they end up in the final invariant mass distribution. This final distribution is shown in Fig. 78 including two ratios to compare the background expectation to the observed data.

The two ratios are calculated for the pre-fit as well as for the post-fit distribution. To compare the effect of the post-fit distribution in more detail, both ratios are plotted on top of each other in Fig. 79. The systematic uncertainties are reduced by a factor of four in the post-fit, while the ratio gets closer to unity. How the reduction of systematic uncertainties spreads over the different sources of uncertainty is shown in Fig. 80.

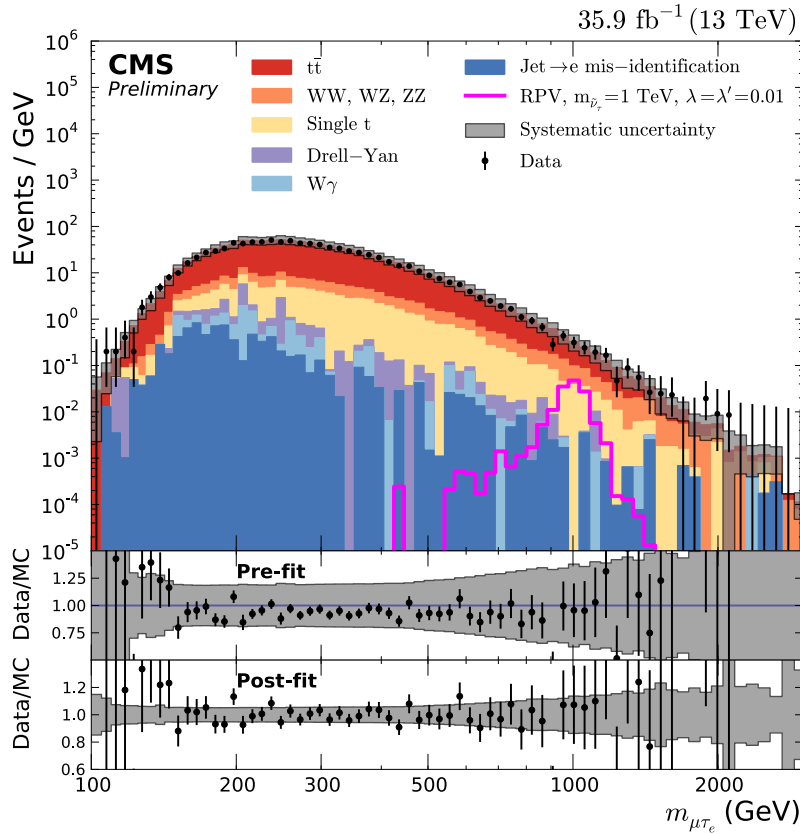


Figure 78: Invariant mass distribution of all selected $\mu\tau_e$ pairs in the analysis. The binning is chosen according to the invariant mass resolution determined in Sec. 4.8. The ratio of the number of data to the number of background events is calculated from the shown pre-fit distribution and the post-fit one, which is the input to the statistical interpretation.

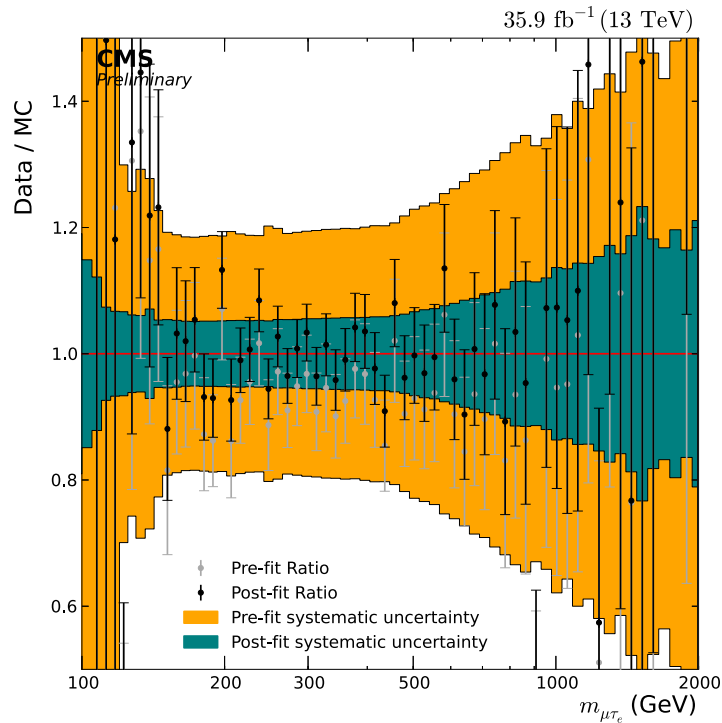


Figure 79: Comparison of the pre-fit and post-fit ratios of the invariant mass distribution shown in Fig. 78. The pre-fit ratio in grey with the corresponding systematic uncertainty in orange, as well as the post-fit ratio in black with its systematic uncertainty in green. The systematic uncertainties are reduced by a factor four in the post-fit, while the ratio gets closer to unity.

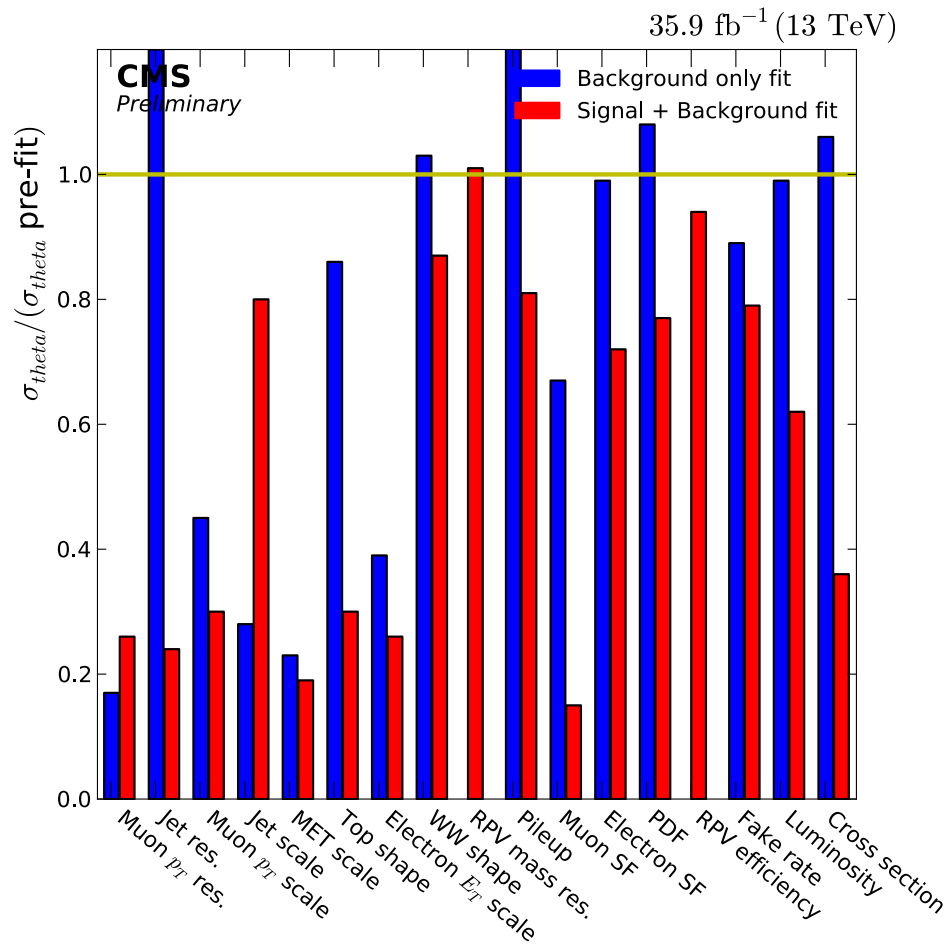


Figure 80: Size of the systematic uncertainties in the post-fit σ_θ , relative to the pre-fit ones (σ_θ pre-fit). Shown is the fit of the background only fit in blue, as well as the background plus signal fit (RPV $m_{\tilde{\nu}_\tau} = 1$ TeV, $\lambda_{332} = \lambda'_{311} = 0.01$) in red. In the post-fit most uncertainties are reduced, even more pronounced in the signal plus background fit. For the uncertainties that are only applied on the signal expectation only the background+signal fit result is shown, as it is not constraint in the background only fit.

Most uncertainties are reduced in the post-fit, even more in the signal plus background fit. Some exceptions, where the uncertainty gets inflated, are for sub-dominant uncertainties, resulting still in a reduction of the total systematic uncertainty, shown in Fig. 79.

To compare the background expectation with the observed data in a quantitative way, the number of events is compared in Tab. 9. The number of observed events in four invariant mass bins is given there. For the comparison in the same bins the number of expected background events with its corresponding statistical and systematic uncertainties is given. Within the uncertainties the data agree with the background expectation.

The event with the highest observed invariant mass in the $\mu\tau_e$ channel from 2016 is shown in Fig. 81. The invariant mass of the muon-tau pair is 2063 ± 69 GeV³.

³ The uncertainty of the invariant mass measurement is derived from the uncertainty on the electron energy and muon p_T measurement.

Table 9: Number of expected and observed events for different bins of invariant mass. Also the statistical and systematic uncertainties on the number of background events are given.

Mass range (GeV)	Observed events	Expected events \pm (stat.) \pm (sys.)
$m_{\mu\tau} < 500$	10311	$10970 \pm 50 \pm 2090$
$500 < m_{\mu\tau} < 1000$	1211	$1317 \pm 9 \pm 344$
$1000 < m_{\mu\tau} < 1500$	60	$56.6 \pm 1.6 \pm 21.4$
$1500 < m_{\mu\tau}$	7	$6.0 \pm 0.38 \pm 2.28$

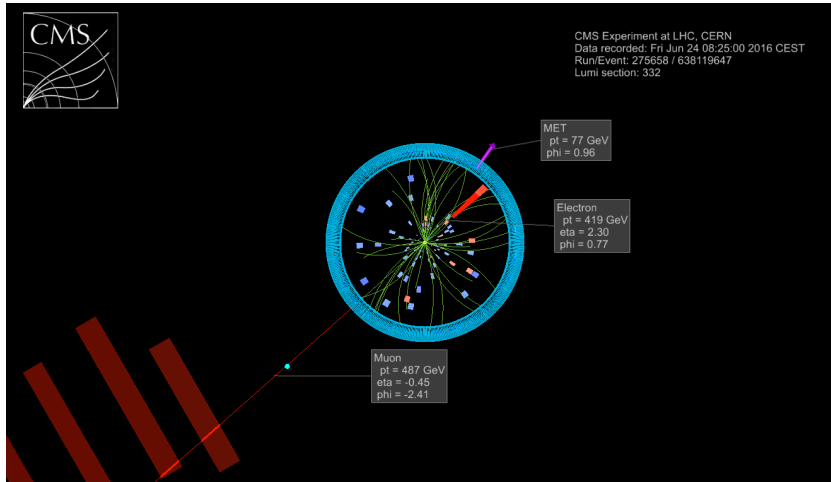


Figure 81: Event visualization of the event with the highest invariant mass in the $\mu\tau_e$ channel, that was recorded in 2016. Clearly visible is the muon in red, with the corresponding hits in the muon chambers, as well as the energy deposit in the ECAL in red from the electron in the background. E_T^{miss} is visualized by the pink arrow. The $\mu\tau_e$ pair has an invariant mass of 2063 ± 69 GeV, calculated as described in Sec. 4.2.3.

To have a good comparison of the background expectation with the observed data, the cumulative invariant mass distribution, shown in Fig. 82, is useful. For each bin in the distribution the number of events is integrated from the bin onwards. This allows for a comparison at high mass, where the distribution is dominated by statistical fluctuations.

All these distributions show that the background expectation describes the observed data over the whole mass range within the uncertainties.

5.2 STATISTICAL INTERPRETATION

The final step of the analysis is the statistical interpretation of the invariant mass distributions. The observed data agree with the background expectation within the systematic uncertainties. This general conclusion has to be quantified by the statistical interpretation. As a first step the agreement between the observed data and the background hypothesis is quantified with the p-value. Afterwards limits on the new physics models are set, as no signs for the models are seen in the data.

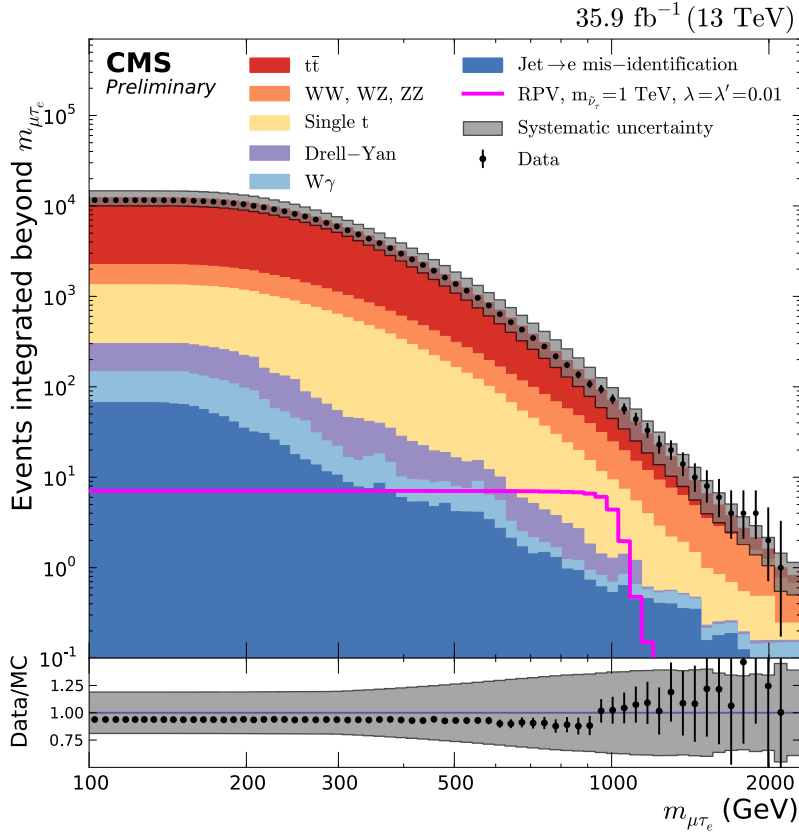


Figure 82: Cumulative invariant mass distribution of all selected $\mu\tau_e$ pairs. For each bin the number of events above this bin is integrated. The ratio shows clearly that there is an agreement between data and background expectation at high invariant masses, which is not so clearly visible in the differential mass distribution in Fig. 78.

The p-value is the probability to observe for the given background only model a deviation equal to or more extreme than observed in the data. For this approach the probability density distribution for the background model needs to be defined. Integrating then this distribution from the observed value until infinity results in the p-value for the given signal model.

The probability density function or test statistic is defined via the ratio of likelihoods in Eq. 24.

$$q_0 = -2 \ln \left(\frac{\mathcal{L}(\text{data} | r = 0, \hat{\theta}_0)}{\mathcal{L}(\text{data} | r = \hat{r}, \hat{\theta})} \right) \quad (24)$$

The ratio is the ratio of the same likelihood, in the nominator evaluated for the background only hypotheses (the signal normalization modifier is then $r = 0$) and the systematic uncertainties or nuisance parameters evaluated for the background only $\hat{\theta}_0$ fit. In the denominator the likelihood is evaluated for the best fit value of the signal expectation ($r = \hat{r}$) and the corresponding post-fit nuisance parameters.

The observed p-value distribution as a function of the mass parameter of interest for the $e\mu$ channel is shown in Fig. 83

The likelihood is defined as the product of individual likelihoods for each bin of the invariant mass distribution. These individual likelihoods are defined as:

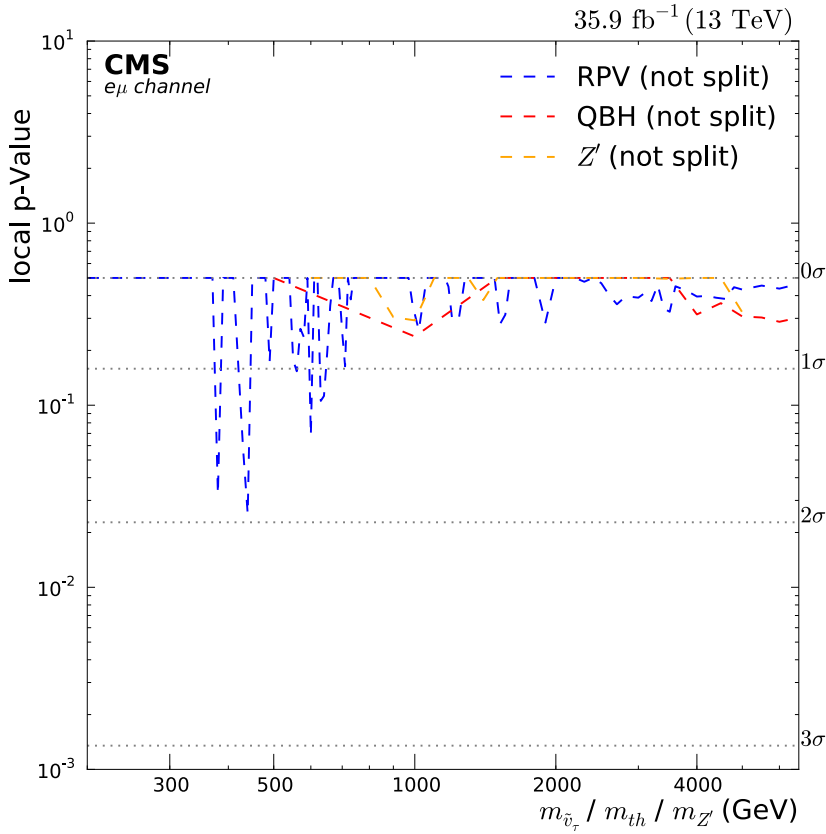


Figure 83: The distribution of the p-value is shown for the $e\mu$ channel. For the RPV SUSY model it is shown as a function of $m_{\tilde{\nu}_\tau}$, for the QBH model as a function of m_{t_h} and for the Z' model as a function of $m_{Z'}$. As a comparison the p-values for Gaussian sigmas are shown as dotted lines. The biggest deviations between observed data and background expectation and therefore smallest p-value are found in the RPV model for 350 GeV and 450 GeV. The deviations are all smaller than 2σ and therefore not significant.

$$\mathcal{L} = \frac{(r \cdot s(\theta) + b(\theta))^n}{n!} e^{-(r \cdot s(\theta) + b(\theta))} \cdot \prod_k C(\theta_k)$$

It is the product of first the Poisson distribution which is a function of the number of signal events s , the signal strength modifier r , the number of background events b and the number of observed events n . The second term is the constraint term to each nuisance parameter $C(\theta_k)$, which is either a Gaussian or a log-normal distribution. How the different nuisance parameters are treated in detail is explained in the limit setting procedure, later in this section.

The different signal models result in different p-values as can be seen in Fig. 83, the QBH signal resulting in the broadest distributions of the three models has the highest p-values for the whole mass range as only very wide fluctuations could result in a small p-value. A similar argument is true for the Z' model which is a wide resonance and therefore results only in big p-values. For the narrow resonance in the RPV SUSY model, statistical fluctuations in individual bins can result in small p-values. The smallest observed local p-values are still bigger than two Gaussian sigmas and therefore no indication of new physics. A comparison how the different $e\mu$ channel categories con-

tribute to observed p-values can be seen in Fig. 84. As the different deviations are in different bins for different event categories the cancel each other. Therefore, deviations in individual categories do not result in overall deviations, which would be the case if a signal would be present.

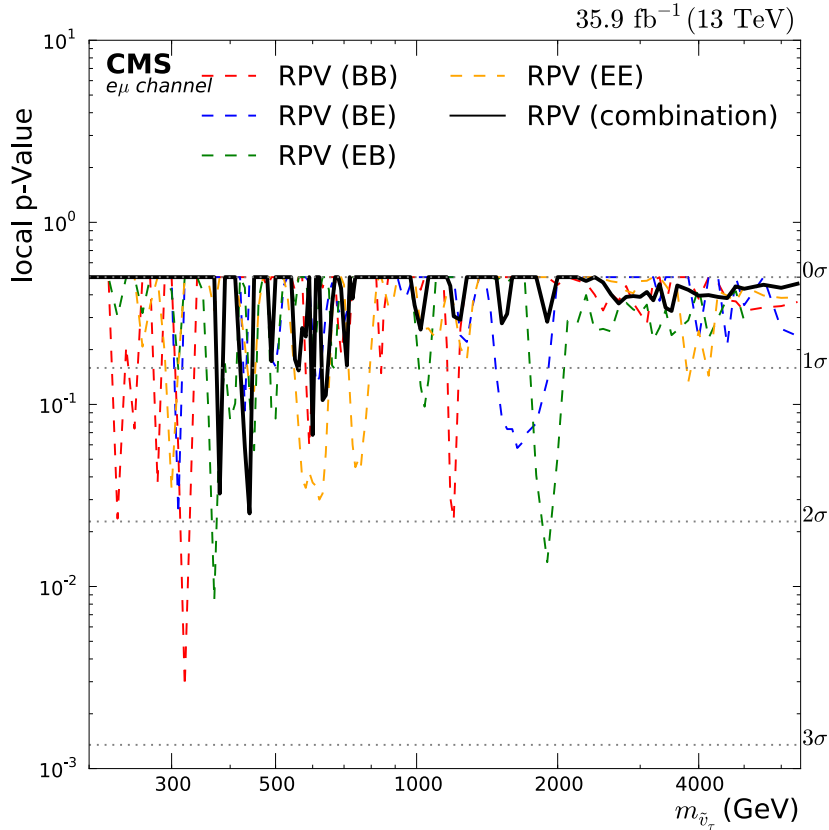


Figure 84: Distributions of p-values for the RPV SUSY model in the $e\mu$ channel for the different event categories and for the combination. Small p-values in some event categories do not add to each other as they are in different mass bins. Therefore, this is an indication for the assumption that no signal is present in the observed data.

In all these distributions the Look Elsewhere Effect has to be taken into account, which says that by looking into many possible models and mass hypotheses the probability for seeing a deviation increases linearly by the number of test regions [110]. To correct for that, the local p-value has to be modified by the trial factor which is proportional to the number of test regions. In the RPV model with its narrow resonance this results in a trial factor $\mathcal{O}(100)$ and reduces the significance of the p-values to close to zero.

The last shown p-value distribution, is for the RPV SUSY model in all three studied channels in Fig. 85. In the tau channels some smaller p-values are observed, but no significant deviations.

Combining the good agreement between the observed data with the background expectation in the invariant mass distributions and corresponding ratios with the p-value distributions leads to the conclusion that no new physics is found in the studied dataset. So the next step is to quantify the exclusion of the studied new physics models,

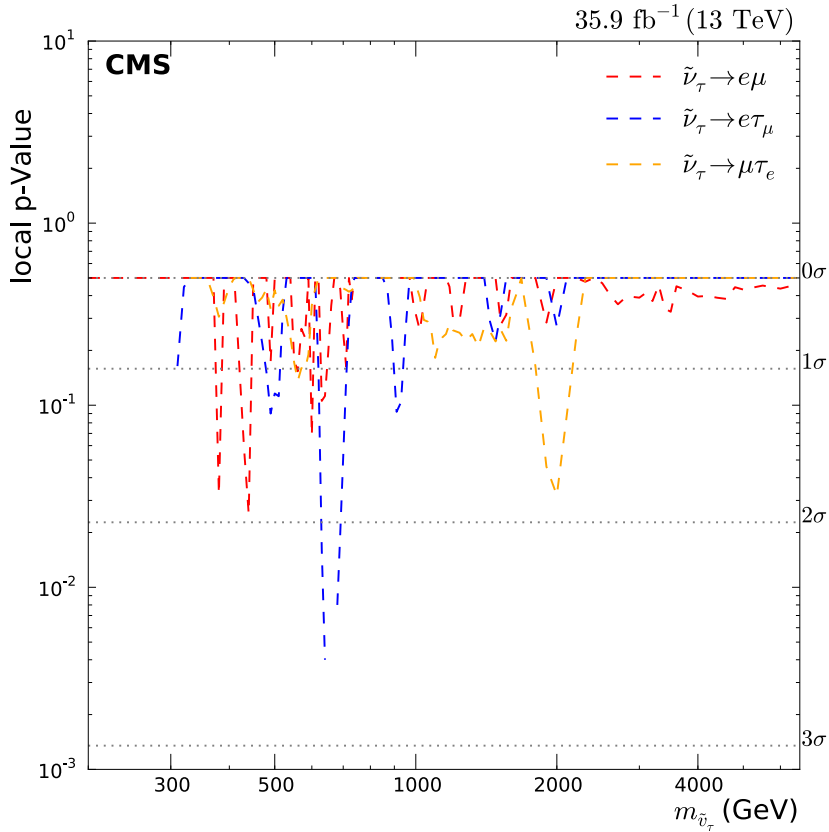


Figure 85: Distributions of p-values for the RPV SUSY model in the three studied channels. The biggest deviation is observed in the $e\tau_\mu$ channel, but at 2.5σ local significance it is no indication for a potential signal.

by setting limits on the allowed model parameter space. The procedure of setting these limits is explained in the next section, followed by the final limits.

5.3 LIMITS

The basic idea of the limit setting procedure is based on Bayes theorem, which can be formulated as follows:

$$P(\text{theory} | \text{data}) = \frac{P(\text{data} | \text{theory}) \cdot P(\text{theory})}{P(\text{data})} \propto P(\text{data} | \text{theory}) \cdot P(\text{theory}) \quad (25)$$

It describes the conditional probability for a theory being true under the condition of the data [4]. In Bayesian statistics, probabilities are interpreted as degrees of believe, therefore the probability of the theory under the assumption of the data can be interpreted as the degree of believing in the theory given the observed data. This quantity can then be used to derive the cross section limit by setting a limit on this probability. It depends on the probability of the data given the theory times the probability of the theory. This is the so called prior-probability of the theory, short: prior. The first term of the equation is the likelihood of the data under the assumption of the theory. The probability of the data in the denominator is not necessary for the calculation as all

probabilities need to be normalized and this constraint can be used to go from the nominator only probability to the full results.

The theory for the new physics model is quantified by the signal strength modifier

$$r = \frac{\sigma_r}{\sigma_{\text{theory}}} \quad (26)$$

which scales the cross section and therefore the normalization of the theory. The prior $\pi(r)$ and likelihood $L(n_{\text{obs}}|r)$ depend then on r , the likelihood also depends on the number of observed events n_{obs} as a representation of the observed data. Combining these constraints and Eq. 25 results in the basic equation for the limit setting, with the normalization constrained it results in a fully determined equation.

$$P(r|n_{\text{obs}}) = \frac{L(n_{\text{obs}}|r) \cdot \pi(r)}{C} = \frac{L(n_{\text{obs}}|r) \cdot \pi(r)}{\int L(n_{\text{obs}}|r') \cdot \pi(r') dr'} \quad (27)$$

The likelihood for observing n_{obs} events is given by the Poisson distribution and depends on the number of background events b , the number of signal events s and the signal strength modifier r :

$$L(n_{\text{obs}}|r) = \frac{(r \cdot s + b)^{n_{\text{obs}}}}{n_{\text{obs}}!} e^{-(r \cdot s + b)} \quad (28)$$

The prior incorporates the knowledge about the theory before the experiment. In the search for new physics there is no clear preference for specific values of r , the only constraint is that the cross section should be positive and therefore r should also be bigger than zero. To consider these ideas in this search a so called flat prior is used:

$$\pi(r) = \begin{cases} 0 & \text{for } r < 0 \\ 1 & \text{for } r \geq 0 \end{cases} \quad (29)$$

The next step is to calculate the 95 % confidence level upper limit r_{95} by integrating the probability of Eq. 27 from minus infinity until r_{95} , which is defined as the integral limit where the integral is equal to 0.95.

$$0.95 = \int_{-\infty}^{r_{95}} P(r|n_{\text{obs}}) dr = \frac{1}{C} \int_{-\infty}^{r_{95}} L(n_{\text{obs}}|r) \cdot \pi(r) dr \quad (30)$$

This procedure takes the statistical uncertainty of signal and expected background events⁴ into account via the Poisson distribution, but the systematic uncertainties are not yet considered. To take the systematic uncertainties into account additional nuisance parameters ν have to be included for each uncertainty. There are three different kinds of uncertainties which are taken into account. For each kind of uncertainty ν is added differently to the probability as defined in Eq. 27. The first kind of uncertainty are scaling uncertainties (like luminosity), the second one are shape uncertainties (like muon p_T resolution) and the third one are the statistical uncertainties of the Monte Carlo simulation. How they are added as nuisance parameters ν to the probability in Eq. 27 is explained in the following list:

⁴ This is the uncertainty on the number of weighted events. The uncertainty on the number of generated events due to limited Monte Carlo sample sizes is considered as a systematic uncertainty explained in detail in Sec. 4.9.

- For scaling uncertainties a multiplicative factor g is introduced with its uncertainty σ_g . These factors modify the probability in Eq. 27 by scaling the number of signal and background events with the factor g . An additional prior has to be included for the nuisance parameter g in Eq. 27. In principle a combined prior has to be constructed, but as all considered uncertainties are independent of each other, independent priors can be used that are multiplied with each other. For all scaling uncertainties a log-normal distribution is used as the prior. This probability distribution can be approximated by a Gaussian distribution for a big number of events but non-negative for a small number of events and therefore the ideal choice for scaling uncertainties, it is defined as:

$$P_{g,\sigma_g}(x) = \frac{1}{x\sqrt{2\pi}\sigma_g} e^{-\frac{(\ln x - g)^2}{2\sigma_g^2}} \quad (31)$$

- For shape uncertainties the central value of background or signal events in each bin x_0 is known, as well as the number of events shifted up and down by the uncertainty in this bin x_{\pm} . These three discrete values have to be transferred into a continuous probability density function to handle them like the other uncertainties. To do that a morphing parameter f is introduced with an accompanying Gaussian prior multiplied to Eq. 27 for f with a mean of zero and a width of one. The number of expected events is replaced by a function $x(f)$. For $|f| < 1$ the number of events $x(f)$ is extrapolated quadratically, for values of f outside the range it is extrapolated linearly. This results in a continuous distribution as a function of f :

$$x(f) = \begin{cases} \frac{f(f-1)}{2}x_- - (f-1)(f+1)x_0 + \frac{f(f+1)}{2}x_+ & \text{for } |f| < 1 \\ \frac{x_+ + x_-}{2} + f \cdot \frac{x_+ - x_-}{2} & \text{else} \end{cases} \quad (32)$$

The number of background and signal events in Eq. 27 is replaced by $x(f)$ and the additional Gaussian prior for f is multiplied with Eq. 27 for each shape uncertainty.

- For the limited Monte Carlo sample sizes, the detailed procedure, how this uncertainty is taken into account is described in Sec. 4.9.1. Depending on the size of the uncertainty the number of events n is modified by the uncertainty σ_n as $n \pm x \cdot \sigma_n$ with an additional Gaussian prior for x . The alternative is a Poisson prior for x with the number of events modified by just multiplying with x : $n \cdot x$. The additional prior is multiplied with the probability in Eq. 27.

The dependence on all the nuisance parameters $\nu = (g_1, \dots, g_n, f_1, \dots, f_m)$ can be eliminated by integrating over them:

$$P(r | n_{obs}) = \int P(r, \nu | n_{obs}) d\nu \quad (33)$$

The calculation of this integral over $\nu = (\nu_1, \dots, \nu_{i=n+m})$ in i dimensions is what takes most of the computing time of the whole limit setting process. To make this calculation even possible the Markov-Chain Monte Carlo (MCMC) method is used [111]. In this method a random walk is performed to evaluate a probability distribution

$P(x = (x_1, \dots, x_i))$ numerically, the calculation of the integral of this distribution is then no effort anymore. The MCMC algorithm starts from a random starting point x_0 and chooses another random point x_t . If $P(x_t)$ is smaller than $P(x_0)$, then x_t is the new starting point with the probability $P(x_t)/P(x_0)$. Otherwise x_0 stays the starting point for the next iteration. By this procedure the distribution $P(x)$ is sampled for enough MCMC steps, because points with high probability are sampled more often than points with a small one. Running this for a lot of steps and recording x of each step, it will converge towards $P(x)$.

The last step to the complete limit setting procedure is to include the information of the shape of the invariant mass distribution, the procedure up to now only includes the information of one single bin. This can be done by multiplying the likelihoods for each bin i in the invariant mass distribution, Eq. 30 is then modified to:

$$0.95 = \frac{1}{C} \int_{-\infty}^{r_{95}} \pi(r) \cdot \prod_{i \in \text{bins}} L(n_{\text{obs},i} | r) dr \quad (34)$$

This allows to take information from all bins in the invariant mass distributions and the shape of the signal is this way considered in the statistical interpretation.

This whole procedure gives the observed limit as one value for $r_{95}(\text{obs})$ for each possible signal hypothesis, which is the final result of the whole analysis. The other interesting quantity in this limit setting procedure is the expected limit, which is the cross section that could be excluded if no signal were present in the data. For this calculation the number of observed events is replaced by a random number of events according to the number of expected background events according to its uncertainties. The up and down shifted values x_{\pm} are also random numbers according to the probability distributions of the uncertainty. This then gives one value for $r_{95}(\text{exp})$, repeating that a few hundred times allows to calculate the median expected limit as well as 68% and 95% confidence bands. The comparison of the expected limit with the observed one shows if there are deviations in the observed data from the background expectation (null hypothesis).

To study the effect on the limits the impacts of the systematic uncertainties are calculated. For each nuisance parameter the effect of shifting the background expectation by $\pm 1\sigma$ is calculated while all other nuisance parameters are unchanged. This gives the impact of this nuisance parameter on the signal strength modifier for a fixed input strength of one. These impacts on the limit together with the post-fit systematic uncertainties allows to study the effect of the different sources of systematic uncertainties on the limit. The distributions of both quantities are shown for each channel in the following sections.

In the following sections the limits for all channels and the different models are presented.

5.3.1 $e\mu$ channel

In this section the resulting limits for the $e\mu$ channel are presented. The three different studied models are all used individually to calculate limits. The inputs used for the calculation are the invariant mass distributions for the four event categories, shown in Fig. 69, 70, 71 and 72. They are used in the limit calculation as four separate channels,

by multiplying the four likelihoods. The gain of splitting the invariant mass distribution into four η categories can be seen in Fig. 111 in the appendix for the Z' model. The cross section limit is improved by up to 30% due to the η windows compared to an inclusive analysis.

RPV SUSY The input for the limit calculation are the observed data and background invariant mass distributions. The signal hypotheses are dived from a Gaussian with the mean value of the probe mass and the width from the invariant mass resolution parameterization, shown in Fig. 46. The signal is then normalized to the signal cross section and the parametrized acceptance times efficiency as shown in Fig. 41. This allows to probe arbitrary signal masses and not only the ones simulated as a Monte Carlo sample. The impacts of the nuisance parameters on the limit for the RPV model are shown in Fig. 86.

The impact distribution shows how the systematic uncertainties actually influence the final limit. The dominant uncertainty over the whole mass range is the uncertainty on the acceptance times efficiency of the signal. This uncertainty is nearly independent on the signal mass and scales the final limit according to its uncertainty values, shown in Fig. 41 as an uncertainty band. The uncertainty on the mass resolution becomes important at higher signal masses, in contrast to the other dominant uncertainties it always worsens the limit. The mass resolution can fluctuate within its uncertainties, but the worst resolution value, still possible within the uncertainties, will dominate the limit setting. When the mass resolution becomes smaller the uncertainty will be increased in the post-fit to accommodate this shift of the mean value. This increased uncertainty leads to a worse limit, even if the mean mass resolution becomes smaller. This can also be seen in the post-fit pulls, the uncertainty values are reduced in the post fit for the mean of the mass resolution, but the mean of the uncertainty is unchanged. This is due to the fact that the worst resolution value will always dominate the limit setting, so even when the uncertainty gets smaller it will still worsen the limit. This can also be seen in the post-fit pulls, the values are reduced in the post-fit, but asymmetrically and less for higher masses, where the effect becomes bigger. Similarly the impacts increase with the signal mass.

Luminosity and muon scale factor just scale the background expectation and therefore either worsen or improve the limit accordingly. More interesting is the effect of the WW background shape uncertainty. It is negligible at low signal mass, but becomes increasingly important at high masses. In contrast the shape uncertainty on the dominant $t\bar{t}$ background contribution has a small impact on the final limit for the whole mass range. The $t\bar{t}$ background is dominant at low invariant masses, therefore this uncertainty can always be reduced in the post-fit in this mass range. This can be seen by the small uncertainty values in the post-fit pulls. For the WW background, which is important only at high invariant masses, this is not possible, resulting in only a marginal reduction of the uncertainty in the post-fit. As the contribution of this background process and therefore also its uncertainty becomes more important at high masses, the influence of this uncertainty at higher signal mass increases. All other systematic uncertainties play only a very minor role for the limit and do not have a clear pattern.

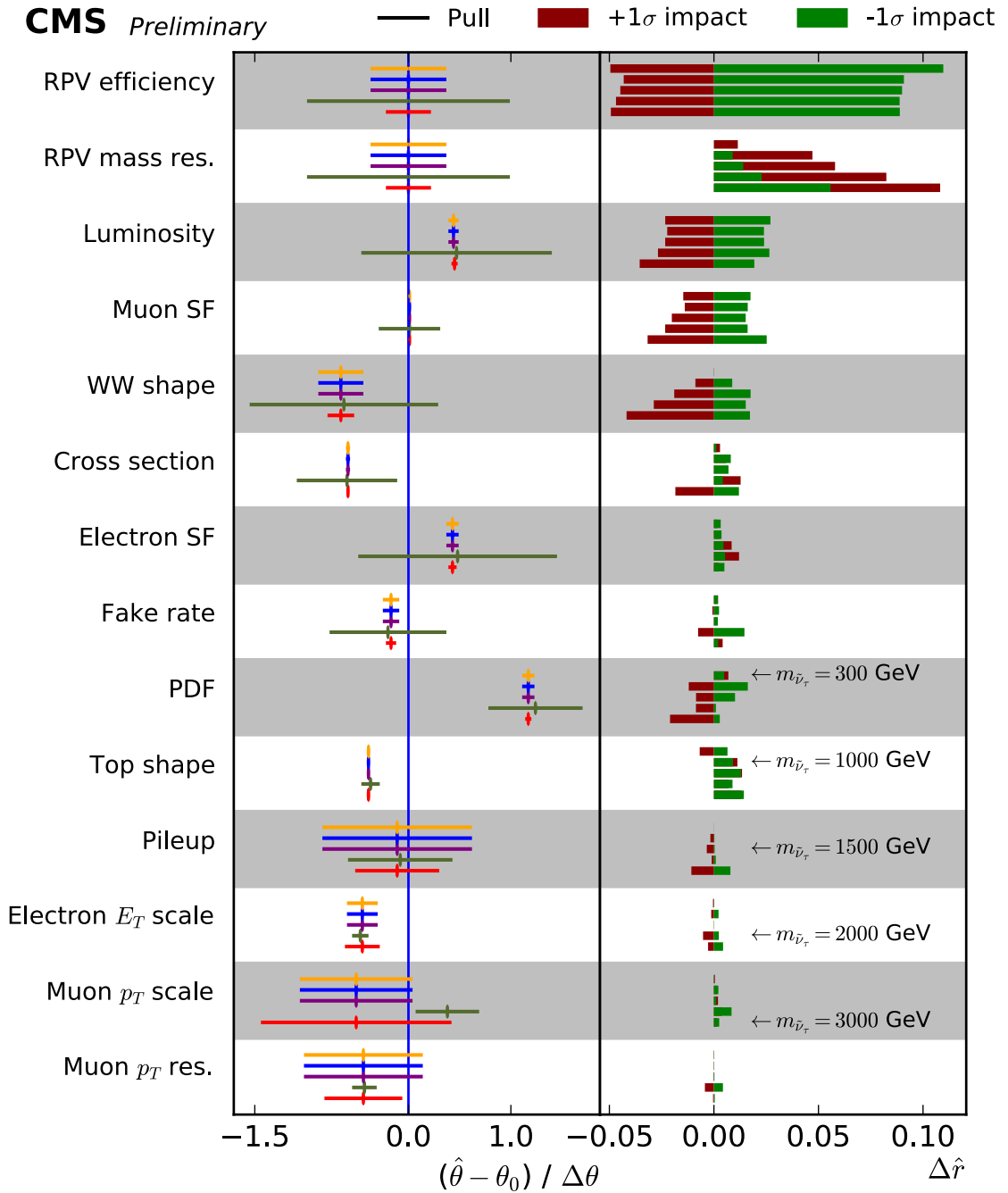


Figure 86: Impact of the nuisance parameters on the RPV limit in the $e\mu$ channel for $\lambda_{132} = \lambda_{231} = \lambda'_{311} = 0.01$. Each line represents one systematic uncertainty, as introduced in Sec. 4.9. In the left column the size as well as the mean of the post-fit uncertainty relative to the pre-fit one is shown as a reference. The right column shows the impact of the $\pm 1\sigma$ variations on the signal strength modifier. To show the effect of the resonance mass on the impacts, each nuisance parameter line is shown for five different $m_{\tilde{\nu}_\tau}$, from 300 GeV to 3 TeV.

The limit on the RPV model in the $e\mu$ channel is then calculated from the four event categories and including all systematic uncertainties. The resulting limit on the signal strength modifier r can be transformed into a limit on the model cross section

by multiplying r with the theory cross section. This cross section limit is shown in Fig. 87. The general shape of the limit is shaped by the acceptance times efficiency and the background distribution. For medium masses the number of background events dominates the decrease of the cross section limit. For very low masses the reduction of the cross section limit is due to the reduced acceptance times efficiency. At high masses the acceptance times efficiency stays constant while there are no background events anymore. This results in the flat limit for high masses. In general the observed limit follows the shape of the expected limit. For some mass points the observed data slightly deviates from the background expectation. This difference was already seen in the p-value distribution in Fig. 83, but all deviations stay within the two sigma bands of the expected limit.

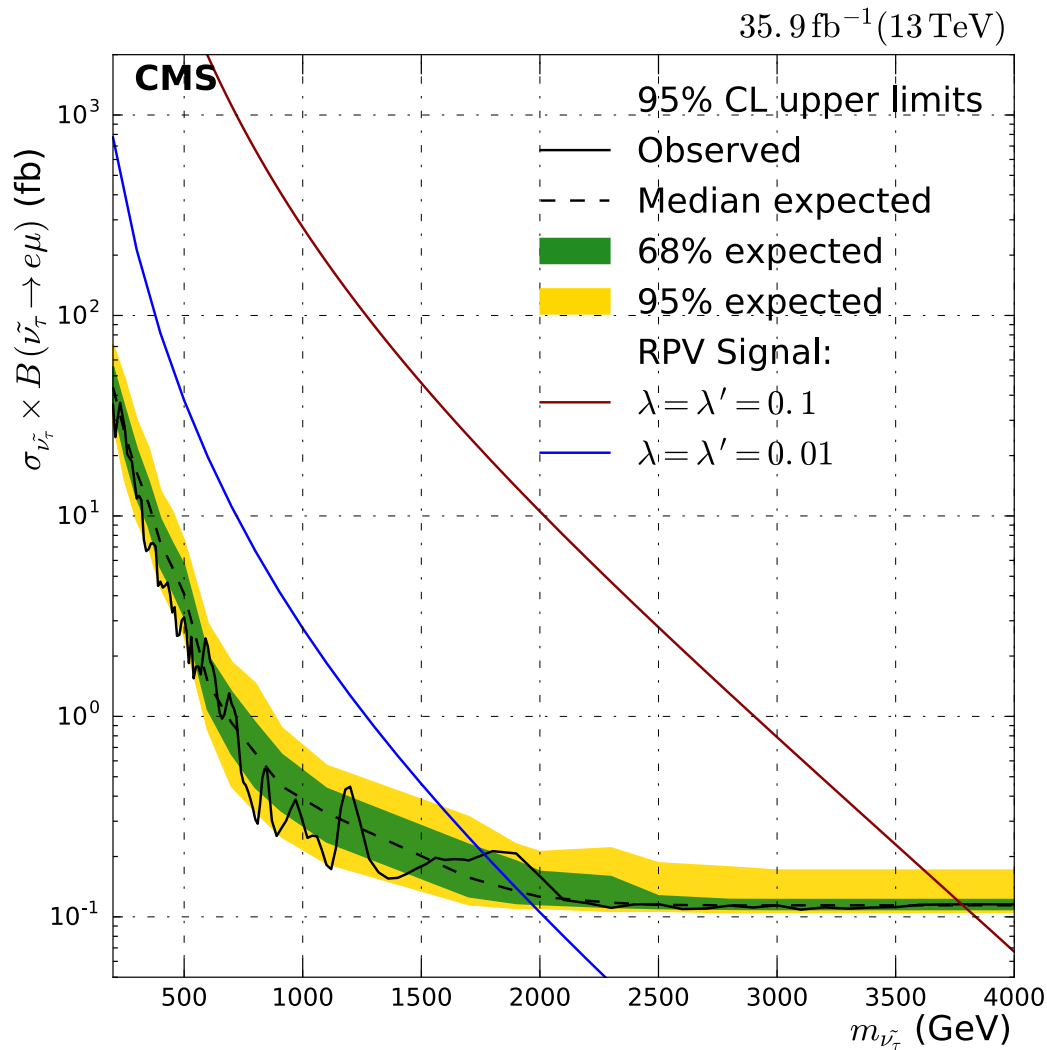


Figure 87: Limit on the RPV SUSY model cross section of the $e\mu$ channel at 95% confidence level. Shown is the observed limit as a black line, the median expected limit as a dashed black line. The 68% and 95% uncertainty intervals of the expected limits are shown as green and yellow bands respectively. For two example coupling values the cross sections of the RPV model are shown. If the excluded cross section intersects with the theory cross section, smaller $m_{\tilde{\nu}_\tau}$ are excluded.

Comparing the excluded cross section with the theory cross section allows to derive a mass exclusion for a given coupling value. For any given mass value, where the excluded cross section is smaller than the theory one, this mass is excluded. For a coupling of $\lambda_{132} = \lambda_{231} = \lambda'_{311} = 0.01$ an expected mass limit of $m_{\tilde{\nu}_\tau} > 1.9$ TeV with an observed mass limit of $m_{\tilde{\nu}_\tau} > 1.8$ TeV can be derived. For $\lambda_{132} = \lambda_{231} = \lambda'_{311} = 0.1$ the expected mass limit is at $m_{\tilde{\nu}_\tau} > 3.7$ TeV, while the observed one is also at $m_{\tilde{\nu}_\tau} > 3.7$ TeV.

How the different event categories contribute to the final combined limit is illustrated in Fig. 88. Shown are the individual expected and observed limits for all four event categories as well as the combination.

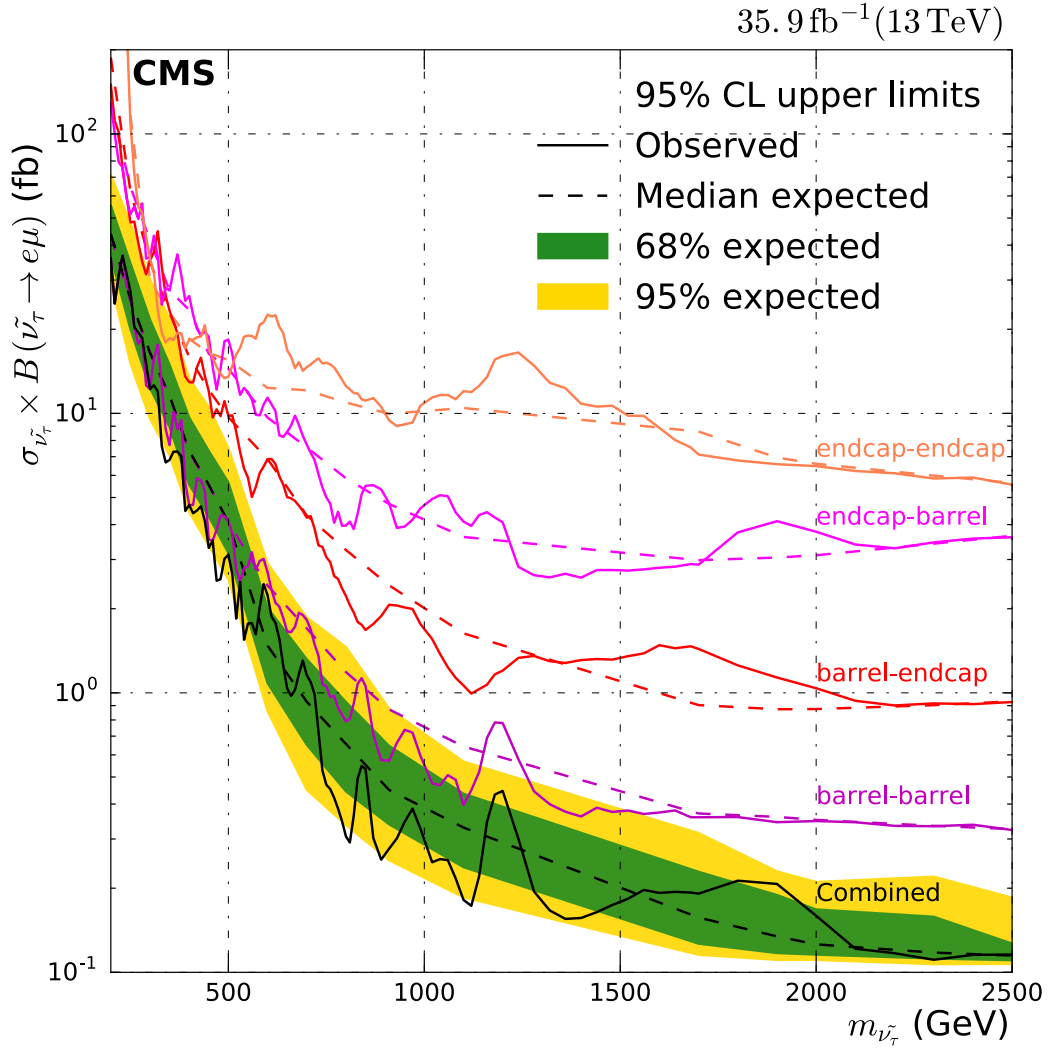


Figure 88: Limit on the RPV SUSY model cross section of the $e\mu$ channel at 95% confidence level. Shown is the same limit as in Fig. 87, including the observed and expected limits as well as the uncertainty bands. Also shown are the expected limit for all four event categories in the $e\mu$ channel as dashed lines and the observed limit of each category as solid lines. Over most of the mass region the combined limit is dominated by the barrel-barrel category.

Over most of the mass range the combined limit is dominated by the barrel-barrel category due to the high efficiency and good mass resolution, at high masses all the

different categories contribute to the combined limit. At low masses the limits of all the categories are very close and contribute therefore equally to the combined limit.

The cross section limit in Fig. 87 is valid for any signal with the same signal shape and acceptance as the RPV signal with $\lambda_{132} = \lambda_{231} = \lambda'_{311} = 0.01$, which is assumed in the limit. This is a great advantage of this analysis that due to the limited selection criteria the result could be used for other models as well. For all RPV coupling values, not yet excluded by direct searches, the intrinsic width $\Gamma_{\tilde{\nu}_\tau}$ can be neglected compared to the detector resolution and therefore the signal shape as well as the efficiency are identical for the different coupling values. This allows that the observed excluded cross section $\sigma \cdot \text{BR}_{\text{obs}}^{\text{excl}}(m_{\tilde{\nu}_\tau})$ shown in Fig. 87 can be used to derive the limit contour in the $m_{\tilde{\nu}_\tau}$ - λ'_{311} parameter plane as a function of a given fixed value $\lambda_{132}^{\text{fix}}$. In the narrow-width approximation, the cross section scales with the RPV couplings as (see Equation 2):

$$\sigma \cdot \text{BR}(\tilde{\nu}_\tau \rightarrow e^\pm \mu^\mp) = k(m_{\tilde{\nu}_\tau}) \cdot \frac{(\lambda'_{311})^2 \left((\lambda_{132}^{\text{fix}})^2 + (\lambda_{231}^{\text{fix}})^2 \right)}{3(\lambda'_{311})^2 + \left((\lambda_{132}^{\text{fix}})^2 + (\lambda_{231}^{\text{fix}})^2 \right)} \quad (35)$$

with a mass dependent constant $k(m_{\tilde{\nu}_\tau})$. From Eq. 35 follows for $\lambda'_{311} \ll \lambda_{132} = \lambda_{231}$, that the signal cross section becomes independent of $\lambda_{132} = \lambda_{231}$. For $\lambda'_{311} \gg \lambda_{132} = \lambda_{231}$ it reaches the maximal value

$$\sigma_{\text{max}}(m_{\tilde{\nu}_\tau}, (\lambda_{132}^{\text{fix}})^2 + (\lambda_{231}^{\text{fix}})^2) = k(m_{\tilde{\nu}_\tau}) \cdot \frac{2}{3} (\lambda_{132}^{\text{fix}})^2$$

If this maximal cross section is not excluded for a given parameter pair $(m_{\tilde{\nu}_\tau}, \lambda_{132} = \lambda_{231})$, then no limit can be set on the coupling λ'_{311} . Otherwise, the limit on the coupling λ'_{311} is given by Equation 36.

$$\lambda'_{311}{}^{\text{limit}}(m_{\tilde{\nu}_\tau}, (\lambda_{132}^{\text{fix}})^2 + (\lambda_{231}^{\text{fix}})^2) = \sqrt{\frac{((\lambda_{132}^{\text{fix}})^2 + (\lambda_{231}^{\text{fix}})^2)}{\frac{k(m_{\tilde{\nu}_\tau})}{\sigma \cdot \text{BR}_{\text{obs}}^{\text{excl}}(m_{\tilde{\nu}_\tau})} \cdot ((\lambda_{132}^{\text{fix}})^2 + (\lambda_{231}^{\text{fix}})^2) - 3}} \quad (36)$$

Limit contours for the RPV signal are shown in Fig. 89.

The excluded parameter space in the $m_{\tilde{\nu}_\tau}$ - λ'_{311} plane for different given $\lambda_{132} = \lambda_{231}$ values is shown. For small $m_{\tilde{\nu}_\tau}$ the exclusion is independent of $\lambda_{132} = \lambda_{231}$, while for higher masses the excluded region expands with bigger values of $\lambda_{132} = \lambda_{231}$. This difference is mainly due to the increased branching ratio for higher values of $\lambda_{132} = \lambda_{231}$, while at lower masses the dependence of $\lambda_{132} = \lambda_{231}$ vanishes, resulting in the same exclusion for all $\lambda_{132} = \lambda_{231}$ values.

These results can now be compared to previous searches for RPV SUSY. As introduced in Sec. 2.2.4 low energy experiments can set a limit on the product of the two couplings for $m_{\tilde{\nu}_\tau} = 100 \text{ GeV}$ of $|\lambda'_{311} \cdot \lambda_{312}| < 4.1 \cdot 10^{-9}$ [5, 25]. As can be read off from Fig. 89 the limit on both couplings is for the most stringent case at low masses in the order of $\lambda = \lambda' = \mathcal{O}(10^{-3})$, therefore the product of the two couplings is still three orders of magnitude away from the limit, set by low energy experiments. This comparison holds for one given mass hypothesis of $m_{\tilde{\nu}_\tau} = 100 \text{ GeV}$, for the other probed masses the resulting limits can not be compared to the low energy result.

A comparison with direct searches at colliders is more straight forward as the analysis principle is similar. The most stringent limits are from the 2015 data taking period

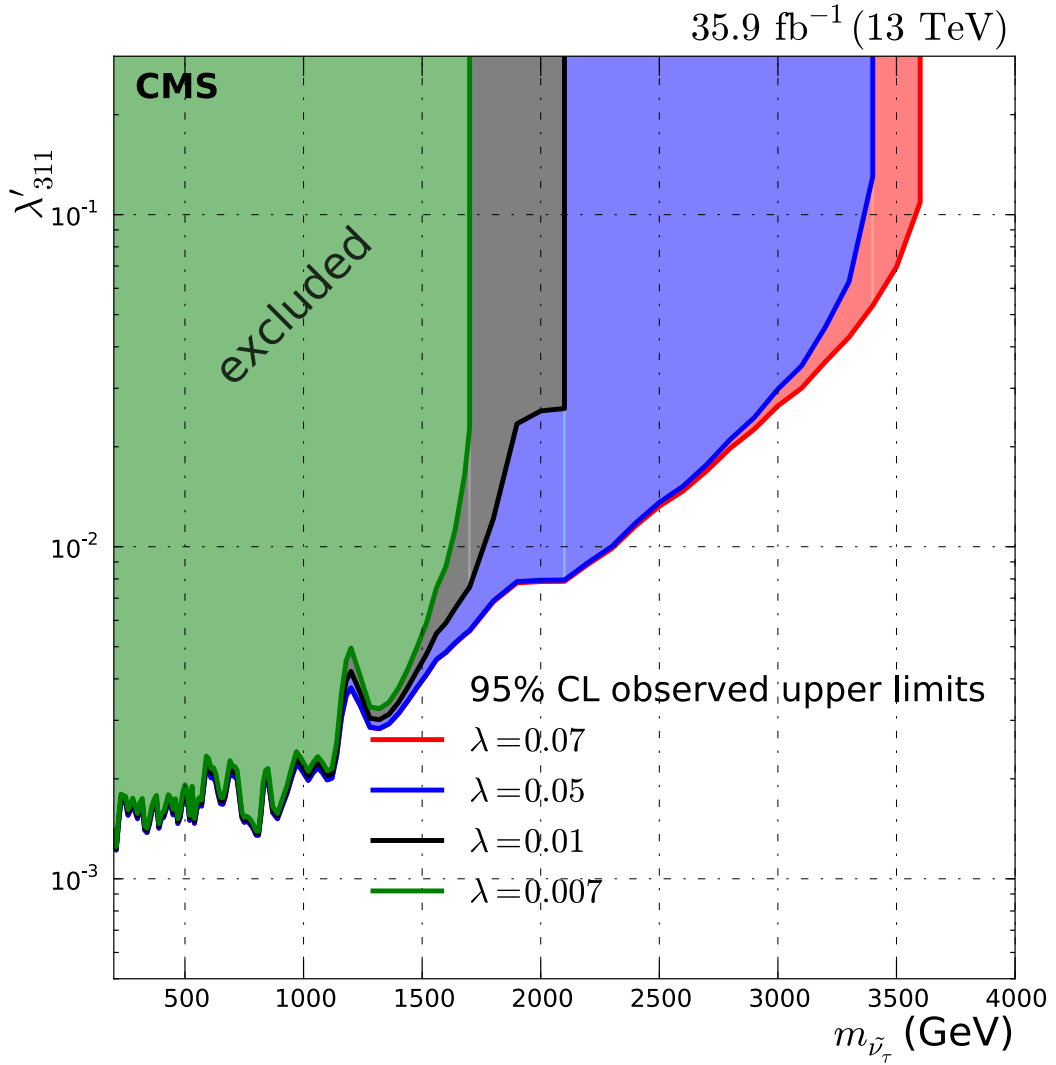


Figure 89: 95% confidence level observed limit contour for the RPV signal in the $m_{\tilde{\nu}_\tau}$ - λ'_{311} parameter space. The values of the other coupling $\lambda_{132} = \lambda_{231}$ are fixed to 0.07, 0.05, 0.01 and 0.007. The parameter space top left of the observed limit is excluded.

at the LHC at 13 TeV, they yield a limit on $m_{\tilde{\nu}_\tau}$ of about 1.0 TeV for couplings of 0.01 and 2.7 TeV for couplings of 0.1 [1, 31]. This analysis can improve the limits to 1.7 TeV for couplings of 0.01, and to 3.7 TeV for couplings of 0.1, this is therefore at the moment the most restrictive limits set on this model in direct searches.

QBH For the QBH model, the signal shape is taken directly from Monte Carlo simulation, as the shape cannot be easily described by one analytical function for the whole mass range as the Gaussian for the RPV model. Another reason is that due to the wide signal in the invariant mass distribution a fine scanning of the signal mass is not necessary, while for the narrow resonance in the RPV model this feature is crucial.

The first step is, like for the RPV model, to look at the impact distribution for the different nuisance parameters in the statistical interpretation of the QBH model. The distribution is shown in Fig. 90. It shows the post-fit systematic uncertainties as well

as the impacts on the limit on the signal strength modifier for all nuisance parameters for five different threshold masses.

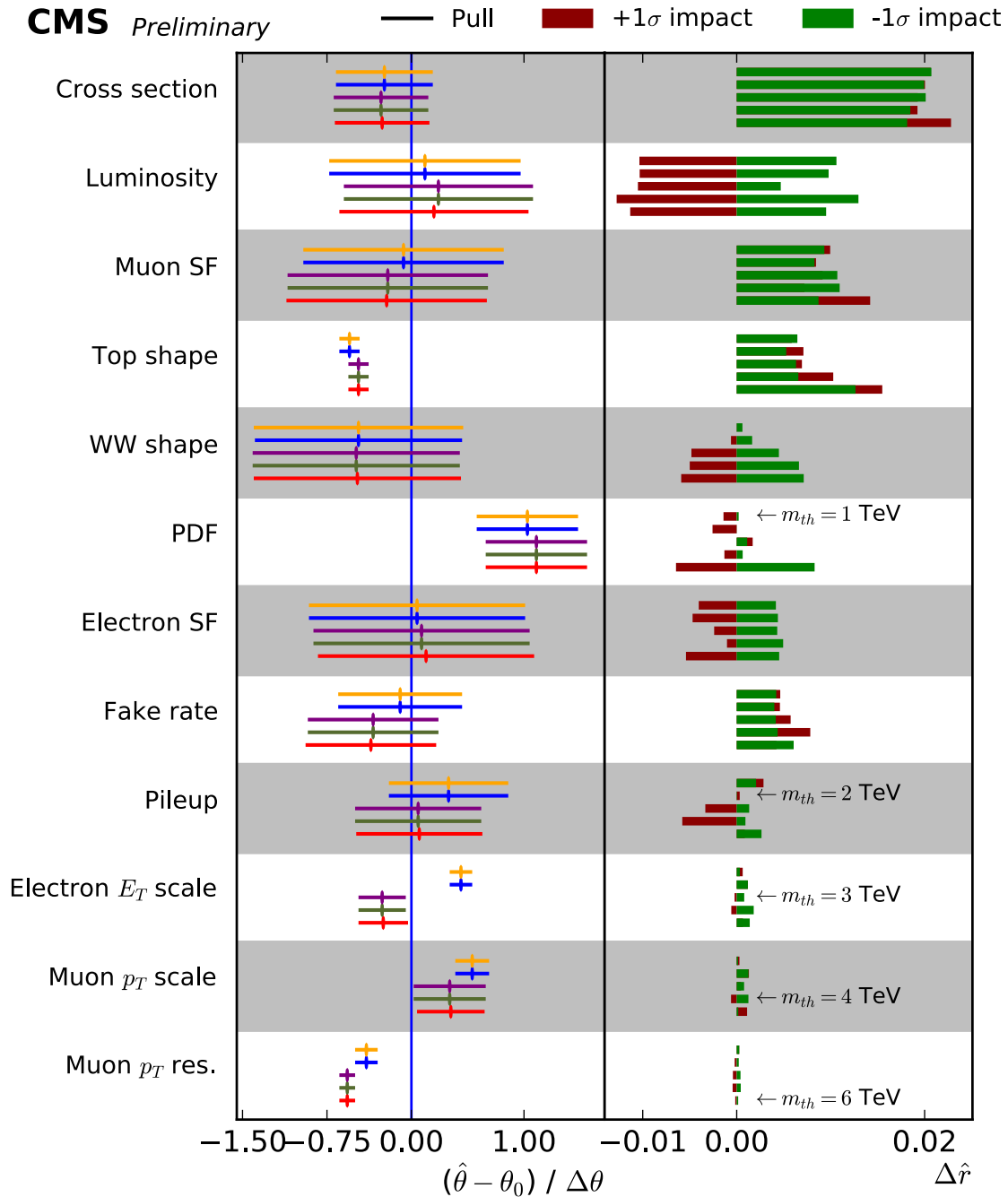


Figure 90: Impact of the nuisance parameters on the QBH limit in the $e\mu$ channel for one extra dimension. Each line represents one systematic uncertainty, as introduced in Sec. 4.9. In the left column the size of the post-fit uncertainty relative to the pre-fit one is shown as a reference. The right column gives the impact of the $\pm 1\sigma$ variations on the signal strength modifier. To show the effect of the threshold mass on the impacts, each nuisance parameter line is shown for five different m_{th} .

Some differences to the impacts in the RPV SUSY model are obvious, as the shape comes for the QBH model directly from the simulation, there is no additional uncer-

tainty associated with the normalization or shape of the signal. Other uncertainties like the WW shape uncertainty behave very similarly for both models. The main differences are some uncertainties which always result in a worse limit, namely the uncertainty on the background cross section, the muon scale factors, the shape of the $t\bar{t}$ background and the fake rate uncertainty. These are all uncertainties that have a mass dependence, but already play a role at low invariant mass. In the post-fit all of these uncertainties can be constrained at low invariant masses, but due to the mass dependence, they can mimic a broad signal at high masses and therefore worsen the limit. This argument is not true for the WW shape uncertainty as it cannot be fixed at low masses. In general, there is no large dependence on the threshold mass, the effect of the nuisance parameters is similar for all signal hypotheses. The effects of the uncertainties on the signal strength modifier are similar in size as for the RPV model, but as the dominant uncertainties of the RPV model are not present, the total effect of the systematic uncertainties is smaller.

The resulting limit on the QBH model is presented in Fig. 91 at a 95% confidence level in the $e\mu$ channel.

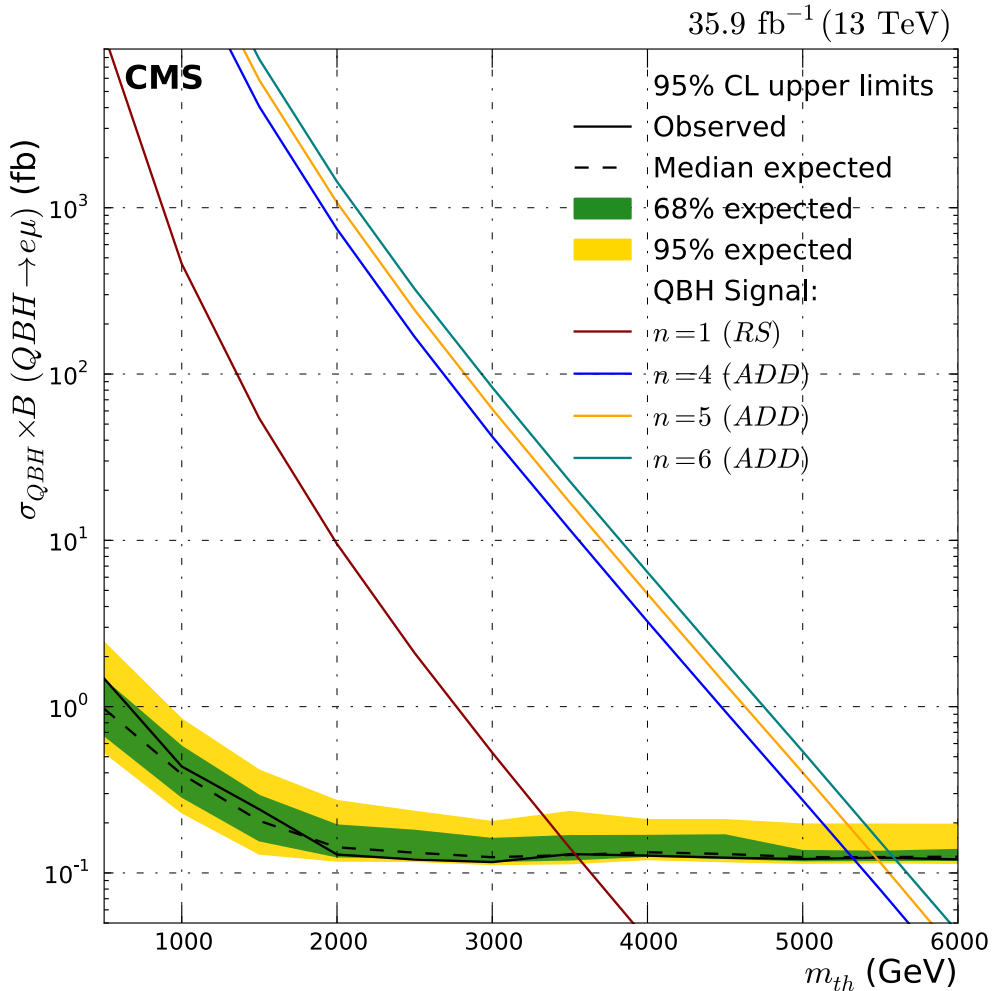


Figure 91: Limit on the QBH model cross section of the $e\mu$ channel at 95% confidence level. Shown is the observed limit as a black line, the median expected limit as a dashed black line. The 68% and 95% uncertainty intervals of the expected limits are shown as green and yellow bands respectively. For four different numbers of extra dimensions the cross section of the QBH model are shown. If the excluded cross section is smaller than the theory cross section, this m_{th} is excluded.

The QBH limit from Fig. ?? contains less features than the RPV one due to the large signal width. This large signal width results in a big fraction of the invariant mass spectrum contributing to the limit, so fluctuations in individual bins cancel out over various bins, while in the RPV model the narrow resonance can be dominated by individual bins.

Over the whole range of m_{th} the observed limit agrees with the expected limit within the 1σ band. Most of the probed mass range is background free, resulting in a flat limit from 2 TeV upwards. For $n = 1$ extra dimensions, threshold masses below $m_{th} < 3.5$ TeV at 95% confidence level can be excluded. For $n = 4$, $n = 5$ and $n = 6$ the exclusion reaches threshold masses of $m_{th} < 5.4$ TeV, $m_{th} < 5.5$ TeV and $m_{th} < 5.6$ TeV.

Comparing the results to other direct searches for QBH at colliders yield weaker limits. For $n = 6$ the strongest limits are at 8.9 TeV [35], while this analysis results in a limit of $m_{th} < 5.6$ TeV. However, these most stringent limits were set in a different final state with a higher cross section, therefore the limits are expected to be stronger there. Compared to past searches in the $e\mu$ channel, the strongest set limit for $n = 6$ is at 4.6 TeV [1, 31], therefore this analysis improves significantly on the set limits. Also for $n = 1$, the limit in the $e\mu$ channel can be improved from 2.5 TeV to $m_{th} < 3.5$ TeV. So the analysis improves results in the $e\mu$ channel by a big margin, while the strongest limits set on the model are still out of reach. The details of the model, like different decay modes, can only be determined if a QBH is found, therefore all different searches are relevant and in the $e\mu$ decay channel this analysis sets the most stringent limits.

Z' The procedure for the Z' model is the same as for the QBH model, the signal shape is taken directly from the signal simulation. The distribution of impacts due to the different nuisance parameters is shown in Fig. 92.

The distribution of impacts looks very similar to the QBH one, shown in Fig. 90. Four uncertainties always worsen the limit due to its impact on the shape explained in detail for the QBH distribution. It shows that regarding the systematic uncertainties the Z' model is closer to the QBH model than the RPV one. Especially at high masses the width of the signal results in a clear deviation from the narrow resonance of the RPV model. Also the size of the impact is very similar to the QBH one, meaning the impact on the strength modifier is smaller than for the RPV model.

The final cross section limit on the Z' model in the $e\mu$ channel is shown in Fig. 93.

The limit is very similar to the QBH one up to masses of 2 TeV, from there the limit is not flat anymore as for the QBH or RPV model. This is a consequence of the signal shape, at low and medium masses (up to 2 TeV) the signal is a broad resonance in the invariant mass distribution. Therefore, it also has some similarities to the RPV model, but due to the larger width more bins are contributing to the limit. From about $m_{Z'} = 2$ TeV upwards the shape starts to change significantly. There is still the broad resonance around the resonance mass, but also an increasing off-shell production at very low masses (This can be seen in a shape comparison for different $m_{Z'}$ values shown in Fig. 112 in the appendix). Due to this increasing low energy contribution the signal never reaches the background free region, resulting in a worsening of the limit for high masses. The off-shell production has no specific shape and is therefore not dominated by individual bins. Due to this feature, there are no fluctuations that contribute at high masses and the observed limit closely follows the expected one. In

general the observed limit agrees over the whole probed mass range with the expected one within the $\pm 1\sigma$ band.

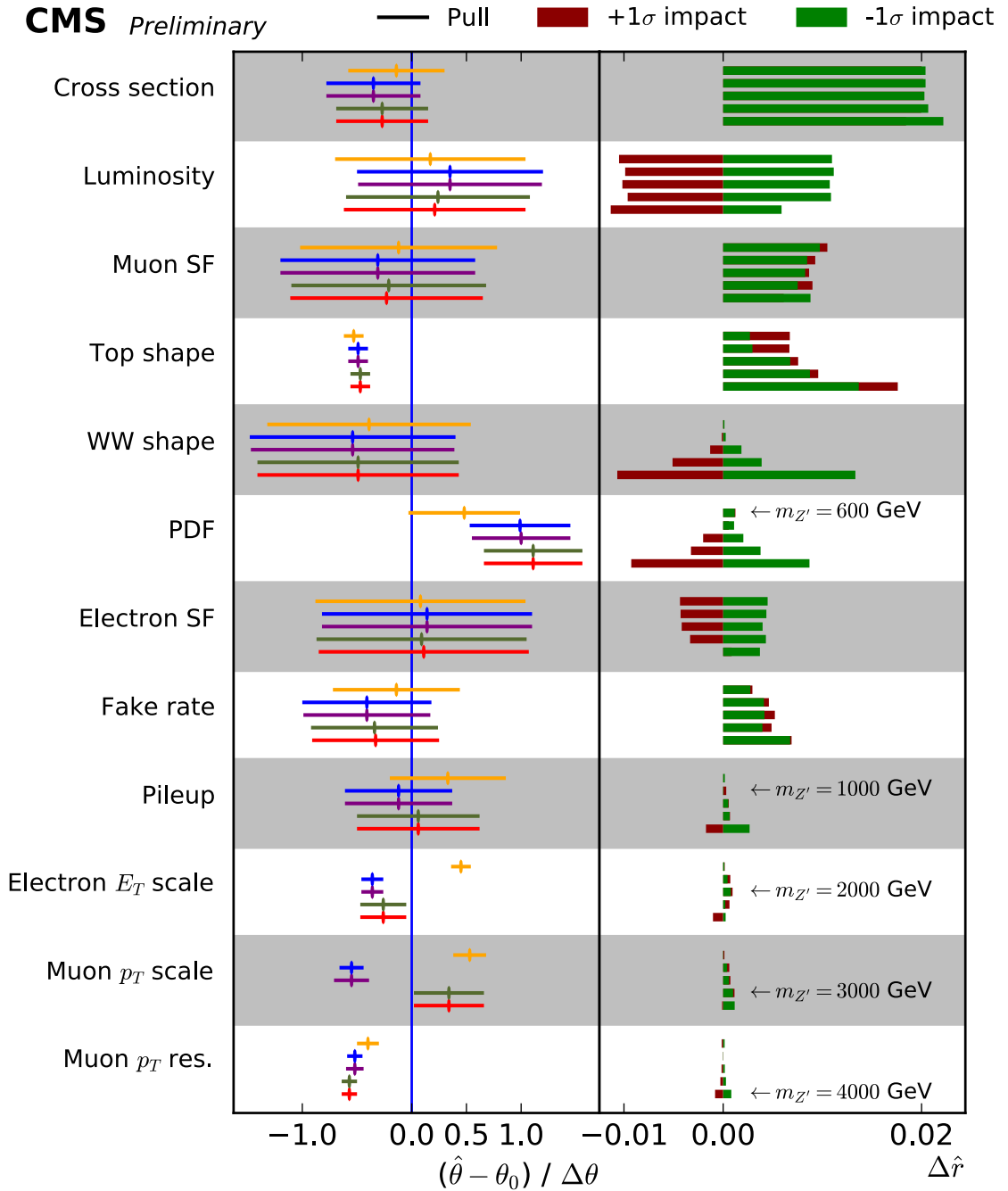


Figure 92: Impact of the nuisance parameters on the Z' limit in the $e\mu$ channel. Each line represents one systematic uncertainty, as introduced in Sec. 4.9. In the left column the size of the post-fit uncertainty relative to the pre-fit one is shown as a reference. The right column gives the impact of the $\pm 1\sigma$ variations on the signal strength modifier. To show the effect of the resonance mass on the impacts, each nuisance parameter line is shown for five different $m_{Z'}$.

Comparing the cross section limit with the theory cross section of the Z' model results in a mass limit of $m_{Z'} > 4.4 \text{ TeV}$ at 95 % confidence level. Indirect constraints on

the model are not easily comparable to this result, but there were past direct searches for $Z' \rightarrow e\mu$ which result in a mass limit of 3.0 TeV [31]. This analysis can therefore increase the direct limit on the Z' model by 1.4 TeV, resulting in the strongest direct limit on this model.

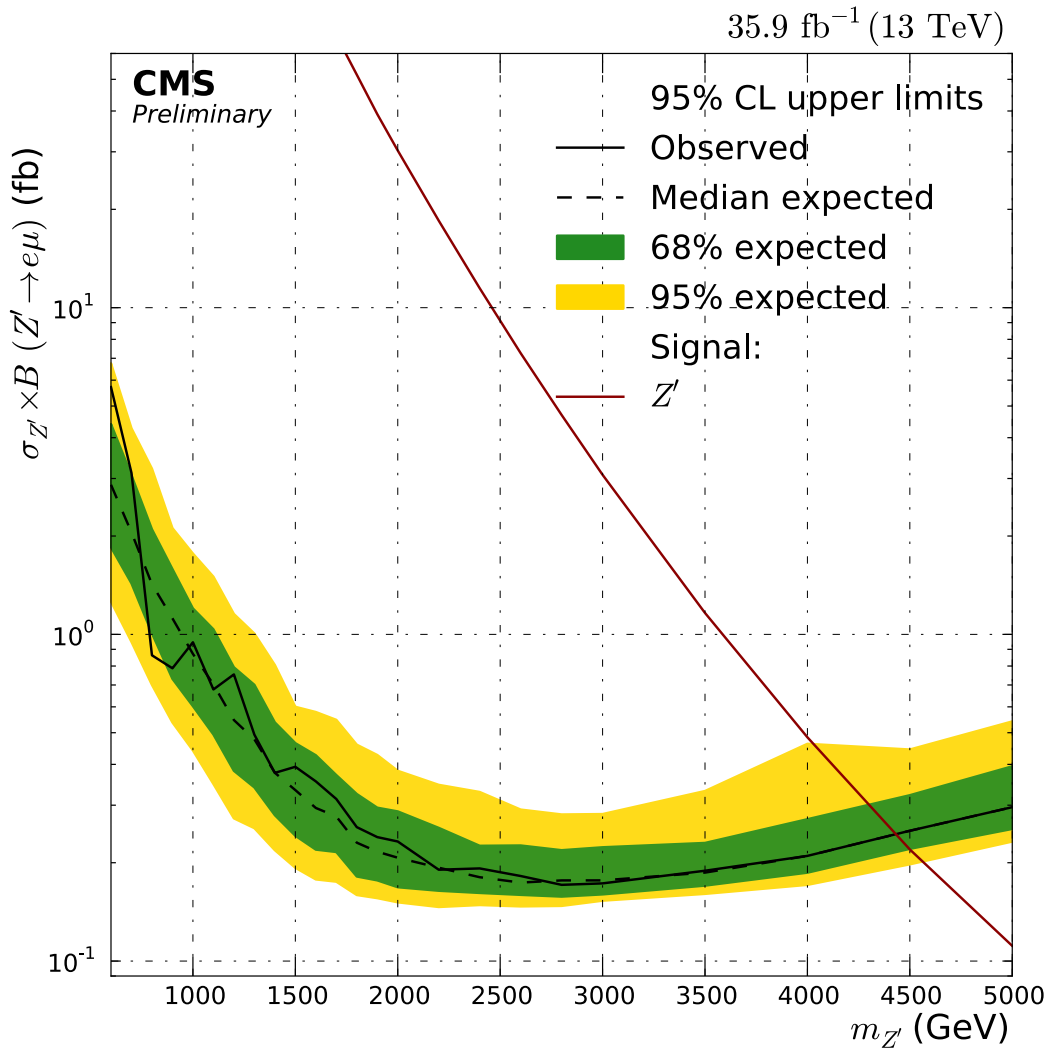


Figure 93: Limit on the Z' model cross section of the $e\mu$ channel at 95% confidence level. Shown is the observed limit as a black line, the median expected limit as a dashed black line. The 68% and 95% uncertainty intervals of the expected limits are shown as green and yellow bands respectively. The cross section of the Z' model is shown. If the excluded cross section becomes smaller than the theory cross section, all $m_{Z'}$ below this point are excluded.

5.3.2 $e\tau_\mu$ channel

In the $e\tau_\mu$ channel only the RPV model is studied. In principle also the QBH and Z' models can produce final states of $e\tau$ but this would be exactly the same model as in the $e\mu$ channel. This would mean the results of the different channels could be combined and due to the tau decay branching ratio this channel would never contribute

significantly. For the RPV model this argument does not hold, as the fundamental couplings are different, therefore a combination of the channels is not possible.

The first step like in the $e\mu$ channel is to calculate the impact distributions, which is shown in Fig. 94.

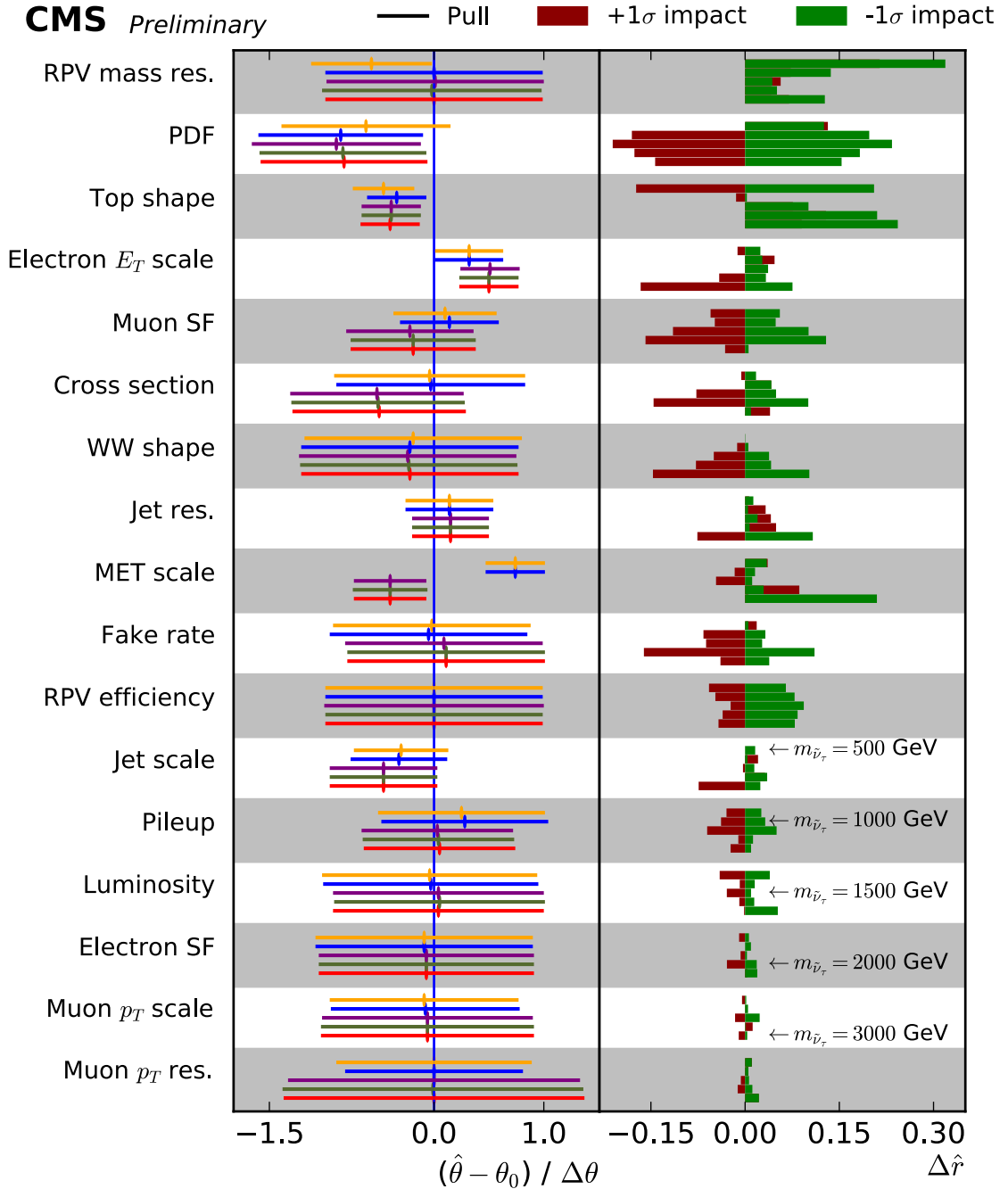


Figure 94: Impact of the nuisance parameters on the RPV limit in the $e\tau_\mu$ channel for $\lambda_{331} = \lambda'_{311} = 0.01$. Each line represents one systematic uncertainty, as introduced in Sec. 4.9. In the left column the size of the post-fit uncertainty relative to the pre-fit one is shown as a reference. The right column gives the impact of the $\pm 1\sigma$ variations on the signal strength modifier. To show the effect of the resonance mass on the impacts, each nuisance parameter line is shown for five different $m_{\tilde{\nu}_\tau}$.

The approach for the limit setting in this channel is identical to the RPV model in the $e\mu$ channel. The background is taken as the histograms shown in the invariant mass distribution in Fig. 73. The RPV signal is dived from a Gaussian distribution with the width of the invariant mass resolution shown in Fig. 47. This signal is then normalized to the cross section for this mass hypothesis and the acceptance times efficiency from Fig. 42. The main difference between the $e\mu$ channel and the $e\tau_\mu$ one is the different shape of the background with a maximum at $m_{e\tau} \sim 300$ GeV and a drop in higher and lower masses.

The different background shape reduces the possibilities to fix the systematic uncertainties at low masses. This can be seen in the impact distribution in the RPV model in the $e\tau_\mu$ channel shown in Fig. 94. Systematic uncertainties which are drastically reduced in the post-fit, like the $t\bar{t}$ shape uncertainty, are reduced far less in the $e\tau_\mu$ channel due to lack of low energy events. Also, additional systematic uncertainties like the jet energy scale have to be considered due to the E_T^{miss} in the final state. There is no clear dominant nuisance parameter in the impact distribution. Many uncertainties have a comparable impact on the signal strength modifier, otherwise the effects visible are similar to the RPV signal in the $e\mu$ channel. The mass resolution uncertainty only worsens the limit, for other uncertainties the effects depend on $m_{\tilde{\nu}_\tau}$. The overall effect of the nuisance parameters on the signal strength modifier is a factor 2 – 3 bigger than in the $e\mu$ channel, mainly due to a lesser reduction of the uncertainties in the post-fit.

At very low masses the cross section limit worsens into the picobarn range, due to the reduced signal efficiency. It improves until from about 2.5 TeV the limit is set in a background free region and therefore the limit stays constant from there. The observed limit follows closely the expected one and stays within the $\pm 2\sigma$ uncertainty band.

The observed limit closely follows the expected limit within the uncertainty bands. For the benchmark coupling of $\lambda = \lambda' = 0.01$ the cross section limit is too weak to set any mass limit at all. For $\lambda = \lambda' = 0.1$ a mass limit of $m_{\tilde{\nu}_\tau} < 2.9$ TeV can be set.

The cross section limit in Fig. 95 can be used similarly to the $e\mu$ channel result to derive a limit in the $m_{\tilde{\nu}_\tau}$ - λ'_{311} parameter plane. The main difference is that λ_{132} is replaced by λ_{331} to correspond to the final state of $e\tau$ instead of $e\mu$. Otherwise the formulae from Eq. 35 and Eq. 36 still hold. The derived limit contours for the RPV signal are shown in Fig. 96.

The excluded parameter space in the $m_{\tilde{\nu}_\tau}$ - λ'_{311} plane for different given λ_{331} values is shown. For small $m_{\tilde{\nu}_\tau}$ the exclusion is independent of λ_{331} , while for higher masses the excluded region expands with bigger values of λ_{331} . For very low masses the limit weakens as the signal efficiency gets worse, while for medium and high masses the behaviour is similar to the limit in the $e\mu$ channel.

Previous direct searches for $q_d\bar{q}_d \rightarrow \tilde{\nu}_\tau \rightarrow e\tau$ have been performed in the past by the ATLAS collaboration in the hadronic decay mode of the tau [112]. The resulting limit on the RPV model for $\lambda'_{311} = 0.11$ and $\lambda_{331} = 0.07$ is $m_{\tilde{\nu}_\tau} > 2.2$ TeV. From Fig. 96 the comparable mass limit is $m_{\tilde{\nu}_\tau} > 2.6$ TeV. The difference of the two analyses is the decay mode of the tau used, so even with the smaller leptonic branching ratio this new analysis is more sensitive due to the larger integrated luminosity used in this analysis. This is therefore the most stringent limit of a direct search for this model.

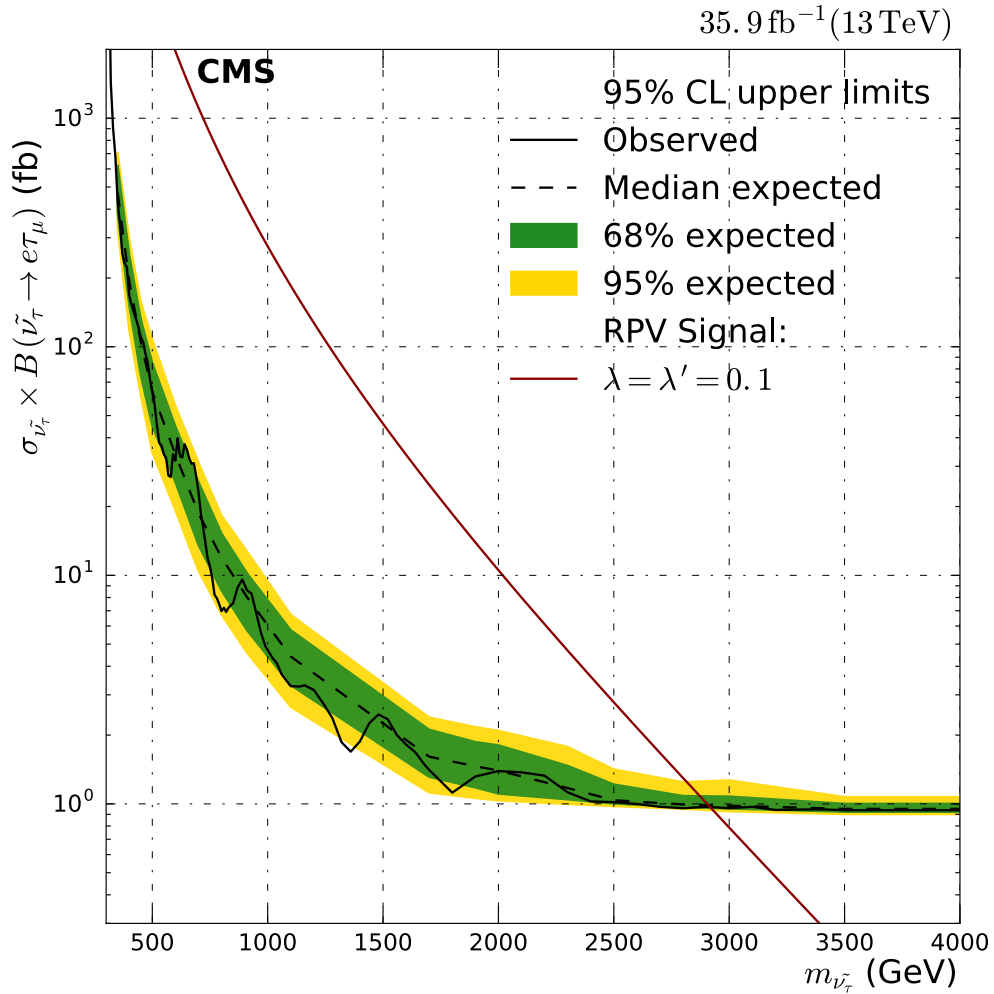


Figure 95: Limit on the RPV SUSY model cross section of the $e\tau_\mu$ channel at 95% confidence level. Shown is the observed limit as a black line, the median expected limit as a dashed black line. The 68% and 95% uncertainty intervals of the expected limits are shown as green and yellow bands respectively. For an example coupling values the cross section of the RPV model are shown. If the excluded cross section is smaller than the theory cross section, this $m_{\tilde{\nu}_\tau}$ is excluded.

5.3.3 $\mu\tau_e$ channel

The approach for limit setting in the $\mu\tau_e$ channel is identical to the $e\tau_\mu$ channel. The background histograms are taken from the invariant mass distribution in Fig. 78, while the signal is calculated following a Gaussian distribution with the width according to the mass resolution of Fig. 48 and normalized to the theoretical cross section and the acceptance times efficiency from Fig. 43.

The impact distribution for the RPV model in the $\mu\tau_e$ channel is shown in Fig. 97.

The effect of the different nuisance parameters is very similar to the results in the $e\tau_\mu$ channel. Due to a lack of low energy events, the fit will not reduce the uncertainties as much as in the $e\mu$ channel. This is illustrated in the left column of post-fit uncertainties. The resulting impacts also show a very similar behaviour, e.g. that there is no clear dominant uncertainty, but many contributing uncertainties.

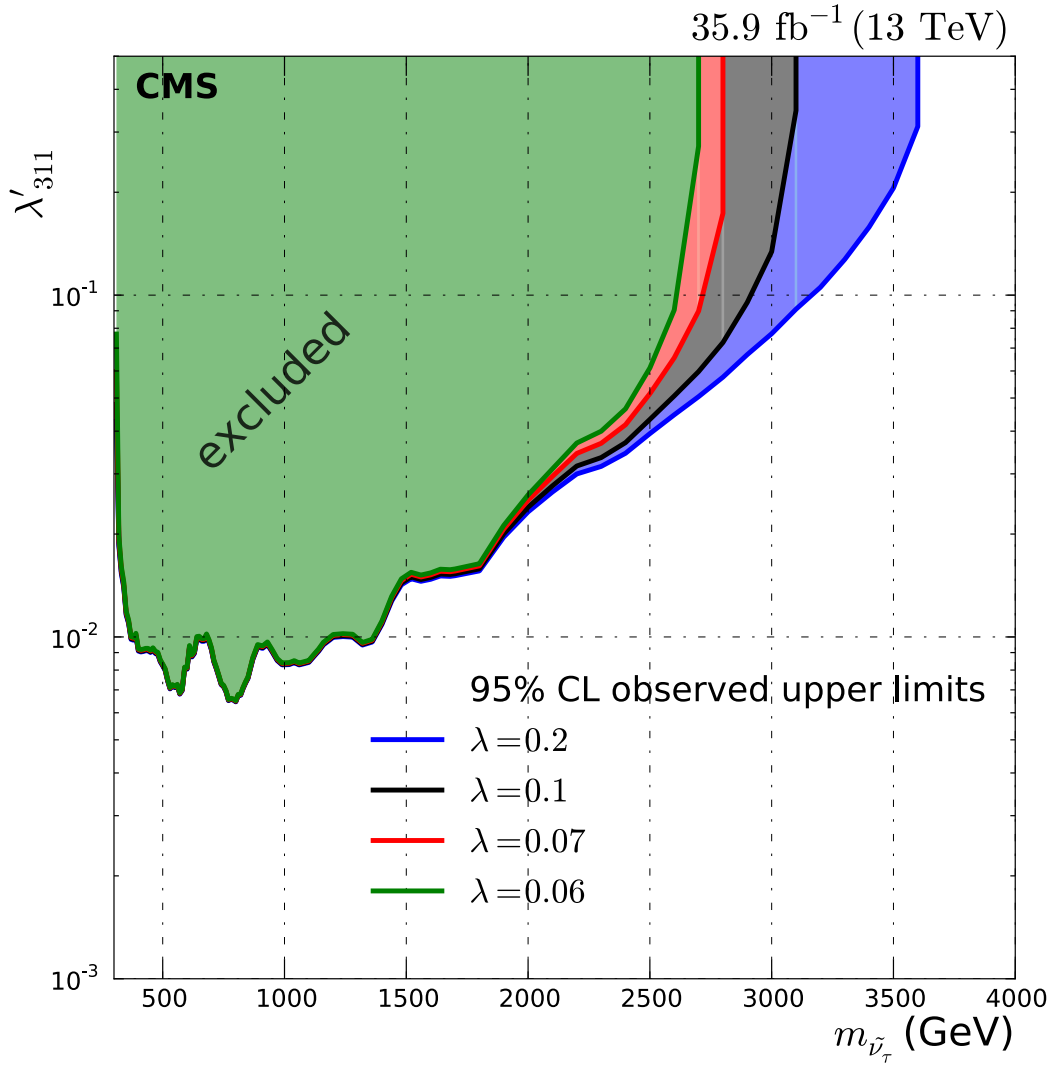


Figure 96: 95% confidence level observed limit contour for the RPV signal in the $m_{\tilde{\nu}_\tau}$ - λ'_{311} parameter space. The values of the other coupling λ_{331} are fixed to 0.06, 0.07, 0.1 and 0.2. The parameter space top left of the observed limit is excluded.

The cross section limit calculated for the RPV model in the $\mu\tau_e$ channel at 95% confidence level is shown in Fig. 98.

Due to the slightly higher signal efficiency than in the $e\tau_\mu$ channel, the limit does not worsen so much at very low masses. It improves with rising mass as the background decreases until about 3 TeV. In the background free region at higher masses a constant limit can be set. The observed limit follows closely the expected one and stays within the $\pm 2\sigma$ uncertainty band.

For the benchmark coupling from the $e\mu$ channel $\lambda = \lambda' = 0.01$ no mass limit can be set as the cross section limit itself is too weak, but for $\lambda = \lambda' = 0.1$ a mass limit of $m_{\tilde{\nu}_\tau} < 3.0$ TeV can be set. The expected and observed limits agree with each other well in this mass range.

Like in the other two RPV interpretations, the cross section limit can be used to derive a limit in the $m_{\tilde{\nu}_\tau}$ - λ'_{311} parameter plane. The same calculations as in Eq. 35 and

Eq. 36 can be used, just replacing $\lambda_{132} = \lambda_{231}$ with λ_{332} . The derived limit contours for the RPV signal are shown in Fig. 99.

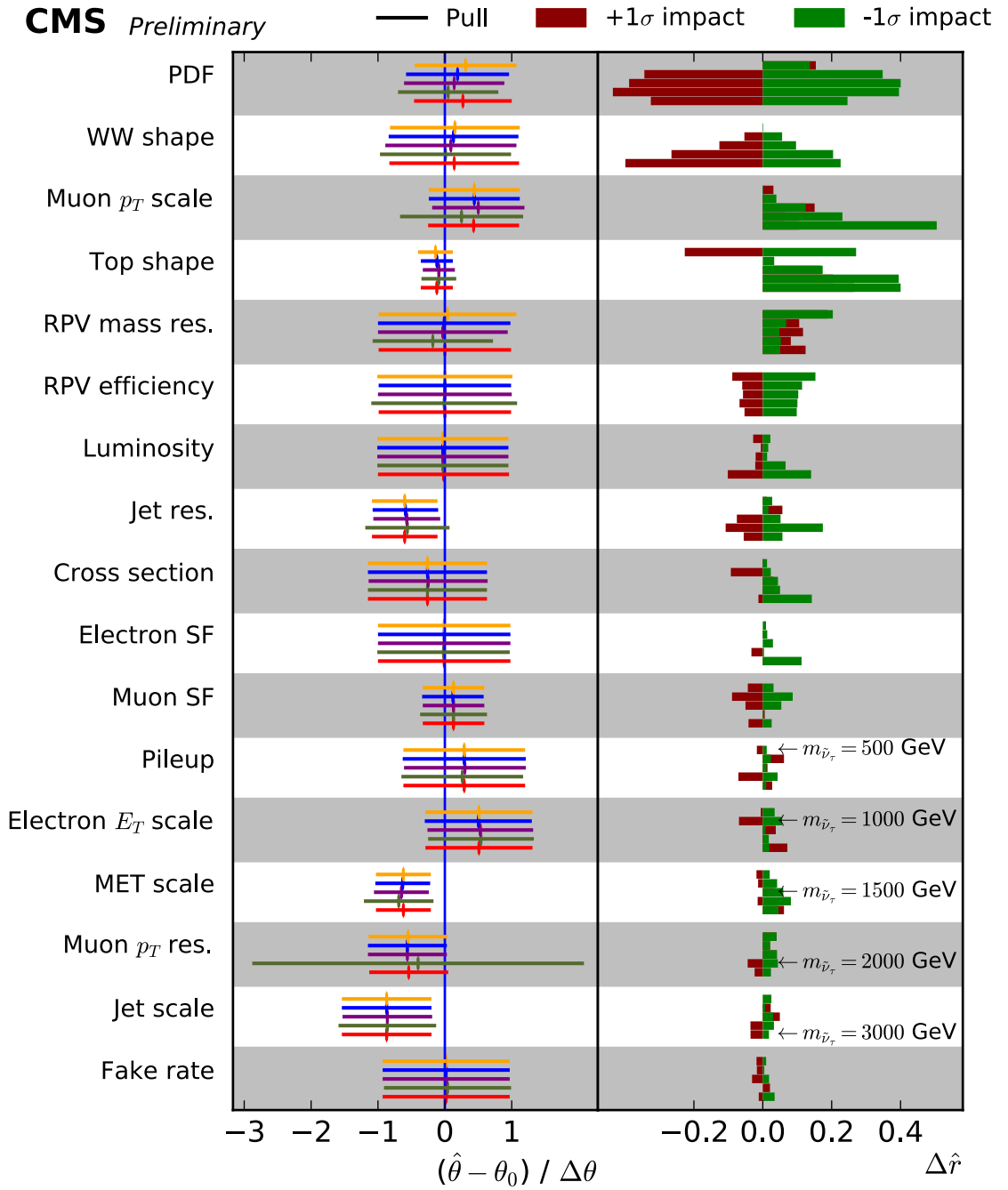


Figure 97: Impact of the nuisance parameters on the RPV limit in the $\mu\tau_e$ channel for $\lambda_{332} = \lambda'_{311} = 0.01$. Each line represents one systematic uncertainty, as introduced in Sec. 4.9. In the left column the size of the post-fit uncertainty relative to the pre-fit one is shown as a reference. The right column gives the impact of the $\pm 1\sigma$ variations on the signal strength modifier. To show the effect of the resonance mass on the impacts, each nuisance parameter line is shown for five different $m_{\tilde{\nu}_\tau}$.

The excluded parameter space in the $m_{\tilde{\nu}_\tau}$ - λ'_{311} plane for different given λ_{332} values is shown. For small $m_{\tilde{\nu}_\tau}$ the exclusion is independent of λ_{332} , while for higher masses the excluded region expands with bigger values of λ_{332} . The limit has not the same degradation for very low masses as the result of the $e\tau_\mu$ channel but is very similar to the $e\mu$ channel over the whole mass range.

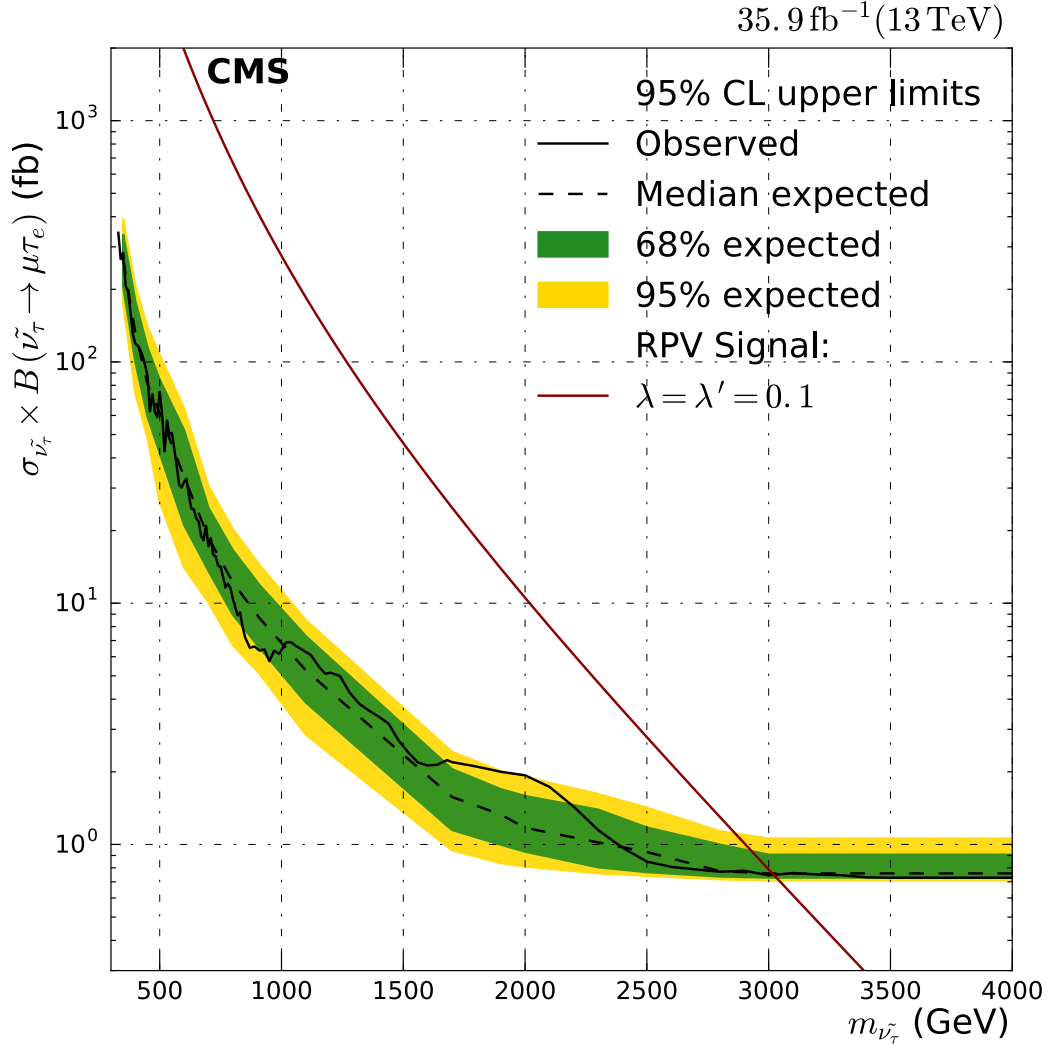


Figure 98: Limit on the RPV SUSY model cross section of the $\mu\tau_e$ channel at 95% confidence level. Shown is the observed limit as a black line, the median expected limit as a dashed black line. The 68% and 95% uncertainty intervals of the expected limits are shown as green and yellow bands respectively. For an example coupling values the cross section of the RPV model are shown. If the excluded cross section is smaller than the theory cross section, this $m_{\tilde{\nu}_\tau}$ is excluded.

Previous direct searches for $q_d\bar{q}_d \rightarrow \tilde{\nu}_\tau \rightarrow \mu\tau$ have been performed in the past by the ATLAS collaboration in the hadronic decay mode of the tau [112]. The resulting limit on the RPV model for $\lambda'_{311} = 0.11$ and $\lambda_{332} = 0.07$ is $m_{\tilde{\nu}_\tau} > 1.9$ TeV. From Fig. 99 the comparable mass limit is $m_{\tilde{\nu}_\tau} > 2.8$ TeV. The difference of the two analyses is the decay mode of the tau used, so even with the smaller leptonic branching ratio this new analysis is more sensitive. Due to the larger integrated luminosity used in this analysis, it sets the most stringent limits from direct searches on this model.

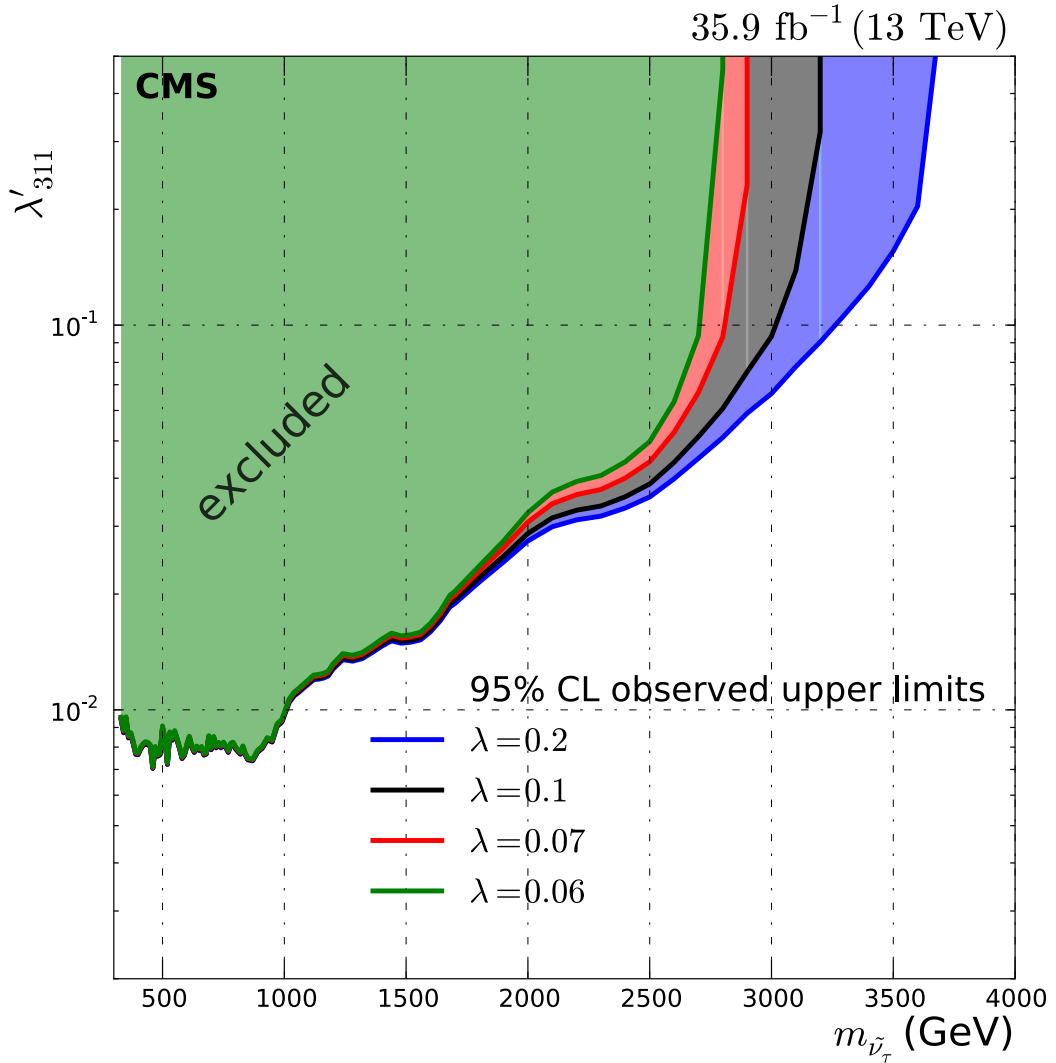


Figure 99: 95% confidence level observed limit contour for the RPV signal in the $m_{\tilde{\nu}_\tau}$ - λ'_{311} parameter space. The values of the other coupling λ_{332} are fixed to 0.06, 0.07, 0.1 and 0.2. The parameter space top left of the observed limit is excluded.

5.3.4 Comparison to other direct searches

For the studied three models and three channels different mass limits were set and compared to previous analyses, as well as indirect constraints. To give an overview how this analysis performs in comparison to the previous results, the different limits are listed in Tab. 10. Only for direct searches the comparison can be made accurately as no additional assumptions on processes or couplings have to be made.

For all models and channels the limits are improved by a big margin, the improvement ranging from 400 GeV to 1.4 TeV. Many of the results are the most stringent limits ever set on these models, while all of them are the most stringent ones in direct searches in the studied decay modes.

Table 10: Comparison of the different set mass limits by this analysis with previous direct searches.

Channel	Model	Previous limit	Limit from this analysis
$e\mu$	RPV, $\lambda_{132} = \lambda_{231} = \lambda'_{311} = 0.01$	1.0 TeV	1.7 TeV
	RPV, $\lambda_{132} = \lambda_{231} = \lambda'_{311} = 0.1$	2.7 TeV	3.7 TeV
	QBH, $n = 1$ (RS)	2.5 TeV	3.5 TeV
	QBH, $n = 6$ (ADD)	4.6 TeV	5.6 TeV
	Z'	3.0 TeV	4.4 TeV
$e\tau_\mu$	RPV, $\lambda_{331} = 0.07, \lambda'_{311} = 0.11$	2.2 TeV	2.6 TeV
$\mu\tau_e$	RPV, $\lambda_{332} = 0.07, \lambda'_{311} = 0.11$	1.9 TeV	2.8 TeV

SUMMARY & CONCLUSIONS

In this thesis the search for new high mass phenomena in final states with an electron and muon was presented. First the theoretical background and motivation for the analysis were explained, especially the models for new physics, which are studied in the analysis were introduced. The CMS experiment used to record the proton–proton collisions was introduced next. Then the various aspects of the event selection were explained in detail. The background and signal simulation, various selection criteria and corrections as well as the considered systematic uncertainties were introduced. This all results in the invariant mass distributions which are then used as input for the statistical interpretation.

The analysis was performed in three different final states containing an electron and a muon. These three channels are $e\mu$, $e\tau_{\mu\mu}$ and $\mu\tau_e$. In all three channels the observed data agree with the background expectation within the uncertainties. No signs of the studied new physics models were seen in the data. The final results of the analysis are therefore exclusion limits on the parameter space of the studied models.

The invariant mass distribution of the $e\mu$ channel is interpreted in three possible models of new physics. The first one is the R-parity violating supersymmetry, which would result in a narrow resonance in the invariant mass spectrum. Limits were set on the three parameters of the model, the production coupling λ'_{311} , the decay coupling $\lambda_{132} = \lambda_{231}$ and the mass of the resonance $m_{\tilde{\nu}_\tau}$. For assumed couplings of $\lambda'_{311} = \lambda_{132} = \lambda_{231} = 0.01$ masses below $m_{\tilde{\nu}_\tau} = 1.7$ TeV can be excluded at 95% confidence level. These are the most stringent limits on this model from direct searches, improving the limits from previous search results by 700 GeV. The second studied model is the production of quantum black holes in the presence of extra dimensions. This model would result in a signal shape in the invariant mass spectrum, that starts at the model parameter of the threshold mass m_{th} and decreases for higher masses. Limits were set on the model parameters m_{th} and number of extra dimensions n . The observed limits range from $m_{\text{th}} > 3.5$ TeV for $n = 1$ up to $m_{\text{th}} > 5.6$ TeV for $n = 6$. While these are the most stringent limits set in this final state, searches for quantum black holes in other final states are even more sensitive. The last model studied in the $e\mu$ channel is of a new additional boson Z' , that decays into an electron and a muon. The signal shape is a resonance in the invariant mass distribution with a width of about 3%. A limit on the mass of the new boson of $m_{Z'} > 4.4$ TeV could be set. This is the best limit on this specific model from direct detection. The results of this channel and a simpler version of the analysis were published during the work on this thesis in a preliminary publication with 2015 data (See Ref. [1]) and was submitted to JHEP for publication with 2016 data (See Ref. [2]).

In the $e\tau_\mu$ channel the invariant mass distribution is only interpreted in terms of the R-parity violating supersymmetry model. Due to the collinear reconstruction of the tau from the muon and E_T^{miss} the resonance still can be reconstructed. This allows for a similar search for a resonance as in the $e\mu$ channel even in the presence of E_T^{miss} . For assumed couplings of $\lambda'_{311} = \lambda_{331} = 0.1$ masses below $m_{\tilde{\nu}_\tau} = 2.9$ TeV can be set. Pre-

vious limits from direct searches for this model can be improved by 400 GeV, resulting in the most stringent limits. Further improvements could be reached by studying the hadronic decay of the tau due to the higher branching ratio.

In the last, the $\mu\tau_e$ channel, the invariant mass distribution is interpreted only in the R-parity violating supersymmetry model like in the $e\tau_\mu$ channel. The approach of the two channels is very similar in general. Also in the $\mu\tau_e$ channel the collinear tau reconstruction is used to reconstruct the resonance shape. For coupling values of $\lambda'_{311} = \lambda_{332} = 0.1$ a mass limit of $m_{\tilde{\nu}_\tau} > 3.0$ TeV can be set. This result improves the limits from previous searches for this model by 900 GeV and is now the most stringent limit. Possible improvements are similar to the $e\tau_\mu$ channel, as also in this channel sensitivity could be gained by studying hadronically decaying taus and exploiting their higher branching ratio.

SAMPLES

A.1 DATASETS

Table 11: Data sets used in this analysis

Datasets	run range	integrated luminosity (pb^{-1})
/SinglePhoton/Run2016B-23Sep2016-v3/MINIAOD	273150 – 275376	5933.3
/SinglePhoton/Run2016C-23Sep2016-v1/MINIAOD	275656 – 276283	2646.0
/SinglePhoton/Run2016D-23Sep2016-v1/MINIAOD	276315 – 276811	4353.4
/SinglePhoton/Run2016E-23Sep2016-v1/MINIAOD	276831 – 277420	4049.7
/SinglePhoton/Run2016F-23Sep2016-v1/MINIAOD	277932 – 278808	3160.1
/SinglePhoton/Run2016G-23Sep2016-v1/MINIAOD	278820 – 280385	7554.5
/SinglePhoton/Run2016H-PromptReco-v2/MINIAOD	281207 – 284035	8545.0
/SinglePhoton/Run2016H-PromptReco-v3/MINIAOD	284036 – 284068	216.8
/SingleMuon/Run2016B-23Sep2016-v3/MINIAOD	273150 – 275376	5933.3
/SingleMuon/Run2016C-23Sep2016-v1/MINIAOD	275656 – 276283	2646.0
/SingleMuon/Run2016D-23Sep2016-v1/MINIAOD	276315 – 276811	4353.4
/SingleMuon/Run2016E-23Sep2016-v1/MINIAOD	276831 – 277420	4049.7
/SingleMuon/Run2016F-23Sep2016-v1/MINIAOD	277932 – 278808	3160.1
/SingleMuon/Run2016G-23Sep2016-v1/MINIAOD	278820 – 280385	7554.5
/SingleMuon/Run2016H-PromptReco-v2/MINIAOD	281207 – 284035	8545.0
/SingleMuon/Run2016H-PromptReco-v3/MINIAOD	284036 – 284068	216.8
Sum	273150 – 284068	36458.8

A.2 SIGNAL SIMULATION

Table 12: Information about the individual signal Monte Carlo samples from official production used in the analysis. The explicit simulated parameter points with their properties are listed in Tab. 13 for the RPV model, in Tab. 14 for the QBH model and in Tab. 15 for the Z' model.

Name signal sample	Generator	Order
RPVresonantToEMu_M-*_LLE_LQD-*_TuneCUETP8M1_13TeV-calchep-pythia8	CalcHEP	LO
QBHToEMu_M-*_n*_ADD_TuneCUETP8M1_13TeV-QBH-pythia8	QBH	LO
ZPrimeToEMu_M-*_TuneCUETP8M1_13TeV-pythia8	Pythia 8	LO

Table 13: Summary of simulated RPV signal samples. Each sample contains 15000 generated events. The cross section is taken from the event generator CalcHEP using the PDF set CTEQ6L1. The NLO QCD k-factor is calculated as described in [13].

$\lambda_{132} = \lambda_{231}$	λ'_{311}	$m_{\tilde{\nu}_\tau}$ in GeV	$\sigma \cdot \text{BR}(\tilde{\nu}_\tau \rightarrow e^\pm \mu^\mp)$ in pb	NLO (QCD) k-factor
0.01	0.01	200	585.35	1.34
0.01	0.01	300	158.04	1.36
0.01	0.01	400	59.97	1.37
0.01	0.01	500	27.612	1.37
0.01	0.01	600	14.415	1.37
0.01	0.01	700	8.1833	1.37
0.01	0.01	800	4.9538	1.36
0.01	0.01	900	3.1345	1.35
0.01	0.01	1000	2.0611	1.34
0.01	0.01	1200	0.96973	1.32
0.01	0.01	1400	0.49332	1.30
0.01	0.01	1600	0.26708	1.27
0.01	0.01	1800	0.14995	1.25
0.01	0.01	2000	0.08639	1.22
0.01	0.01	2500	0.023951	1.16
0.01	0.01	3000	0.0071592	1.11
0.01	0.01	3500	0.002136	1.08
0.01	0.01	4000	0.00064163	1.05
0.01	0.01	4500	0.00018451	1.05
0.01	0.01	5000	$5.1376 \cdot 10^{-05}$	1.08
0.01	0.01	5500	$1.3505 \cdot 10^{-05}$	1.17
0.01	0.01	6000	$3.3123 \cdot 10^{-06}$	1.36
0.01	0.01	6500	$7.8732 \cdot 10^{-07}$	1.68
0.1	0.1	3000	0.71654	1.12
0.1	0.1	3500	0.21681	1.08
0.1	0.1	4000	0.065772	1.06
0.2	0.2	4000	0.28243	1.06
0.2	0.2	4500	0.090249	1.05
0.2	0.2	5000	0.030614	1.10
0.2	0.2	5500	0.011984	1.23
0.2	0.2	6000	0.0058464	1.33
0.2	0.2	6500	0.0035114	1.0
0.5	0.5	4000	2.601	1.06
0.5	0.5	4500	1.0769	1.05
0.5	0.5	5000	0.51715	1.09
0.5	0.5	5500	0.29041	1.18
0.5	0.5	6000	0.18438	1.4
0.5	0.5	6500	0.12693	1.6

Table 14: Summary of simulated QBH signal samples.

N_{dim}	Signal mass in GeV	$\sigma \cdot \text{BR}(\text{QBH} \rightarrow e\mu)$ in pb
1	500	11.04
1	1000	0.4599
1	1500	0.05398
1	2000	0.009511
1	2500	0.002102
1	3000	0.0005291
1	3500	0.0001413
1	4000	0.00003940
1	4500	0.00001132
1	5000	0.000003231
1	5500	0.000000927
1	6000	0.000000260
1	6500	0.000000071
4	500	719.0
4	1000	32.79
4	1500	4.046
4	2000	0.7437
4	2500	0.1673
4	3000	0.04206
4	3500	0.01158
4	4000	0.003251
4	4500	0.0009388
4	5000	0.0002738
4	5500	0.00007917
4	6000	0.00002227
4	6500	0.000006042
6	500	1354
6	1000	62.78
6	1500	7.802
6	2000	1.434
6	2500	0.3250
6	3000	0.08314
6	3500	0.02264
6	4000	0.006433
6	4500	0.001849
6	5000	0.0005384
6	5500	0.0001535
6	6000	0.00004408
6	6500	0.00001187

Table 15: Summary of simulated Z' signal samples.

Signal mass in GeV	$\sigma \cdot \text{BR}(Z' \rightarrow e\mu)$ in pb
500	10.11
600	4.772
700	2.605
800	1.844
900	1.181
1000	0.6157
1100	0.4658
1200	0.3278
1300	0.2398
1400	0.1635
1500	0.1329
1600	0.09283
1700	0.06432
1800	0.04263
1900	0.04336
2000	0.03056
2200	0.02034
2400	0.01184
2600	0.007589
2800	0.004399
3000	0.002951
3500	0.001134
4000	0.0005233
4500	0.0002056
5000	0.0001126

A.3 BACKGROUND SIMULATION

Table 16: Information about the background Monte Carlo samples from the official production.

Generator	Process	Kinematic Cuts (in GeV)	σ_{used} (pb)	k-fact used	N_{events}
Drell-Yan					
POWHEG	$Z \rightarrow \mu\mu$	$50 \leq m_{\mu\mu} \leq 120$	1975.0	No	2.8M
POWHEG	$Z \rightarrow \mu\mu$	$120 \leq m_{\mu\mu} \leq 200$	19.32	No	100k
POWHEG	$Z \rightarrow \mu\mu$	$200 \leq m_{\mu\mu} \leq 400$	2.731	No	100k
POWHEG	$Z \rightarrow \mu\mu$	$400 \leq m_{\mu\mu} \leq 800$	0.241	No	100k
POWHEG	$Z \rightarrow \mu\mu$	$800 \leq m_{\mu\mu} \leq 1400$	0.01678	No	100k
POWHEG	$Z \rightarrow \mu\mu$	$1400 \leq m_{\mu\mu} \leq 2300$	0.00139	No	100k
POWHEG	$Z \rightarrow \mu\mu$	$2300 \leq m_{\mu\mu} \leq 3500$	8.948e-05	No	100k
POWHEG	$Z \rightarrow \mu\mu$	$3500 \leq m_{\mu\mu} \leq 4500$	4.135e-06	No	100k
POWHEG	$Z \rightarrow \mu\mu$	$4500 \leq m_{\mu\mu} \leq 6000$	4.56e-07	No	100k
POWHEG	$Z \rightarrow \mu\mu$	$m_{\mu\mu} \geq 6000$	2.066e-08	No	100k
POWHEG	$Z \rightarrow ee$	$50 \leq m_{ee} \leq 120$	1975.0	No	3M
POWHEG	$Z \rightarrow ee$	$120 \leq m_{ee} \leq 200$	19.32	No	100k
POWHEG	$Z \rightarrow ee$	$200 \leq m_{ee} \leq 400$	2.731	No	100k
POWHEG	$Z \rightarrow ee$	$400 \leq m_{ee} \leq 800$	0.241	No	100k
POWHEG	$Z \rightarrow ee$	$800 \leq m_{ee} \leq 1400$	0.01678	No	100k
POWHEG	$Z \rightarrow ee$	$1400 \leq m_{ee} \leq 2300$	0.00139	No	100k
POWHEG	$Z \rightarrow ee$	$2300 \leq m_{ee} \leq 3500$	8.948e-05	No	100k
POWHEG	$Z \rightarrow ee$	$3500 \leq m_{ee} \leq 4500$	4.135e-06	No	100k
POWHEG	$Z \rightarrow ee$	$4500 \leq m_{ee} \leq 6000$	4.56e-07	No	100k
POWHEG	$Z \rightarrow ee$	$m_{ee} \geq 6000$	2.066e-08	No	100k
amcatnlo	$Z \rightarrow \tau\tau \rightarrow e\mu$	-	1867	No	25M
t\bar{t}					
POWHEG	$t\bar{t} \rightarrow 2\ell 2\nu$	-	76.6311 (LO)	Yes, 1.116	104M
t\bar{t} tail samples					
POWHEG	$t\bar{t}$	$500 \leq m_{\ell\ell} \leq 800$	0.286	Yes, 1.116	200k
POWHEG	$t\bar{t}$	$800 \leq m_{\ell\ell} \leq 1200$	0.02864	Yes, 1.116	199k
POWHEG	$t\bar{t}$	$1200 \leq m_{\ell\ell} \leq 1800$	0.002677	Yes, 1.116	199k
POWHEG	$t\bar{t}$	$m_{\ell\ell} \geq 1800$	0.0001533	Yes, 1.116	40k
Single top					
POWHEG	$tq \rightarrow \ell\nu b q$ (t channel)	-	103.02 (NNLO)	No	3.3M
POWHEG	$\bar{t}q \rightarrow \ell\nu \bar{b} q$ (t channel)	-	80.95 (NNLO)	No	1.7M
POWHEG	$tW \rightarrow 2\ell 2\nu b$	-	38.09 (NNLO)	No	1M
POWHEG	$\bar{t}W \rightarrow 2\ell 2\nu \bar{b}$	-	38.09 (NNLO)	No	1M
amcatnlo	$tq/\bar{t}q \rightarrow \ell\nu b q/\bar{b} q$ (s channel)	-	3.36 (NLO)	No	1M
$W\gamma$					
MADGRAPH	$W\gamma \rightarrow \ell\nu\gamma$	-	405.271 (LO)	1.2066	6M
MADGRAPH	$W\gamma \rightarrow \ell\nu\gamma$	$p_T^\gamma > 500$	0.012 (LO)	1.2066	1M
Diboson					
POWHEG	$WZ \rightarrow 3\ell\nu$	-	4.42965 (NLO)	No	1.9M
POWHEG	$ZZ \rightarrow 2\ell 2\nu$	-	0.5644 (NNLO)	No	8.4M
POWHEG	$ZZ \rightarrow 4\ell$	-	1.256 (NNLO)	No	6.7M
POWHEG	$WW \rightarrow 4q$	-	51.723 (NNLO)	No	2M
POWHEG	$WW \rightarrow \ell\nu q q$	-	49.997 (NNLO)	No	2M
POWHEG	$WW \rightarrow 2\ell 2\nu$	-	12.178 (NNLO)	No	1.9M
WW tail samples					
POWHEG	$WW \rightarrow 2\ell 2\nu$	$200 \leq m_{\ell\ell} \leq 600$	0.1322	No	200k
POWHEG	$WW \rightarrow 2\ell 2\nu$	$600 \leq m_{\ell\ell} \leq 1200$	0.005404	No	200k
POWHEG	$WW \rightarrow 2\ell 2\nu$	$1200 \leq m_{\ell\ell} \leq 2500$	0.0003393	No	198k
POWHEG	$WW \rightarrow 2\ell 2\nu$	$m_{\ell\ell} \geq 2500$	0.000051484	No	39k

CONVENTIONS

B.1 DEFINITIONS IN ADDITIONAL DISTRIBUTIONS

In various distributions throughout this thesis, additional figures are used to make features or agreement between different parts of the distribution more clear. The exact definitions of the quantities shown in these additional figures are given below.

- **Ratio:** The ratio of number of observed data events to expected background or MC events is shown in many figures. The calculation of the ratio is done for each individual bin with its corresponding uncertainty band, derived from the systematic uncertainties on the background expectation $\sigma(N_{MC})$. Data/MC ratio R , defined as:

$$R = \frac{N_{data}}{N_{MC}}$$

With the uncertainty:

$$\sigma(R) = \frac{N_{data}}{N_{MC}} \cdot \sigma(N_{MC})$$

- **Residuals:** The residuals are calculated to quantify the agreement of a parameterization with the points it is fitted to. The residuals q are calculated for each bin x in a distribution from the content of the bin y and the value of the parameterization in this bin $f(x)$.

$$q = y - f(x)$$

The uncertainty $\sigma(q)$ is then derived from the uncertainty of the bin content $\sigma(y)$

$$\sigma(q) = \sigma(y)$$

- **Pulls:** The pulls are calculated to quantify the agreement of a parameterization with the points it is fitted to. The pulls are residuals normalized to the uncertainty of the distribution. The pulls p are calculated for each bin x in a distribution from the content of the bin y , the value of the parameterization in this bin $f(x)$ and the uncertainty of the bin content $\sigma(y)$.

$$p = \frac{y - f(x)}{\sigma(y)}$$

The uncertainty $\sigma(p)$ is then derived from the uncertainty of the bin content $\sigma(y)$

$$\sigma(p) = \frac{\sigma(y)}{\sigma(y)} = 1$$

B.2 COORDINATE SYSTEM

The origin of the CMS coordinate system is the nominal collision point in the center of the experiment [113]. The y-axis is defined as pointing vertically upwards, and the x-axis is pointing radially inward toward the center of the LHC. The z-axis is therefore defined along the beam axis. In the x-y-plane, the radial coordinate r and the azimuthal angle ϕ (starting at the x-axis) are measured. The polar angle θ is measured in the y-z-plane from the z-axis. The polar angle is usually expressed via the pseudorapidity η which is defined as $\eta = -\ln \tan(\theta/2)$, because differences in η are Lorentz invariant.

B.3 CONVENTIONS

Definition of quantities used in this analysis:

- p_T
 p_T is the momentum perpendicular to the beam axis. It is defined by $p_T = p \cdot \sin\theta$
- \cancel{E}_T
 The missing transverse energy \cancel{E}_T (or E_T^{miss}) represents the vector sum of \vec{p}_T of all not measured particles. The particles leave the detector, but the momentum and energy perpendicular to the beam axis must be zero, because it was zero before the collision. With the conservation of momentum it must be zero afterwards.

B.3.1 *Natural units*

Throughout this whole analysis, natural units in the sense that

$$\hbar = c = k_B = 1 \tag{37}$$

with the reduced Planck constant \hbar , the speed of light c and the Boltzmann constant k_B are used. With this convention, the relevant quantities for this analysis, momenta, masses and energies can all be expressed in eV.

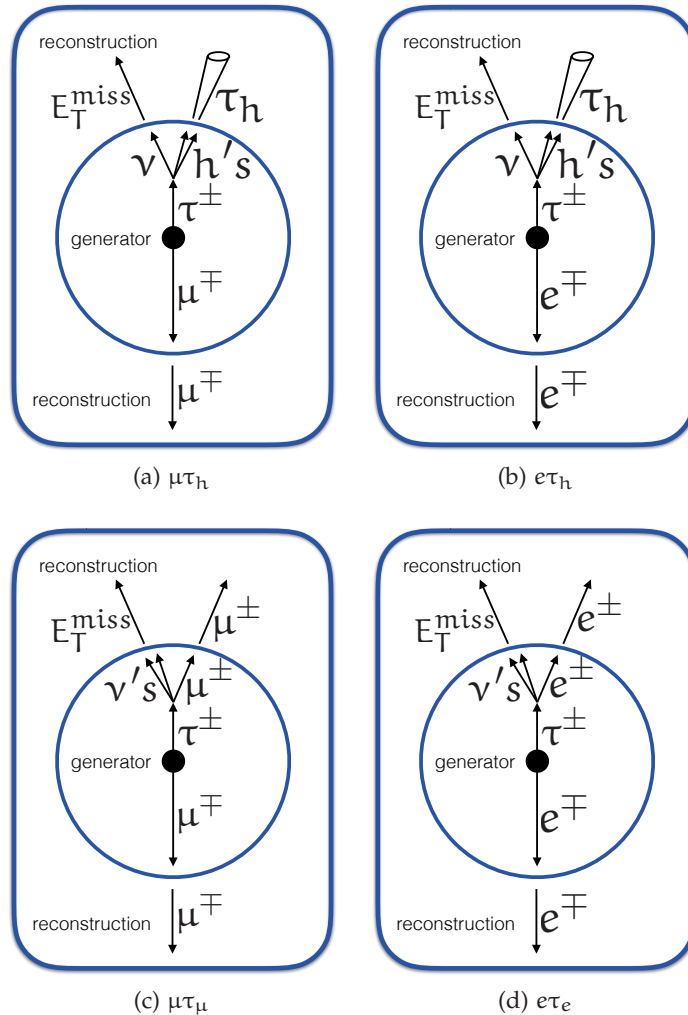


Figure 100: Schematic illustration of the possible channels with two charged leptons that do not conserve lepton number and are not studied in this analysis. Shown is the part of the interaction which is not detected, labeled generator, which is the production of $e\tau$ or $\mu\tau$ and the subsequent decay of the tau if applicable in either electron muon or hadrons plus neutrinos. On the outside the signature of the event as seen in the detector is illustrated, labeled reconstruction. The charged leptons are reconstructed as they are, the hadrons are reconstructed as a hadronic jet, while the neutrinos can be detected only indirectly as missing E_T .

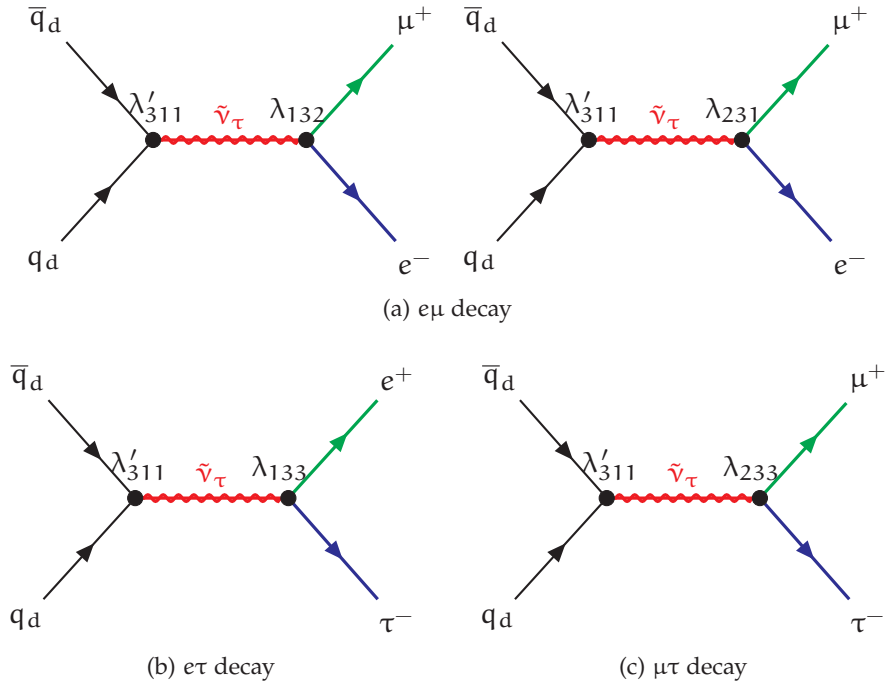


Figure 101: Resonant production of a $\tilde{\nu}_\tau$ in $d\bar{d}$ annihilation and subsequent decay into a $e\mu$ pair (top row) with the production and the two possible decay couplings λ'_{311} and λ_{132} or λ_{231} . In the second row the production of the $e\tau$ or $\mu\tau$ final states via the couplings λ_{133} and λ_{233} are shown.

Table 17: Scale factors for the muon trigger, applied in the analysis to correct the different efficiencies in the observed data and the simulation. The scale factors are all determined with the Tag and Probe method by the muon group of CMS. The scale factors are mostly very close to unity and are determined as a function of p_T and $|\eta|$.

p_T range (GeV)	$0.0 < \eta < 0.9$	$0.9 < \eta < 1.2$	$1.2 < \eta < 2.1$	$2.1 < \eta < 2.4$
$52 < p_T < 55$	0.97695 ± 0.00062	0.95294 ± 0.00079	0.98649 ± 0.00105	0.91691 ± 0.00286
$55 < p_T < 60$	0.98168 ± 0.00065	0.95809 ± 0.00098	0.99263 ± 0.00112	0.93428 ± 0.00290
$60 < p_T < 80$	0.98096 ± 0.00061	0.95766 ± 0.00089	0.99387 ± 0.00104	0.93956 ± 0.00277
$80 < p_T < 120$	0.97889 ± 0.00153	0.95330 ± 0.00230	0.99120 ± 0.00251	0.94508 ± 0.00715
$120 < p_T < 200$	0.97156 ± 0.00257	0.94037 ± 0.00745	0.99685 ± 0.00558	0.96414 ± 0.02094
$200 < p_T < 300$	0.97724 ± 0.00683	0.94351 ± 0.01860	0.95613 ± 0.01694	0.82307 ± 0.14418
$300 < p_T < 400$	1.00521 ± 0.01699	0.94253 ± 0.03891	1.12374 ± 0.13813	1.00338 ± 0.06692
$400 < p_T < 800$	0.96481 ± 0.03469	0.97546 ± 0.05785	0.90319 ± 0.16419	0.74985 ± 0.29108

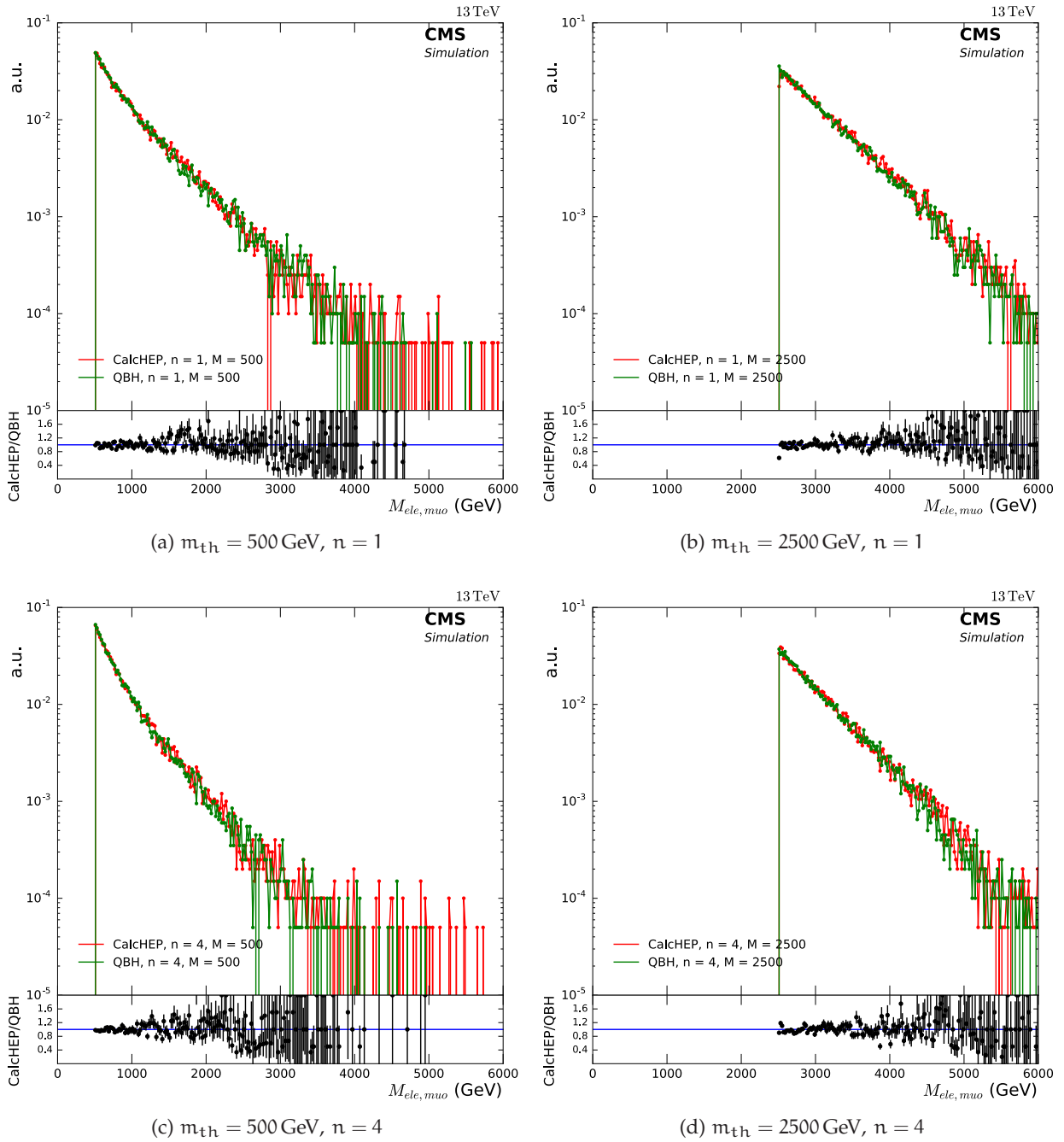


Figure 102: Shape comparison of QBH signal produced with the QBH generator (green) and CalcHEP (red). Shown is the invariant mass distribution of both generators normalized to unity to compare the shapes. The normalization is compared in Fig. 18. Also the ratio of the two generators is plotted as a function of mass. The two left distributions are for a threshold mass of 500 GeV, the right two distributions for 2500 GeV. The top row distributions are for $n = 1$ extra dimensions, while the bottom row is for $n = 4$. No significant difference between the distributions from both generators can be found.

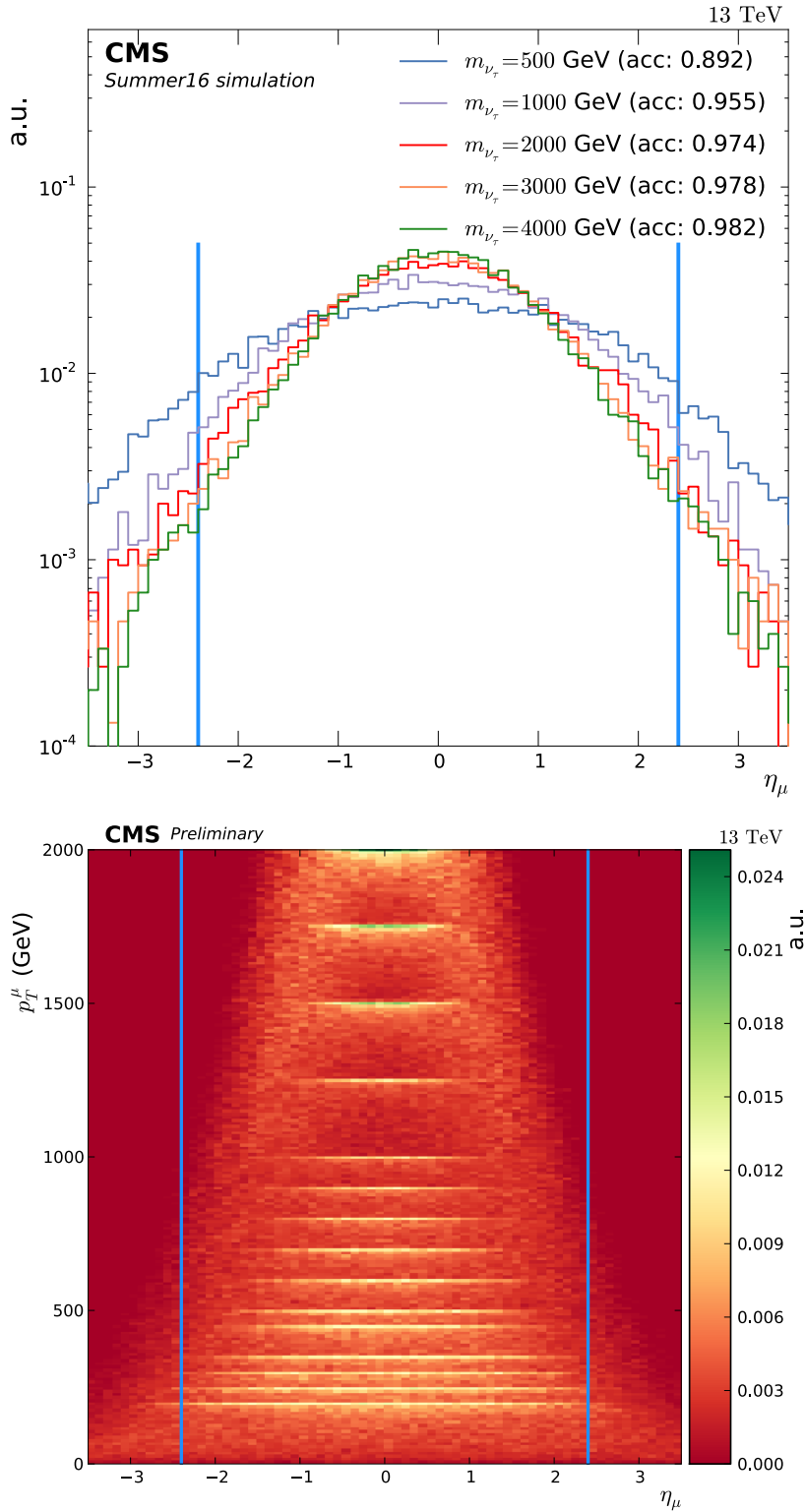


Figure 103: Study of the muon acceptance (as defined in (1) in Sec. 4.2.2) for the RPV signal model. The upper figure shows the η_μ distributions for different values of $m_{\tilde{\nu}_\tau}$, normalized to unity. Also shown is the acceptance requirement $|\eta| < 2.4$ as well as the resulting fraction of accepted events in the legend. It can be seen that the fraction of events in the acceptance regions increases and saturates for $m_{\tilde{\nu}_\tau} \sim 2$ TeV at $\sim 98\%$. This is expected for a uniform distribution in $\cos\theta$ of the muon. The lower figure shows the p_T of the muon against η_μ as well as the acceptance criteria. It can be seen that for higher p_T , the distribution become more central. This is due to the effect that the muons are uniformly distributed in $\cos\theta$ and the momentum is about half the mass of $\tilde{\nu}_\tau$, but higher values of η result in lower p_T as a bigger momentum fraction is carried along the z axis. Therefore, all muons at high eta are shifted to lower p_T , resulting in the very high acceptance of muons at high p_T . The same argument can also be made for electrons with the acceptance shown in Fig. 19.

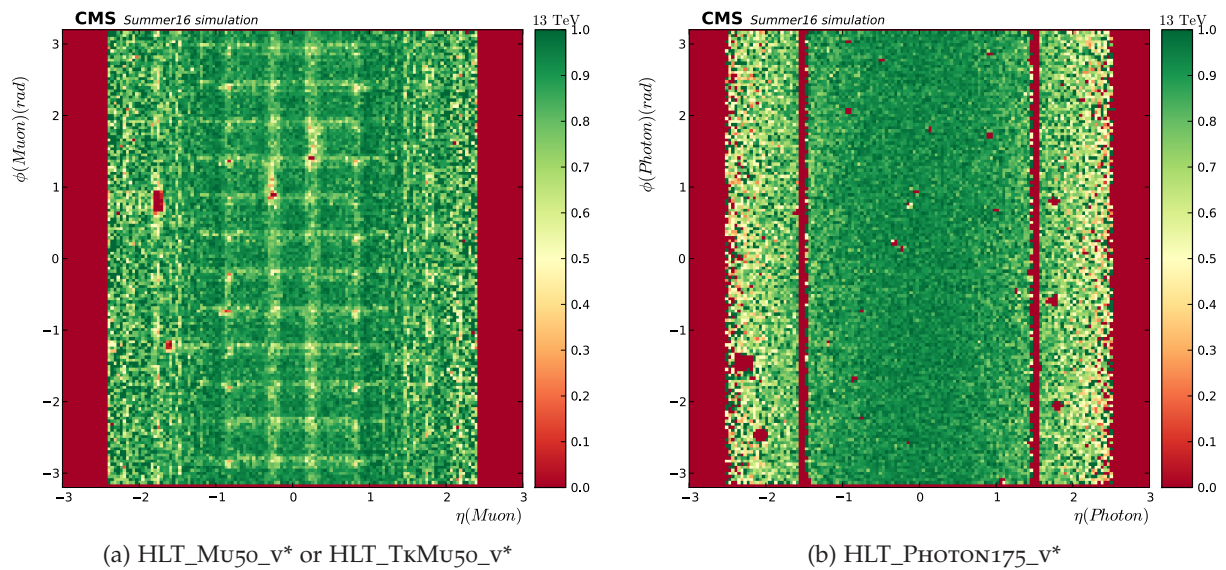


Figure 104: Trigger efficiency for muons and electrons each as a function of η and ϕ . The efficiencies are defined in Eq. 13 and Eq. 14 for muons and electrons respectively. The efficiencies are determined on RPV signal simulation, but as they are determined for electron and muon individually they are also applicable to other signals. The features seen in the efficiencies are purely due to the geometry of the used detector components. In the single muon trigger efficiency the shape and coverage of the muon chambers can be seen, while in the cracks between the chambers the efficiency is lower. For the single photon trigger the shape of the ECAL and especially the transition region between barrel and end caps can be seen.

Table 18: Scale factors for the muon identification (as defined in (1)-(2) in Sec. 4.2.2), applied in the analysis to correct the different efficiencies in the observed data and the simulation. The scale factors are all determined with the Tag and Probe method by the muon group of CMS. The scale factors are all very close to unity and are determined as a function of p_T and $|\eta|$.

p_T range (GeV)	$0.0 < \eta < 0.9$	$0.9 < \eta < 1.2$	$1.2 < \eta < 2.1$	$2.1 < \eta < 2.4$
$20 < p_T < 25$	0.98743 ± 0.00224	0.97473 ± 0.01198	0.98729 ± 0.00125	0.97842 ± 0.00354
$25 < p_T < 30$	0.98433 ± 0.02517	0.97375 ± 0.01877	0.98721 ± 0.00121	0.97540 ± 0.02131
$30 < p_T < 40$	0.98571 ± 0.00029	0.97631 ± 0.00155	0.98916 ± 0.00032	0.97489 ± 0.00089
$40 < p_T < 50$	0.98731 ± 0.02063	0.97784 ± 0.00032	0.99040 ± 0.00023	0.97625 ± 0.00056
$50 < p_T < 55$	0.98342 ± 0.00069	0.97689 ± 0.00112	0.98673 ± 0.00946	0.97087 ± 0.00210
$55 < p_T < 60$	0.98284 ± 0.00114	0.97665 ± 0.00386	0.98606 ± 0.00129	0.96643 ± 0.00363
$60 < p_T < 120$	0.99379 ± 0.00130	0.97784 ± 0.00201	0.99006 ± 0.00366	0.96755 ± 0.00392

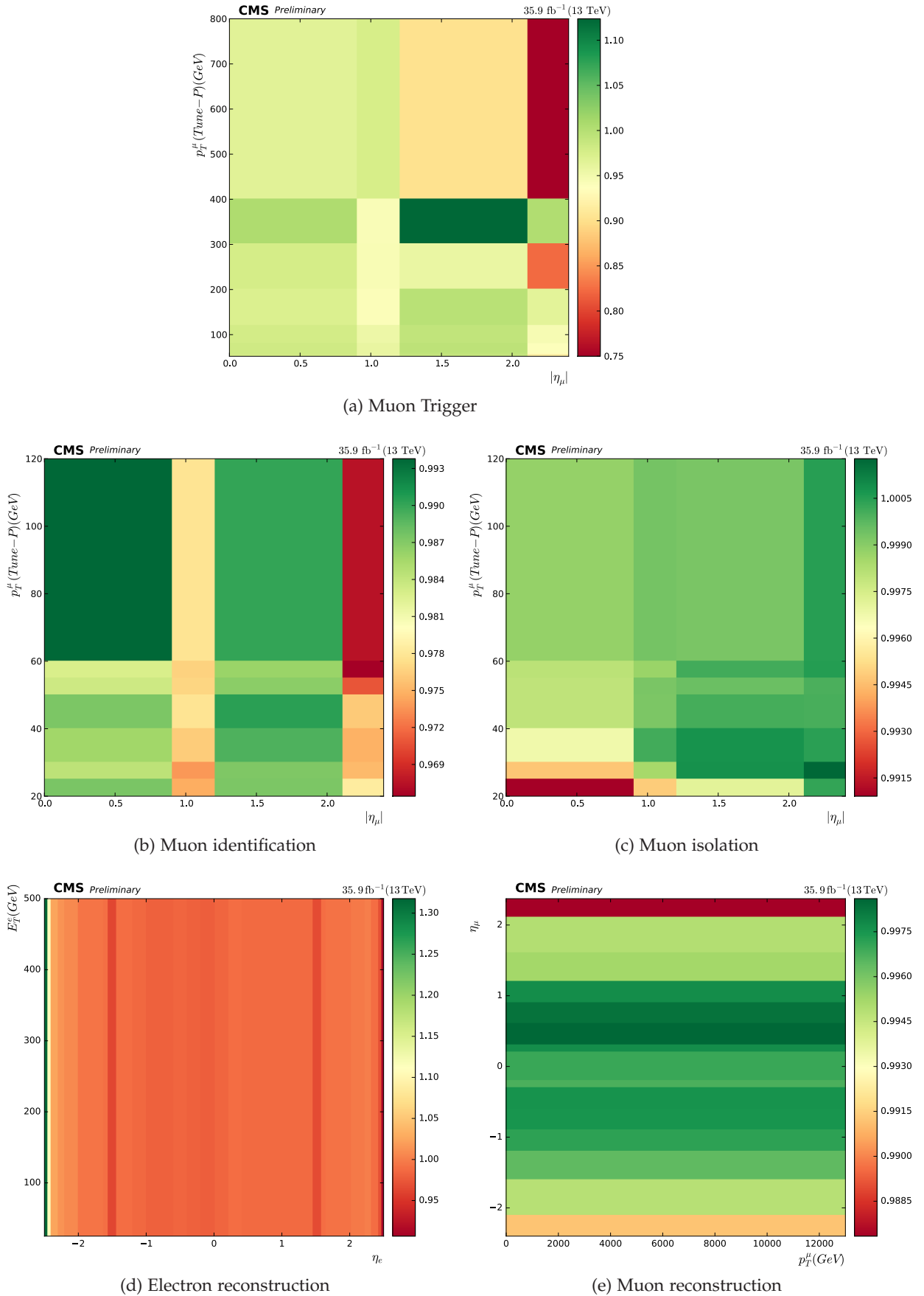


Figure 105: Scale factors applied in the analysis to correct the different efficiencies in the observed data and the simulation. The scale factors are all determined with the Tag and Probe method by the muon or egamma group of CMS. The scale factors are all very close to unity and are determined as a function of p_T and $|\eta|$. The five shown scale factors are for the two muon triggers combined, the muon identification, the muon isolation, the electron reconstruction and the muon reconstruction.

Table 19: Scale factors for the muon isolation (as defined in (3) in Sec. 4.2.2), applied in the analysis to correct the different efficiencies in the observed data and the simulation. The scale factors are all determined with the Tag and Probe method by the muon group of CMS. The scale factors are all very close to unity and are determined as a function of p_T and $|\eta|$.

p_T range (GeV)	$0.0 < \eta < 0.9$	$0.9 < \eta < 1.2$	$1.2 < \eta < 2.1$	$2.1 < \eta < 2.4$
$20 < p_T < 25$	0.99091 ± 0.00106	0.99485 ± 0.00164	0.99713 ± 0.00081	1.00030 ± 0.00125
$25 < p_T < 30$	0.99472 ± 0.00052	0.99850 ± 0.00096	1.00080 ± 0.00049	1.00177 ± 0.00076
$30 < p_T < 40$	0.99674 ± 0.00016	1.00011 ± 0.00030	1.00077 ± 0.00018	1.00043 ± 0.00029
$40 < p_T < 50$	0.99796 ± 0.00008	0.99922 ± 0.00476	1.00006 ± 0.00009	1.00002 ± 0.00011
$50 < p_T < 55$	0.99798 ± 0.00019	0.99925 ± 0.00439	0.99948 ± 0.00020	0.99995 ± 0.00058
$55 < p_T < 60$	0.99804 ± 0.00027	0.99868 ± 0.00027	1.00008 ± 0.00031	1.00054 ± 0.00057
$60 < p_T < 120$	0.99880 ± 0.00022	0.99932 ± 0.00039	0.99924 ± 0.00023	1.00047 ± 0.00053

Table 20: Cut-flow table of events in the $e\tau_\mu$ channel. Shown are the number of integrated events after each selection step (as defined in Sec. 4.6.1) for the observed data, an example RPV signal, and the background expectation. The background expectation is given also split in the different contributing processes. For the number of signal events as well as the total background expectation the fraction of events with respect to the pre-selection level are given.

Selection step	pre-selection	$\Delta\phi(e, \mu)$	$\Delta\phi(\mu, E_T^{\text{miss}})$	p_T^e/p_T^μ	p_T^e/p_T^τ
Data	76984	50550	15730	7330	7329
RPV, $m_{\tilde{\nu}_\tau} = 1 \text{ TeV}$, $\lambda = \lambda' = 0.01$	6376	6337	6319	6255	6244
event fraction	1.00	0.99	0.99	0.98	0.98
Total background	80725	53914	17099	7903	7901
event fraction	1.00	0.67	0.21	0.10	0.10
Jet \rightarrow e mis – identification	1398	1138	683	280	280
$W\gamma$	959	574	249	154	154
Drell – Yan	855	317	112	77	77
Single t	6504	4410	1366	677	676
WW, WZ, ZZ	5551	3875	975	585	584
$t\bar{t}$	65457	43600	13715	6131	6130

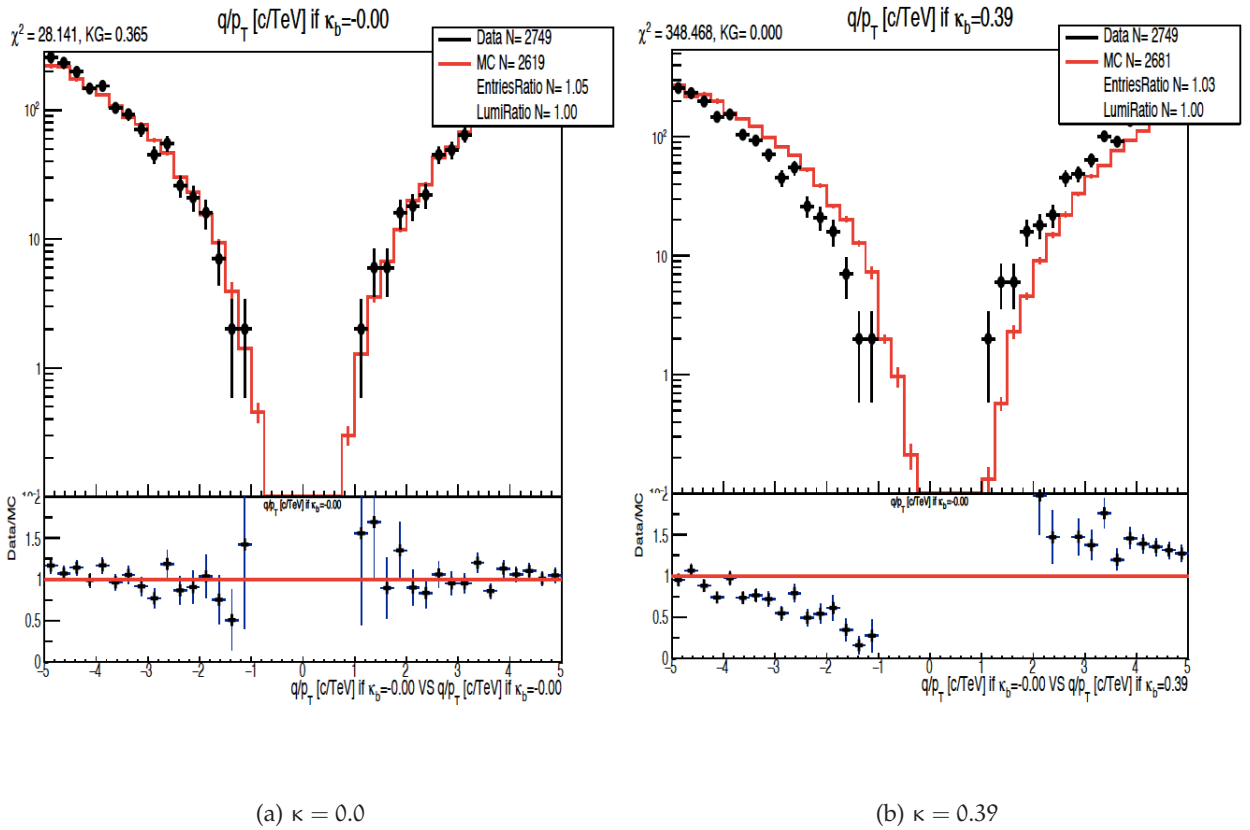
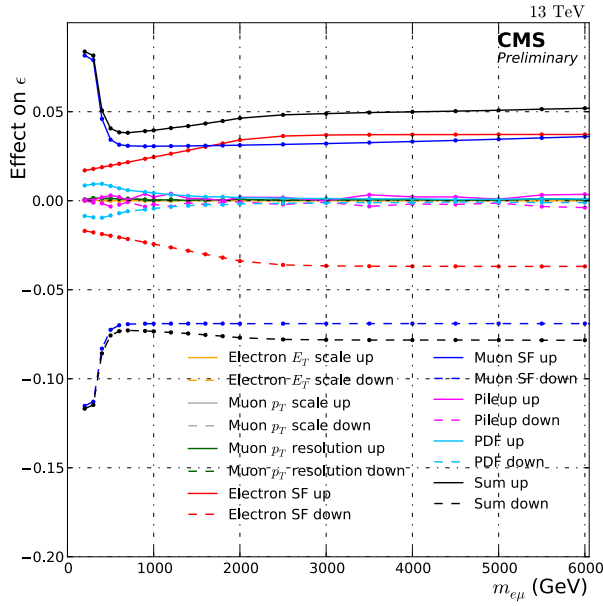
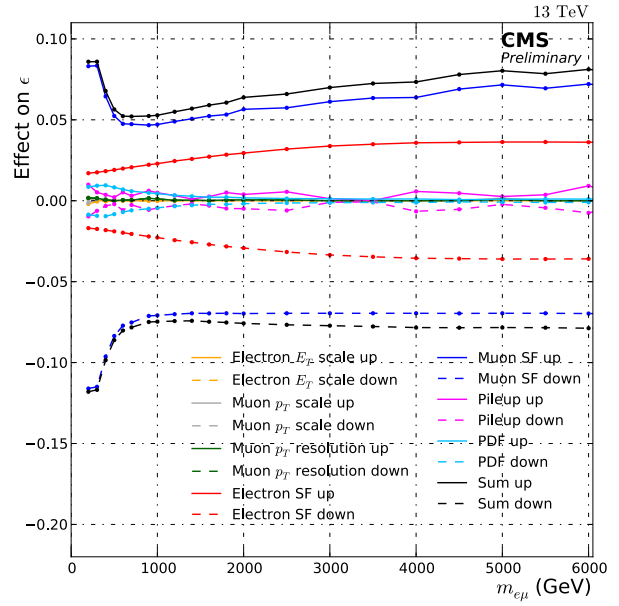


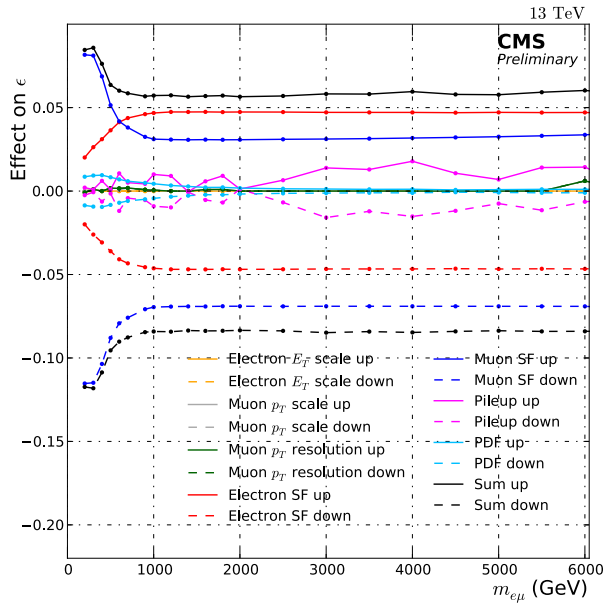
Figure 106: Distribution of q/p_T for the observed data as well as simulated events. The left distribution shows the events without any additional bias κ . In the simulated events in the right distribution a bias of $\kappa = 0.39$ was injected (both from Ref. [93]). It can be clearly seen that a bias of zero results in a better agreement between simulation and the data. Calculating now a χ^2 as a measure for the agreement between simulation and data as a function of the injected κ allows to identify the bias that leads to the best agreement between data and simulation as well as the uncertainty.



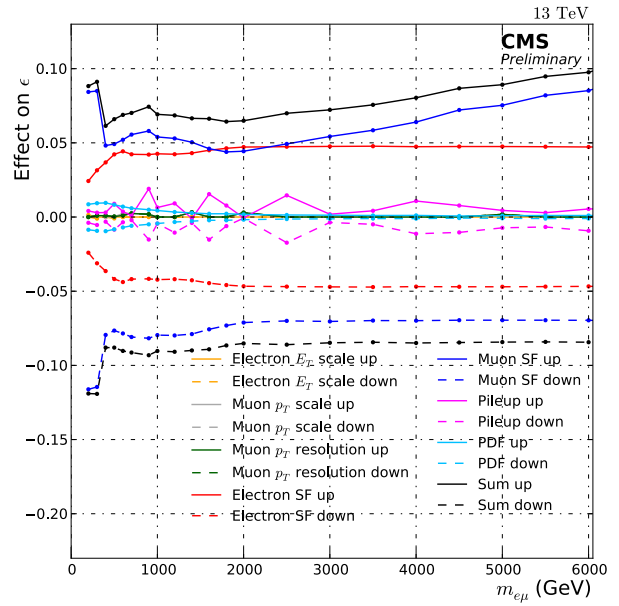
(a) Barrel-Barrel



(b) Barrel-Endcap

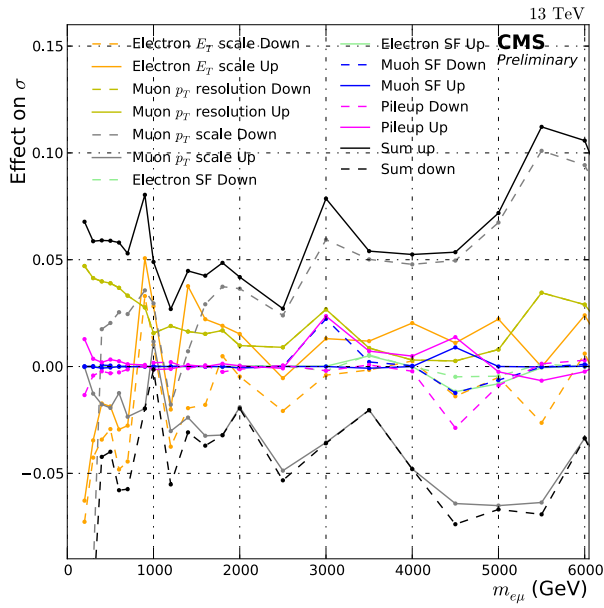


(c) Endcap-Barrel

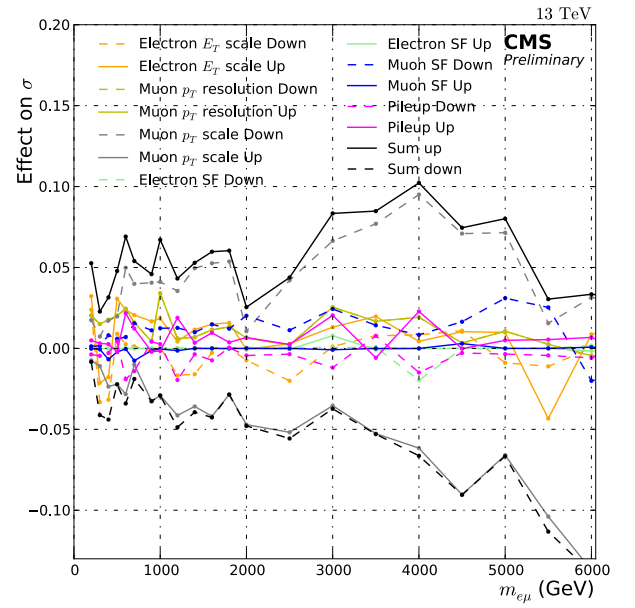


(d) Endcap-Endcap

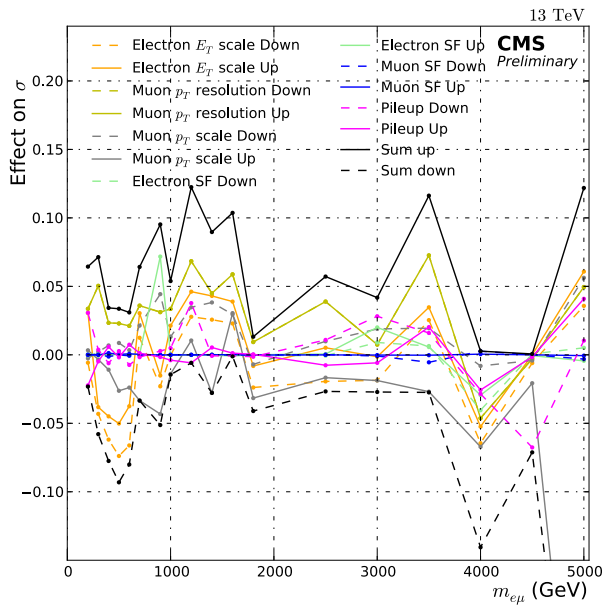
Figure 107: Effect of the systematic uncertainties on the RPV SUSY signal as a function of $\tilde{\nu}_\tau$ mass. The figures show the relative effect on the acceptance times efficiency, which is dominated by the muon scale factor uncertainty. The contributions are shown for all four event categories of the $e\mu$ channel.



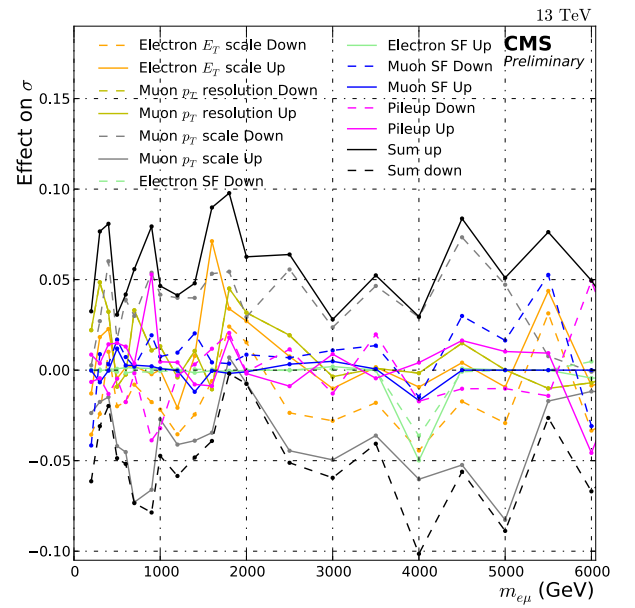
(a) Barrel-Barrel



(b) Barrel-Endcap



(c) Endcap-Barrel



(d) Endcap-Endcap

Figure 108: Effect of the systematic uncertainties on the RPV SUSY signal as a function of $\tilde{\nu}_\tau$ mass. The figures show the relative effect on the invariant mass resolution and therefore the signal width, which is dominated by the muon p_T scale uncertainty. The contributions are shown for all four event categories of the $e\mu$ channel.

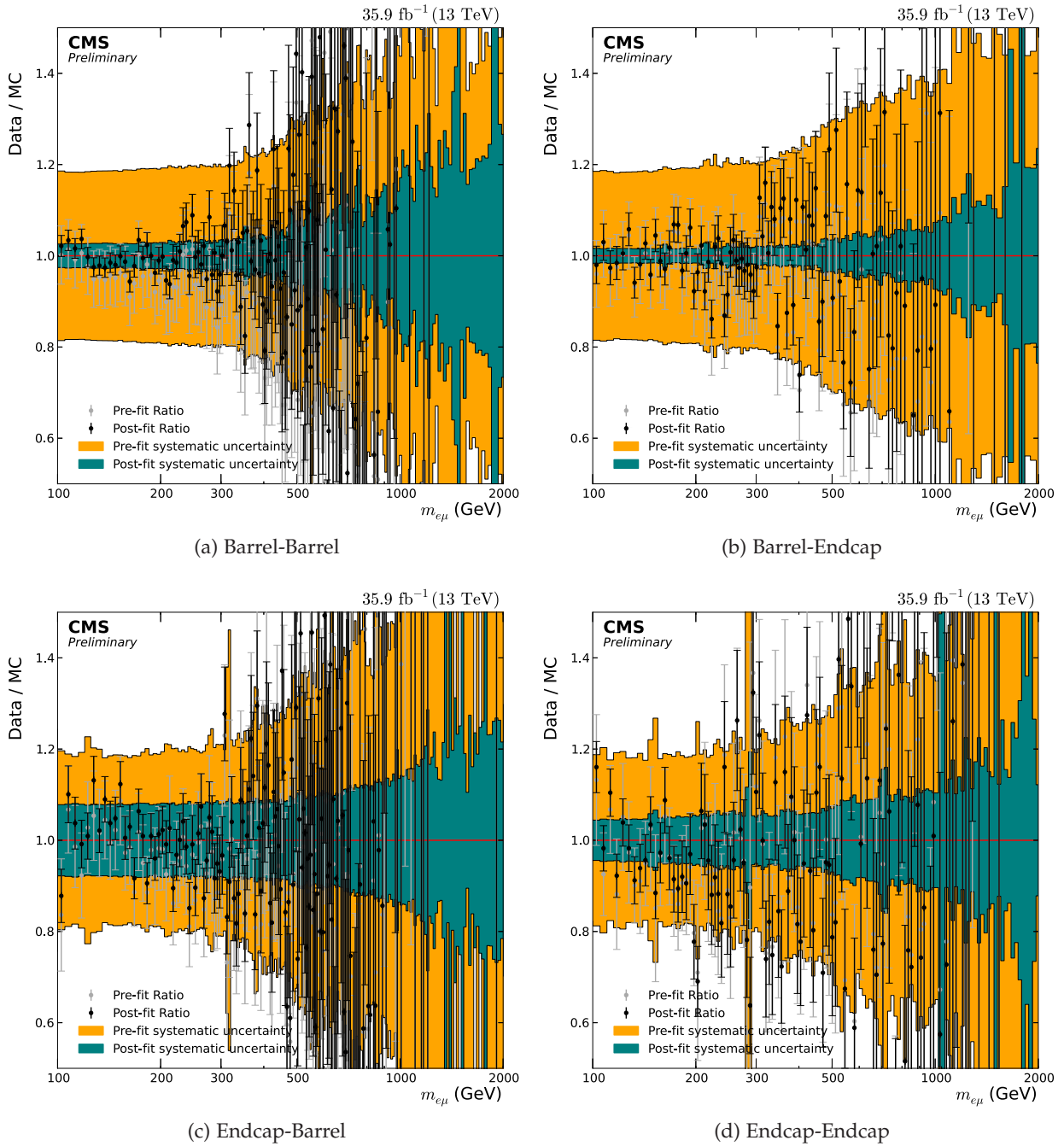


Figure 109: Comparison of the pre-fit and post-fit ratios of the invariant mass distribution shown in Fig. ?? and Fig. ?? for the different event categories in the $e\mu$ channel. The pre-fit ratio in grey with the corresponding systematic uncertainty in orange, as well as the post-fit ratio in black with its systematic uncertainty in green is shown for each category. The systematic uncertainties are reduced by a large factor ranging from two to five in the post-fit, while the ratio gets closer to unity in all categories.

Table 21: Cut-flow table of events in the $\mu\tau_e$ channel. Shown are the number of integrated events after each selection step (as defined in Sec. 4.6.2) for the observed data, an example RPV signal, and the background expectation. The background expectation is given also split in the different contributing processes. For the number of signal events as well as the total background expectation the fraction of events with respect to the pre-selection level are given.

Selection step	pre-selection	$\Delta\phi(e, \mu)$	$\Delta\phi(\mu, E_T^{\text{miss}})$	p_T^e/p_T^μ	p_T^e/p_T^τ
Data	76983	50549	16355	11590	11589
RPV, $m_{\tilde{\nu}_\tau} = 1 \text{ TeV}$, $\lambda = \lambda' = 0.01$	7451	7352	7308	7078	7061
event fraction	1.00	0.99	0.98	0.95	0.95
Total background	80726	53913	17462	12359	12354
event fraction	1.00	0.67	0.22	0.15	0.15
Jet \rightarrow e mis – identification	1398	1138	74	67	67
$W\gamma$	959	574	110	81	81
Drell – Yan	856	317	162	155	155
Single t	6504	4410	1461	1043	1041
WW, WZ, ZZ	5551	3875	1114	906	905
$t\bar{t}$	65458	43599	14541	10106	10104

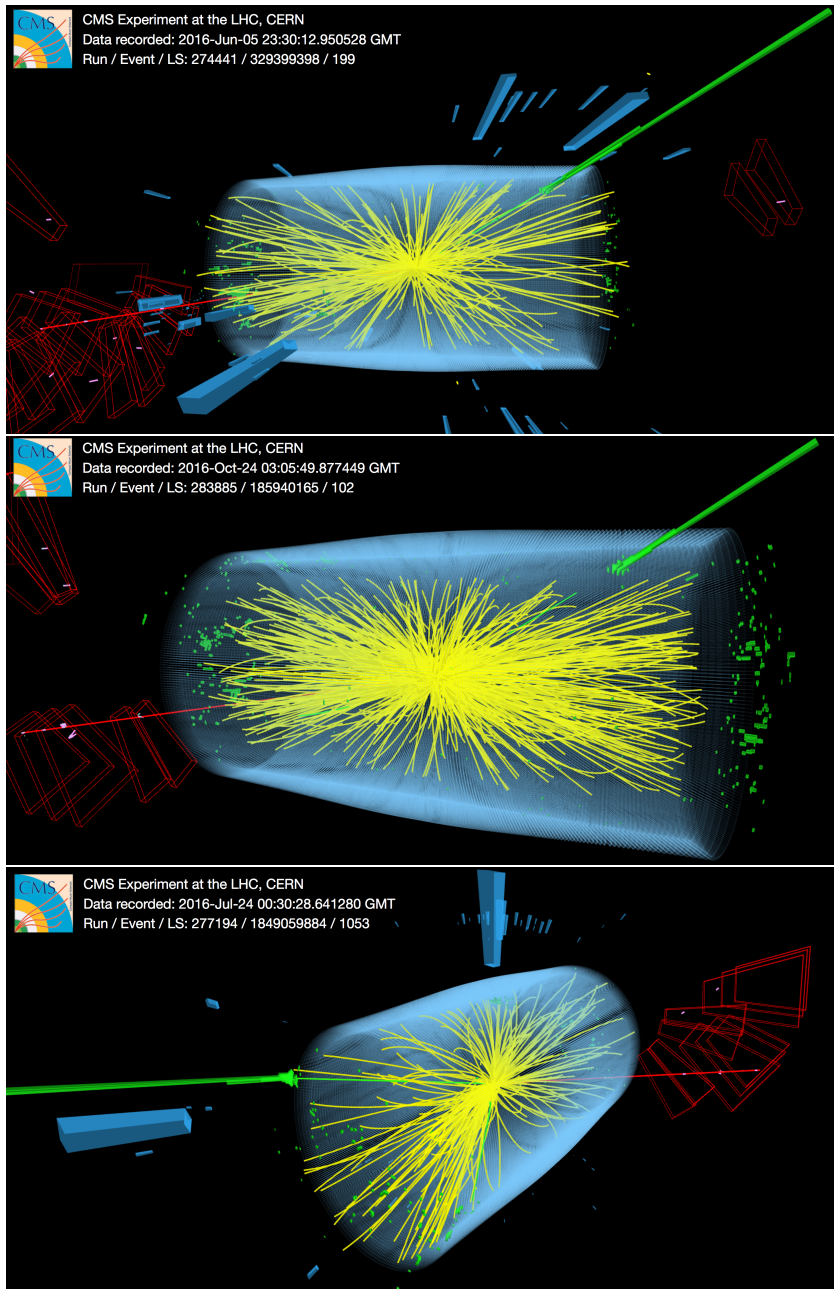


Figure 110: Event visualization of the three next to highest invariant mass events in the $e\mu$ channel, that was recorded in 2016. Clearly visible are the muons in red, with the corresponding hits in the muon chambers, as well as the energy deposits in the ECAL in green from the electrons. The $e\mu$ pair in the top event has an invariant mass of 1759 GeV, the one in the center 1600 GeV and the bottom one 1547 GeV.

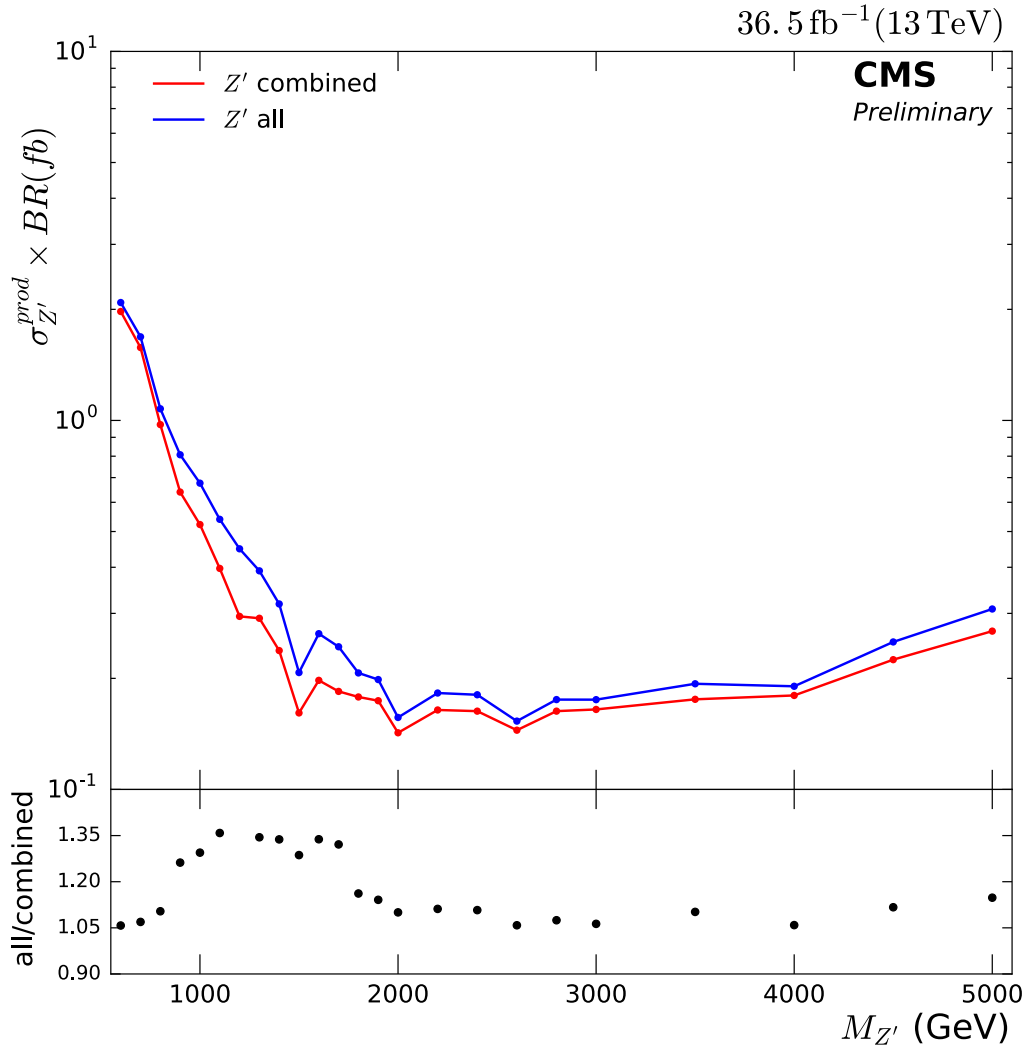


Figure 111: Comparison of the expected cross section limit at 95% confidence level for the Z' model with and without the event categorization. The combination of the four categories is shown in red, just calculating the limit from all events without the splitting in categories is shown in blue. The ratio of the two cross section limits is also shown at the bottom. The categorization improves the cross section limit over the whole mass range by at least 5% and up to 35% at masses around 1 TeV. Therefore, it is worse to split the events in categories to gain this additional reach in the cross section.

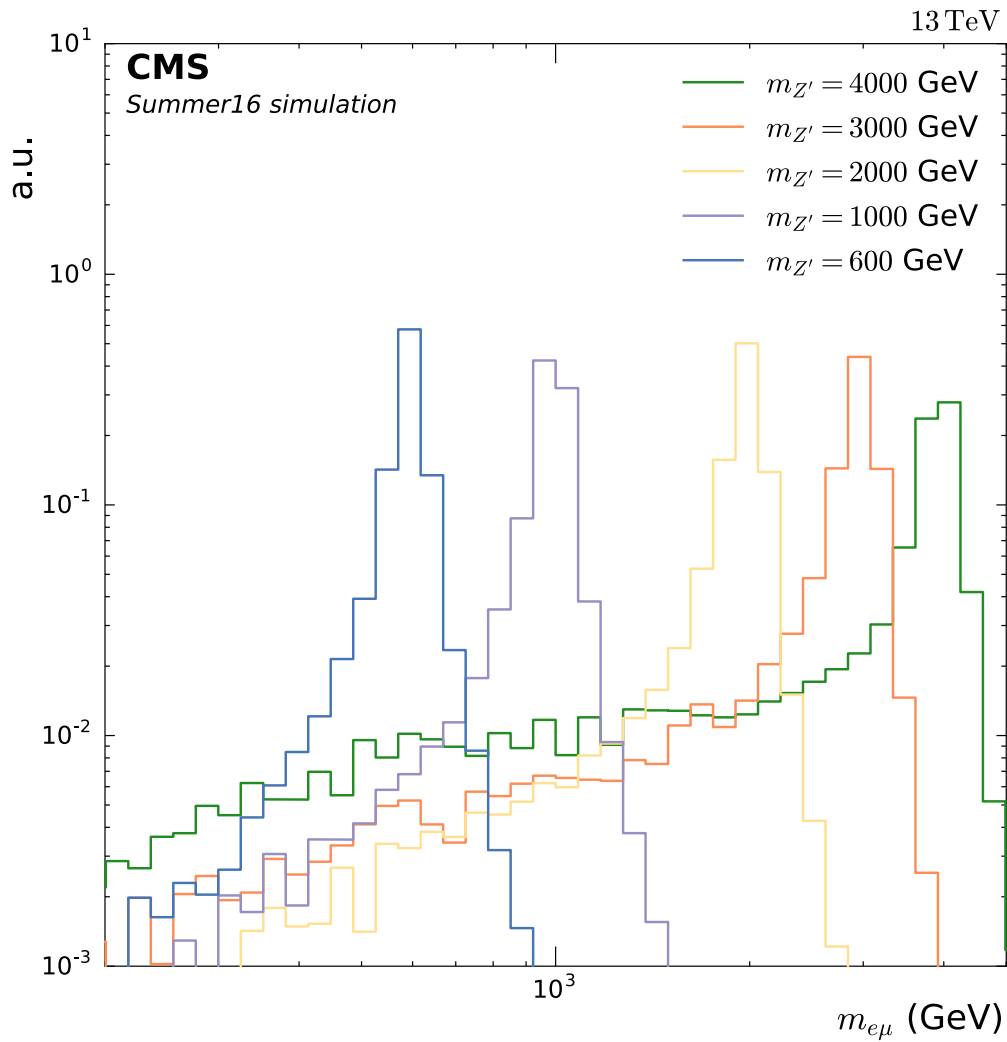


Figure 112: Shape comparison of the invariant mass distribution of five example Z' signals. All signals are normalized to compare only the shape. It can be seen while the resonant peak of the signal is similar for all $m_{Z'}$ values, the only difference being the mass resolution. At high $m_{Z'}$ the off-shell production at low $m_{e\mu}$ increases due to the non negligible width of the signal.

BIBLIOGRAPHY

- [1] CMS Collaboration. *Search for high-mass resonances and quantum black holes in the $e\mu$ final state in proton-proton collisions at $\sqrt{s} = 13$ TeV*. Tech. rep. CMS-PAS-EXO-16-001. Geneva: CERN, 2016. URL: <https://cds.cern.ch/record/2149046> (cit. on pp. 1, 17, 18, 124, 127, 139).
- [2] CMS Collaboration. “Search for lepton-flavor violating decays of heavy resonances and quantum black holes to $e\mu$ final states in proton-proton collisions at $\sqrt{s} = 13$ TeV.” In: *Submitted to JHEP* (2018). arXiv: 1802.01122 [hep-ex]. URL: <https://cds.cern.ch/record/2302916> (cit. on pp. 1, 139).
- [3] David J Griffiths. *Introduction to elementary particles; 2nd rev. version*. Physics textbook. New York: Wiley, 2008. URL: <https://cds.cern.ch/record/111880> (cit. on p. 5).
- [4] C. Patrignani and Particle Data Group. “Review of Particle Physics.” In: *Chinese Physics C* (2016), p. 100001. URL: <http://stacks.iop.org/1674-1137/40/i=10/a=100001> (cit. on pp. 5, 6, 42, 115).
- [5] Robert H. Bernstein and Peter S. Cooper. “Charged Lepton Flavor Violation: An Experimenter’s Guide.” In: *Phys. Rept.* (2013), pp. 27–64. DOI: 10.1016/j.physrep.2013.07.002. arXiv: 1307.5787 [hep-ex] (cit. on pp. 6, 17, 123).
- [6] Stephen P. Martin. “A Supersymmetry primer.” In: (1997). [Adv. Ser. Direct. High Energy Phys.18,1(1998)]. DOI: 10.1142/9789812839657_0001, 10.1142/9789814307505_0001. arXiv: 9709356 [hep-ph] (cit. on pp. 8, 9).
- [7] R. Barbier, C. Berat, et al. “R-parity violating supersymmetry.” In: *Phys. Rept.* (2005), pp. 1–202. DOI: 10.1016/j.physrep.2005.08.006. arXiv: 0406039 [hep-ph] (cit. on p. 9).
- [8] Particle Data Group, J. Beringer, et al. “Review of Particle Physics.” In: *Phys. Rev. D* (2012), p. 010001. DOI: 10.1103/PhysRevD.86.010001 (cit. on p. 9).
- [9] L. E. Ibanez and G. Ross. “Discrete gauge symmetries and the origin of baryon and lepton number conservation in supersymmetric versions of the standard model.” In: *Nucl. Phys. B* (1992), pp. 3–37. DOI: 10.1016/0550-3213(92)90195-H (cit. on p. 10).
- [10] Herbi K. Dreiner, Christoph Luhn, et al. “What is the discrete gauge symmetry of the MSSM?” In: *Phys. Rev. D* (2006), p. 075007. DOI: 10.1103/PhysRevD.73.075007. arXiv: 0512163 [hep-ph] (cit. on p. 10).
- [11] Peter W. Graham, David E. Kaplan, Surjeet Rajendran, and Prashant Saraswat. “Displaced Supersymmetry.” In: *JHEP* 07 (2012), p. 149. DOI: 10.1007/JHEP07(2012)149. arXiv: 1204.6038 [hep-ph] (cit. on p. 10).
- [12] Alexander Belyaev, Neil D. Christensen, et al. “CalcHEP 3.4 for collider physics within and beyond the Standard Model.” In: *Comput. Phys. Commun.* (2013), pp. 1729–1769. DOI: 10.1016/j.cpc.2013.01.014. arXiv: 1207.6082 [hep-ph] (cit. on pp. 11, 35).

- [13] H. K. Dreiner, S. Grab, et al. “Supersymmetric NLO QCD Corrections to Resonant Slepton Production and Signals at the Tevatron and the LHC.” In: *Phys. Rev. D* (2007), p. 035003. arXiv: [0611195 \[hep-ph\]](#) (cit. on pp. [12](#), [35](#), [142](#)).
- [14] Lisa Randall and Raman Sundrum. “A Large mass hierarchy from a small extra dimension.” In: *Phys. Rev. Lett.* (1999), pp. 3370–3373. DOI: [10.1103/PhysRevLett.83.3370](#). arXiv: [9905221 \[hep-ph\]](#) (cit. on p. [13](#)).
- [15] N. Arkani-Hamed, S. Dimopoulos, and R. Dvali. “The Hierarchy Problem and New Dimensions at a Millimeter.” In: *Phys. Lett. B* (1998), p. 263. arXiv: [9803315 \[hep-ph\]](#) (cit. on p. [13](#)).
- [16] Nemanja Kaloper. “Brane-induced gravity’s shocks.” In: *Phys. Rev. Lett.* 94 (2005). [Erratum: *Phys. Rev. Lett.*95,059901(2005)], p. 181601. DOI: [10.1103/PhysRevLett.94.181601](#). arXiv: [hep-th/0501028 \[hep-th\]](#) (cit. on p. [13](#)).
- [17] Csaba Csaki. “TASI lectures on extra dimensions and branes.” In: *From fields to strings: Circumnavigating theoretical physics. Ian Kogan memorial collection (3 volume set)*. 2004, pp. 605–698. arXiv: [0404096 \[hep-ph\]](#) (cit. on p. [13](#)).
- [18] X. Calmet. “A review of Quantum Gravity at the Large Hadron Collider.” In: *Mod. Phys. Lett A* (2010), p. 1553. arXiv: [1005.1805 \[hep-ph\]](#) (cit. on p. [13](#)).
- [19] H. Yoshino and Y. Nambu. “Black hole formation in the grazing collision of high-energy particles.” In: *Phys. Rev. D* (2003), p. 024009. arXiv: [0209003 \[gr-qc\]](#) (cit. on p. [14](#)).
- [20] H. Yoshino and V. S. Rychkov. “Improved analysis of black hole formation in high-energy particle.” In: *Phys. Rev. D* (2005), p. 104028. arXiv: [0503171 \[hep-th\]](#) (cit. on p. [14](#)).
- [21] K. S. Thorne. “NONSPHERICAL GRAVITATIONAL COLLAPSE: A SHORT REVIEW.” In: (1972) (cit. on p. [15](#)).
- [22] Douglas M. Gingrich. “Black hole cross-section at the large hadron collider.” In: *Int. J. Mod. Phys. A* (2006), pp. 6653–6676. DOI: [10.1142/S0217751X06035087](#). arXiv: [0609055 \[hep-ph\]](#) (cit. on p. [15](#)).
- [23] Paul Langacker. “The Physics of Heavy Z' Gauge Bosons.” In: *Rev. Mod. Phys.* (2009), pp. 1199–1228. DOI: [10.1103/RevModPhys.81.1199](#). arXiv: [0801.1345 \[hep-ph\]](#) (cit. on p. [15](#)).
- [24] Thomas G. Rizzo. “ Z' phenomenology and the LHC.” In: (2006). arXiv: [0610104 \[hep-ph\]](#) (cit. on p. [16](#)).
- [25] Amand Faessler, T.S. Kosmas, et al. “Constraints on R-parity violating supersymmetry from muon electron nuclear conversion.” In: *Nucl. Phys. B* (2000), pp. 25–44. arXiv: [9904335 \[hep-ph\]](#) (cit. on pp. [17](#), [123](#)).
- [26] CDF Collaboration. “Search for R-Parity Violating Decays of τ Sneutrinos to $e\mu$, $\mu\tau$, and $e\tau$ Pairs in $p\bar{p}$ Collisions at $\sqrt{s} = 1.96$ TeV.” In: *Phys. Rev. Lett.* (2010) (cit. on p. [17](#)).
- [27] Do Collaboration. “Search for Sneutrino Production in $e\mu$ Final States in 5.3fb^{-1} of $p\bar{p}$ Collisions at $\sqrt{s} = 1.96$ TeV.” In: *Phys. Rev. Lett.* (2010) (cit. on p. [17](#)).

- [28] Georges Aad et al. "Search for a heavy narrow resonance decaying to $e\mu$, $e\tau$, or $\mu\tau$ with the ATLAS detector in $\sqrt{s} = 7$ TeV pp collisions at the LHC." In: *Physics Letters B* (2013), pp. 15–32. ISSN: 0370-2693. DOI: <http://dx.doi.org/10.1016/j.physletb.2013.04.035>. URL: <http://www.sciencedirect.com/science/article/pii/S0370269313003249> (cit. on p. 17).
- [29] Georges Aad et al. "Search for a Heavy Neutral Particle Decaying to $e\mu$, $e\tau$, or $\mu\tau$ in pp Collisions at $\sqrt{s} = 8$ TeV with the ATLAS Detector." In: *Phys. Rev. Lett.* (2015), p. 031801. DOI: [10.1103/PhysRevLett.115.031801](https://doi.org/10.1103/PhysRevLett.115.031801). arXiv: [1503.04430](https://arxiv.org/abs/1503.04430) [hep-ex] (cit. on p. 17).
- [30] CMS Collaboration. "Search for lepton flavour violating decays of heavy resonances and quantum black holes to an $e\mu$ pair in proton–proton collisions at $\sqrt{s} = 8$ TeV." In: *The European Physical Journal C* (2016), p. 317. ISSN: 1434-6052. DOI: [10.1140/epjc/s10052-016-4149-y](https://doi.org/10.1140/epjc/s10052-016-4149-y). URL: <https://doi.org/10.1140/epjc/s10052-016-4149-y> (cit. on p. 17).
- [31] Morad Aaboud et al. "Search for new phenomena in different-flavour high-mass dilepton final states in pp collisions at $\sqrt{s} = 13$ TeV with the ATLAS detector." In: *Eur. Phys. J. C* (2016), p. 541. DOI: [10.1140/epjc/s10052-016-4385-1](https://doi.org/10.1140/epjc/s10052-016-4385-1). arXiv: [1607.08079](https://arxiv.org/abs/1607.08079) [hep-ex] (cit. on pp. 17, 18, 124, 127, 129).
- [32] X. Calmet, S. D. H. Hsu, et al. "Quantum gravity at a TeV and the renormalization of Newton's constant." In: *Phys. Rev. D* (2008), p. 125015. arXiv: [0803.1836](https://arxiv.org/abs/0803.1836) [hep-th] (cit. on p. 18).
- [33] Xavier Calmet. "Virtual Black Holes, Remnants and the Information Paradox." In: *Class. Quant. Grav.* (2015), p. 045007. DOI: [10.1088/0264-9381/32/4/045007](https://doi.org/10.1088/0264-9381/32/4/045007). arXiv: [1412.6270](https://arxiv.org/abs/1412.6270) [gr-qc] (cit. on p. 18).
- [34] Albert M Sirunyan et al. "Search for new physics with dijet angular distributions in proton-proton collisions at $\sqrt{s} = 13$ TeV." In: *JHEP* (2017), p. 013. DOI: [10.1007/JHEP07\(2017\)013](https://doi.org/10.1007/JHEP07(2017)013). arXiv: [1703.09986](https://arxiv.org/abs/1703.09986) [hep-ex] (cit. on p. 18).
- [35] Morad Aaboud et al. "Search for new phenomena in dijet events using 37 fb^{-1} of pp collision data collected at $\sqrt{s} = 13$ TeV with the ATLAS detector." In: (2017). arXiv: [1703.09127](https://arxiv.org/abs/1703.09127) [hep-ex] (cit. on pp. 18, 127).
- [36] Georges Aad et al. "Search for Quantum Black-Hole Production in High-Invariant-Mass Lepton+Jet Final States Using Proton-Proton Collisions at $\sqrt{s} = 8$ TeV and the ATLAS Detector." In: *Phys. Rev. Lett.* (2014), p. 091804. DOI: [10.1103/PhysRevLett.112.091804](https://doi.org/10.1103/PhysRevLett.112.091804). arXiv: [1311.2006](https://arxiv.org/abs/1311.2006) [hep-ex] (cit. on p. 18).
- [37] Georges Aad et al. "Search for high-mass dilepton resonances in pp collisions at $\sqrt{s} = 8$ TeV with the ATLAS detector." In: *Phys. Rev. D* (2014), p. 052005. DOI: [10.1103/PhysRevD.90.052005](https://doi.org/10.1103/PhysRevD.90.052005). arXiv: [1405.4123](https://arxiv.org/abs/1405.4123) [hep-ex] (cit. on p. 18).
- [38] Brandon Murakami. "The Impact of lepton flavor violating Z-prime bosons on muon g-2 and other muon observables." In: *Phys. Rev. D* (2002), p. 055003. DOI: [10.1103/PhysRevD.65.055003](https://doi.org/10.1103/PhysRevD.65.055003). arXiv: [hep-ph/0110095](https://arxiv.org/abs/hep-ph/0110095) [hep-ph] (cit. on p. 18).
- [39] Lyndon Evans and Philip Bryant. "LHC Machine." In: *Journal of Instrumentation* (2008), S08001. URL: <http://stacks.iop.org/1748-0221/3/i=08/a=S08001> (cit. on p. 19).

- [40] Esma Anais Mobs. “The CERN accelerator complex. Complexe des accélérateurs du CERN.” General Photo. 2016. URL: <http://cds.cern.ch/record/2225847> (cit. on p. 19).
- [41] CERN - BE-CO Group. “CERN Accelerator Performance and Statistics.” 2016. URL: <https://acc-stats.web.cern.ch/acc-stats/#lhc/overview-panel> (cit. on p. 20).
- [42] Tai Sakuma and Thomas McCauley. “Detector and Event Visualization with SketchUp at the CMS Experiment.” In: *Journal of Physics: Conference Series* (2014), p. 022032. URL: <http://stacks.iop.org/1742-6596/513/i=2/a=022032> (cit. on p. 21).
- [43] David Barney. “CMS Detector Slice.” CMS Collection. 2016. URL: <https://cds.cern.ch/record/2120661> (cit. on p. 23).
- [44] CMS Collaboration. *CMS TriDAS project: Technical Design Report, Volume 1: The Trigger Systems*. Technical Design Report CMS CERN/LHCC 2000-38 (cit. on p. 23).
- [45] I. Bird, K. Bos, et al. “LHC computing Grid. Technical design report.” In: CERN-LHCC-2005-024 (2005). Ed. by I. Bird (cit. on p. 24).
- [46] Vardan Khachatryan et al. “Performance of Electron Reconstruction and Selection with the CMS Detector in Proton-Proton Collisions at $\sqrt{s} = 8\text{ TeV}$.” In: *JINST* (2015), P06005. DOI: [10.1088/1748-0221/10/06/P06005](https://doi.org/10.1088/1748-0221/10/06/P06005). arXiv: [1502.02701](https://arxiv.org/abs/1502.02701) [[physics.ins-det](https://arxiv.org/abs/1502.02701)] (cit. on pp. 25, 47, 79).
- [47] W Adam, R Frühwirth, et al. “Reconstruction of electrons with the Gaussian-sum filter in the CMS tracker at the LHC.” In: *Journal of Physics G: Nuclear and Particle Physics* (2005), N9. URL: <http://stacks.iop.org/0954-3899/31/i=9/a=N01> (cit. on p. 25).
- [48] CMS Collaboration. “2015 ECAL detector performance plots.” In: CMS-DP-2015-057 (2015). URL: <https://cds.cern.ch/record/2114735> (cit. on p. 26).
- [49] CMS Collaboration. “Muon Reconstruction in the CMS Detector.” In: *CMS Analysis Note AN-08-097* (2009) (cit. on pp. 27, 28).
- [50] CMS Collaboration. “Design and Implementation of the Muon High-Level Trigger in CMS.” In: *CMS Physics Analysis Summary MUO-10-003* (2011) (cit. on p. 27).
- [51] R. Frühwirth. “Application of Kalman filtering to track and vertex fitting.” In: *Nucl. Instrum. Meth. A* (1987), pp. 444–450. DOI: [10.1016/0168-9002\(87\)90887-4](https://doi.org/10.1016/0168-9002(87)90887-4) (cit. on p. 28).
- [52] CMS Collaboration. “Search for New High-Mass Resonances Decaying to Muon Pairs in the CMS Experiment.” In: *CMS Analysis Note AN-07-038* (2008) (cit. on p. 28).
- [53] Jordan Tucker. “Tracker-plus-first-muon-station (TPFMS) reconstructor and the TMR cocktail.” In: *Talk from May 6* (2010). URL: <https://indico.cern.ch/subContributionDisplay.py?subContId=3&contribId=0&confId=93943> (cit. on p. 28).

- [54] Piotr Traczyk. “TeV Muons & Picky Muon Reco.” In: *Talk from May 6* (2010). URL: <https://indico.cern.ch/subContributionDisplay.py?subContId=2&contribId=0&confId=93943> (cit. on p. 29).
- [55] Piotr Traczyk and CMS Collaboration - MuonPOG. “Muon Object Review.” In: *Talk from November 28* (2012). URL: <https://indico.cern.ch/getFile.py/access?contribId=6&resId=0&materialId=slides&confId=172473> (cit. on p. 29).
- [56] Raffaella Radogna. “Search for high-mass resonances decaying into muon pairs with the CMS experiment at LHC.” PhD thesis. 2016 (cit. on p. 30).
- [57] CMS Collaboration. “Missing transverse energy performance of the CMS detector.” In: *Journal of Instrumentation* (2011), p. 9001. DOI: [10.1088/1748-0221/6/09/P09001](https://doi.org/10.1088/1748-0221/6/09/P09001). arXiv: [1106.5048](https://arxiv.org/abs/1106.5048) [physics.ins-det] (cit. on p. 30).
- [58] CMS Collaboration. “Particle-Flow Event Reconstruction in CMS and Performance for Jets, Taus, and MET.” In: *CMS Physics Analysis Summary PFT-09-001* (2009) (cit. on p. 31).
- [59] Stefan Höche. “Introduction to parton-shower event generators.” In: *Proceedings, Theoretical Advanced Study Institute in Elementary Particle Physics: Journeys Through the Precision Frontier: Amplitudes for Colliders (TASI 2014): Boulder, Colorado, June 2-27, 2015*, pp. 235–295. DOI: [10.1142/9789814678766_0005](https://doi.org/10.1142/9789814678766_0005). arXiv: [1411.4085](https://arxiv.org/abs/1411.4085) [hep-ph] (cit. on p. 33).
- [60] S. Banerjee. “CMS simulation software.” In: *J. Phys. Conf. Ser.* (2012), p. 022003. DOI: [10.1088/1742-6596/396/2/022003](https://doi.org/10.1088/1742-6596/396/2/022003) (cit. on p. 34).
- [61] S. Agostinelli, J. Allison, et al. “Geant4 a simulation toolkit.” In: *Nuclear Instruments and Methods in Physics Research Section A: Accelerators, Spectrometers, Detectors and Associated Equipment* (2003), pp. 250–303. ISSN: 0168-9002. DOI: [https://doi.org/10.1016/S0168-9002\(03\)01368-8](https://doi.org/10.1016/S0168-9002(03)01368-8). URL: <http://www.sciencedirect.com/science/article/pii/S0168900203013688> (cit. on p. 34).
- [62] J. Allison, K. Amako, et al. “Geant4 developments and applications.” In: *IEEE Transactions on Nuclear Science* (2006), pp. 270–278. ISSN: 0018-9499. DOI: [10.1109/TNS.2006.869826](https://doi.org/10.1109/TNS.2006.869826) (cit. on p. 34).
- [63] J. Allison, K. Amako, et al. “Recent developments in Geant4.” In: *Nuclear Instruments and Methods in Physics Research Section A: Accelerators, Spectrometers, Detectors and Associated Equipment Supplement C* (2016), pp. 186–225. ISSN: 0168-9002. DOI: <https://doi.org/10.1016/j.nima.2016.06.125>. URL: <http://www.sciencedirect.com/science/article/pii/S0168900216306957> (cit. on p. 34).
- [64] Torbjörn Sjöstrand, Stephen Mrenna, et al. “PYTHIA 6.4 physics and manual.” In: *JHEP* (2006), p. 026. DOI: [10.1088/1126-6708/2006/05/026](https://doi.org/10.1088/1126-6708/2006/05/026). arXiv: [0603175](https://arxiv.org/abs/0603175) [hep-ph] (cit. on p. 35).
- [65] Torbjörn Sjöstrand, Stephen Mrenna, et al. “A Brief Introduction to PYTHIA 8.1.” In: *Comput. Phys. Commun.* (2008), pp. 852–867. DOI: [10.1016/j.cpc.2008.01.036](https://doi.org/10.1016/j.cpc.2008.01.036). arXiv: [0710.3820](https://arxiv.org/abs/0710.3820) [hep-ph] (cit. on p. 35).

- [66] M. Bondarenko, A. Belyaev, et al. “High Energy Physics Model Database : Towards decoding of the underlying theory (within Les Houches 2011: Physics at TeV Colliders New Physics Working Group Report).” In: (2012). arXiv: 1203.1488 [hep-ph]. URL: <https://hepmdb.soton.ac.uk> (cit. on p. 35).
- [67] Johannes Bellm et al. “Herwig 7.0/Herwig++ 3.0 release note.” In: *Eur. Phys. J. C* (2016), p. 196. DOI: 10.1140/epjc/s10052-016-4018-8. arXiv: 1512.01178 [hep-ph] (cit. on p. 35).
- [68] Lars Sonnenschein et al. “Search for a LFV resonance in the e-mu, e-tau and mu-tau final states.” In: *Talk from August 16* (2012). URL: https://indico.cern.ch/event/197885/contributions/1479637/attachments/292354/408610/nonHadronic_16Aug2012.pdf (cit. on p. 35).
- [69] Douglas M. Gingrich. “Monte Carlo event generator for black hole production and decay in proton-proton collisions.” In: *Comput. Phys. Commun.* (2010), pp. 1917–1924. DOI: 10.1016/j.cpc.2010.07.027. arXiv: 0911.5370 [hep-ph] (cit. on p. 35).
- [70] CMS Collaboration EGamma POG. “Egamma ID Recipes for Run2.” In: *Twiki from 03.08* (2017). URL: <https://twiki.cern.ch/twiki/bin/view/CMS/EgammaIDRecipesRun2?rev=43> (cit. on p. 37).
- [71] Sam Harper et al. “HEEP Electron ID and isolation.” In: *Twiki from 30.08* (2017). URL: <https://twiki.cern.ch/twiki/bin/view/CMS/HEEPElectronIdentificationRun2?rev=28> (cit. on p. 37).
- [72] CMS Collaboration Muon POG. “Muon POG.” In: *Twiki from 06.09* (2017). URL: <https://twiki.cern.ch/twiki/bin/view/CMS/MuonPOG?rev=169> (cit. on pp. 40, 56).
- [73] CMS Collaboration Muon POG. “Baseline muon selections for Run-II.” In: *Twiki from 09.01* (2017). URL: <https://twiki.cern.ch/twiki/bin/view/CMS/SWGuideMuonIdRun2?rev=28> (cit. on p. 40).
- [74] Jordan Tucker. *Muon momentum resolution and charge mis-id using cosmic muons: some comparisons between 2011 data/MC*. slides: URL: <https://indico.cern.ch/event/183007/contributions/316223/attachments/248827/348006/tucker.pdf> (cit. on p. 47).
- [75] CMS Collaboration - JetMET POG. *MET Filters for Run II*. URL: <https://twiki.cern.ch/twiki/bin/view/CMS/MissingETOptionalFiltersRun2> (cit. on p. 48).
- [76] Halil Saka. *HCAL Noise and Noise Filters in 2016*. slides: URL: https://indico.cern.ch/event/534040/contributions/2178680/attachments/1280427/1901837/HCALnoise_JamboreeMeeting_27May2016.pdf (cit. on p. 48).
- [77] L. Thomas. *2016 Beam Halo Filter Update*. slides: URL: <https://indico.cern.ch/event/518559/contributions/2132815/attachments/1264581/1871184/beamhalostatus.pdf> (cit. on p. 49).
- [78] S. Argirò and others. *MET tails and filters for Run II startup*. slides: URL: <https://indico.cern.ch/event/376354/contributions/890337/subcontributions/68711/attachments/750171/1029181/edm-dpg-metfilters-12March2015.pdf> (cit. on p. 49).

- [79] Ken Call and others. *EcalDeadCellTriggerPrimitiveFilter and Variations on 2015D data*. slides: URL: <https://indico.cern.ch/event/502965/contributions/2012834/attachments/1240656/1824209/20160309MET.pdf> (cit. on p. 49).
- [80] Isabell Melzer-Pellmann. *Report from the MET Scanners*. slides: URL: https://indico.cern.ch/event/591506/contributions/2387636/attachments/1381281/2099935/2016_12_01_MET_Scanning_Report_PPD.pdf (cit. on p. 49).
- [81] Paolo Nason. "A New method for combining NLO QCD with shower Monte Carlo algorithms." In: *JHEP* (2004), p. 040. DOI: [10.1088/1126-6708/2004/11/040](https://doi.org/10.1088/1126-6708/2004/11/040). arXiv: [0409146](https://arxiv.org/abs/0409146) [hep-ph] (cit. on p. 51).
- [82] Stefano Frixione, Paolo Nason, et al. "Matching NLO QCD computations with Parton Shower simulations: the POWHEG method." In: *JHEP* (2007), p. 070. DOI: [10.1088/1126-6708/2007/11/070](https://doi.org/10.1088/1126-6708/2007/11/070). arXiv: [0709.2092](https://arxiv.org/abs/0709.2092) [hep-ph] (cit. on p. 51).
- [83] Simone Alioli, Paolo Nason, et al. "A general framework for implementing NLO calculations in shower Monte Carlo programs: the POWHEG BOX." In: *JHEP* (2010), p. 043. DOI: [10.1007/JHEP06\(2010\)043](https://doi.org/10.1007/JHEP06(2010)043). arXiv: [1002.2581](https://arxiv.org/abs/1002.2581) [hep-ph] (cit. on p. 51).
- [84] J. Alwall, R. Frederix, et al. "The automated computation of tree-level and next-to-leading order differential cross sections, and their matching to parton shower simulations." In: *JHEP* (2014), p. 079. DOI: [10.1007/JHEP07\(2014\)079](https://doi.org/10.1007/JHEP07(2014)079). arXiv: [1405.0301](https://arxiv.org/abs/1405.0301) [hep-ph] (cit. on p. 51).
- [85] B Clerbaux et al. *Search for High Mass Di-Electron Resonances with 2016 Data*. CMS Note 2016/190. 2016. URL: http://cms.cern.ch/iCMS/jsp/openfile.jsp?tp=draft&files=AN2016_190_v7.pdf (cit. on p. 53).
- [86] CMS Collaboration - PVT group. *Pileup reweighting*. URL: https://twiki.cern.ch/twiki/bin/view/CMS/PileupJSONFileforData#2015_Pileup_JSON_Files (cit. on p. 55).
- [87] Kyeongpil Lee et. al. "Single Muon Trigger Efficiencies of 80X Data and MC using T&P Method." In: *Presentation in Muon POG Meeting, Dec 14* (2016). URL: https://twiki.cern.ch/twiki/pub/CMS/MuonWorkInProgressAndPagResults/2016.12.14_MuonPOGTriggerSF_KPLee_v1.pdf (cit. on p. 56).
- [88] Fabrice Couderc. "2016 RECO SFs for Moriond17." In: *Presentation in Egamma POG Meeting, Jan 25* (2017). URL: https://indico.cern.ch/event/604907/contributions/2452907/attachments/1401460/2139067/RecoSF_ApprovalMoriond17_25Jan2017.pdf (cit. on p. 57).
- [89] B. Clerbaux et. al. "Search for high mass di-electron resonances with the full 2016 data." In: *CMS Note CMS AN-2016/404* (2016) (cit. on p. 57).
- [90] Erica Brondolin et. al. "2016 first results for muon tracking efficiency using tag and probe method." In: *Presentation in Cross POG Meeting, July 12* (2016). URL: https://indico.cern.ch/event/555227/contributions/2241170/attachments/1307875/1955811/EricaBrondolin_20160712_TagAndProbe_XPOG.pdf (cit. on p. 57).

- [91] Gael L. Perrin. “Muon ID Scale-Factor on 2016 ReReco.” In: *Presentation in Muon POG Meeting, Dec 14* (2016). URL: https://indico.cern.ch/event/595070/contributions/2405095/attachments/1388822/2114847/MC_12_12_2016.pdf (cit. on p. 57).
- [92] M. Oreglia. “A Study of the Reactions $\psi' \rightarrow \gamma\gamma\psi$.” PhD thesis. SLAC, 1980. URL: <http://www-public.slac.stanford.edu/sciDoc/docMeta.aspx?slacPubNumber=slac-r-236.html> (cit. on p. 72).
- [93] Alberto Escalante del Valle et. al. “Muon momentum scale at HighPt: Update in Generalized Endpoint.” In: *Presentation in Muon POG Meeting, April 4* (2016). URL: https://indico.cern.ch/event/516188/contributions/2039530/attachments/1252319/1847050/MuonScale_updatedV2.pdf (cit. on pp. 78, 156).
- [94] G. Abbiendi et. al. “Search for High-Mass Resonances Decaying to Muon Pairs in pp Collisions at $\sqrt{s} = 13$ TeV with the full 2016 data set of 37 fb^{-1} and combination with 2015 result.” In: *CMS Note CMS AN-2016/391* (2017) (cit. on pp. 78, 79).
- [95] CMS Collaboration - Muon POG. *Muon efficiencies*. URL: <https://twiki.cern.ch/twiki/bin/viewauth/CMS/MuonReferenceEfsRun2> (cit. on p. 79).
- [96] J. S. Conway. “Incorporating Nuisance Parameters in Likelihoods for Multi-source Spectra.” In: *Proceedings, PHYSTAT 2011 Workshop on Statistical Issues Related to Discovery Claims in Search Experiments and Unfolding*. 2011, pp. 115–120. DOI: [10.5170/CERN-2011-006.115](https://doi.org/10.5170/CERN-2011-006.115). arXiv: [1103.0354](https://arxiv.org/abs/1103.0354) [physics.data-an] (cit. on p. 80).
- [97] Roger J. Barlow and Christine Beeston. “Fitting using finite Monte Carlo samples.” In: *Comput. Phys. Commun.* (1993), pp. 219–228. DOI: [10.1016/0010-4655\(93\)90005-W](https://doi.org/10.1016/0010-4655(93)90005-W) (cit. on p. 81).
- [98] CMS Collaboration. “CMS Luminosity Measurements for the 2016 Data Taking Period.” Geneva, 2017. URL: <https://cds.cern.ch/record/2257069> (cit. on p. 81).
- [99] CMS Collaboration - Physics Validation group. *Utilities for Accessing Pileup Information for Data*. URL: <https://twiki.cern.ch/twiki/bin/view/CMS/PileupJSONFileforData> (cit. on p. 81).
- [100] CMS Collaboration - JetMET group. *Jet Energy Resolution*. URL: https://twiki.cern.ch/twiki/bin/view/CMS/JetResolution\#JER_Scaling_factors_and_Uncertai (cit. on p. 82).
- [101] CMS Collaboration - JetMET group. *MET Uncertainties*. Code at: URL: <https://github.com/cms-met/cmssw/blob/puppiMetFix803/PhysicsTools/PatUtils/python/tools/runMETCorrectionsAndUncertainties.py\#L731-\#L760> (cit. on p. 83).
- [102] LHC Physics. *NNLO+NNLL top-quark-pair cross sections*. URL: <https://twiki.cern.ch/twiki/bin/view/LHCPhysics/TtbarNNLO> (cit. on p. 83).
- [103] T. Gehrmann, M. Grazzini, et al. “ W^+W^- Production at Hadron Colliders in Next to Next to Leading Order QCD.” In: *Phys. Rev. Lett.* (2014), p. 212001. DOI: [10.1103/PhysRevLett.113.212001](https://doi.org/10.1103/PhysRevLett.113.212001). arXiv: [1408.5243](https://arxiv.org/abs/1408.5243) [hep-ph] (cit. on p. 83).

- [104] LHC Physics. *NLO single-top channel cross sections*. URL: <https://twiki.cern.ch/twiki/bin/view/LHCPhysics/SingleTopRefXsec> (cit. on p. 83).
- [105] CMS Collaboration - GEN group. *Standard Model Cross Sections for CMS at 13 TeV*. URL: <https://twiki.cern.ch/twiki/bin/viewauth/CMS/StandardModelCrossSectionsat13TeV> (cit. on p. 83).
- [106] Jon Butterworth et al. "PDF4LHC recommendations for LHC Run II." In: (2015). arXiv: 1510.03865 [hep-ph] (cit. on p. 84).
- [107] Richard D. Ball et al. "Parton distributions for the LHC Run II." In: *JHEP* (2015), p. 040. DOI: 10.1007/JHEP04(2015)040. arXiv: 1410.8849 [hep-ph] (cit. on p. 84).
- [108] S. Kallweit, Lindert, et al. "NLO QCD+EW predictions for $2\ell 2\nu$ diboson signatures at the LHC." In: (2017). arXiv: 1705.00598 [hep-ph] (cit. on p. 85).
- [109] Benjamin D. Pecjak, Darren J. Scott, et al. "Resummed differential cross sections for top-quark pairs at the LHC." In: *Phys. Rev. Lett.* (2016), p. 202001. DOI: 10.1103/PhysRevLett.116.202001. arXiv: 1601.07020 [hep-ph] (cit. on p. 87).
- [110] Eilam Gross and Ofer Vitells. "Trial factors or the look elsewhere effect in high energy physics." In: *Eur. Phys. J. C* (2010), pp. 525–530. DOI: 10.1140/epjc/s10052-010-1470-8. arXiv: 1005.1891 [physics.data-an] (cit. on p. 114).
- [111] R. M. Neal. "Probabilistic Inference Using Markov Chain Monte Carlo Methods." In: Technical Report CRG-TR-93-1 (1993) (cit. on p. 117).
- [112] M. Aaboud et al. "Search for new phenomena in different-flavour high-mass dilepton final states in pp collisions at $\sqrt{s} = 13$ TeV with the ATLAS detector." In: *The European Physical Journal C* (2016), p. 541. DOI: 10.1140/epjc/s10052-016-4385-1 (cit. on pp. 131, 135).
- [113] CMS Collaboration. "The CMS experiment at the CERN LHC." In: *Journal of Instrumentation* (2008), S08004. URL: <http://stacks.iop.org/1748-0221/3/i=08/a=S08004> (cit. on p. 148).